A Physical Approach To Interfacial Strength In Fibre Reinforced Thermoplastic Composites

A thesis presented in fulfilment of the requirements for the degree of Doctor of Philosophy

By

Liu Yang

Department of Mechanical Engineering

University of Strathclyde

Glasgow Scotland

UK

2011

DECLARATION OF AUTHENTICITY AND AUTHOR'S RIGHTS

This thesis is the result of the author's original research. It has been composed by the author and has not been previously submitted for examination which has led to the award of a degree

Signed:

Date:

ACKNOWLEDGEMENTS

I would like to thank

- my supervisor, Professor James Thomason, for giving me such an excellent opportunity to get involved in this composite research project, constant encouragement and invaluable guidance throughout this work, and great freedom to tackle the problems independently, for helping me cultivate scientific thinking and improve scientific communication skills, and for caring about my life and my family.

- Glasgow Research Partnership in Engineering (GRPE) for the generous financial support as well as Saudi Basic Industries Corporation (SABIC) and Owns Corning-vetrotex for the material supply.

- Chris Cameron, James Kelly, Jim Docherty, and Andy Crocket of the Department of Mechanical Engineering for their tremendous technical support to my laboratory work; Ian Airdrie of the Department of Chemical and Process Engineering for his help with the use of DSC; Dr John Liggett, of the Department of Pure and Applied Chemistry for the access to his laboratory; Dr Wenzhong Zhu of School of Engineering in University of The West of Scotland for the access to facilities for the nanoindentation test.

- my colleagues and friends, Fiona Gentles, Susan Reilly, Haihu Liu, Jianping Meng, for their constructive advice on my work and joyful time we spent together.

- my family and parents for the deep love they give me.

Contents

Abstract

It is well known that the fibre-matrix interface plays a key role in delivering the valuable merits of the fibre composites. In the case of thermosetting matrices the extent of fibre-matrix interaction can be considerably enhanced by improving the reactivity of the fibre surface with the reactive polymers and ultimately forming the efficient chemical bonds across the fibre-matrix interface. In the case of non-reactive matrices such as many of the thermoplastics employed in the composites industry, however, the practical adhesion is thought to be primarily the result of physical interactions combined with internal residual stresses between the fibres and the matrix. In order to control the interface of thermoplastic composites properly and thereby to provide the composites with improved mechanical performance and structural integrity, it is therefore essential to clearly understand the underlying mechanisms of adhesion in fibre reinforced thermoplastic composites.

In this work, the interface of the uncoated E-glass fibre (GF) and polypropylene homopolymer (PP) was mechanically studied. The thermo-mechanical properties of both constituents were first characterised. Two conventional pull-out techniques, the microbond and single fibre pull-out, were then developed in the laboratory. Excellent compatibility was found between these two test methods in this case. The value of 7.3 MPa for interfacial shear strength (IFSS) of GF-PP was obtained and the interface was likely to fail in a shear yielding style. Moreover, it was discovered that the thermo-oxidative degradation of PP matrix could occur when the microbond samples were made in air at elevated temperature. Degradation of PP matrix proved detrimental to the measured IFSS of GF-PP. It was therefore strongly recommended

that PP microbond samples should be formed in an inert atmosphere, such as nitrogen. However, it turned out that forming axisymmetrical PP microdroplets under nitrogen was very difficult at 220°C due to high viscosity and non-polar nature of the non-degraded PP. Studies on both PP microbond and macroscopic degraded PP samples showed that the change in their thermo-mechanical properties was mainly responsible for the decrease in IFSS in terms of a decrease in the compressive radial residual stress (CRRS) at the interface.

In order to investigate the effect of CRRS on the measured IFSS of GF-PP, a novel technique was developed by adapting the microbond testing to be carried out in a temperature controlled environment provided by a thermomechanical analyser (TMA). Excellent comparability was obtained for the IFSS of GF-PP measured at room temperature by the TMA-microbond and the "normal" microbond test configurations. TMA-microbond test was carried out in the temperature range -40°C up to 100°C and the results showed a highly significant inverse dependence of measured IFSS on testing temperature, particularly in the PP glass transition region. The compressive radial stress (CRS), including CRRS and the component resulting from molecular interaction, was estimated to account for the measured IFSS at different temperatures by combining with different values for coefficient of static friction (CSF) at GF-PP interface. This was carried out through a simple coulomb friction law. It was then concluded that at room temperature the fibre-matrix adhesion only made up of 29% of measured IFSS, while the CRRS is responsible for 71% of measured IFSS, which supports the hypothesis that the principal contribution to apparent IFSS of GF-PP comes from a static friction resulting from the combination of CRRS and CSF at the fibre-matrix interface.

List of Symbols and Abbreviations

E_{cl}	longitudinal elastic modulus in continuous fibre reinforced composites
σ_{cl}	longitudinal tensile stress in a continuous fibre reinforced composite
E_f	longitudinal elastic modulus of the fibre
E_m	elastic modulus of the matrix
σ_f	longitudinal tensile stress of the fibre
σ_m	tensile stress of the matrix
V_f	fibre volume fraction
V_m	matrix volume fraction
T	temperature
T_t	test temperature
T_p	processing temperature
t_p	processing time
L	fibre length
L_0	the length of a conceptual link
N	the number of the links in a fibre with a length of L
P_{L_0}	failure probability of the link
S_{L_0}	survival probability of the link
P_L	failure probability of the chain
S_L	survival probability of the chain
σ	applied stress
σ_l	lower strength limit in Weibull analysis
σ_u	upper strength limit in Weibull analysis
σ_0	scale parameter in Weibull analysis
m	shape parameter in Weibull analysis
$\overline{\sigma}$	mean fibre strength
$\overline{\sigma}_0$	mean strength of the link
q	mixing parameter in Weibull analysis

A_f	cross-sectional area of the fibre
D_f	fibre diameter
ΔL	measured displacement
ΔL_f	displacement of the fibre
ΔL_s	displacement of the fixture
ΔF	applied force
C_s	system compliance
ΔT	temperature difference
ΔL_{sp}	change of specimen length
ΔL_{obs}	measured change in length
α_{stage}	mean CLTE for stage
ΔL_{blank}	change of baseline due to heating
k	calibration coefficient
$\langle \alpha_l \rangle$	mean coefficient of linear thermal expansion
T_g	glass transition temperature
T_{eim}	melting extrapolated onset temperature
T_{pm}	melting peak temperature
T_{eic}	crystallisation extrapolated onset temperature
T_{pc}	crystallisation peak temperature
ΔH_m	heat of fusion
E'	storage modulus
E''	loss modulus
δ	phase angle between applied force and measured displacement
$\tan\delta$	damping index
x_c	degree of crystallinity
W_a	work of adhesion
γ_{SV}	surface free energy of the solid-vapour
γ_{LV}	surface free energy of the liquid-vapour

γ_{SL}	surface free energy of the liquid-solid interface
θ	contact angle at the contact of three phases
G_{ic}	interfacial fracture toughness
τ_{ult}	interfacial shear strength
τ_{app}	apparent interfacial shear strength
σ_{ult}	adhesional strength
F_{max}	completely debonding load
L_e	fibre embedded length
A_e	fibre embedded area
D_m	maximum resin droplet diameter
F_{fr}	interfacial friction force
τ_{fr}	interfacial friction strength
σ_{rad}	compressive radial residual stress
F_d	initial debonding force
L_{fr}	free fibre length
L_{max}	maximum embedded fibre length
σ_d	fibre stress at debonding
G	energy release rate
σ_{fu}	ultimate strength of the fibre
σ_y	tensile strength at yielding
τ_y	shear strength at yielding
μ_{dy}	coefficient of dynamic friction
F_{st}	static friction
P	normal force across the interface
μ_{st}	coefficient of static friction
σ_n	compressive radial stress across the interface
μ_{st}^*	upper boundary of the coefficient of static friction
ΔP	pressure difference between liquid and vapour
R_1, R_2	two principal radii of curvature at a point in the surface

T_{ref}	stress free temperature
α_f	coefficient of thermal expansion of the fibre
α_m	coefficient of thermal expansion of the matrix
ν_f	Poisson's ratio of the fibre
ν_m	Poisson's ratio of the matrix
V	total volume of the microbond sample
$D_m^{'}$	the diameter of the converted matrix cylinder
APS	γ-aminopropyltriethoxysilane
CDF	cumulative distribution function
CLTE	coefficient of linear thermal expansion
CRS	compressive radial stress
CRRS	compressive radial residual stress
CSF	coefficient of static friction
CSM	continuous stiffness measurement
CTE	coefficient of thermal expansion
CV	coefficient of variation
DMA	dynamic mechanical analyser
DSC	differential scanning calorimetry
GF	E-glass fibre
IFFS	interfacial friction strength
IFNS	interfacial normal strength
IFSS	interfacial shear strength
I-MBT	Instron-microbond test
iPP	isotactic polypropylene
IR	index of refraction
LEFM	linear elastic fracture mechanics
MBT	microbond test
MFR	melt flow rate
MW	molecular weight
MWD	molecular weight distribution

PDF	probability density function
PE	linear polyethylene
PP	polypropylene homopolymer
RTS	residual thermal stress
SEM	scanning electronic microscope
SFPT	single fibre pull-out test
S/V	surface-to-volume ratio
TDA	thermodilatometry
TGA	thermogravimetric analyser
TMA	thermomechanical analyser
TMA-MBT	TMA-microbond test

List of Figures

List of Tables

Introduction

In general the fibre-matrix interface plays a key role in delivering the valuable merits of the fibre composites. It is due to the presence of this interface between the fibre and the matrix that the fibre composites are able to produce a combination of mechanical properties that cannot be achieved with either of the constituents acting alone. For example, the fracture energy of glass is 6.98 J/m^2, that of a typical plastic 219.87 J/m^2 and a composite of the two 174500 J/m^2. Moreover, the fibre-matrix interface has long been recognised to have a critical influence on the overall mechanical performance of the composites such as the stiffness and strength. It is because of this fundamental role that the interface plays in determining composite properties, tremendous efforts have been dedicated to controlling the interface properties, which are becoming gradually accepted as design and process variables to be tailored for particular end applications.

It is well known that the properties of an interface are governed largely by the chemical/morphological nature and physical/thermodynamic compatibility between the two constituents. Furthermore, these factors can also be significantly altered in the process of composite formation. To control the interface properly and thereby to provide the composite with improved mechanical performance and structural integrity, it is therefore essential to understand the mechanisms of interfacial adhesion, which may have distinct difference between thermosetting and thermoplastic composites. The former normally involve a potentially reactive interface, whose efficiency is routinely improved by forming the strong chemical bonds across the fibre-matrix interface. Most thermoplastics employed in the

composites industry, however, have non-reactive nature and the practical adhesion in thermoplastic composites is considered to be primarily the result of physical interactions combined with internal residual stresses between the fibres and the matrix. This project is carried out to test this hypothesis and obtain a better understanding of the underlying mechanisms of interfacial strength in fibre reinforced thermoplastic composites.

In this work, the combination of glass fibre (GF) and polypropylene (PP) was first selected and mechanical properties of both constituents were then characterised. This work is covered in chapter 1 and 2 respectively. To characterise the mechanical performance of the GF-PP interface, two conventional single fibre techniques, microbond and single fibre pull-out, were developed and described in chapter 3. Sample preparation for microbond samples proved quite challenging due to the thermo-oxidative degradation of PP matrix could occur. The effect of thermo-oxidative degradation of PP matrix on interfacial strength is discussed in chapter 4. In order to investigate the effect of internal residual stress on the adhesion of GF-PP, a novel technique was developed by adapting the microbond to be carried out in a temperature controlled environment provided by a thermomechanical analyser (TMA). This work is described in chapter 5. Overall conclusions and suggestions for further work can be found in chapter 6.

In terms of the structure of the thesis, the author finds it more relevant and efficient to distribute the literature review as well as the reference into each chapter rather than have a bulk independent section.

Chapter 1

Mechanical Characterisation of Glass Fibre

1.1 Literature review

1.1.1 Definition of glass and its atomic structure

As one of the most familiar substances one could encounter in daily life, glass plays an essential role in today's science and industry. A glass is defined as an inorganic substance in a condition which is continuous with, and analogous to, the liquid state of that substance, but which, as a result of a reversible change in viscosity during cooling, has attained so high a degree of viscosity as to be for all practical purposes rigid [1]. Thus, on the sufficiently short time scales of usual experiments the glass can essentially be regarded as an amorphous solid formed by rapid cooling from its very low viscosity state. Such melt quenching gives rise to insufficient time that molecules (depending on what material the glass is based on) would need for arrangment into a regular structure (i.e. crystallisation); instead, they are more or less frozen in the positions they had in the liquid phase. This accounts for the fact that their structure does not possess a long-term order or three-dimensional periodicity as in crystalline materials. However, the characteristics of rigidness imply that glasses have a high degree of short-range order (i.e. at the scale of a few angstroms). Solids that exhibit this type of positional disorder are called glasses [2]. For silica (SiO_2)-based glasses this short-range order is considered to stem from the local atomic polyhedra based on SiO_2 , which forms the basis of very nearly all commercial glasses [1]. The molecule SiO_2 does not exist in the way the chemical formula

assumes but as a polymer $(SiO_2)_n$; in the form of quartz silica consists of a continuous three-dimensional network of repeated rings containing 3 or 6 SiO_4 groups [1]. As the basic structural unit of silicates and silicate glasses, the SiO_4 has a tetrahedral structure with the four oxygens at the corners and the silicon at the centre of the tetrahedron (see Figure 1.1).

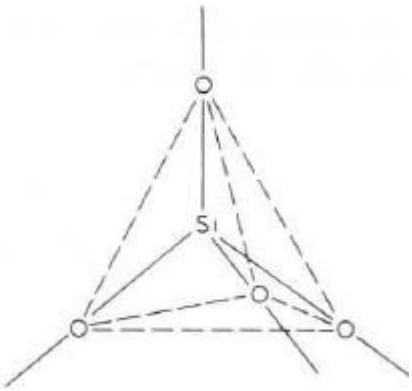

Fig. 1.1 The silica tetrahedron, the basic structural unit of silicates and silicate glasses [1]

1.1.2 Silicate glass composition

A glass would form after silica is heated at 2000°C until fluid and then undergo a rapid cooling process. Glass or glass fibres made of silica have advantages such as high modulus and strength, good chemical and temperature resistance, high UV transmission, and extremely low coefficient of thermal expansion. However, the nature of high temperature needed for silica glass formation means that this process is too costly to be accepted as a commercial routine. Therefore, additional metal oxides are mixed with silica to lower the processing temperature down to 1300°C to 1600°C and in turn improve the formability. The introduction of other oxides, for instance, Al_2O_3, B_2O_3, CaO etc, can modify the silica network by interrupting its

continuity and in turn making its structure more irregular. Addition of such elements therefore tends to lower the stiffness and strength, but improves the formability. Depending on how they interfere with the silica network, these oxides are generally categorised into three groups. One group includes oxides that are capable of forming their own network and others that can modify the silica network fall into the second group called network modifiers. The third group includes some intermediate oxides that can do both [1]. By manipulating these ingredients, a variety of compositions have been commercially established to give a wide range of glass products with different properties. These products have found themselves a vast market for various applications. Among them is the reinforcement in polymer composites, in which a certain amount of the reinforcement in some type of form is embedded in the polymer normally called matrix. Although the reinforcement in a composite may be fibrous or particulate, most of the major high performance developments in recent times have been in the area of fibrous reinforcement. In fact, since commercial production of reinforced polymers began around 1940, glass fibres have remained the highest volume fibre reinforcement for plastics [3]. Figure 1.2 shows comparison of global reinforcement fibre use in 2010.

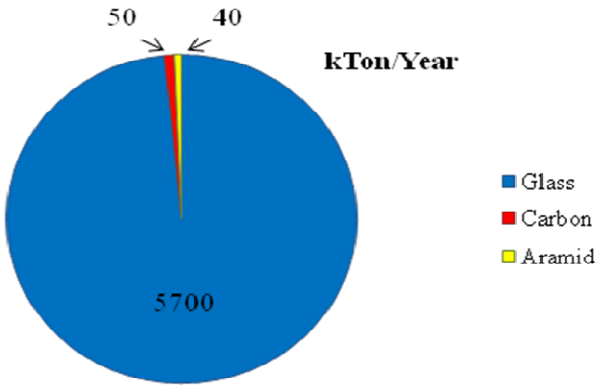

Fig. 1.2 Global reinforcement fibre use in 2010 [4]

This high demand is primarily the result of the high performance (specific tensile strength and specific modulus) per unit cost of the glass fibre reinforcement.

Commercial compositions for glass fibres vary considerably and have been historically designated by letters such as E, C, and S). Each letter represents a small range of compositions as shown in Table 1.1.

Table 1.1 composition ranges of commercial glass fibres (weight %) [5]

	E	S	C	A
SiO_2	52–56	64.3–65	60–65	72–72.5
Al_2O_3	12–16	24.8–25	2–6	0.6–1.5
B_2O_3	0–13		2–7	
CaO	16–25	0.01	13–16	9–10
MgO	0–6	10–10.3	3–4	2.5–3.5
K_2O			0–2	
Na_2O	0–1	0–0.27	7.5–12	13–14.2
TiO_2	0–0.4			
Fe_2O_3	0.05–04	0–0.2		
F_2	0–0.5			
SO_3				0.7

The letters imply certain special properties. For example, E= electrical (low electrical conductivity), C= chemical (high chemical durability), S= strength (high strength), and A= alkali (soda lime glass). From the point of view of composite technology the E-glass fibre is currently of the most importance, since it accounts for over 99% of all continuous glass fibre produced in the world and dominates the world market for reinforcing fibre. Table 1.2 lists the typical range of properties of E-glass fibre together with others.

Table 1.2 Properties of commercial glass fibres [5]

Properties	E	S	C	A
Specific gravity: fibre	2.54–2.55	2.48–2.49	2.49	2.50
Thermally compacted	2.58–2.62	2.51–2.52	2.54	
Index of refraction at 589.3nm: fibre	1.547	1.523	1.541	1.512
Thermally compacted	1.552–1.562	1.529		
Dielectric constant (at 21°c, 10^6hz)	5.86–6.6	4.53–4.6	6.24–6.30	6.90
Specific heat (cal g^{-1} °c^{-1})	0.192	0.176	0.19–0.21	
Linear expansion coefficient ($\times10^{-6}$ °C^{-1})	4.9–6.0	2.9–5.0	7.0–7.2	9.0
Liquidus temperature (°C)	1065–1120	1500		
Fiberizing temperature (°C)	1270–1300	1565		1280
Strain point (°C)	616	760	552	
Annealing point (°C)	657	810	588	
Softening point (°C)	845	968	750	695–720
Young's modulus: fibre (GPa)	72.4–76	84–88	70	72.5
Thermally compacted (GPa)	86	95		
Possion's ratio	0.20–0.22			
Virgin fibre tensile strength at RT (GPa)	3.5	4.6	2.7–3.1	2.41
Fracture toughness (MPa $m^{1/2}$)	0.90	1.2		
Stress corrosion susceptibility exponent	28–31	40		

It can be seen that E-glass fibre has fairly high Young's modulus, high strength and relatively low liquidus temperature. When it comes to reinforcement materials, Young's modulus and failure strength are usually the parameters that tend to draw the most concern, because they determine to what extent the material would potentially reinforce other components in composite materials. For example, in the case of continuous fibre reinforced composites, their elastic modulus and stress in the axis of the fibres (i.e. longitudinal direction) are governed by a rule of mixture expressed by Equation (1.1) and (1.2) respectively,

$$E_{cl} = E_f V_f + E_m V_m \qquad (1.1)$$

$$\sigma_{cl} = \sigma_f V_f + \sigma_m V_m \qquad (1.2)$$

where E_{cl} and σ_{cl} are tensile modulus and stress of the composites in the longitudinal direction; E_f and σ_f are longitudinal tensile modulus and stress of the fibre; E_m and σ_m are tensile modulus and stress of the matrix; and V_f and V_m are fibre volume fraction and matrix volume fraction respectively.

1.1.3 Glass fibre forming process

It is known that physical properties of a glass fibre are controlled by not only the composition but also the forming history, which involves the temperature of molten glass and the thermo-mechanical history during fibre attenuation [5]. The variation in these conditions can lead to changes in the underlying atomistic structure and bonding. Figure 1.3 shows a typical glass fibre forming process.

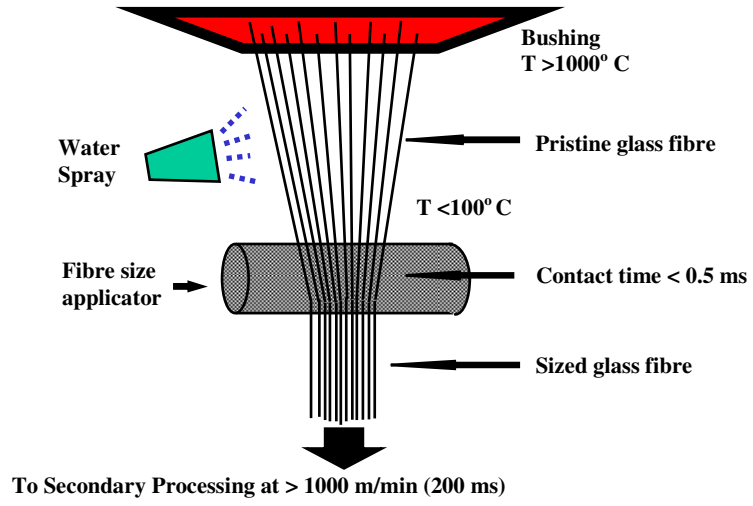

Fig. 1.3 Glass fibre forming process [4]

Raw materials or glass marbles are first melted in a ceramic furnace and subsequently fed into a platinum-alloy furnace named bushing, which has a

multiplicity of nozzles ranging from 0.75 to 2.0 mm in its base [1]. The molten glass flows under gravity through those nozzles and are immediately cooled down by fine water sprays below the bushing. Next follows a fibre size applicator which provides a moving surface coated with fibre size with which the moving fan of filaments makes contact, thus picking up the fibre size. The sizing pickup occurs over a contact distance of approximately 10 mm [1]. These individual filaments are collected by a gathering shoe (not shown in Figure 1.3), which combines them to form a strand or a number of smaller strands. The fibre strands are then guided to enter the secondary processing stage, which will convert the fibres into final products, for example, roving or chopped fibre as shown in Figure 1.4.

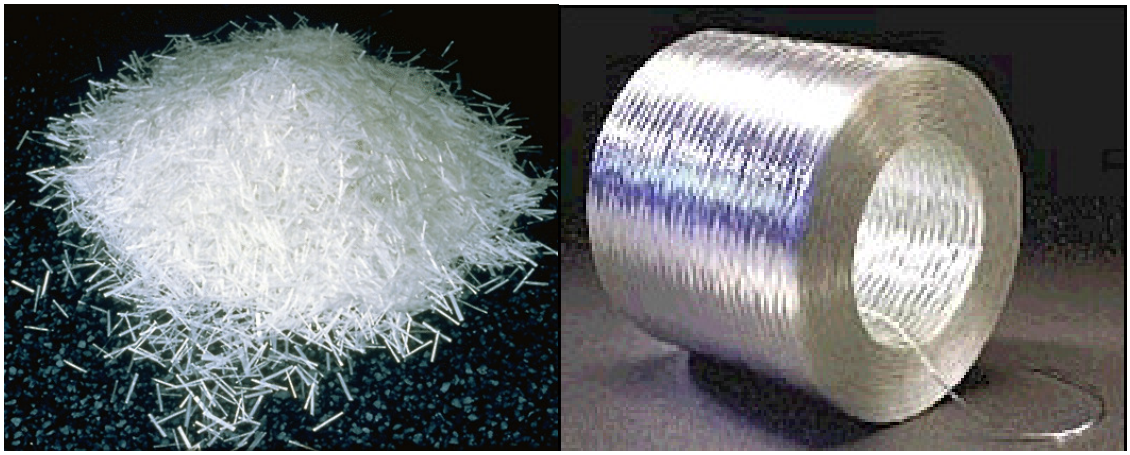

(a) (b)

Fig. 1.4 Chopped glass fibre (a) and roving (b) [4]

Control of the fibre diameter is achieved by adjusting the viscosity of the glass (dependent on composition and temperature), the diameter of the nozzles and the winding speed. The glass fibres immediately below the bushing are usually considered as the pristine fibres or virgin fibres, which are considered not to have severe surface defects caused by subsequent manufacturing process and handling but may still have inherent defects as a result of thermal fluctuations. By making a very

rapid contact with the rolling applicator, a certain type of fibre size normally in an aqueous emulsion is applied to the glass fibre surface. The size is crucial to the handleability of the fibres and their compatibility with matrix resins. The formulations of glass fibre sizes are specified by the products to be made and their performance in the composites made from them. In most cases, the fibre size must be formulated to combine lubrication with specified handling characteristics of the strand to cover the various stages during the manufacture of glass fibre reinforcing products and to deposit onto the glass fibre surface specific chemicals designed to improve the adhesion between the fibres to the matrix resin. The glass fibre size, thus, consists of the following main components:

(i) film former, which when dried, holds the filaments together in a strand and protects the filaments from damage through fibre-fibre contact and fibre-process contact.

(ii) auxiliary agents that normally include lubricants, antistatic agent, wetting agent.

(iii) coupling agent used to improve the adhesion between the fibre and the matrix. Nearly all currently used coupling agents are based on certain type of organofunctional silane, which has a general structure as illustrated below.

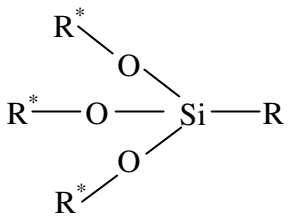

R^* is methyl (CH_3) or ethyl (C_2H_5) and R is a reactive or resin compatible functional group which may interact with either or both the film former and the matrix resin. In the aqueous size, the Si-OR^* groups hydrolyse. This is often acid catalysed by adjusting the pH to ≈ 3.5 with acetic acid [6]. The silanol groups can further react with both each other and glass fibre surface, leading to a complex deposit on the glass surface. It is generally accepted that there are three distinct layers or components deposited onto the glass surface as observed by differing hydrolytic stabilities:

(i) a strongly chemisorbed layer at the immediate glass surface,

(ii) a chemisorbed tridimensional layer of polysiloxane, and

(iii) a physisorbed layer of cyclic and linear oligomers [6].

1.1.4 Difference between glass and glass fibre

From the glass fibre forming process described above, one can tell that glass fibre differs from bulk glass of the same composition in three major respects. First, the glass fibre undergoes much more rapid cooling from its molten state, which is of the order of 10^{-4}–10^{-3}s/°C. Quenching from very high temperatures increases the temperature gradient from the fibre surface to the core, which may lead to a thin surface layer whose structure differs from that in the core. Bartenev [7, 8] investigated the effect of fibre structure on its strength and suggested that there exists a thin surface layer, which can increase the fibre strength by freezing a more homogeneous high temperature glass structure in the surface layer, orientation of the structural network of the glass along the axis of the fibre, and building up residual

thermal stresses between the layer and the core. However, there is no experimental evidence of the presence of residual stresses in thin glass fibres (of $\leq$ 20μm) and theoretical estimates also indicate that these stresses are negligible in fibres [5]. Second, the glass fibre experiences mechanical loading along the axis of the fibre. Mechanical loading applied to the fibre during the fibre attenuation may cause orientation of the atomic structure along the longitudinal direction. Consequently anisotropy in the properties of the glass fibre may occur [9]. However, this along with the existence of the thin surface layer still remains open to debate [10]. Third, the glass fibre possesses a much higher ratio of surface area to weight. For an average fibre diameter of 10 μm, 10 g of fibre have a surface area of approximate 2 m^2 [1]. Fibre surface plays a very critical role in composite materials. As will be indicated later, glass surface has the predominant effect on its own practical strength. Furthermore, the physical and chemical states of this outer boundary determine in what manner the surface will interact with the matrix. Consequently between the fibre and the matrix may be formed a special zone termed as interface or interphase, which may have the composition and structure, and hence properties completely distinguish from both constituents. Parallel to the increasing recognition of the importance and complexity of this region has been the tremendous research effort put into developing better understanding of the interface and in turn tailoring the performance of the composite materials by modifying this area.

1.1.5 Young's modulus and glass strength

Like density and refractive index, Young's modulus is a structure-related property and in the case of glass fibre it depends on the composition of the glass and its

forming history. The composition dependence of modulus has been well exhibited in Table 1.2 In addition, Young's moduli of fibres of the same composition have been found to increase with an increase in fibre diameter [11]. The severe quenching of the glass in the process of fibre forming leads to decrease in modulus, which can be compensated by subsequent heat treatment [12]. The strength (i.e. tensile strength) of glass fibres, on the other hand, presents a more complex picture, but this may well be due to the larger amount of research that has been devoted to it. Theoretically, the tensile strength of silica glass should be in the region of 14 GPa, which has also been observed in some specially made fibres [13]. Most glasses have moduli of elasticity of approximately 70 GPa, and thus it is seen that from theoretical consideration, assuming the validity of Hook's law to the breaking stress, strains of 20% should be possible. However, extensions of this order are never realised, owing to a practical strength considerably lower than the theoretical one. In practice, the tensile strength of bulk glass is found to be very low. This is mainly attributed to the surface condition of the glass, namely due to stress concentrations arising from structural (Griffiths) flaws in the surface, or scratches (as seen in Figure 1.5 [14]) or dirt particles embedded in the surface during manufacturing processes [15]. This can be demonstrated by removing the surface by chemical etching [16].

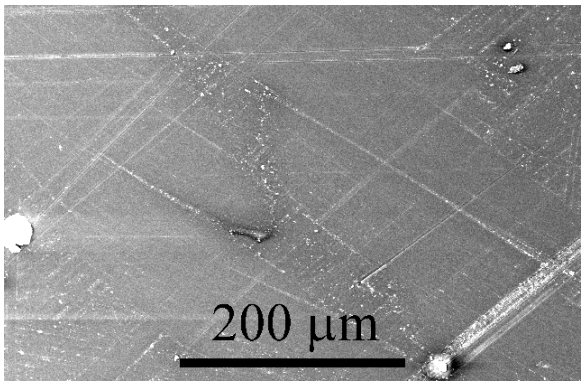

Fig. 1.5 SEM photograph of the surface of a glass rod as received [14]

The Griffiths flaw theory originated from the foundational paper of fracture mechanics published by A. A. Griffith in 1921 [17]. In this paper, Griffith postulated that glass contained numerous microscopic flaws and cracks and that surface defects were more detrimental to the fracture strength than internal ones. For thin fibres, however, a microscopic flaw on the surface would have a catastrophic effect on strength; it is now believed that surface defects of the Griffith type are very few on fine fibres, and that the main reason for failure of glass fibres is stress corrosion induced by water and ion exchange in the glass surface [18, 19]. While the Griffith criterion for fracture predicted a critical stress for spontaneous failure, other researchers started to realise that glass fracture was actually a kinetic process, which involves a chemical reaction between the water inevitably adsorbed in the glass surface or/and moisture in the atmosphere and the stressed siloxane bonds at the crack tip, leading to slow growth of the crack length [20]:

$$\underset{}{H_2O\ (\text{adsorbed})} + \underset{(\text{Siloxane bond})}{\equiv Si{-}O{-}Si\equiv} \xrightarrow{(\text{tensile stress})} \underset{(\text{broken bonds})}{2Si{-}OH}$$

The reaction rate has proved to be controlled by the force applied to the glass and the amount of water vapour in the atmosphere [18, 21-23]. This stress corrosion mechanism has been used to explain a well known phenomenon: static fatigue, or delayed failure, wherein a pre-existing crack under constant stress less than the strength that would be obtained without fatigue slowly grows from subcritical to critical Griffith size that results in a transition from the relatively slow crack growth associated with stress corrosion to the fast crack propagation associated with purely mechanical failure. Although stress corrosion on a pre-existing crack is well understood, fatigue is also observed in pristine fibres and the reason for it still

remains unclear. The delayed failure and related aspects for glass fibre have been studied by many workers, who tested glass samples with different compositions in different test conditions, namely test method (pure tension or bending), strain rate, temperature, and relative humidity [18, 21, 24, 25]. As a consequence, a slow crack growth model has been developed to take into account the effect of stress corrosion on measured strength. Equation (1.3) describes completely the dependence of measured strength $S(T, \varepsilon^{\bullet}, X)$ on strain rate, temperature, and relative humidity of the testing environment [5].

$$S(T, \varepsilon^{\bullet}, X) = \frac{S_{LN}}{\left[1 + \Phi S^{3}(T, \varepsilon^{\bullet}, X)\right]^{1/(N-2)}} \qquad (1.3)$$

$$\Phi = \left[\frac{(N-2)V_0 X^{\alpha} \exp(-Q/RT) Y^{2}}{2(N+1)\varepsilon^{\bullet} E(T) K_{IC}^{2}(T)} \right]$$

where T, $\varepsilon^{\bullet}$, and X are temperature, strain rate, and the humidity, N is a positive constant called the stress corrosion susceptibility coefficient, S_{LN} is liquid nitrogen temperature strength, Q is the activation energy for stress corrosion, R is the gas constant, $K_{IC}(T)$ is the fracture toughness at temperature T, $E(T)$ is the Young's modulus at temperature T, α is the humidity exponent, V_0 is velocity of glass at the tip exit, and Y is the dimensionless constant relating stress to stress intensity factor. It has been shown that the predictions of the slow crack growth model are in quantitative agreement with the data on the strength of E-glass fibre, provided a value in the range of 25 to 30 assumed for the stress corrosion susceptibility coefficient. Equation (1.3) clearly shows that for a glass fibre that has a specific

composition and undergoes a specific forming process, its strength also depends on the way it is measured. In other words, the measured strength is a function of testing variables. Figure 1.6 shows an exhaustive list of the parameters which may influence the measured fibre strength.

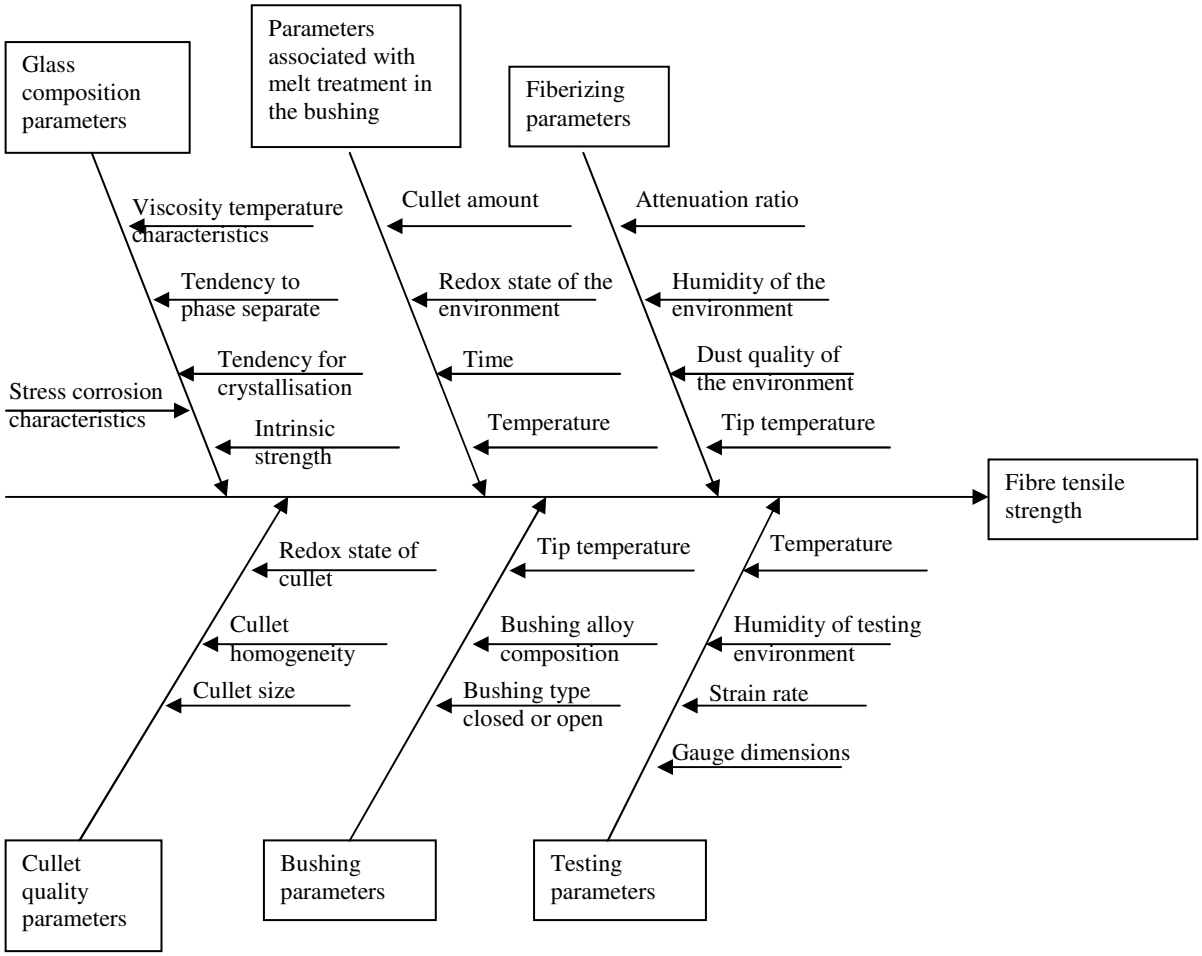

Fig. 1.6 Fish-bone chart of the experimental parameters which may influence the measured strength of melt-dawn fibres [20]

It is probably due to the fact that the measured fibre strength can be affected by so many factors that recently different terms for the measured strength of glass and glass fibre have been proposed [13, 20, 26, 27]. These terms are listed in Table 1.3.

Table 1.3 Types of measured strengths [26]

	Fatigue-free	Inert	Environmental Fatigue
Intrinsic	σ_0^*	σ_i^*	σ^*
Extrinsic	σ_0	σ_i	σ

Strength measured in the absence of extrinsic defects is called intrinsic strength. The intrinsic strength is measured when the following conditions are satisfied [26]:

(i) No dependence of measured strength on fibre diameter or length

(ii) The coefficient of variation in strength values is approximate two times the coefficient of variation in the fibre diameter values.

(iii) High measured fracture strengths (or fracture strains).

In the case of glass fibre, the intrinsic strength may be obtained by testing pristine fibres, which usually involves a careful preparation of the starting materials, careful forming fibres in ultra-clean environment, capturing fibre samples before they come in contact with any other surface (such as the size applicator or the gathering shoe), and testing of a large number of small fibre lengths immediately after capture with minimum additional handling [20]. It should be emphasised that the intrinsic strength is still affected by fatigue and all intrinsic defects such as point defects, structural inhomogeneities caused by frozen-in density, composition fluctuations, and nanoscale roughness on glass surface [20, 26]. Fatigue under inert condition (such as vacuum and dry environment) is referred to as inert fatigue, whereas environmentally enhanced fatigue is termed as environmental fatigue. Note that the inert condition can also be created by testing at a sufficiently low temperature or in normal

environment using very rapid strain rates. When fatigue does not occur at all, the measured strength is defined as fatigue-free strength. These terms are also applied to non-pristine fibres that do have extrinsic defects. The strengths of non-pristine fibres are extrinsic by definition and controlled by flaws. Extrinsic strengths show a larger coefficient of variation, which is mainly attributed to the variation in the severity of the most severe flaws in different samples. In light of such nomenclature, one may say that intrinsic fatigue strength for E-glass fibre is approximately 3.5 GPa and intrinsic inert strength for E-glass fibre is approximately 5.8 GPa.

A brief summary should be given before moving on to another major characteristic of the strength of glass fibre. The strength of a pristine glass fibre (i.e. intrinsic strength) is determined by composition of the glass and its structure. The intrinsic strength does not vary with its length and diameter (i.e. volume). The strength of a non-pristine glass fibre (i.e. extrinsic strength) is controlled by the most severe flaw on it. The extrinsic strength is a function of test variables such as the strain rate used, the relative humidity and the temperature of the testing environment because of the fatigue based on stress corrosion mechanism. The slow crack growth model has been developed to quantitatively account for these effects on fatigue in the non-pristine fibre. The intrinsic strength is also found to be influenced by test variables in a similar way to non-pristine fibre. However, the reason for that is not completely clear.

1.1.6 Dimension effect and Weibull distribution

Dimension effect is another major brittle solid characteristic that researchers have long been aware of. It basically states a simple fact that when the strength of brittle solids is determined by random distributed flaws with various dimensions, the

average measured strength will decrease as the volume of the sample increases. In the case of glass fibre, dimension effect is reflected in the strength reduction with the increase in either tested fibre length or diameter [28-31]. The is because the larger the sample dimension is, the more statistically probable it is for the sample to encounter more severe flaws no matter whether there exist one or multiple populations of flaws along the length of fibres. Thus, dimension effect cannot be seen when the sample dimension is either infinite large or small. The former will always give the lowest value for the strength determined by the most severe flaw in the entire flaw population and the latter will generate intrinsic strength as defined earlier, since the sample is too small to contain any flaw. In practice, the general capability of instrumentation hardly allows the samples close to those extreme conditions to be tested. Therefore, when brittle fibres with finite dimensions are prepared under identical conditions, the measured strength has a distribution rather than a unique value. In this sense the variation in measured strength for brittle solids can be considered to originate from the combination of randomness of flaw dimension and finiteness of measured sample dimension.

It is because of this unpredictable variation that it is recognised that measured strength needs to be analysed using different probabilistic approaches. Among them is the most successful Weibull distribution, which was pioneered in 1939 by W. Weibull [32]. Later in 1951 he applied the statistical treatment to the fibre strength [33]. The approach is referred to as the weakest link theory, which assumes that a length L of chain-like structure is composed of N length L_0 links in series (i.e. $N = \frac{L}{L_0}$) and fracture of the chain occurs when the weakest link fails. This correctly

reflects the behaviour of a brittle solid, for a crack, developed from the most critical defect, immediately induces the failure of the material. The assumptions of this model are:

(1) the stress field in each element is uniform

(2) the strength of one element is independent of that of the other elements

(3) all elements have the same failure probability for a given applied stress.

In terms of defects, the first assumption implies that local modifications of the stress field around defects are negligible so that each link can be considered as being subjected to a uniform stress field, the second assumption means that there is no interaction between the defects, and the third assumption implies that the defect distribution must be homogeneous and isotropic. When the chain is under an applied stress σ_f, the failure probability of each link, P_{L_0}, is the probability that this applied stress is greater than or equal to the strength of the link, while the probability of survival of each link, S_{L_0}, is the probability that this applied stress is lower than the strength of the link. Apparently, $S_{L_0} = 1 - P_{L_0}$. The survival of the entire chain S_L for the applied stress σ requires the simultaneous survival of each of its N links. Thus, the survival probability of the chain is $S_L = S_{L_0}^N$. If P_L is the probability of failure of the chain, $S_L = 1 - P_L$. Therefore, there are following equations:

$$1 - P_L = \left(1 - P_{L_0}\right)^N \qquad (1\text{-}4)$$

$$P_L = 1 - \exp\left[N \ln\left(1 - P_{L_0}\right)\right] \qquad (1\text{-}5)$$

Equation (1.4) reflects the dimension effect in terms of the number of links N. When the dimension effect is concerned in two-dimension (i.e. surface) or three-dimension (i.e. volume), N can be considered as the number of the relevant basic elements that consist of the material. Since $N = \frac{L}{L_0}$ in this case, the Equation (1.5) can be written as:

$$P_L = 1 - \exp\left[\frac{L}{L_0}\ln\left(1 - P_{L_0}\right)\right] \qquad (1.6)$$

The next step is to replace $\ln\left(1 - P_{L_0}\right)$ with any appropriate monotonic function decreasing from 0 when $\sigma = 0$, as $P_{L_0} = 0$, to $-\infty$ when $\sigma = +\infty$ as $P_{L_0} = 1$. In order to meet above conditions, Weibull chose the simplest mathematical expression, $-\left(\frac{\sigma - \sigma_l}{\sigma_0}\right)^m$ for $\sigma \geq \sigma_l$. σ_l is a lower strength limit below which there is a zero failure probability. In practice, the incorporation of σ_l affects the results of the Weibull analysis only to a limited extent, since it is a location parameter. Furthermore, it is very difficult to determine σ_l experimentally as it lies at the low tail of the strength distribution. In this region the statistical uncertainty of the data is quite high. For simplicity σ_l is, thus, usually taken as zero. Statistically σ_0 is a scale parameter, which describes the intensity of the distribution and m is a shape parameter and also called Weibull modulus, which governs the shape of the respective density and distribution functions. Thus, we have

$$\ln\left(1 - P_{L_0}\right) = -\left(\frac{\sigma}{\sigma_0}\right)^m \qquad (1.7)$$

Substituting into Equation (1.6), the cumulative distribution function (CDF) for the length L can be obtained:

$$P_L = 1 - \exp\left[-\frac{L}{L_0}\left(\frac{\sigma}{\sigma_0} \right)^m \right] \qquad (1.8)$$

When $L=L_0$, CDF for the length L_0 can be obtained:

$$P_{L_0} = 1 - \exp\left[-\left(\frac{\sigma}{\sigma_0} \right)^m \right] \qquad (1.9)$$

It is noticed from Equation (1.8) and (1.9) that the chain with the length of L and its building links with the length of L_0 actually share the same set of scale and shape parameters. Again, it is seen that the strength of each link is assumed to be identically and independently distributed; that is, the failure or survival of each link is independent of its neighbours, and the strength distribution of each link is also a Weibull distribution with identical scale and shape parameters. If $N = \frac{L}{L_0}$ is grouped into σ_0 in Equation 1.8 and let $\sigma_0^{'} = \sigma_0 N^{-1/m}$, Equation 1.8 can be written in the form of

$$P_L = 1 - \exp\left[-\left(\frac{\sigma}{\sigma_0^{'}} \right)^m \right] \qquad (1.10)$$

or

$$\ln\left[-\ln\left(1 - P_L(\sigma)\right) \right] = m\ln(\sigma) - m\ln(\sigma_0^{'})$$

$\sigma_0^{'}$ is termed as Weibull characteristic strength according to ASTM C1239-07 [34]. It is obviously dependent on test specimen dimension and Weibull modulus. The probability density function (PDF), is the first differential of the cumulative distribution function with respect to σ. Thus the PDF for Equation (1.10) is:

$$f(\sigma) = \frac{m}{\sigma_0^{'}}\left(\frac{\sigma}{\sigma_0^{'}}\right)^{m-1} \exp\left[-\left(\frac{\sigma}{\sigma_0^{'}}\right)^{m}\right] \qquad (1.11)$$

The mean and variance calculated by this distribution are given by

$$\overline{\sigma} = \sigma_0^{'}\Gamma(1+1/m) \qquad (1.12)$$

and

$$\langle\sigma\rangle^2 = \left(\sigma_0^{'}\right)^2\left\{\Gamma\left(1+2/m\right)-\left[\Gamma\left(1+1/m\right)\right]^2\right\} \qquad (1.13)$$

The coefficient of variation (CV), thus, can be calculated by

$$CV = \frac{\langle\sigma\rangle}{\overline{\sigma}} = \left\{\frac{\Gamma\left(1+2/m\right)}{\left[\Gamma\left(1+1/m\right)\right]^2}-1\right\}^{1/2} \qquad (1.14)$$

It can be clearly seen from above equations that the mean strength is determined by the length of the chain (i.e. N), the shape and the scale parameters, while CV is not associated with sample dimensions but only depends on the shape parameter. In addition, if the mean strength of each link is $\overline{\sigma}_0$, from the Equation (1.12) the ratio of the mean strength $\overline{\sigma}$ to $\overline{\sigma}_0$ will be

$$\frac{\bar{\sigma}}{\bar{\sigma}_0} = \frac{1}{N^{1/m}} \qquad (1.15)$$

The dimension effect is directly indicated by the Equation (1.15). The mean strength of the chain decreases with increasing the number of the links. The correlation is influenced by shape parameter as shown in Figure 1.7.

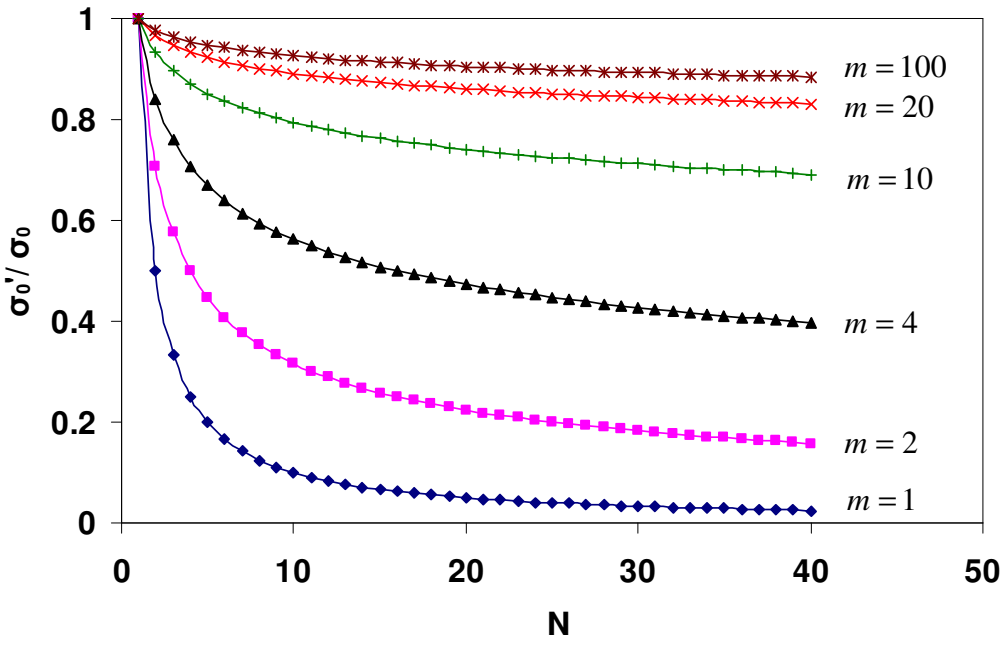

Fig. 1.7 Dimension effect on the ratio of mean strength of the chain to that of each link

It can be seen that the mean strength of the chain decreases sharply with the first few links added. For example, the mean strength of the chain containing 10 links drops approximately 46% with respect to the mean strength of each link, when $m = 4$, which is a typical value for commercial E-glass fibre. As more links are incorporated into the chain, the decrease in the mean strength of the chain becomes less significant and gradually tends to level out. It is also notable that the initial reduction speed of mean strength and the overall strength reduction are affected to a lesser extent as the shape parameter increases and such influence becomes less effective with the

increase of the shape parameter, especially after m=20. This means that as the shape parameter increases the mean strength of the chain approaches to the mean strength of each link and the incorporation of more links will have less effect on the strength reduction. In other words, the dimension effect is insignificant when the shape parameter is high. Thus, the shape parameter does indicate the strength variability. Since the extrinsic strength is controlled by flaws on the chain surface, the shape parameter can also reflect the homogeneity of the flaws. Figure 1.7 only shows the effect of chain dimension (i.e. N) on the mean strength. Figure 1.8 illustrates the effect of chain dimension on the PDF.

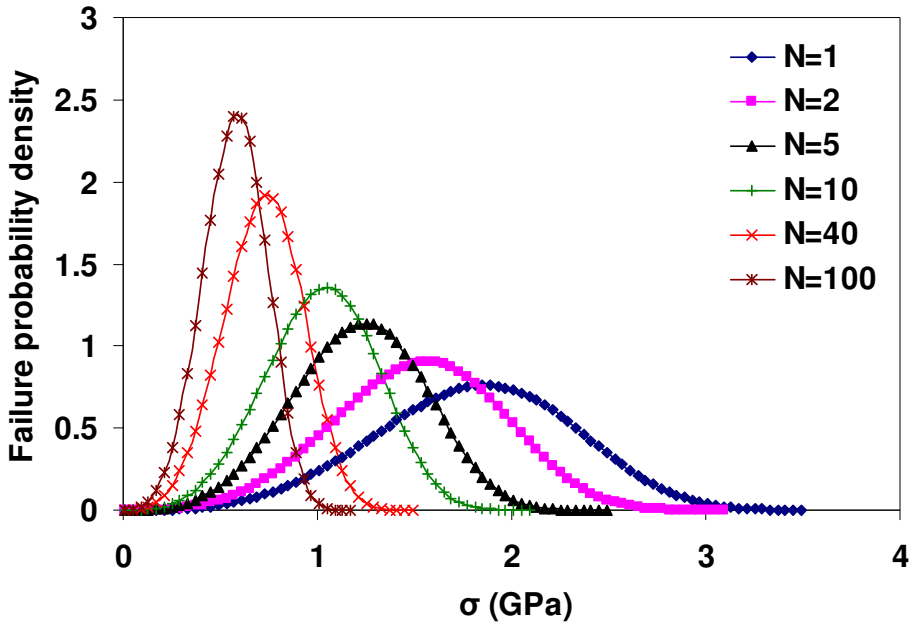

Fig. 1.8 Dimension effect on failure probability density when $m = 4$ and $\sigma_0 = 2$

Not only can dimension effect be observed from the fact that the curve shifts towards left with the increase of N, but the curve spreads out less as well. This implies that N has a similar function to that of the scale parameter as suggested earlier by $\sigma_0^{'} = \sigma_0 N^{-1/m}$. In this sense the following discussion on the significance of the

shape and scale parameter to the flaw characteristics will be based on the basic link of the chain.

According to Schmitz and Metacalfe [30, 35], two aspects are required in order to describe a population of defects, namely severity of defect and separation, which are the mean of the distribution and the standard deviation respectively for a Gaussian distribution. Weibull formalism, however, is different and shape and scale parameters provide a kinetic interpretation for a population of flaws. Figure 1.9 and 1.10 present the theoretical probability density with varying shape and scale parameters.

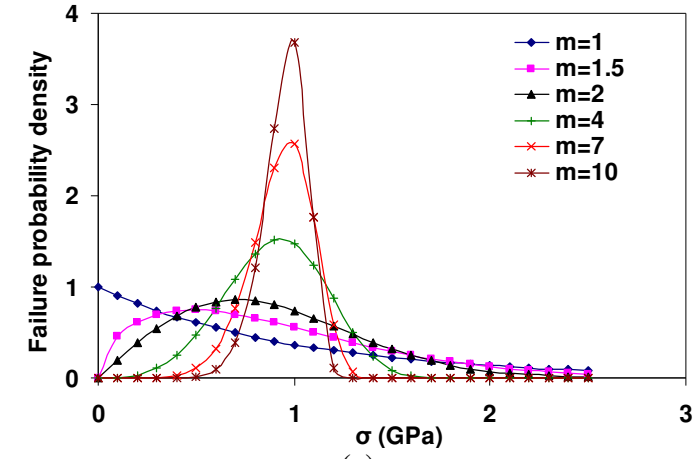

(a)

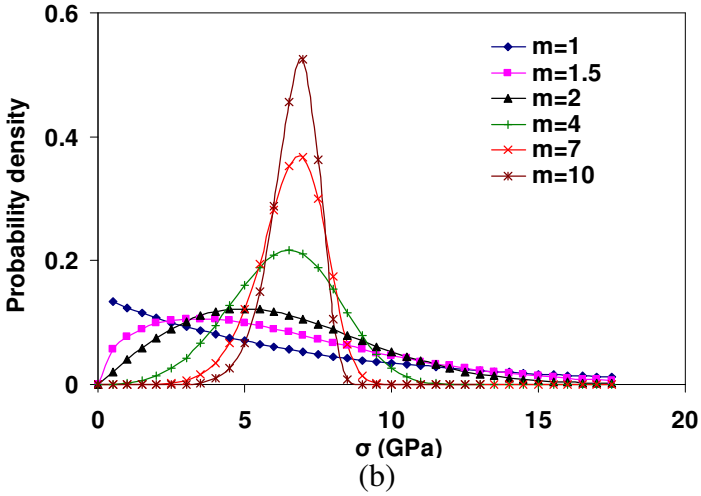

(b)

Fig. 1.9 Effect of the shape parameter on failure probability density when $\sigma_0 = 1$ in (a) and $\sigma_0 = 7$ in (b).

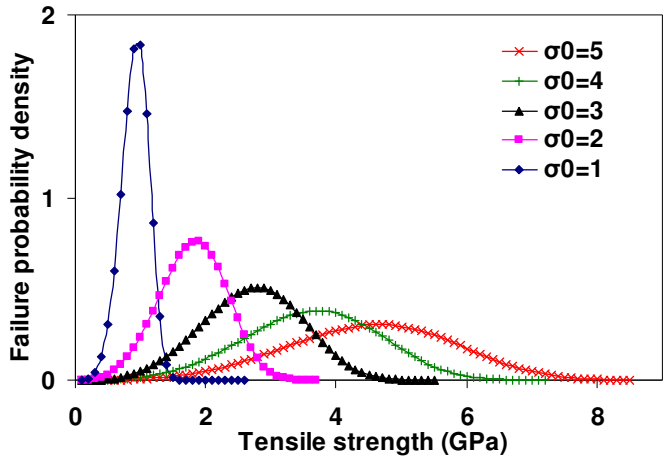

(a)

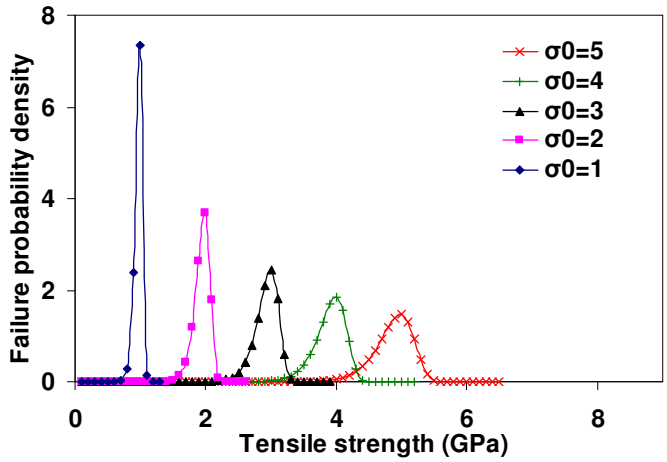

(b)

Fig. 1.10 Effect of the scale parameter on failure probability density when $m = 4$ in (a) and $m = 20$ in (b)

The influence of m is quite similar in both cases: $\sigma_0 = 1$ and $\sigma_0 = 7$. Severity decreases with increasing m at low values (say, $m < 4$) and then remains at the σ_0 value. For m values greater than 4, the changes of m are more representative of the separation than the severity. In this range, the scale parameter is representative of the mean strength concentration factor. An increase of the value of the scale parameter is representative of a decrease of the flaw severity and increase of the separation when m remains constant. Thus, m and σ_0 are both related to separation and severity of

the flaws. If one of the parameters remains constant, or if the changes are important, a qualitative interpretation is possible.

In practice, using Weibull distribution based on the equations derived above, the statistical analysis of a series of tensile tests on individual fibres (i.e. single fibre tensile test) can be carried out in the following way [36]. A number *n* of tensile tests are performed at a given gauge length L so that failure probability, P_L, only depends on σ. The results are arranged in order of increasing failure stress, $\sigma_1 < \cdots < \sigma_i < \cdots < \sigma_n$. An experimental cumulative failure probability $P_L(\sigma_i)$ is calculated for each fibre of rank *i* having failed at a stress σ_i. Unless an infinite number of fibres are tested, which is clearly impossible, the most general expression for estimation of $P_L(\sigma_i)$ must take into account the possibility of fibres breaking at lower stresses than that of the weakest specimen as well as breaking at higher stresses than the strongest fibre tested. In other words, the values for $P_L(\sigma_i)$ should be estimated in such a way that the calculated shape and scale parameter are unbiased estimators of the real values. Various expressions of this probability have been proposed : $P = \frac{i-0.5}{n}$, $P = \frac{i}{n+1}$, $P = \frac{i-0.3}{n+0.4}$, and $P = \frac{i-0.375}{n+0.25}$, where n is the number of data points and i is the rank of the *ith* data point. The variation of the experimental failure probability $P_L(\sigma)$ can then be plotted as a function of the strength of the fibres in the form of $\ln\left[-\ln\left(1-P_L(\sigma)\right)\right]$ vs. $\ln(\sigma)$. According to Equation (1.10), the gradient of the curve gives a measure of the Weibull shape parameter, *m* and then the scale parameter, σ_0 can be determined from the intercept. One disadvantage of determining the values of the unknown parameters of Equation

(1.10) from the experimental data for exclusively one gauge length is that the majority of samples will fail over a limited range of stress levels and little information of the flaw population outside this range will be obtained. This difficulty can be partially overcome by using data for more gauge lengths. The same approach can be applied to each gauge length to obtain the shape and scale parameters. In addition, according to Equation (1.12), a plot of $\ln(\overline{\sigma})$ as a function of $\ln(L)$ for several gauge lengths also gives a straight line with a gradient of $-1/m$. If the Weibull CDF is the appropriate model for the strength distribution of tested material, theoretically two methods above should generate the same m. However, this is hardly the case. The shape parameter obtained from individual gauge length tends to be less than that obtained from the slope of $\ln(\overline{\sigma})$ vs. $\ln(L)$ plot [30]. The difference is attributed to the modification of the flaw population caused by additional defects created during handling the fine fibres and an artificial selection process due to more significantly weaker fibres being broken before they can be tested [30]. In addition, there are doubts as to whether the failure of fibres falls within the limits of the theory. This is because the fibres are very fine and it is not true that the same distribution of defects can be expected to exist in all small sections of the fibre [35]. Apart from those linear regression methods (or graphical methods) above, the maximum likelihood method is also usually employed to estimate the parameters of the Weibull distribution [36]. Other commonly used experimental methods for determination of the Weibull distribution parameters include fibre bundle test and fragmentation test [37-40]. In fibre bundle test, fibre strength distribution parameters are extracted from the load-displacement data of a tensile test of the fibre bundle. The fragmentation test provides fibre break number as a function of applied strain for a fibre embedded in

matrix, which yields Weibull strength distribution parameters for a single fibre while the other test methods rely on pooling of the fibre strength data obtained from different fibres.

Weibull statistics is very valuable and widely developed in analysing fibre strength data. The popularity of the Weibull distributions arises from two factors. First, it is often found that the Weibull distribution simply provides a more accurate description of the observed data. Second, the Weibull probability density function, unlike most others, is flexible in shape. Depending on the value of m, the Weibull density function can reduce to or approximate the shape of various other density functions as shown in Figure 1.9. Thus, when very little information is available concerning the underlying life distribution, the Weibull distribution allows description of the data without imposing stringent assumptions concerning the shape of the unknown density function. In addition, current theories of composite strength usually require knowledge of the fibre strength and its distribution at gauge lengths of the order of the critical length for the stress transfer (0.1 to 0.2mm). Although a direct attempt at measuring the fibre tensile strength at gauge lengths around that range has been made [41], the Weibull distribution allows for extrapolating the fibre strength to such gauge lengths as implied in the plot of $\ln(\bar{\sigma})$ vs. $\ln(L)$.

Weibull CDF is essentially based on the assumption that tested material only possesses one type of flaw population described by one set of shape and scale parameters. If this is the case, the experiment data analysed in both graphical methods will be well fitted by a straight line signifying the validity of Weibull distribution. However, many workers have reported that carbon and glass fibres strength distribution dominated by one type of flaws occurs in a limited range of

fibre length [30, 42]. Fibres tested at some gauge lengths, depending on the material, yield curves that have to be fitted by different lines in the graphical methods. It is considered that different slopes generally indicate the effect of different types of flaw population [35]. To deal with this problem, different models have been proposed on the basis of Weibull weakest link model. The bimodel was developed by Beetz on carbon fibres by considering a combination of the individual survival probabilities for weakest link models of each kind of defects. The CDF of the whole chain is then given by [42]:

$$P_L = 1 - q\exp\left[-N\left(\frac{\sigma}{\sigma_{01}}\right)^{m_1}\right] - (1-q)\exp\left[-N\left(\frac{\sigma}{\sigma_{02}}\right)\right]^{m_2} \qquad (1.16)$$

where q is the mixing parameter, i.e. the fraction of failures due to flaws in one type of population (type *A*) defined by one set of shape parameter, m_1 and scale parameter, σ_{01}. The rest fraction of failures is attributed to flaws in the other type of population (type *B*) defined by the other set of shape parameter, m_2 and scale parameter, σ_{02}. Apparently it is assumed that no interaction occurs between type *A* and type *B* flaws. Type *A* flaws are usually referred to as more severe flaws than type *B* flaws. In this approach, the chain is conceptually divided into two categories of links corresponding to the respective categories of defects and a law of mixtures is applied at the chain level. It is argued by Zinck *et al.* that this approach leads to two weakest elements accounting for failure and is not in agreement with the fundamental principle of the weakest link, according to which the failure occurs in a chain when its weakest link fails [43, 44]. Depending on how the two different flaw populations coexist within the fibre, Johnson developed three mathematical forms of the failure

distributions [45]. They are exclusive, concurrent, and partially concurrent distribution. Exclusive distribution is based on the assumption that each link of the chain contains one of the two flaw populations, but not both. This is the same as the assumption in Beetz's bimodal. The concurrent distribution assumes that each link is subject to both flaw populations. The partially concurrent distribution is derived by assuming that all the fibres have flaw population *A* (i.e. type *A* flaws) and a fraction of the fibres contain only this common flaw. The remaining portion of the fibres contains flaw population *B* (i.e. type *B* flaws). From a practical standpoint, the assumption that both flaw populations cannot appear in the same fibre seems questionable unless samples were made by different methods. In contrast, the assumption that each fibre possesses both flaw populations seems quite reasonable. The assumption for partially concurrent model seems quite feasible as well but it gives the most complex PDF among them. The fact of having two or even more different flaw populations should not bring about any change in general dimension effect when these flaw populations do not coexist in a link. It is obvious that the fraction of failure due to the more severe defects increases when increasing the chain length. The value of the mixing parameter, thus, should be a function of the chain length. However, this was not considered in the Weibull bimodal by Beetz. A simple improvement has been made by considering a gauge length-dependent mixing parameter in the following form [43, 44]:

$$q(L) = q_0 \frac{L}{L_0} \qquad (1.17)$$

with q_0 as the fraction of failures due to type *A* defects determined experimentally at the gauge length L_0. Instead of turning the Weibull unimodal into bimodal by incorporating another flaw population, Stoner *et al* mixed the Weibull unimodal with another probability distribution arising from end effects associated with the failure adjacent to the fibre ends [45]. These fibres ends are normally secured on a card using glue and subjected to a more complex stress state due to misalignment between upper and lower ends and/or the stress concentrations at the fibre-glue interface. Other models have tried to deal with a well recognised physically unsatisfactory boundary condition that the Weibull distribution requires the stress equal to infinity for certainty of failure (i.e. $P_L = 1$) as implied in Equation (1.9). These models incorporated an upper strength limit, σ_u into the Weibull distribution and defined m as the damage coefficient.

1.1.7 Effect of surface treatment on strength of glass fibre

Despite the great success that the Weibull statistics has achieved in description of the strength behaviour of glass fibres, this approach does not generate any information on flaws because it avoids any physical consideration about flaws (e.g. shape and dimension of flaws). Lack of this knowledge will give rise to difficulties in obtaining a better understanding of the fracture mechanisms controlled by different flaws and interpreting the effects of the sizing process on the strength of glass fibres. Thus, it was argued that linear elastic fracture mechanics (LEFM) should be considered as a complementary approach, although LEFM is not able to account for the observed dimension effect [46]. The combination of both approaches has been used by Zinck *et al* to indicate the healing effect of coating on the strength of glass

fibres [46]. This healing effect was presented by using Weibull statistic to analyse the data for fibre strength in a $\ln[-\ln(1-P_L(\sigma))]$ vs. $\ln(\sigma)$ plot, in which the low strength gave higher failure probability for uncoated E-glass fibre than E-glass fibre coated with γ-aminopropyltriethoxysilane (APS). Little difference in failure probability for both types of fibres with high strength implied that improvement in the fibre strength was limited to a threshold for the fibre strength (e.g. approximate 1.2 GPa in Zinck's work). In the context of LEFM and assuming the crack shape as a plane perpendicular to the fibre axis, the strength threshold was then related to flaws' critical dimension below which defects are not healed. The critical dimension (e.g. in the 100 nm range for E-glass fibre) was further compared with the hydrodynamic radius of aggregates of 1wt% APS measured by quasielastic laser light scattering spectroscopy. 150 nm for the aggregates of 1wt% APS was found in good agreement with the critical dimension in the 100 nm order. Thus, the healing was considered to be effective when the aggregates of APS were able to effectively fill the flaws so that a three-dimensional network could be formed through sufficient interactions between flaws and APS aggregates as shown in Figure 1.11.

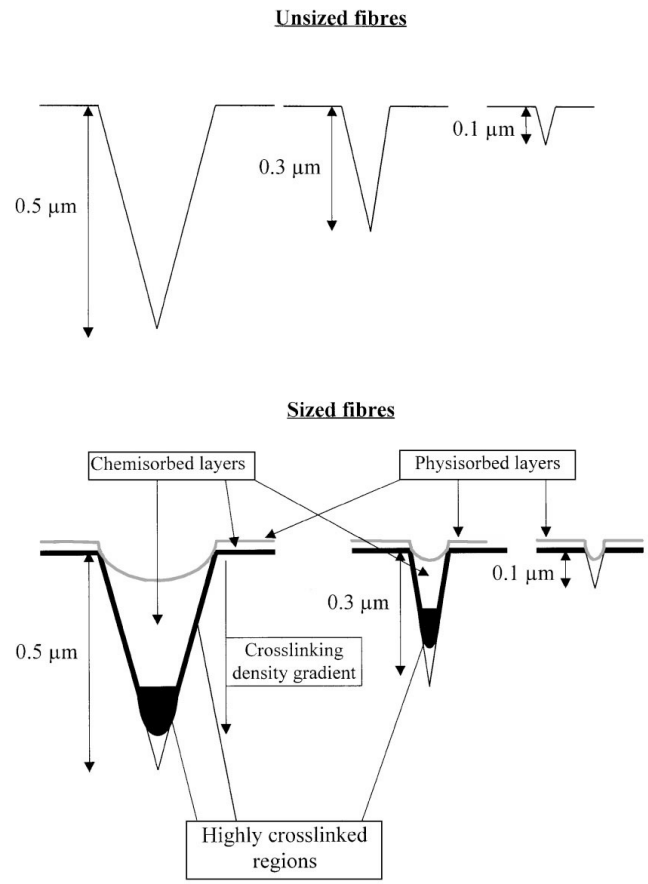

Fig. 1.11 Schematical representation of flaws; effect of a surface treatment [46]

This result was supported by Feih *et al* who obtained the uncoated E-glass fibre via burning off the APS at 500 °C [47]. In addition, a larger flaw critical dimension, 200-270 nm, was derived based on the semi-circular crack shape and considered to have better agreement with the size of APS aggregates. They also employed fractography as a powerful method to show that the fibre failure originated from severe surface defects. With the same methodology, Zinck *et al* made a comprehensive summary on the healing effect for surface flaws by comparing E-glass fibres with no size, APS, different film formers, and APS/film former combinations [48]. It was shown that the film former not only has great influence on the healing of flaws on its own but also has synergetic effect with APS.

In summary, glass fibre strength exhibits dimension effect, which can be reasonably well explained by Weibull statistic based on the weakest link theory. The behaviour of strength of glass fibres is controlled by the flaws on the surface. Glass fibres can have multiple flaw populations, which can be further modified by surface treatment. The surface treatment may bring about healing of pre-existing flaws by filling flaws with coating components to reduce the flaw dimension.

From this review, one can see that the research on the strength of glass fibre has been carried out mainly in two aspects: one is focused on fundamental interest in the strength of glass fibres and the other involves attempt at understanding strength behaviour and improving the strength of given glass fibres. The former is now facing questions such as why pristine fibres exhibit fatigue much like fibres containing microcracks and other questions that also need answering for glass in general. The latter needs to draw a clear picture of fracture mechanism based on physical knowledge of flaws on the glass fibre and finds out how to improve the fibre strength. In addition, statistic models without the conflict between their formalisms and basic principles should be developed to account for the multimodal distribution of fibre strength.

1.2 Experimental

1.2.1 Single fibre tensile test

Boron free E-glass fibres from Owens Corning-Vetrotex were investigated in this work and Table 1.4 summarises the materials tested and also includes other information such as average fibre diameters, product type, and surface coating.

Table 1.4 Glass fibres tested

Glass	Product type	Average Diameter (μm)	Surface coating
E	Roving	17.4 ± 1.3	/
E	Roving	17.3 ± 1.3	γ-APS

The fibres were analysed as received from the manufacturer in the form of 20 kg square-end wound packages (internal unwind). Fibres near the bottom and top of the packages are likely to have been damaged during packing, storage, and transportation. Therefore, only the strands from the middle of the packages are selected for testing. The fibre strength was determined by using the single fibre tensile test referred to ASTM C1557-03 [49]. Separation of individual fibres was carried out in the following manner: One end of a bundle is taped to a lamp frame in front of a dark background for better visibility as shown in Figure 1.12(a). Instead of separating a fibre from the free end, the upper part of the bundle was partially cut to let the outmost fibres stick out as seen in Figure 1.12(a). A fibre was then gently pulled outward-downward from the upper free end and eventually separated from the bundle. This would avoid fibre rubbing during the separation as much as possible. Individual fibres were glued onto card tabs with a central cutout that matched the gauge length chosen for the test as illustrated in Figure 1.12(b).

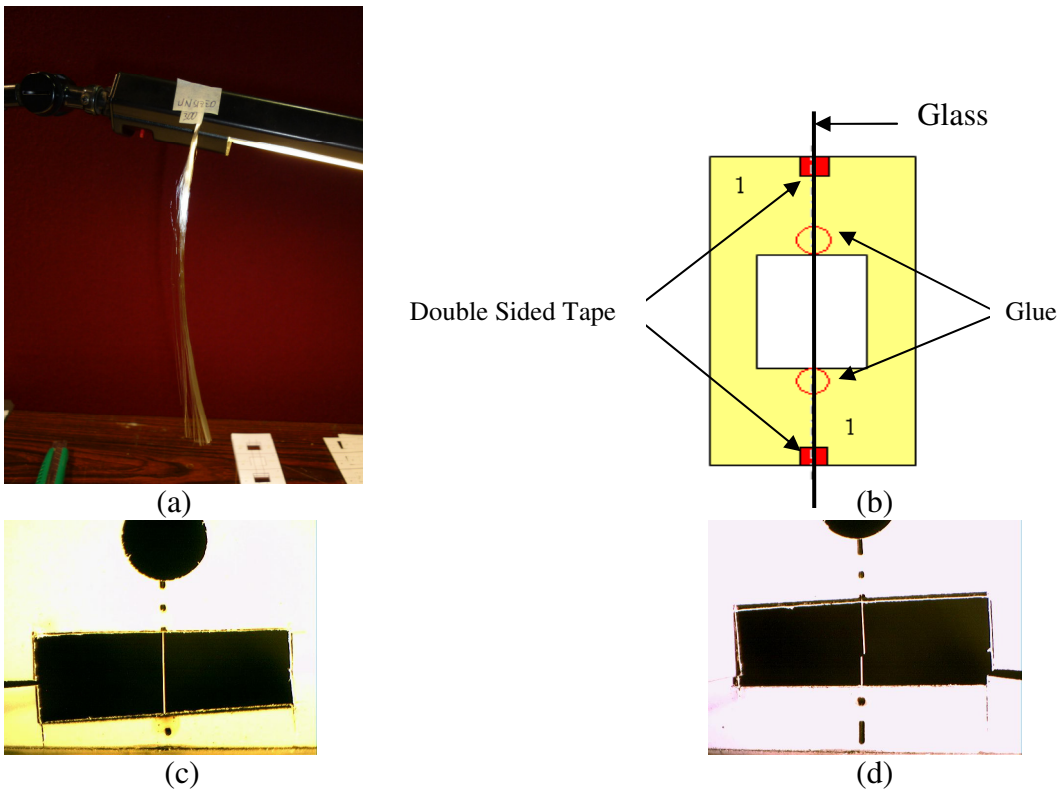

Fig. 1.12 Procedure for single fibre tensile test

It should be noted that the gauge length is actually defined by the distance between the fibre exit points from the glue. The glue should, thus, be placed at the contact point between the fibre and the slot. Loctite super gel glue was used in this work. The tab ends were gripped in a universal testing machine (Instron Model 3342) equipped with a 10 N load cell and operated through the software, Instron Bluehill®2. According to ASTM C1557-03, the axis of the fibre should be coaxial with the line of action of the testing machine within $\delta \le l_0/50$ to prevent bending strain and/or stress concentrations at the point of fibre exit from the tab. δ is the tolerance and l_0 is the fibre gauge length. After the specimen had been mounted in the test machine, a section of the tab was carefully cut away, leaving the specimen free to be loaded during the test as shown in Figure 1.12(c). Strains were estimated

by the machine displacement in this case. Only the tests where the sample broke along the gauge length (see Figure 1.12(d)) were used for further data processing.

A typical load-extension curve is shown in Figure 1.13. All fibres failed in a brittle manner by exhibiting a sharp drop in stress after ultimate failure stress.

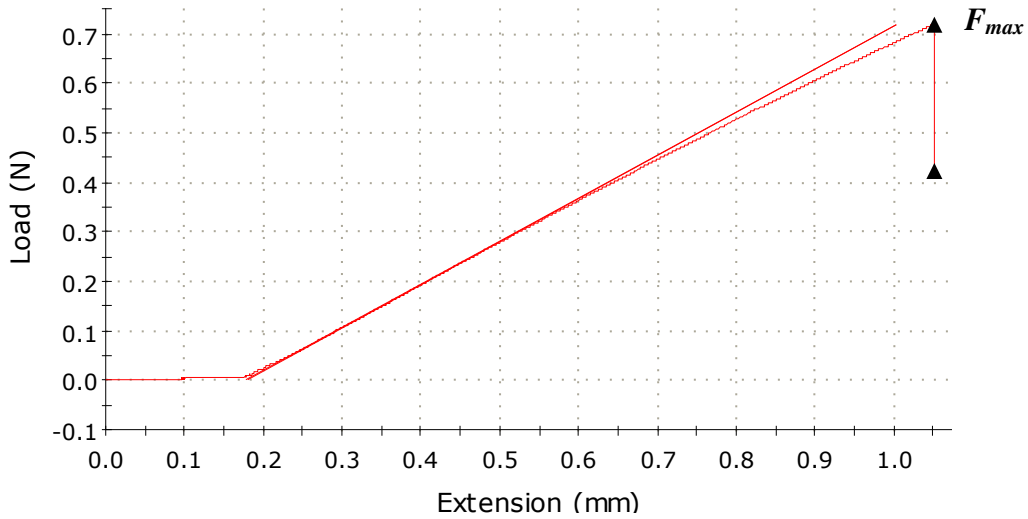

Fig. 1.13 Typical load-extension curve for a single fibre tensile test

Assuming the glass fibres along the gauge length have a uniform circular cross-section normal to the axis of the fibres, the fibre strength was then calculated from the load at break and the cross-sectional area, $A_f = \pi D_f^2 / 4$, calculated using individual diameters, D_f , measured before the tension test by Nikon Epiphot Inverted optical microscopy as illustrated in Figure 1.14.

Fig. 1.14 Measurement of glass fibre diameter using optical microscope

During handling of the fibre in the microscope, the fibre was not in contact with the objective. The value of apparent Young's modulus of the fibre was determined by the slope of the fitting line in Figure 1.13 and can be automatically calculated by Automatic Young's Modulus function in Bullhill®2 software. The modulus was calculated in the following way:

- searches the data between the first data point that is greater than or equal to 2% of the maximum load and the maximum load value.
- carries out a zero-slope yield calculation to determine if there is a yield point in the data.
- uses the first data point as the start value and the yield point or the maximum load point as the end value, whichever occurs first.
- divides the data on the extension axis between the start and end values into 6 equal regions with 0% overlap.
- applies a least square fit algorithm to all of the points in each region to determine the slope of each region.
- determines the pair of consecutive regions that has the highest slope sum.
- from this pair, determines which region has the highest slope and assigns the modulus to that region.

The gauge lengths of 5, 10, 20, 40, and 80 mm were chosen and approximately 70-100 fibres were tested at each gauge length. The loading rate was adjusted according

to the fibre gauge length so that the fibres were subjected to constant strain rate of 1.5%/min for all gauge lengths. All the tests at different gauge lengths were carried out at room temperature and 50% relative humidity.

1.2.2 Coefficient of thermal expansion (CTE) of glass fibre

Considering the local integrity of the thesis, a brief introduction is laid out prior to the description of how the CTE of glass fibre was measured in this work. Most solid materials expand upon heating and contract when cooled. It is suggested that the anharmonic nature of the atomic vibration is responsible for the phenomenon of solid thermal expansion [50]. Anharmonic forces between the atoms lead to an asymmetric curve for their potential energy function. As the temperature increases so does the vibratory energy. The increase leads to a change in the average separation when the potential energy is not symmetric about its minimum [51]. The separation change also depends on the bond energy between interacting atoms. In general, thermal expansion decreases with increasing bond energy. Thus, the polymers (e.g. polypropylene) with loosely-bonded structures generally expand much more than metals and ceramics (e.g. glass) under the same temperature change. The coefficient of thermal expansion (CTE) is the measure of a material property that is indicative of the extent to which a material expands upon heating [52]. CTE is one of the most fundamental characteristics of a material and is determined by the composition and structure of the material. CTE is a function of temperature although for some materials (e.g. soda lime glasses) the thermal expansion can be proportional to temperature change over some small ranges well below a critical temperature (e.g. glass transition temperature). The definition of CTE in length at a specific

temperature, more usually known as coefficient of linear thermal expansion (CLTE), α_l, can be expressed as:

$$\alpha_l = \frac{dL}{L \times dT} \qquad (1.18)$$

where dL is the infinitesimal change in length of the sample resulting from the infinitesimal change in temperature dT and L is original length in the direction being measured. The parameter, α_l, has units of reciprocal temperature ($°C^{-1}$) such as μm/(m·°C) or 10^{-6}/°C. Apparently, an average CLTE, $\langle \alpha_l \rangle$, can be obtained over a temperature range. When CLTE is constant over the temperate range then $\alpha_l = \langle \alpha_l \rangle$. Similar definitions can be applied to area and volume of the material, giving respective CTE in area, α_s, and volume α_v. For isotropic materials, α_v is approximately $3\alpha_l$.

Three of the main techniques used for CLTE measurement of rigid solids are dilatometry, interferometry, and thermomechanical analysis [52]. The dilatometry technique involves various dilatometers for different applications. With push- rod dilatometer, a specimen is heated in a furnace and displacement of the ends of the specimen is mechanically transmitted to a sensor by means of push rods. ASTM E228-06 covers the determination of the linear thermal expansion of rigid solid materials using push-rod dilatometers [53]. It is generally applicable to materials having absolute CLTE exceeding 0.5 μm/(m·°C) for a 1000°C range. The best precision of CLTE measurement (better than ±40 nm/(m·°C) is provided by optical interference technique, where the displacement of the specimen ends due to

temperature change is measured in terms of the number of wavelengths of monochromic light. ASTM E289-04 (Reapproved 2010) provides a standard method for CLTE measurement with interferometry that is applicable to materials having low and either positive or negative CLTE (below 5 μm/(m·°C)) from –150 to 700°C [54]. The CLTE can also be assessed using a thermomechnical analyser (TMA), which consists of a static specimen holder and a movable probe that can transmit changes in sample length to a transducer that translates movements of the probe into an electrical signal. ASTM E831-06 describes the standard method for evaluating the CLTE of rigid solid materials using TMA [55]. This test method is applicable to the temperature range from -120 to 900°C and the recommended lower limit of CLTE measured with this method is 5 μm/(m·°C).

Despite the fact that a variety of methods exist for the CLTE measurement of solid materials, studies of the CLTE measurement of silicate glass fibre are rather scarce. The literature survey on such aspect usually leads to two main research activities. One involves CLTE measurement on glass with different compositions and structure [56-58]. The other concerns development of models for estimating CLTE of oxide glasses from their composition [57, 59, 60]. Although direct CLTE measurement on a basis of a single glass fibre seems to have been mentioned in Otto's report on compaction effects in E-glass fibres [12], technical details about how to carry out the experiment were not described. This makes it impossible to duplicate the measurement. In contrast, the thermal properties of various single polymeric fibres have been extensively studied. This is probably due to the fact that glass fibres do not normally agree with the requirements for the test specimen in most methods and CLTE of glass fibres has to be measured in tension mode. In addition, the brittleness

of glass fibre brings about extra difficulty in clamping mechanism compared to tough organic fibres. Notwithstanding these problems, we made our first attempt to directly measure CLTE of a single E-glass fibre by using TMA.

TMA has historically been used to make a variety of measurements such as CTE, glass transition temperature and softening temperature etc. Over the past decades, TMA instruments have expanded performance capabilities and improved ease-of-use to make TMA potentially more popular as a component in a complete thermal analysis laboratory. Nowadays, most commercial TMA instruments offer excellent sensitivity, programmable force, and a variety of easy-to-use probe/stage configurations. These different configurations have made a range of deformation modes available, including penetration, compression, tension, and bending. The kind and quality of information obtained from a TMA, thus, depends primarily on probe type and the arrangement of the specimen. Tension mode is most often used in characterising the properties of thin films and fibres. Apart from ability to evaluate CLTE, this technique can also help in assessing the effects of thermal history on process variables such as draw or heat setting. Furthermore, the precise control of applied force and temperature in fully automated instruments has enabled the tension mode to characterise more fundamental viscoelastic properties such as creep and stress relaxation. All thermomechanical experiments essentially measure some variable related to changes in dimension as a function time or temperature. These changes are related to viscoelastic processes within the material. Thus, thermomechanical analysis is most often applied in characterising polymers or polymer composites, where the viscoelastic properties often dominate the material response. When the deformation of a substance under a negligible load is measured

as a function of temperature, the technique is more properly referred to as thermodilatometry (TDA) [61]. The process is further referred to as linear TDA when dimensional change is measured in only one direction.

In this work, thermomechanical analyzer Q400 (TMA Q400) manufactured by TA Instruments was used to measure CLTE of a single uncoated E-glass fibre with the linear TDA technique. Figure 1.15 schematically presents the internal construction of this machine with expansion probe installed.

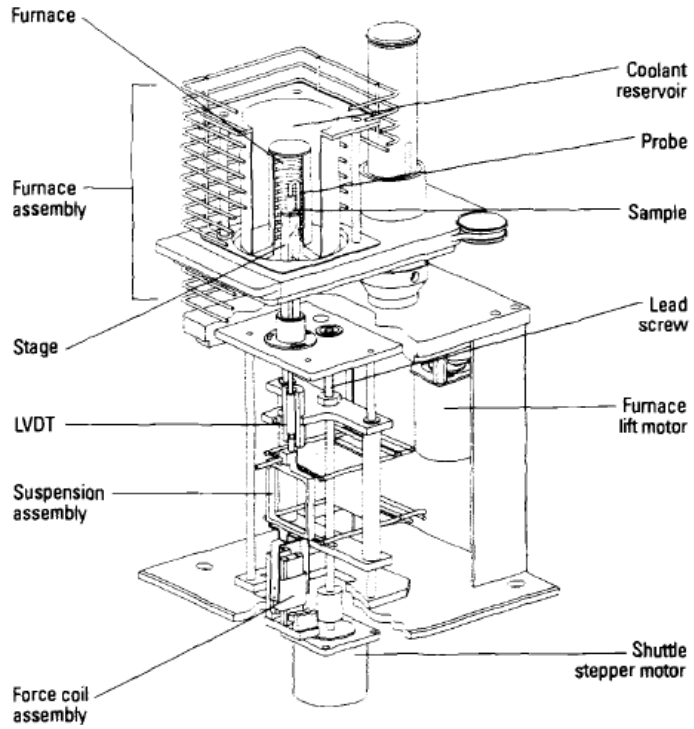

Fig. 1.15 Internal structure of TMA Q400 with expansion probe [61]

The key components in TMA Q400 as in a typical modern thermomechanical analyser include a furnace system for providing a well controlled test environment, stage/probe assembly for holding the specimen, and movable-core linear variable differential transducer (LVDT) whose output is proportional to displacement of the core caused by changes in specimen dimension. Other important components involve

a temperature sensor that can be placed in close proximity to the specimen and an electromechanical coil that can apply force to the sample. To accommodate fibres in the machine, the film/fibre probe was installed to form a tension configuration as shown in Figure 1.16.

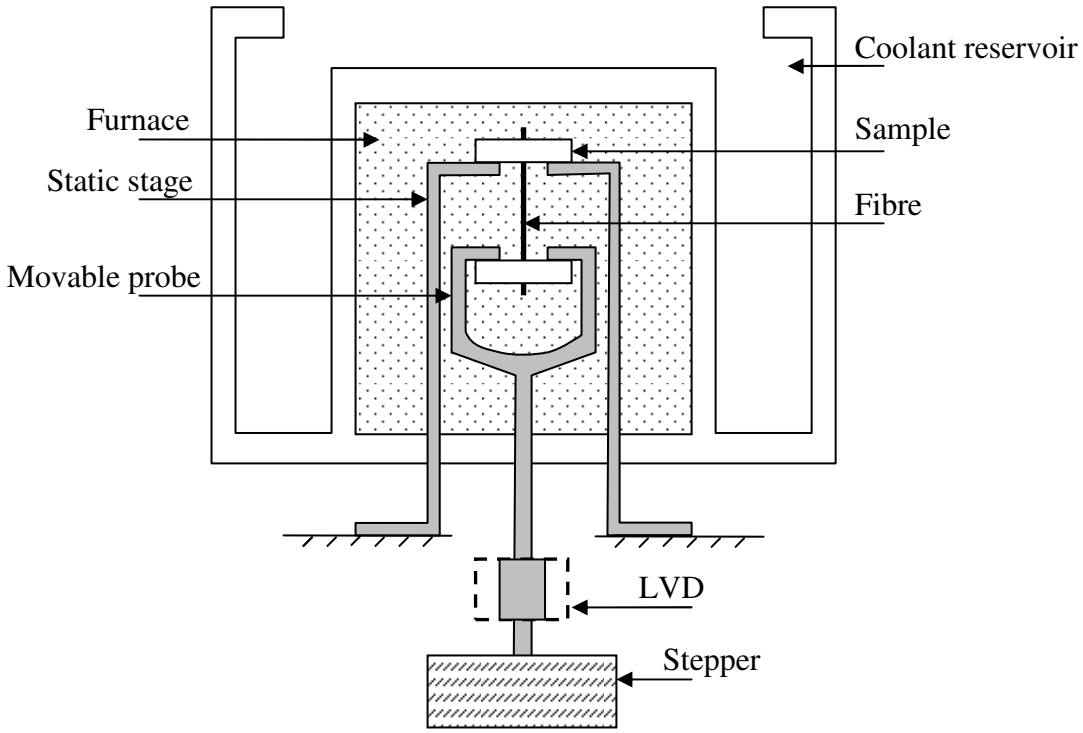

Fig. 1.16 Schematic illustration of a thermomechanical analyser equipped with film/fibre probe

This system consists of concentrically installed stage and probe. The former is fixed on a flat platform, while the inner probe contains the movable core of LVDT and is driven up and down by a stepper motor. Both the fixed stage and movable probe have a 1.2 mm slot on the top for supporting upper and lower sample holders.

The real challenge for CLTE measurement of a single glass fibre lies in using an appropriate sample holder to firmly secure the brittle fibre over a temperature range of -150 to 600°C. The TMA Q400 employed in our work provides a pair of stainless

steel clamps for gripping film samples and cleaved aluminium balls for gripping fibre samples. Such clamping mechanisms work quite well with tough materials, for instance, polymers and natural fibres. However, it proved extremely difficult for delicate glass fibres to survive this brutal clamping process. Even if fibres do survive from crushing, the low compliance nature of both clamps (stainless steel or aluminium) and glass fibre may result in poor contact between the grip surface and the fibre. This tends to give rise to a slipping grip on the fibre and make the results for CLTE measurement unreliable. Alternatively, single glass fibres are often secured on mounting tabs using various adhesives (for example, epoxy, red sealing wax, and gel superglue) as in single fibre tension test [49]. The problem with the normal adhesives is a) much higher CTE compared to glass, b) poor resistance to high temperature, and c) extremely high compliance at elevated temperature, which could mean that the applied load is no longer negligible. Thus, the material needed to hold a single glass fibre in the CLTE measurement as shown in Figure 1.16 should meet the criteria presented in Figure 1.17.

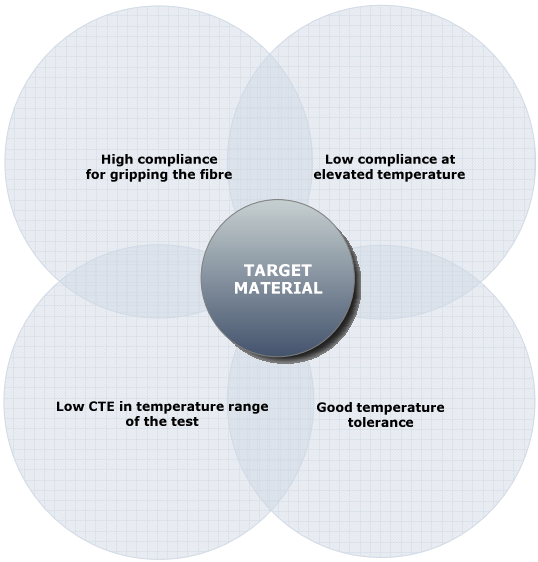

Fig. 1.17 Criteria for selecting material as sample holder in CLTE measurement of glass fibre

It was therefore thought that an inorganic material may be able to fulfil these requirements. After a few attempts at the selection of candidates, Plaster of paris was chosen to serve as the sample holder. Plaster of paris is a material accessible in a general laboratory. It is calcium sulphate-based material which can produce a gypsum paste when mixed with sufficient water. The ends of a single fibre, thus, can be easily included in this paste, which physically solidifies and hardens in a short period of time at ambient conditions. The mechanical properties of the dry set plaster are strongly influenced by porosity, which depends on the amount of water and setting conditions [62, 63]. More importantly, the dry set plaster has low expansivity and high temperature tolerance. In this work, no particular mixture ratio of water to plaster powder was followed to make the paste. Thermomechanical properties of dry set plaster was examined by dynamic three-point bending test using a dynamic mechanical analyser (DMA). It was also found that the adhesion between the plaster and the glass fibre did not sometimes seem adequate to prevent the fibre from slippage during the measurement of initial fibre length, where the 10 mN preforce was applied to the sample along the direction of fibre axis by the inner probe. To ensure the firm grip, the deposited paste at both fibre ends was squeezed by hand until it felt partly set. The sample was then transferred into an oven at 120°C to remove water. The calibration of TMA including force, probe, temperature and length was carried out according to the manual instruction and relevant standards. The alignment of the fibre between the stage and the probe was achieved in the following way: place the upper end on the stage, leave the rest of the sample to hang freely, and bring the probe down to the lower end by measuring the initial length between two ends. No additional load was applied to the sample during the

measurement and the sample was heated at 3°C/min from -60°C to 500°C under 50ml/min nitrogen. A specimen thermocouple was located adjacent to the middle of the fibre. Vibrations were avoided during the measurement.

1.3 Results and discussion

1.3.1 Fibre diameter distribution

Figure 1.18 exhibits the cross section of fibres from the same strand. The variation in fibre diameter can be visually observed.

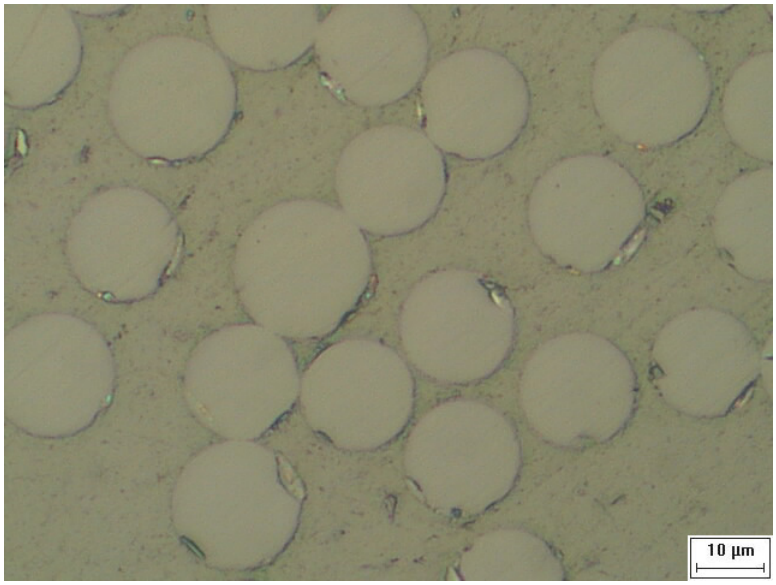

Fig. 1.18 Photo of cross section of fibres from the same strand

Over the course of the investigation, approximately 1000 uncoated and 400 coated glass fibres were measured using the optical microscope to establish a profile for the fibre diameter distribution, which is shown in Figure 1.19.

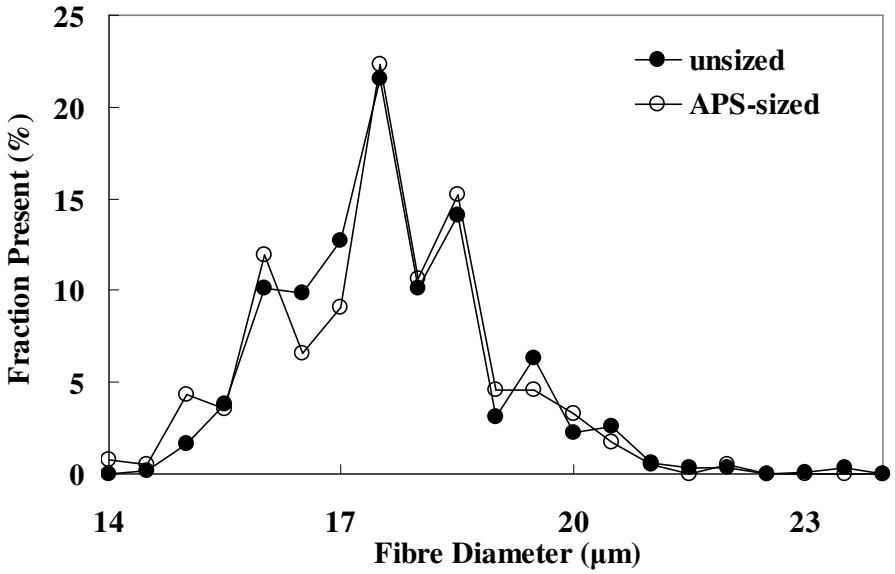

Fig. 1.19 Diameter distribution of uncoated and APS-coated E-glass fibres

It can be seen that E-glass fibres in this study have almost the same diameter distribution for uncoated and coated fibres. This may imply that these fibres were formed under the identical conditions such as bushing temperature, orifice size, and attenuation speed. In terms of manufacturing process, the difference may just lie in whether the size is applied to the fibres or not. It can be noticed in Figure 1.19 that the presence frequency of the mean value is actually only 21% within a fairly broad distribution.

1.3.2 Young's modulus and correction

Young's moduli of uncoated and coated E-glass fibre at different gauge lengths were measured. In the case of a high modulus fibre, it is advisable to take into account the machine compliance for a more accurate evaluation of the Young's modulus of a rigid fibre. In the test where the fibre is secured on a mounting tab, the whole system compliance must be determined and used to correct the experimental

modulus. The description of the method can be found in [49, 64]. Assuming the sample is perfectly aligned in the direction of loading and there is no slippage before the fibre fractures, when the fibre is fully strained the measured displacement, ΔL, is the sum of deformation of the fibre, ΔL_f, and the system deformation (including the clamp, tab, and glue), ΔL_s, i.e.

$$\Delta L = \Delta L_f + \Delta L_s \qquad (1.19)$$

Since glass fibres behave elastically in the tension test the Young's modulus, E_f, can be calculated by Hook's law:

$$E_f = \frac{\Delta F L_f}{A_f \Delta L_f} \qquad (1.20)$$

where L_f is fibre gauge length, ΔL_f is the length change caused by change in applied force, ΔF. Combining Equation (1.19) and (1.20), we have

$$\frac{1}{E} = \frac{1}{E_f} + C_s \frac{A_f}{L_f} \qquad (1.21).$$

where E is the measured fibre modulus and $C_s = \frac{\Delta L_s}{\Delta F}$ is the system compliance.

Therefore, a plot of $(1/E)$ versus (A_f / L_f) will yield a straight line with constant slope of C_s and intercept $(1/E_f)$ as seen in Figure 1.20.

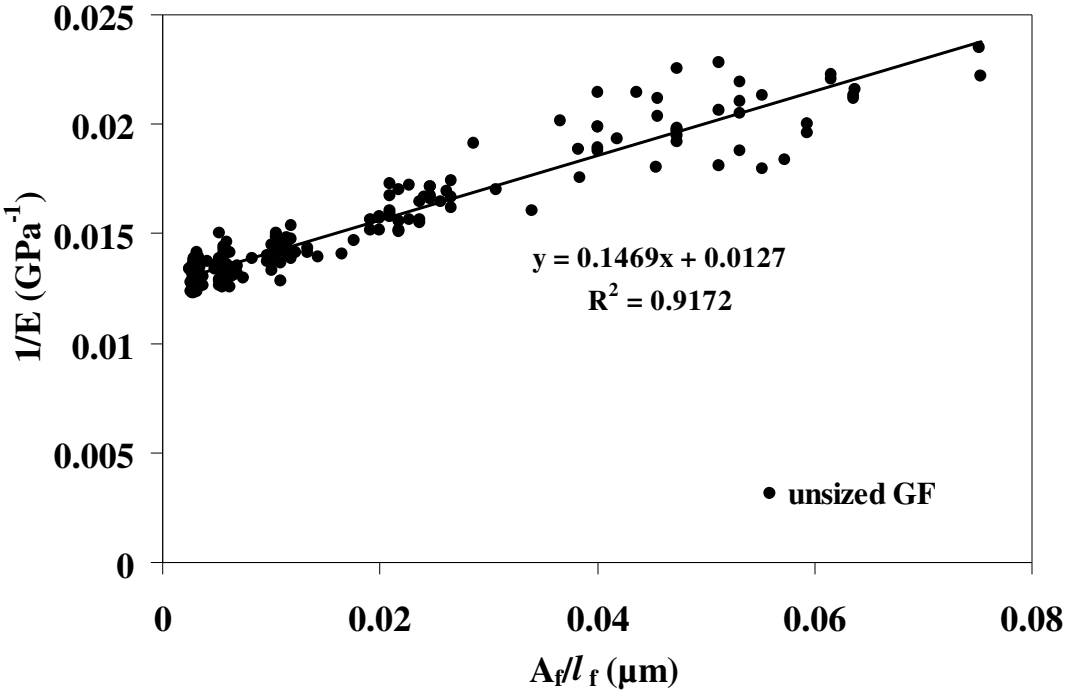

(a)

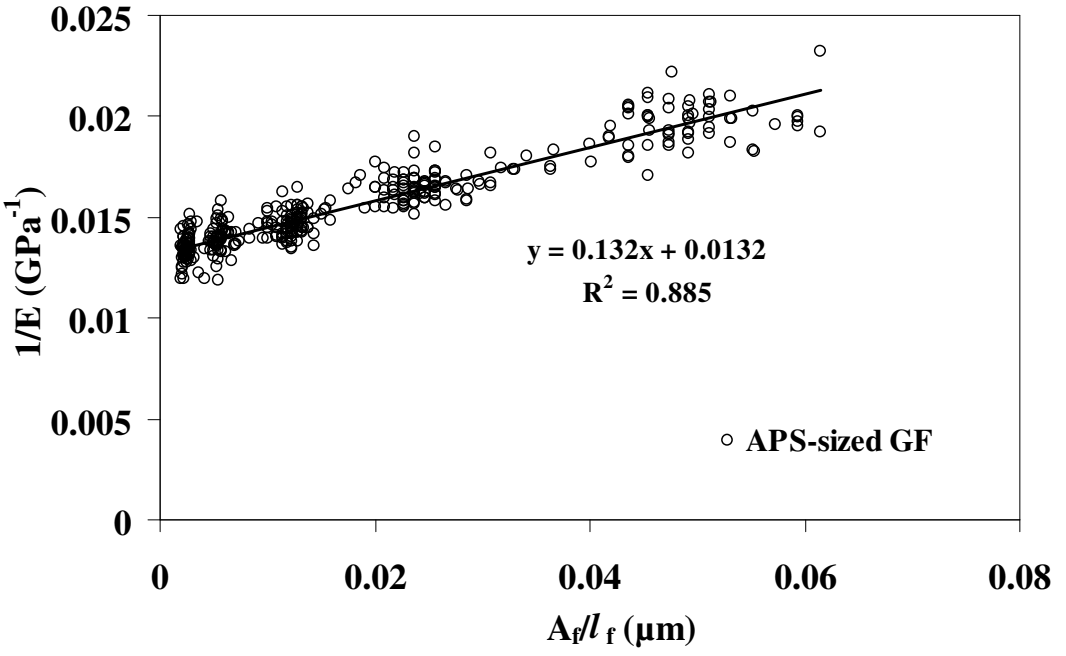

(b)

Fig. 1.20 Young's modulus correction for (a) uncoated glass fibre and (b) APS-coated glass fibre

It might be expected that the system compliance should remain the same if exactly the same system is used throughout all the tests. However, the variations in

properties of the card and glue used in this work were very likely to account for the difference in system compliances shown by the slopes in Figure 1.20. The values of 78.7 GPa and 75.7 GPa can be obtained for Young's moduli of uncoated and coated E-glass fibre respectively. Figure 1.21 shows both experimental and corrected Young's moduli for uncoated and coated E-glass fibres at various gauge lengths.

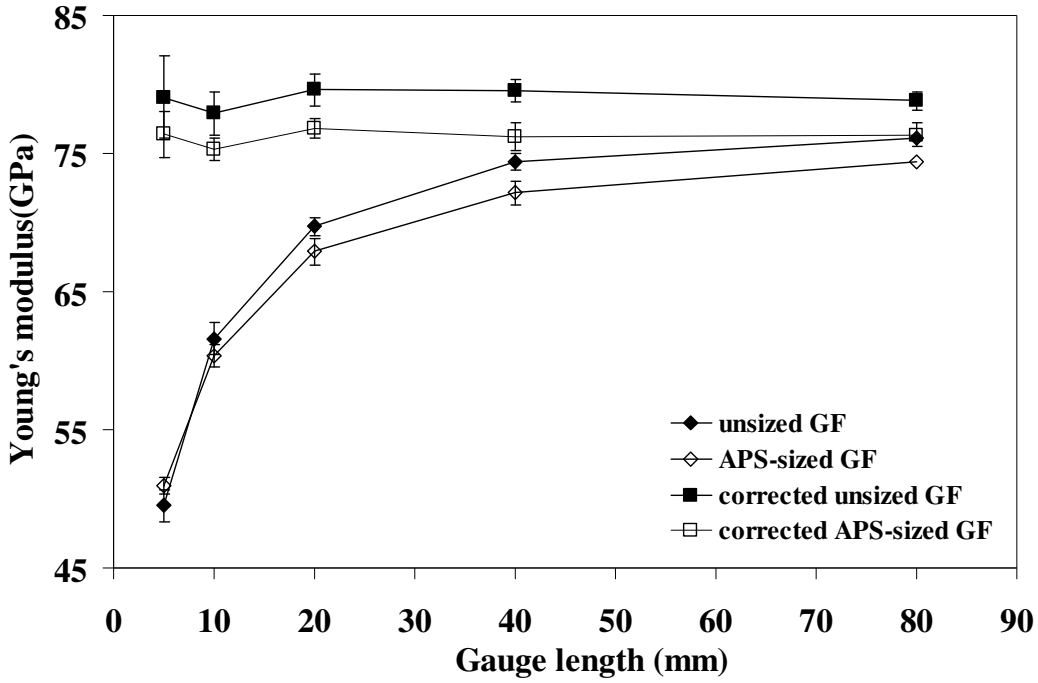

Fig. 1.21 Comparison of uncorrected and corrected Young's moduli of both uncoated and APS-coated glass fibres at different gauge lengths

It can be clearly seen that the apparent dimension effect on the modulus is caused by the system compliance, which influences the modulus to a less extent as the gauge length increases. The corrected modulus, on the other hand, remains fairly constant at different gauge lengths. This result is in agreement with the widely accepted assumption that the fibre modulus is independent of the fibre length. It is interesting to note that the difference from the comparison of moduli between uncoated and coated fibres. Young's modulus of uncoated glass fibre is found to be ~3.6% higher

than that of coated glass fibre as shown in Figure 1.21. To the author's best knowledge, it has not been reported that silane or even size on the fibre surface can lead to significant difference in fibre modulus. Assuming there is a uniform APS layer on the E-glass fibre used in this work, the correlation between the thickness of the layer and its Young's modulus may be determined by rule of mixture. It is shown that even if the modulus of APS layer is close to zero the thickness required to account for the modulus difference obtained from the experiment has to be approximate 172 nm, which is far beyond the typical range of 10–20 nm found in the literature and even much thicker than ~100 nm commercial sizings deposited on the glass fibre [1]. However, it also seems unlikely that the discrepancy in the modulus is caused merely by some kind of experimental error. This will be clarified in further work by using a more accurate method to evaluate E_f of both uncoated and coated fibres.

1.3.3 Fibre strength and distribution

The results for the tensile strength of both uncoated and APS-coated glass fibres are summarised in Table 1.5.

Table 1.5 Average tensile strength of uncoated and APS-coated boron free GF

Gauge length (mm)	Number of sample		Ave. tensile strength±SD	
	Uncoated GF	APS-Coated GF	Uncoated GF	APS-coated GF
5	107	61	1.55±0.38	2.82±0.26
10	97	89	1.51±0.35	2.31±0.81
20	89	87	1.26±0.36	2.28±0.81
40	60	60	1.19±0.42	1.72±0.86
80	72	72	1.14±0.34	1.63±0.87

It can be clearly seen that within each fibre type the tensile strength decreases as the fibre gauge length increases. This is the manifestation of dimension effect discussed in the literature earlier. In addition, the average tensile strength of APS-coated GF was found higher than that of uncoated fibres at each gauge length and particularly at relatively small gauge lengths, APS-coated GF gave almost doubled value for tensile strength compared to uncoated GF. It is also interesting to note that standard deviation for uncoated GF is much lower than that for APS-coated GF except for the fibres at gauge length of 5 mm. More discussion on fibre strength and statistical strength analysis can be found in Appendix (A).

1.3.4 CLTE of glass fibre

Figure 1.24 shows the strain variation of a single boron free uncoated E-glass fibre as a function of temperature during the first heat cycle in CLTE measurement by TMA.

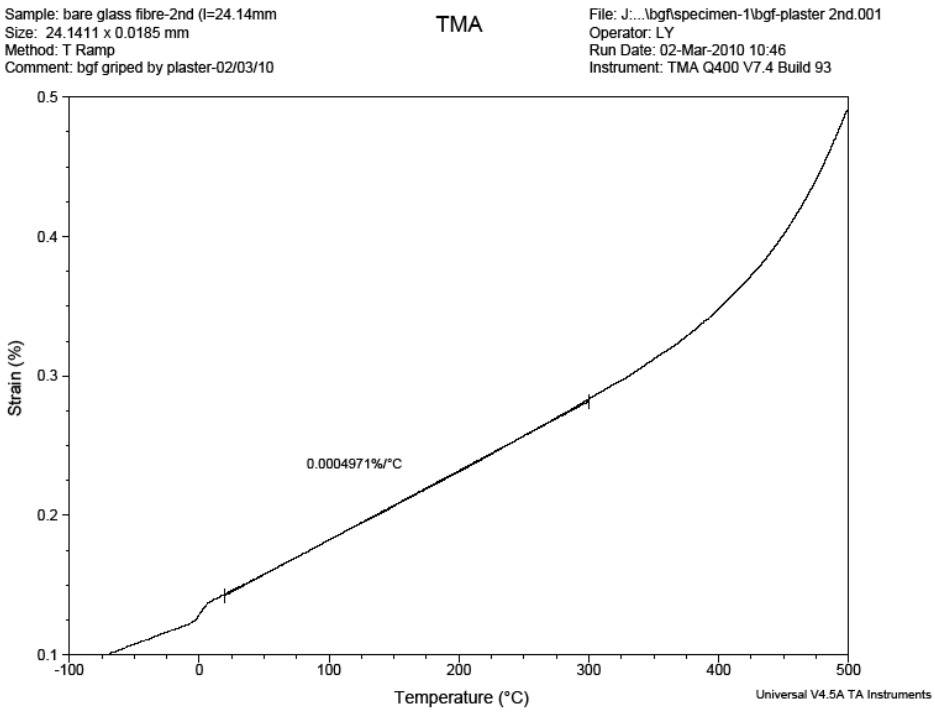

(1)

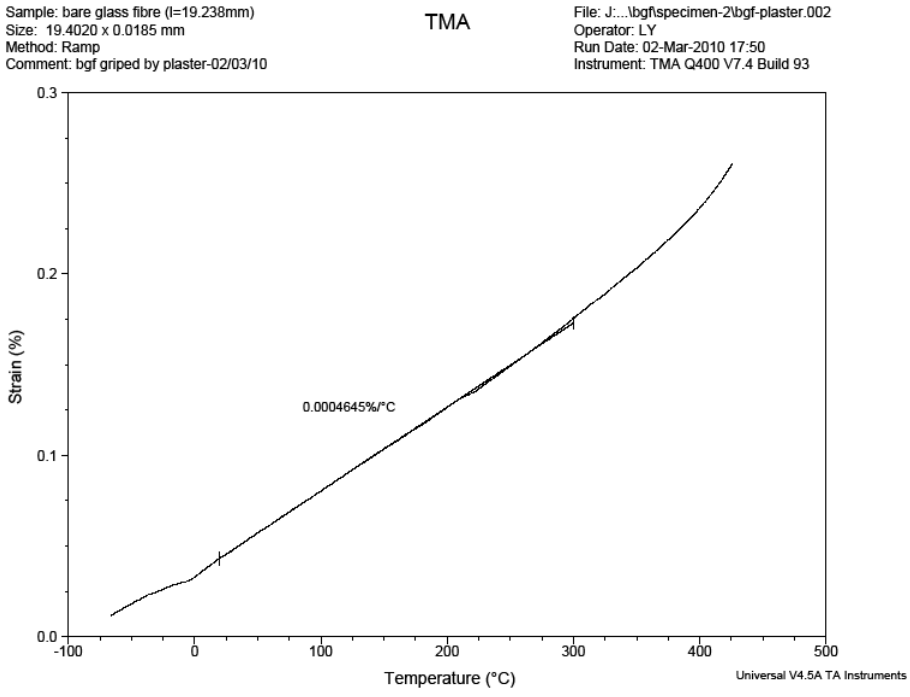

(2)

Fig. 1.22 First heat cycle curve of change in strain of a single boron free uncoated E-glass fibre as function of temperature: (1) fibre (1) and (2) fibre (2)

Fibre (1) and (2) have initial lengths, 24.1 and 19.4 mm, at the room temperature. It can be seen that both samples appear to expand linearly along the fibre axis direction

until approximately 300°C is reached. Assuming both fibre and plaster behave elastically before this temperature, the apparent CLTE can then be calculated from the derivative of the strain with respect to the corresponding temperature according to the Equation (1.18). Based on linear regression method the mean values, 4.64 and 4.97 µm/(m·°C), for CLTE of two individual fibres are obtained within the temperature range of 20–300°C as shown in Figure 1.22. These values are very close to 5 µm/(m·°C), which is the most commonly accepted value for E-glass fibres. Matsumori *et al.* evaluated the accuracy of CLTE measured by TMA in a wide temperature range [65]. One of possible sources of error for this test method is related to the sample dimension change, which is the primary TMA signal. For materials with a high CTE such as polymers this error may be negligible since thermal expansion originated from other components is usually incomparable. For example, polypropylene has the mean CLTE 220 µm/(m·°C) below 120°C whereas the stage and probe in TMA are normally made of vitreous silica, which has only 0.52±0.2 µm/(m·°C) from 20–700°C [55]. Solid glass is known to have a low CTE and the measured dimension change, thus, should be corrected for the expansion of the sample holder. One of the methods developed by Matsumori *et al.* involves the following procedure [65]:

(1) Measure blank, where the measurement instrument baseline is measured using the same test parameters but without a test specimen, that is, with the probe in contact with the stage.

(2) Measure the specimen under the same condition.

(3) Subtract data (1) from data (2).

(4) Calculate CLTE from data (3).

(5) Add the CLTE value of the stage material.

This process can be expressed by Equation 1.22

$$\Delta L_{sp} = \Delta L_{obs} + L\Delta T\alpha_{stage} - \Delta L_{blank} \qquad (1.22)$$

where ΔL_{sp} = change of specimen length, ΔL_{obs} = measured change in length, ΔT = temperature difference over which the change in specimen length is measured, α_{stage} = mean CLTE for stage, and ΔL_{blank} = change of baseline due to heating. In addition, the calibration coefficient, $k = 0.974$, was also determined by using the standard Aluminium sample. The mean CLTE can then be calculated by the Equation 1.23

$$\langle \alpha_l \rangle = \frac{\Delta L_{sp} \times k}{L \times \Delta T} \qquad (1.23)$$

The calculation yields 4.94 and 5.25 μm/(m·°C) for the mean CLTE of fibre (1) and (2) respectively. Although more measurements are required to test the experimental reproducibility, our preliminary attempts have showed that with the aid of plaster as the sample holder material the CLTE of a single glass fibre can be characterised in the temperature range of 20–300°C.

At low temperature the length change remains linear until an abrupt change occurred around 0°C as seen in Figure 1.22. The sudden change in slope of the expansion curve normally indicates a transition of the material from one state to

another. In this case, however, the glass is not expected to undergo any physical transition at 0°C. Since this temperature coincides with the melting point of ice at atmospheric pressure, the slope change may be related to the water adsorbed by the glass. Such change can be exhibited more dramatically in CLTE vs. temperature plot in Figure 1.23.

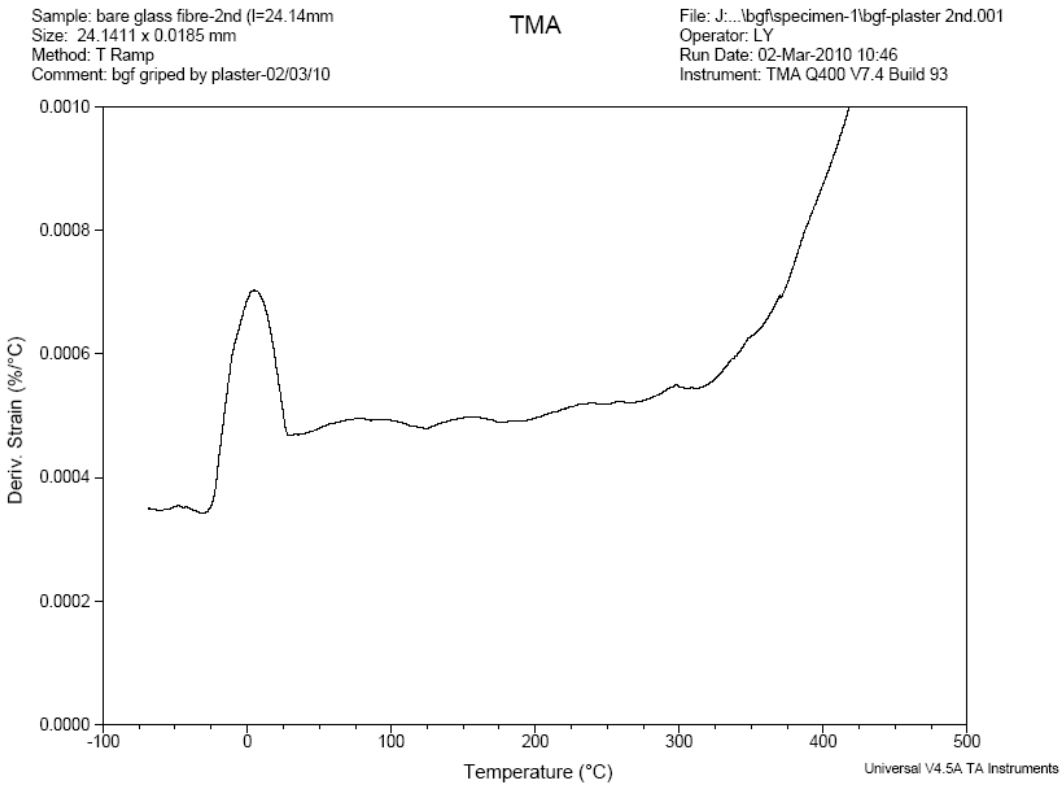

Fig. 1.23 Plot of CLTE as function of temperature for uncoated E-glass fibre

Although the CLTE of the fibre remains fairly constant before and after the transition zone it can be clearly seen that the value at low temperature is actually lower than that at high temperature. The same situation can be found for the other sample. This could also be associated with the adsorbed water on the glass. More work is desired to make this clear.

In the measurement of CLTE of very fine E-glass fibres with the diameter 5 and 7 μm Otto showed the contraction in length of the fibre at elevated temperature (>100°C) in the first heat cycle [12]. This phenomenon is termed as thermal compaction and thought to stem from quench induced non-equilibrium state in the structural configuration of the glass fibre. However, such fibre shrinkage does not appear in the results of this work. This could be due to either the glass fibres used in this study are much thicker with the diameter 18 μm or this contraction is masked by some other factors (e.g. plaster). Figure 1.24 shows the dynamic flexural modulus of the plaster as function of the temperature measured by DMA.

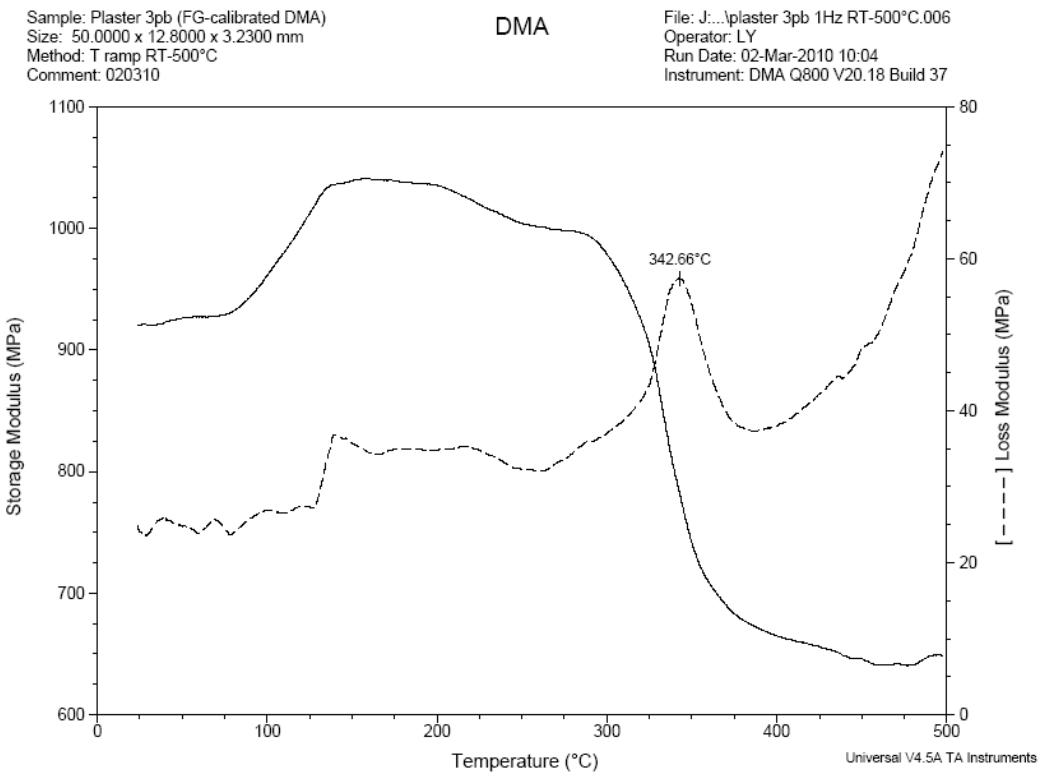

Fig. 1.24 Dynamic flexural modulus of the plaster as function of temperature

The storage modulus of the plaster made in this work is found to undergo an increase at the temperature close to 100°C and experience more significant decrease up to 300°C, which seems to agree with the temperature for the deviation from constant

CLTE in Figure 1.22 and 1.23. The modulus reduction could lead to additional displacement along the direction of the measurement and eventually contribute to the measured length change. If this is the case, one would expect a more dramatic reduction in CLTE than that seen in Figure 1.25 at 100°C. This is probably due to the plaster tested in DMA was not preheated at 120°C as that used in TMA.

1.4 Summary

Mechanical properties of both uncoated and APS-coated boron free E-glass fibre have been characterised by using conventional single fibre tensile testing at a variety of gauge lengths. The Young's modulus for uncoated fibres is found to be 3 GPa (~4%) higher than that for APS-coated fibres. To further confirm this result, more accurate techniques such as ultrasonic method are recommended to measure the modulus of these fibres. The results for the tensile strength of uncoated fibres can be reasonably well fit by unimodal Weibull distribution while the APS-coated fibres show multiple flaw distribution, which requires use of the maximum likelihood method to estimate unknown parameters. APS-coated fibres have showed considerable improvement in the strength controlled by less severe flaws and no effect on the strength controlled by the most severe flaws. This strength enhancement is also related to the fibre length. An attempt to measure the CLTE of a single glass fibre in TMA has been made with the aid of plaster as the sample holder material. The preliminary results showed that the CLTE of the uncoated E-glass fibre is fairly constant in the temperature range of 20–300°C with the value very close to 5 μm/(m·°C). In addition, the adsorbed water on the fibre appears to have an effect on the measured CLTE and more measurements are required to make it clear.

References

[1] Lowenstein KL. The Manufacturing Technology of Continuous Glass Fibres. 1993, Amsterdam: Elsevier.

[2] Chawla KK. Fibrous Materials. 1998, Cambridge University Press.

[3] Hull D,Clyne TW. An Introduction to Composite Materials. 2nd ed. Cambridge Solid State Science Series, ed. Clarke PDR, Suresh PSFRS PIMW. 1996, Cambridge Univerisity Press.

[4] Thomason JL. Lecture at the University of Strathclyde. 2010.

[5] Prabhat KG, Glass fibers for composite materials, in Fibre reinforcements for composite materials, Bunsell AR, Editor. 1988, Elsevier: Amsterdam. p. 19.

[6] Jones FR. Handbook of Polymer-Fibre Composites. Polymer Science And Technology, ed. Brewis DMBiggs D. 1994, Essex and New York: Longman Scientific and Technical.

[7] Bartenev GM. The structure and strength of glass fibers. Journal of Non-Crystalline Solids 1968;1(1):69-90.

[8] Bartenev GM. The structure and strength of glass fibers of different chemical composition. Materials Science and Engineering 1969;4(1):22-28.

[9] Goldstein M,Davies TH. Glass Fibers with Oriented Chain Molecules. Journal of the American Ceramic Society 1955;38(7):223-226.

[10] Brannan RT. Further Evidence Against the Orientation of Structure in Glass Fibers. Journal of the American Ceramic Society 1953;36(7):230-231.

[11] Bateson S. Critical Study of the Optical and Mechanical Properties of Glass Fibers. Journal of Applied Physics 1958;29(1):13-21.

[12] Otto WH. Compaction Effects in Glass Fibers. Journal of the American Ceramic Society 1961;44(2):68-72.

[13] Kurkjian CR, Gupta PK,Brow RK. The Strength of Silicate Glasses: What Do We Know, What Do We Need to Know? International Journal of Applied Glass Science 2010;1(1):27-37.

[14] http://www.doitpoms.ac.uk/tlplib/BD5/printall.php.

[15] Sugarman B. Strength of glass (a review). Journal of Materials Science 1967;2(3):275-283.

[16] Ray NH,Stacey MH. Increasing the strength of glass by etching and ion-exchange. Journal of Materials Science 1969;4(1):73-79.

[17] Griffith AA. The Phenomena of Rupture and Flow in Solids. Philosophical Transactions of the Royal Society of London. Series A, Containing Papers of a Mathematical or Physical Character 1921;221(582-593):163-198.

[18] Schmitz GK,Metcalfe AG. Stress Corrosion of E-Glass Fibers. I&EC Product Research and Development 1966;5(1):1-8.

[19] Jones FR,Rock JW. On the mechanism of stress corrosion of E-glass fibres. Journal of Materials Science Letters 1983;2(8):415-418.

[20] Gupta PK, Strength of glass fibers, in Fiber Fracture, Elices MLlorca J, Editors. 2002, Elsevier Science Ltd: Oxford. p. 127-153.

[21] Charles RJ. Static Fatigue of Glass. I. Journal of Applied Physics 1958;29(11):5.

[22] Gurney C. Delayed fracture in glass. Proceedings of the Physical Society 1947;59(2):169.

[23] Wiederhorn SM,Bolz LH. Stress Corrosion and Static Fatigue of Glass. Journal of the American Ceramic Society 1970;53(10):543-548.
[24] Charles RJ. Static Fatigue of Glass. II. Journal of Applied Physics 1958;29(11):7.
[25] Rodriguez EL. Corrosion of glass fibres. Journal of Materials Science Letters 1987;6(6):718-720.
[26] Kurkjian CR, Gupta PK, Brow RK,Lower N. The intrinsic strength and fatigue of oxide glasses. Journal of Non-Crystalline Solids 2003;316(1):114-124.
[27] Gupta PK,Kurkjian CR. Intrinsic failure and non-linear elastic behavior of glasses. Journal of Non-Crystalline Solids 2005;351(27-29):2324-2328.
[28] Otto WH. Relationship of Tensile Strength of Glass Fibers to Diameter. Journal of the American Ceramic Society 1955;38(3):122-125.
[29] Bartenev GM,Sidorov AB. The effect of length of glass fibers on their strength. Glass and Ceramics 1965;22(9):597-599.
[30] Metcalfe AG,Schmitz GK, Effect of length on the strength of glass fibers, in Fracture toughness testing and its applications, 381 AS, Editor. 1964, American Society of Testing and Materials: Philadelphia, PA. p. 1075-1093.
[31] Schmitz GK,Metcalfe AG. Testing of fibers. Materials Research & Standards 1967;7(4):
[32] Weibull W. A Statistical Theory of the Strength of Materials. Handlingar, Royal Swedish Academy of Engineering Sciences 1939;151
[33] Weibull W. A statistical distribution function of wide applicability. Journal of Applied Mechanics 1951;18:293-297.
[34] ASTM, Standard Practice for Reporting Uniaxial Strength Data and Estimating Weibull Distribution Parameters for Advanced Ceramics. 2007.
[35] Schmitz GK,Metcalfe AG. Characterization of flaws on glass fibers. in 20th Anniversary Technical Conference. 1965: The Society of the Plastics Industry.
[36] Zafeiropoulos NE,Baillie CA. A study of the effect of surface treatments on the tensile strength of flax fibres: Part II. Application of Weibull statistics. Composites Part A: Applied Science and Manufacturing 2007;38(2):629-638.
[37] Andersons J, Joffe R, Hojo M,Ochiai S. Glass fibre strength distribution determined by common experimental methods. Composites Science and Technology 2002;62(1):131-145.
[38] Chi Z, Chou TW,Shen G. Determination of single fibre strength distribution from fibre bundle testings. Journal of Materials Science 1984;19(10):3319-3324.
[39] Masson JJ,Bourgain E. Deterministic method for predicting the strength distribution of a fibre bundle. Journal of Materials Science 1992;27(13):3527-3532.
[40] Zhao FM, Okabe T,Takeda N. The estimation of statistical fiber strength by fragmentation tests of single-fiber composites. Composites Science and Technology 2000;60(10):1965-1974.
[41] Thomason JL,Kalinka G. A technique for the measurement of reinforcement fibre tensile strength at sub-millimetre gauge lengths. Composites Part A: Applied Science and Manufacturing 2001;32(1):85-90.

[42] Beetz Jr CP. The analysis of carbon fibre strength distributions exhibiting multiple modes of failure. Fibre Science and Technology 1982;16(1):45-59.
[43] Zinck P, Pays MF, Rezakhanlou R,Gerard JF. Extrapolation techniques at short gauge lengths based on the weakest link concept for fibres exhibiting multiple failure modes. Philosophical Magazine A 1999;79(9):2103-2122.
[44] Zinck P, Gérard JF,Wagner HD. On the significance and description of the size effect in multimodal fracture behavior. Experimental assessment on E-glass fibers. Engineering Fracture Mechanics 2002;69(9):1049-1055.
[45] Stoner EG, Edie DD,Durham SD. An end-effect model for the single-filament tensile test. Journal of Materials Science 1994;29(24):6561-6574.
[46] Zinck P, Pay MF, Rezakhanlou R,Gerard JF. Mechanical characterisation of glass fibres as an indirect analysis of the effect of surface treatment. Journal of Materials Science 1999;34(9):2121-2133.
[47] Feih S, Thraner A,Lilholt H. Tensile strength and fracture surface characterisation of sized and unsized glass fibers. Journal of Materials Science 2005;40(7):1615-1623.
[48] Zinck P, Mäder E,Gerard JF. Role of silane coupling agent and polymeric film former for tailoring glass fiber sizings from tensile strength measurements. Journal of Materials Science 2001;36(21):5245-5252.
[49] ASTM, Standard Test Method for Tensile Strength and Young's Modulus of Fibers. 2008.
[50] Christman JR. Fundamentals of solid state physics. 1988, New York: John Wiley & Sons.
[51] Richard T. The physics of solids. 2000, New York: Oxford University Press.
[52] ASM I, Thermal expansion, in Thermal properties of metals, Cverna F, Editor. 2002, ASM International: Ohio.
[53] ASTM, Standard Test Method for Linear Thermal Expansion of Solid Materials With a Push-Rod Dilatometer. 2006.
[54] ASTM, Standard Test Method for Linear Thermal Expansion of Rigid Solids with Interferometry. 2010.
[55] ASTM, Standard Test Method for Linear Thermal Expansion of Solid Materials by Thermomechanical Analysis. 2006.
[56] Winks F. Exhibition of an Apparatus for Measuring the Thermal Expansion of Glass. Proceedings Physical Society 1928;41:588-590.
[57] Bouras N, Madjoubi MA, Kolli M, Benterki S,Hamidouche M. Thermal and mechanical characterization of borosilicate glass. Physics Procedia 2009;2(3):1135-1140.
[58] Mironova ML, Chernysheva GL, Oreshnikova NG, Botvinkin OK,Abramyan éa. Thermal expansion of high-silica glass. Glass and Ceramics 1982;39(5):229-231.
[59] Jackson M,Mills B. Thermal expansion of alumino-alkalisilicate and alumino- borosilicate glasses -- comparison of empirical models. Journal of Materials Science Letters 1997;16(15):1264-1266.
[60] Fluegel A. Thermal Expansion Calculation of Silicate Glasses at 210°C Based on the Systematic Analysis of Global Databases. Glass Technology - European Journal of Glass Science and Technology Part A 2010;51(5)
[61] Sauerbrunn SR,Gill PS. Thermomechanical Analysis: Advances in the State of the Art. ASTM STP 1991;1136:120–125.

[62] Badens E, Veesler S, Boistelle R,Chatain D. Relation between Young's Modulus of set plaster and complete wetting of grain boundaries by water. Colloids and Surfaces A: Physicochemical and Engineering Aspects 1999;156:373-379.
[63] Coquard P, Boistelle R, Amathieu L,Barriac P. Hardness, elasticity modulus and flexion strength of dry set plaster. Journal of Materials Science 1994;29(17):4611-4617.
[64] Li CT,Langley NR. Improvement in Fiber Testing of High-Modulus Single-Filament Materials. Journal of the American Ceramic Society 1985;68(8):C-202-C-204.
[65] Matsumori N, Penn J, Nakamura N,Teramoto Y, Evaluating the accuracy of thermomechanical analysis expansion coefficient measurements in a wide temperature range, in Materials Characterization by Thermomechanical Analysis, 1136 AS, Editor. 1991, American Society for Testing and Materials: Philadelphia. p. 32-48.

Chapter 2

Mechanical Characterisation of Polypropylene

2.1 Literature review

2.1.1 Chemistry of polypropylene

Polypropylene (PP) is today one of the most widely used polymeric materials. It has become an integral part of everyone's lifestyle with applications varying from commonplace domestic articles to sophisticated scientific and medical instruments. So what is polypropylene? Strictly defined, PP would simply be whatever was obtained by polymerising propylene, which is usually produced by the cracking of petroleum products such as natural gas or light oils and is the basic building block (i.e. monomer) of PP [1]. As the member of olefin family, propylene is an unsaturated organic compound and has molecular formula C_3H_6, whose molecular structure can be illustrated as

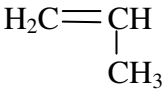

In polymerising propylene, the double bond opens to form another two C-C covalent bonds with another two monomers. This process repeats for a great many times and the polymerised molecule has the following structure

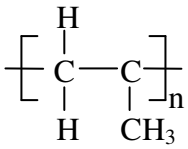

The *n* is, known as the degree of polymerisation, the number of the repeated unit in a PP molecule. It can be seen that little or no unsaturation should be found in PP. The methyl group in the structure above can have different arrangements in the chain, resulting in different types of stereochemical configuration: isotactic PP (Figure 2.1(a)) syndiotactic PP (Figure 2.1(b)) and atactic PP (Figure 2.1(c)).

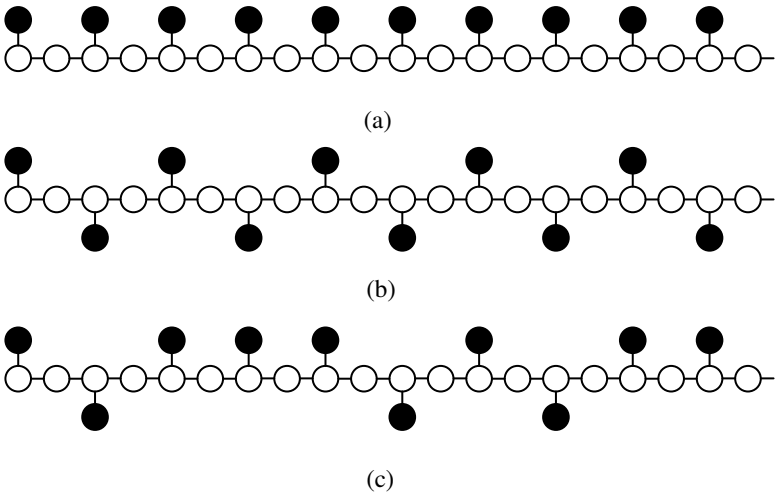

Fig. 2.1 Schematic illustrations of (a) isotactic, (b) syndiotacticm, and (c) atactic PP with pendant carbon atom as black and back-bone carbon atom as white [1]

However, the common features in these molecules are linearity (i.e. no branches) and possibilities for high molecular weight if *n* is high. These characteristics were not achieved prior to 1950, when PP was branched low molecular weight oil with no interest and industrial importance. In the mid-1950s, Ziegler and Natta developed catalysts that were capable of producing stereoregular polymers with high molecular weight from propylene and many other olefins. This was later developed into a new type of chemistry, now known as Ziegler-Natta catalysis. This technology can

manipulate the molecular stereoregularity by controlling the degree of branching, the pendant methyl sequence, and stereo arrangement of the monomer unit (i.e. right or left hand) [1]. The following content will be limited to isotactic PP, which has been of the most importance in both academic research and polymer industry.

2.1.2 Structure and morphology

The structure and morphology of PP have been extensively studied. These aspects have profound effects on the end-use properties of PP. As a saturated linear hydrocarbon polymer, PP has many similarities in its properties to linear polyethylene (PE), which has the simplest basic structure of most polymers [2]. The distinguishing characteristics of PP stem from the presence of the pendant methyl group, which can slightly stiffen the chain and interfere with the molecular symmetry compared to linear PE. The most significant influence of the methyl group is that it can lead to different tacticity, ranging from completely isotactic and syndiotactic structures to atactic molecules as shown in Figure 2.1. The isotactic PP is considered to possess the most regular molecular structure since the methyl groups are all positioned on one side of the molecular backbone. The regularity of the PP allows it to crystallise. However, the molecules of PP cannot crystallise in a planar zigzag form as does PE due to the steric hindrance of the methyl groups. Instead, a helix with three monomer units being required for one turn is adopted. Both right-handed and left-handed helices occur and can fit into the same crystal packing to form a crystallographic unit cell. Different packing geometries in the unit cell lead to four well-known crystal structures: the monoclinic (α) form, the hexagonal (β) form, the triclinic (γ) form and the quenched form [3]. The most common crystal structure by

far is the α-form found in normal melt-crystallised and solution-crystallised PP samples. The unit cells can go on building up a lamellar-shaped crystal, which further involves in the process of forming supermolecular structure of PP. It is therefore said that PP, like other crystalline polymers, exhibits a hierarchy of characteristic scales in its morphology as shown in Figure 2.2 [1, 4].

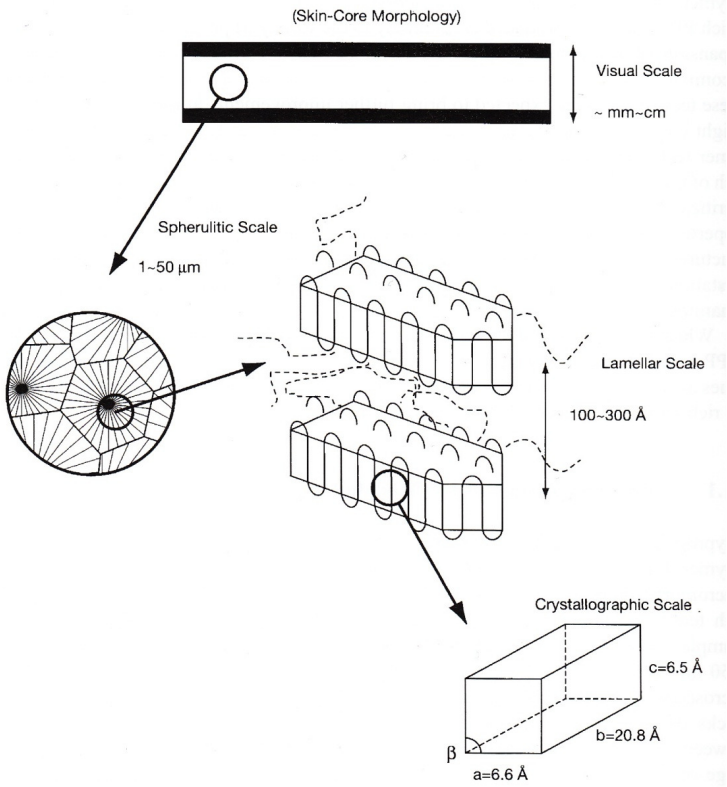

Fig. 2.2 Schematic illustration of a hierarchy of characteristic scales in PP morphology [1]

The unit cell dimensions are shown for the α-form of PP. The lamellae are composed of crystallographically ordered regions. It is also noticeable that the polymer chains are folded in the lamellae. Aggregates of folded-chain crystallites (i.e. lamellae) arranged in definite geometry are designated supermolecular structures [3]. The most frequent supermolecular formations in melt crystallised polymer are spherulites but, under special conditions, other supermolecular geometries may also be formed. Each

spherulite grows uniformly in all spatial directions radially from a nucleus formed either by the density fluctuations that result in the initial chain-ordering process (homogeneous nucleation) or from an impurity (heterogeneous nucleation) in the system. The growth takes place by the formation of a series of lamellar crystals winding helically along the spherulite radius. As the growth of lamellar crystals advances, small-angle branching takes place. The branching of growing crystallites provides complete space filing, which eventually fills out into the characteristic spherical structure. In between the branches are amorphous areas and these, along with the amorphous interfacial regions between the lamellae, make up the disordered content of the semicrystalline polymer. When the nucleation density is high, the spherical symmetry tends to be lost as the spherulite edges impinge on their neighbours to form a mass such as shown in Figure 2.2. From above, one can see that molecular stereoregularity is a critical factor governing the resultant morphology of PP because it determines the crystallisability of the chain. Crystallisation of PP can lead to a relatively high degree of crystallinity, in the range of 40% to 70% [1].

In addition to molecular stereoregularity, there are other structural properties that can affect the morphology of PP such as molecular weight (MW), molecular weight distribution (MWD) (i.e. polydispersity). It is said that lower MW and broader MWD can all lead to an increase in the cystallinity of PP [1]. Low MW allows the polymer chains to rearrange more rapidly and thus create more perfect crystals, whereas high MW PP does not crystallise so easily as lower MW PP.

2.1.3 Processing of Polypropylene

As a member of thermoplastic polymers, PP is shaped into useful products by a wide variety of processes, which has been a major factor in its commercial success. The processes based on PP melt mainly involve extrusion, injection moulding, blow moulding, compression moulding, and so on. It is common practice to extrude and mould PP in the shape of granules, which are generally obtained either by dicing using special granulators or by cutting either hot or cold extruding strands [5]. Commercial grades of PP granules usually contain a great number of additives, which are used to impart stability during the processing and use of PP but also to modify various properties. For example Hindered phenols and amines are normally added into PP as primary antioxidants, which can directly react with the active radical, resulting in nonradical product to be formed [1]. Nucleating agents can affect the physical properties of PP by changing the crystallisation kinetics of PP and plasticisers can reduce the stiffness of PP. Emphasis needs to be placed on three other groups of additives, which are peroxides, surface modifiers, and fillers. In general, the addition of peroxides to PP is intended to improve the processability of PP and achieve the diversity in polymer grades suitable for the different applications by modifying the MW and MWD, which both have a strong influence on rheological properties [6, 7]. This is because that peroxides can initiate and/or promote degradation of the starting PP by giving rise to chain scission of polymer molecules. This will reduce the MW and leads to a narrower MWD [6, 8-10]. Note that certain type of peroxide can also be generated in thermo-oxidative degradation of PP [11] as will be shown in Figure 4.3 in chapter 4. Apparently the introduction of the peroxide, a radical source, can adversely affect the polymer stability.

The poor adhesion of polyolefins arises from their low surface free energy and insufficient chemical functionality of the surface, whose properties can be altered by techniques, including plasma modification [12], flame treatment [13], and surface-graft polymerisation [14]. Various additives can be used to modify the surface properties of PP and improve its adhesion with dissimilar materials such as glass and wood. The most commonly used in PP-based composites is maleic anhydride-grafted polypropylene (MAPP), which serves as an effective compatibilising agent for polar fillers and PP at the interface. It has been demonstrated that it is possible to react solid PP with maleic anhydride (MA) in a solvent-free heterogeneous phase in the presence of dilauryl peroxide, resulting in an modified PP whose characteristics enable it to be advantageously used as a compatibilising agent in the preparation of glass fibre reinforced PP [15]. Numerous fillers are routinely used in PP-based composites and they may be classified into organic and inorganic fillers. The former often involves natural materials [16] and the latter usually include mineral materials such as talc, carbon black [17], calcium carbonate [18], and glass fibre. Among all the fibres, glass fibre has been the most widely used reinforcement in PP and gained tremendous attention from research activities [19-25]. It is used mainly to enhance PP strength and rigidity by serving as a major load bearer in glass fibre reinforced PP composites. Appreciable improvements are, however, only realised after the surface properties of both constituents are altered to obtain a decent adhesive strength at the interface. There is no doubt that various additives could affect morphology of PP at different scales, depending on at which scale the additives interact with PP.

Apart from additives involved in processing PP, the forming processes themselves also play a significant role in determining the final polymer morphology. Molecular

orientation is probably the most evident processing-induced structure in PP. As the term implies, it involves forcing the molecules to line up in a particular direction or plane, rather than being randomly arranged. The molecular orientation is deliberately introduced in some applications such as fibres and films. However, unintended orientation, although to much lesser extent, can also occur in such the process as injection moulding. Injection moulded samples tend to show a clear skin-core morphology consisting of a surface skin layer with a high molecular orientation and an inner core layer composed of spherulites with a low molecular orientation [26, 27]. Furthermore, the processing temperature and pressure are crucial factors that affect the rheological and thermal properties, which influence the macroscopic morphology in injection moulded PP. For example the skin layer thickness decreases with increasing melt temperature and/or mould temperature [27].

2.1.4 Properties of polypropylene

End-use properties of PP are strongly dependent on its structure, morphology, and processing conditions. In fact, the relationship among these aspects plays a key role in general material science and technology. Understanding the correlation between them is normally a central target in a study of materials. For a semicrystalline polymer such as PP, this relationship may be summarised in Figure 2.3.

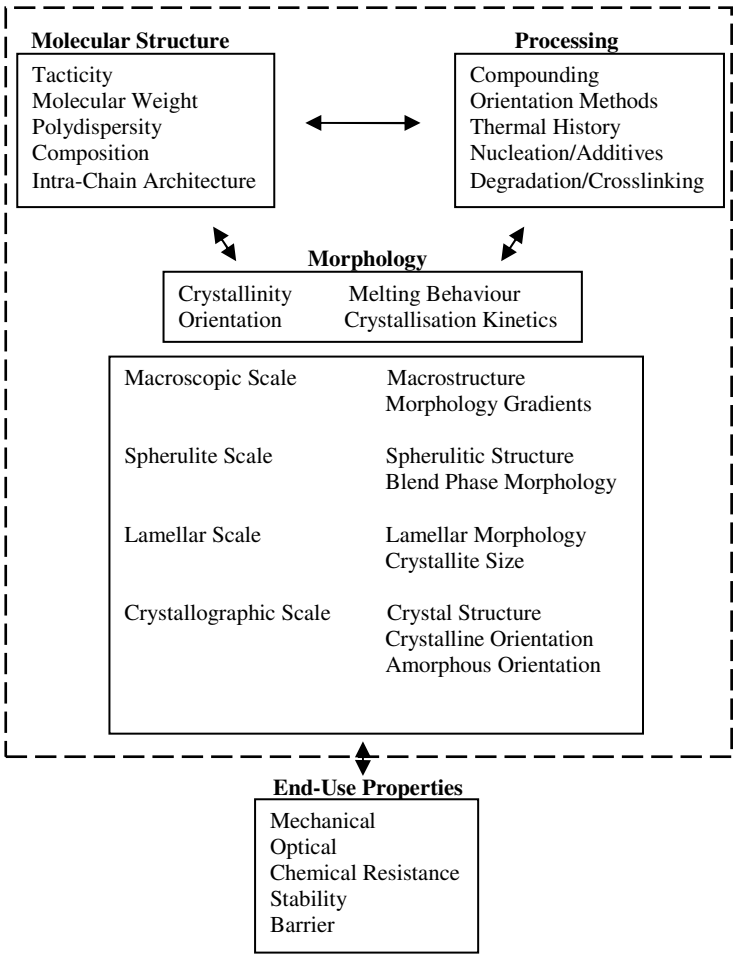

Fig. 2.3 Relationships among polymer structure, processing, morphology, and end-use properties. The polymer morphology is composed of various building blocks over a hierarchy of scales [1]

It can be seen that it is the morphology which provides the most direct link with polymer properties. It is, to large extent, attributed to the importance of intermolecular distances in determining polymer properties. In amorphous region, molecules are randomly loosely arranged and entangled with each other. Glass transition temperature (T_g), which is the onset of the temperature at which molecular segment rotations start to occur, strongly affects many properties of amorphous molecules by the transition from the rubbery to the glassy state as a result of changes in the molecular mobility. On the contrary, the closer packing of the molecules in crystalline region causes an increased density. The decreased intermolecular

distances will also increase the secondary forces holding the chains together and increase the magnitude of properties such as tensile strength, stiffness and softening point. Other typical characteristics of crystalline and amorphous polymers are described below [5].

Amorphous	Crystalline
• *Broad softening range*: thermal agitation of the molecules breaks down the weak secondary bonds. The rate at which this occurs throughout the formless structure varies producing broad temperature range for softening. • *Usually transparent*: the looser structure transmits light so the material appears transparent. • *Low shrinkage*: all thermoplastics are processed in the amorphous state. On solidification, the random arrangement of molecules produces little volume change and hence low shrinkage. • *Low chemical resistance*: the more open random structure enables chemicals to penetrate deep into the material and to destroy many of the secondary bonds • *Poor fatigue and wear resistance*: the random structure contributes little to fatigue or wear properties.	• *Sharp melting point*: the regular close-packed structure results in most of the secondary bonds being broken down at the same time. • *Usually opaque*: the difference in refractive indices between the two phases (amorphous and crystalline) cause interference so the material appears translucent or opaque. • *High shrinkage*: as the material solidifies from the amorphous state the polymers take up a closely packed, highly aligned structure. This produces a significant volume change manifested as high shrinkage. • *High chemical resistance*: the tightly packed structure prevents chemical attack deep within the material. • *Good fatigue and wear resistance*: the uniform structure is responsible for good fatigue and wear properties.

For semicrystalline polymers, the crystalline domains are mainly responsible for the low strain properties such as modulus and yield stress, whereas the amorphous region is thought to account for high strain properties such as toughness and tear. The molecules within amorphous interfacial regions between the crystalline lamellae have segments built into one or more lamellae. Thus, the amorphous molecules are restricted by not only the molecular entanglements but also crystals. These shared and entangled molecules are called tie-molecules, which traverse the amorphous

interface between adjacent lamellae. Tie-molecules have influence on both low and high strain properties [28].

The processing-induced orientation gives rise to anisotropy in the properties of the polymers, with general mechanical properties (e.g. stiffness and tensile strength) higher along the orientation direction than other directions because on application of stress much of the strain is taken up by covalent bonds forming the chain backbone. The oriented chains retain considerable "memory" and with time they may recoil up to some extent by changing confirmation, which can be significantly accelerated by increasing temperature.

The properties of six commercial homopolymer PP (all made by the same manufacturer and subjected to the same test method) which differ in melt flow rate (MFR) are compared in Table 2.1.

Table 2.1 Typical properties of different grades of PP [29]

Name	Melt flow rate at 230 and 2.16 kg (g/10min)	Flexural modulus (GPa)	tensile strength (MPa)	Izod impact notched at 23°C (kJ/m^2)
SABIC PP 531P (PP0.3)	0.3	1.5	30	7
SABIC PP 571P (PP5.7)	5.7	1.8	34	2.7
SABIC PP 575P (PP10.5)	10.5	1.8	34	2
SABIC PP 576P (PP19)	19	1.9	30	2.5
SABIC PP 578N (PP25)	25	2.1	23	2.5
SABIC PP 579S (PP47)	47	1.9	22	2

It shows that a decrease in MW (i.e. increase in MFR) can cause an increase in modulus but decrease in tensile strength and impact strength.

2.2 Experimental

2.2.1 Material

A range of grades of homopolymer isotactic polypropylene were supplied by Saudi Basic Industries Corporation (SBIC). The melt flow rate (MFR) of these grades lies in the range from 0.3 to 47 g/10 min. Not every grade encountered in the following tests went through all the tests, except for the grade with MFR=47 g/10 min (PP47), which is also the grade used for the measurement of adhesion with glass fibre. From now on, each grade of PP will be denoted using the combination of PP and corresponding MFR such as PP0.3 and PP47.

2.2.2 Differential scanning calorimetry

Melting behaviour and crystallisation of different grades of PP were probed by using differential scanning calorimeter (DSC) Q1000. Film samples were made out of PP pellets on a hotplate at temperature of 220°C and cooled down at ambient temperature. The circular shape of the films was then created using a paper punch. The film discs had approximately the diameter of 5.5 mm and thickness of 0.22 mm. The samples weighed 5–6 mg and could perfectly fit in standard DSC pans. A cover was crimped against the pan with the sample sandwiched in between so as to achieve a well sealed environment and intimate thermal contact between the capsules and the samples. This ensured good heat transfer, which is essential for reproducible results.

Nitrogen was used as purge gas during testing and the flow rate was set to be 20 ml/min. The testing procedure was programmed as follows. 1: Data storage Off; 2: Equilibrate at -60.00 °C; 3: Isothermal for 1.00 min; 4: Data storage On; 5: Ramp 10.00 °C/min to 250.00 °C; 6: Isothermal for 1.00 min; 7: Mark end of cycle 1; 8: Ramp 10.00 °C/min to -60.00 °C; 9: Isothermal for 1.00 min; 10: Mark end of cycle 2; 11: Ramp 10.00 °C/min to 250.00 °C; 12: Isothermal for 1.00 min; 13: Mark end of cycle 3. The first thermal cycle was to replace the previous thermal history with the controlled one. The crystallisation was obtained in the second cycle and melting behaviour was recorded in the third cycle. The variation of heat flow with temperature was recorded and typical graph of heat flow against temperature in the cooling cycle and reheating cycle for PP47 is shown in Figure 2.4.

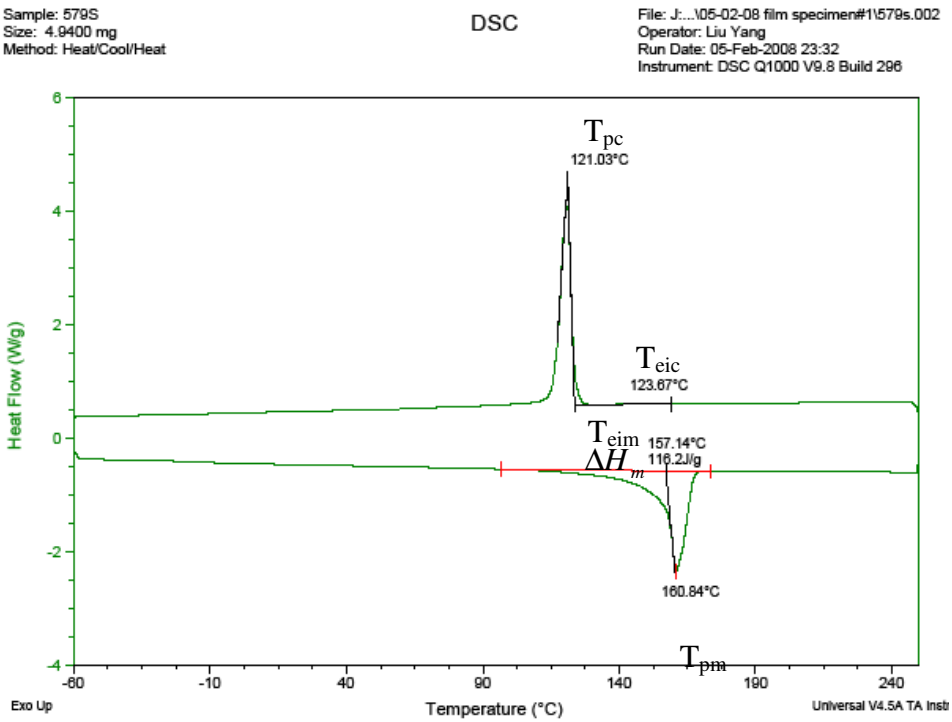

Fig. 2.4 DSC trace with three thermal cycles for PP47 film

From the cooling cycle, crystallisation extrapolated onset temperature, T_{eic}, and crystallisation peak temperature, T_{pc}, were obtained. From the reheating cycle, the

melting extrapolated onset temperature, $T_{eim,}$ and melting peak temperature, $T_{pm,}$ were obtained. Furthermore the heat of fusion, ΔH_m, was calculated through melting peak integration by constructing a baseline by connecting the two points at which the melting endotherm deviated from the relatively straight baseline. Two samples of each grade were tested.

2.2.3 Dynamic mechanical analysis

The viscoelastic properties of various grades of PP were characterised by using dynamic mechanical analyser (DMA) Q800. Bar samples were prepared using a Galomb A-100 hand-operated injection moulding machine at a temperature of 220°C as shown in Figure 2.5, together with the self-manufactured mould and a moulded sample.

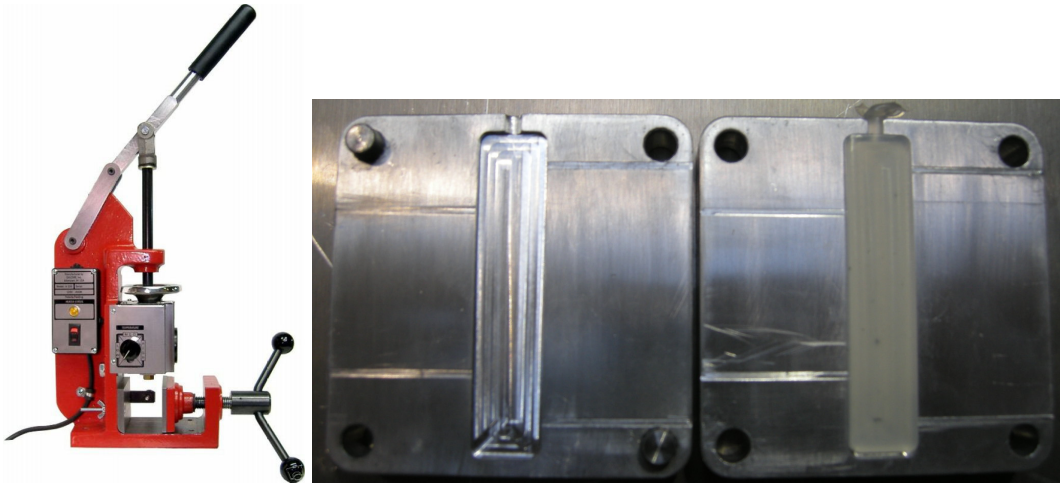

Fig. 2.5 Photo of hand-operated injection moulding machine and the mould for a bar sample

The samples had dimensions 60x12.6x3.2 mm and underwent three-point bending tests with support span length of 50 mm. The experiment settings included heating rate: 3°C/min, temperature range: -60°C to 130°C, frequency: 1 Hz, oscillating

amplitude: 100 µm, static pre-load: 0.1 N, and force track: 150%. All the samples were stored for two days before testing. The test was carried out according to the standard method ASTM D5023-07 [30]. The variation in storage modulus E', loss modulus E'', and damping index, $\tan\delta = E'/E''$ with temperature was recorded and a typical graph of the relationships among them is shown in Figure 2.6.

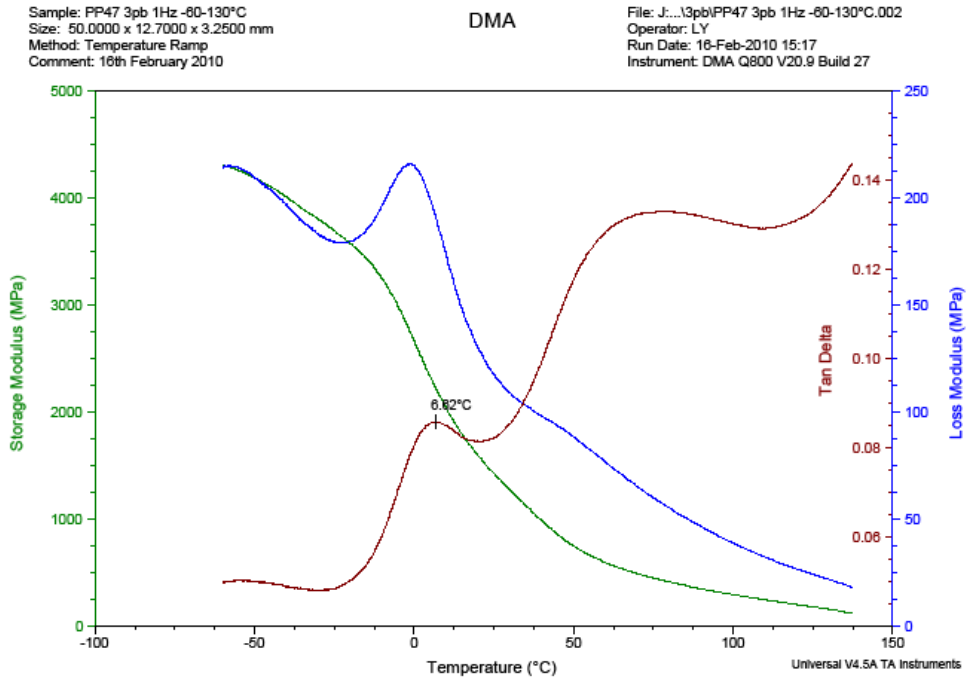

Fig. 2.6 Dynamic mechanical parameters of PP47 as a function of temperature measured by DMA

δ is the phase angle between applied force and measured displacement. Apart from these dynamic mechanical parameters, T_g could also be obtained from the tanδ peak. At least five samples of each grade were tested.

2.2.4 Thermomechanical analysis

The coefficient of linear thermal expansion (CLTE) of PP47 was measured using the thermomechanical analyser (TMA) Q400. Samples were made by having a selected PP47 pellet melted in a Mettler Toledo standard aluminium crucible with dimensions of 6x1.6 mm. The melting was carried out in the thermogravimetric analyser (TGA) Q50 at a temperature of 220°C with nitrogen as purge gas. Samples were retained in the furnace for 4 minutes before cooling down at ambient temperature. Sample dimensions are similar to the crucible dimensions and the exposed surface might need to be polished to produce a flat surface without air bubbles. Figure 2.7 shows a typical sample mounted on the stage and macroexpansion probe.

Fig. 2.7 Photo of iPP47 sample mounted in TMA with macroexpansion probe

Measurements were carried out in the light of TMA experimental instruction and the standard test method ASTM E831-06 [31]. 0.1 N static force was applied to the specimen during testing to ensure that the sensing probe was in contact with the specimen. The specimen was heated at a constant heating rate of 3°C/min over the

temperature range from -60°C to 130°C. The changes in specimen length as a function of temperature were recorded and a typical graph of their relationship is shown in Figure 2.8.

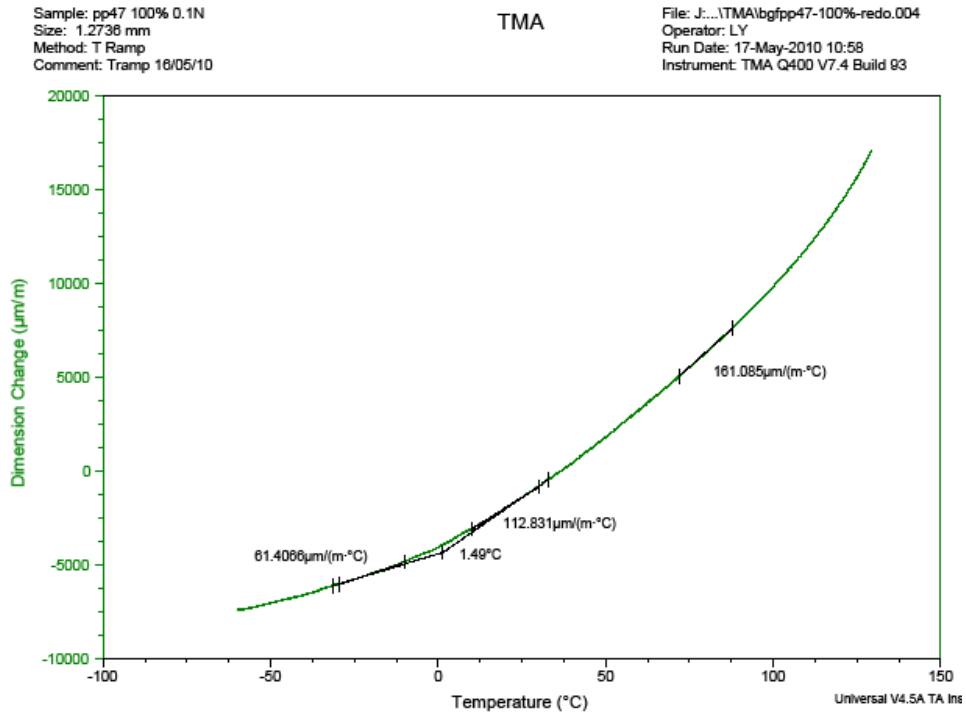

Fig. 2.8 Dimension changes of PP47 as a function of temperature measured by TMA

The mean values of CLTE at different temperatures were then calculated from the slopes of the dimension change versus temperature plots as demonstrated in Figure 2.8. Moreover, the T_g was also determined as the point of intersection of the tangents to the TMA curve before and after the transition [31-32]. At least three samples were measured in this test.

2.2.5 Tensile testing

Tensile properties for PP47 were obtained through a uniaxial tension test. Dumbell-shaped test specimens were injection moulded using an Arburg allrounder

170-90-200 injection moulding machine. The barrel temperatures were set to be 190°C, 195°C, 200°C, and 210°C respectively. The mould temperature was set to be 40°C. The mould pressure was approximately 11.2 MPa and the holding pressure was 7.8 MPa. The total moulding cycle time lasted about 2 minutes due to the moulded part could not be automatically ejected from the mould. The specimens had narrow section with the dimensions 70.00±0.02x10.00±0.02x4.00±0.02 mm. The surface of the samples had many visible scratches due to the marks left in the surface of the mould. The specimens were stored for at least 40 hours and tested prior to 90 hours after moulding. The tensile testing was carried out by using an Instron tensile tester according to ASTM standard method D683-03 with the extension rate set to be 50 mm/min. 9 samples were tested until they eventually ruptured. Figure 2.9 shows a typical loading vs. displacement graph obtained during testing. A linear relationship between the load and displacement, obeying Hooke's law, is held at small sample strain.

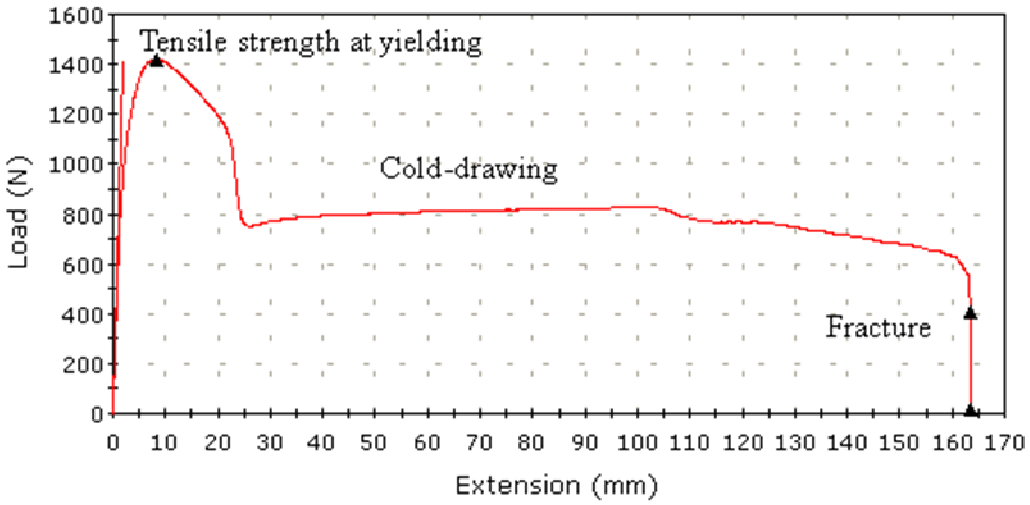

Fig. 2.9 Plot of load vs. extension during tensile testing on injection moulded PP47 sample

The elastic modulus can be obtained by the slope of the linear range combined with the original sample dimensions. Beyond the elastic limit, which is normally not obvious for some materials such as PP, yielding commences and the material is in the plastic range. The manifestation of this range in the graph is the decrease in the slope. When the curve reaches the highest point, where the slope of the curve becomes zero, the localised reduction in cross section, also termed as necking, occurs in the material. This point is known as the tensile strength at yielding and is given by the maximum load carried by the specimen divided by the original cross-sectional area. The neck propagates rather quickly through the specimen under more or less constant load until fracture occurs. Since the load-extension curve for PP does not exhibit a clearly defined yield point, the offset method can be used to indicate this point. The specific procedure to carry out this method can be found in [33].

2.3 Results and discussion

2.3.1 Melting behaviour and crystallisation

The melting curves displayed in Figure 2.4 show some common features in melting behaviour of polymers. For example, the melting process normally extends over a wide temperature range since the size and structure of crystallites vary considerably. Trying to calculate an onset temperature for such process is fairly difficult. The peak maximum temperature of a broad melt is the most meaningful and therefore used in practice. The first heating cycle for PP47 is presented in Figure 2.10, in which double endotherms can be observed.

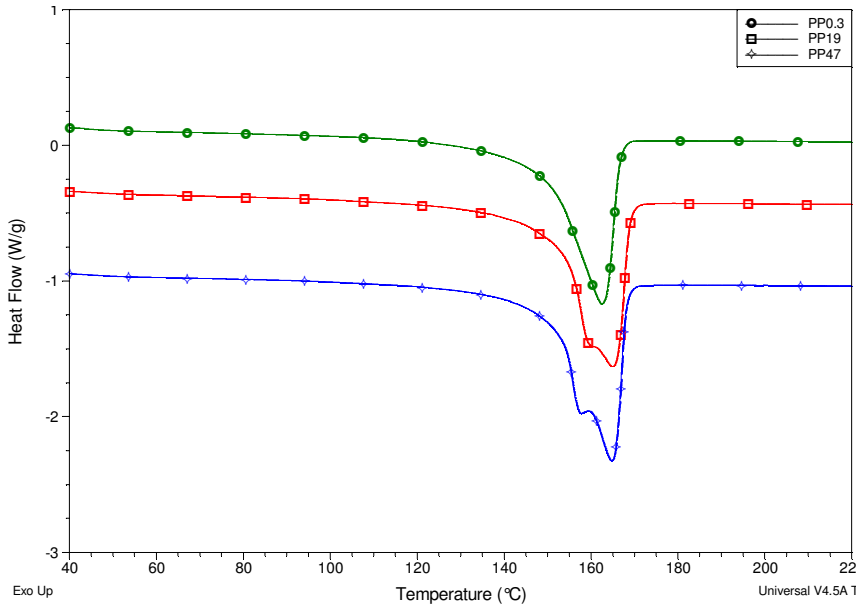

Fig. 2.10 Melting behaviour of PP with different molecular weight in the first cycle

This phenomenon is well known to be caused by recrystallisation, in which perfection of the structure may proceed within the given crystalline modification under favourable thermal conditions such as during the heating [34]. More recently, this double melting behaviour was related to a specific type of spherulite structure, which had predominant cross-hatched lamellae with same thickness in both tangential and radial directions [35]. Recrystallisation is a time- and temperature-dependent process and can be reduced by increasing the heating rate. It is also affected by the MW with low MW giving more remarked recrystallisation [36]. This is the case in this work as shown in Figure 2.10, where Y-axis offset was adjusted for each curve to separate one from another. It is also found in melting curves of all grades tested in DSC that the melting peak in the first heating cycle is always slightly higher than that in the second heating cycle. This could be simply because the specimen has achieved better thermal contact with the pan after the melting process in the first cycle.

Figure 2.11(a) shows the melting temperatures (including both T_{eim} and T_{pm}) of various grades of PP as a function of their corresponding MFR's.

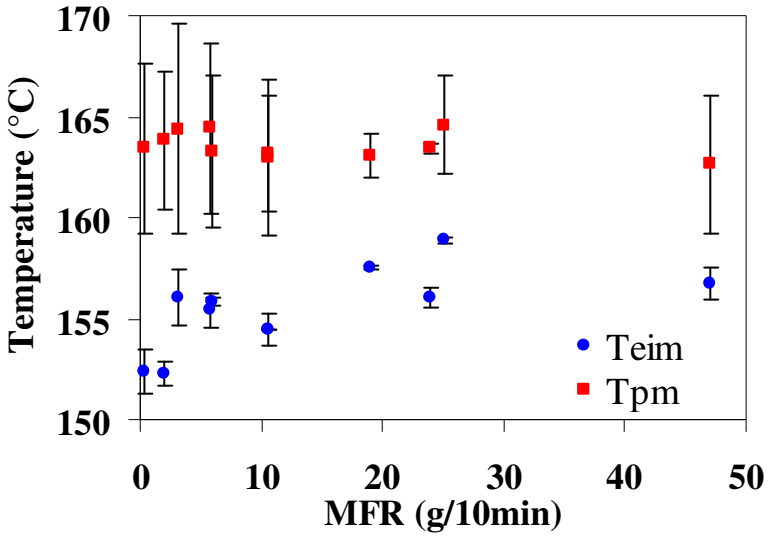

(a)

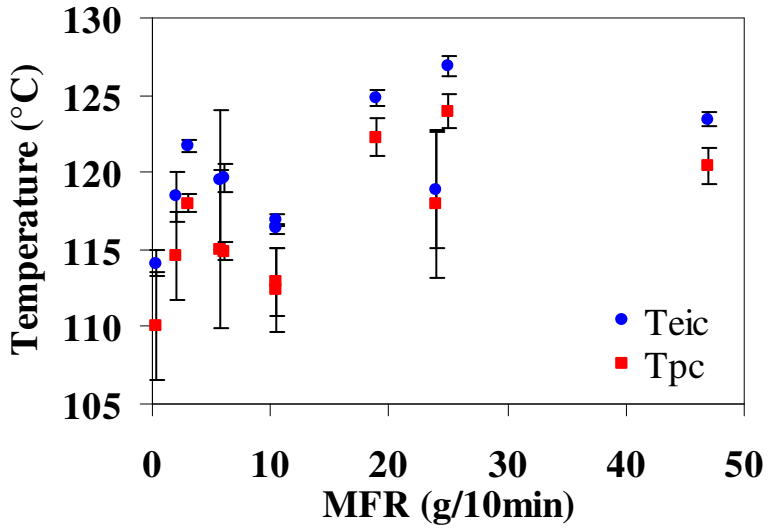

(b)

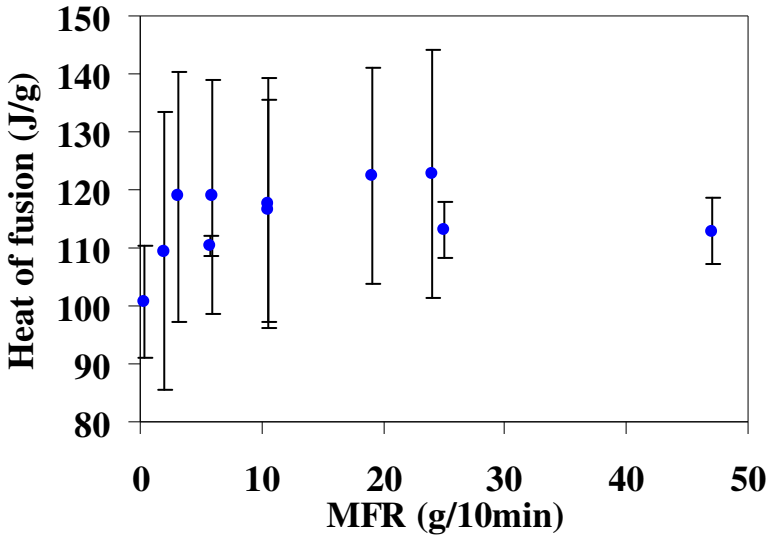

(c)

Fig. 2.11 (a) Melting temperatures, (b) crystallisation temperatures, and (c) heat of fusion of various grades of iPP as a function of MFR measured by DSC

Note it is not the ideal way of evaluating the influence of MW on melting temperatures since there is no consistence in MWD and additives, which could all affect the melting behaviour of PP. Nevertheless, the tendency of an increase in T_{eim} before MFR=25 g/10min can be observed in Figure 2.11. This may result from the fact that it is easier for shorter chains to organise themselves into crystallites. Consequently the crystallites formed with shorter chains have more perfection and give higher T_{eim}. However, this does not seem to be the case for T_{pm}, which does not appear to be affected by MFR. Moreover, the large error bars in the results for T_{pm} measured under the same conditions implies that the impurities in the sample may affect T_{pm} to greater extent than onset temperature. More measurements need to be carried out to reduce the scatter in the results for T_{pm}.

Figure 2.11(b) shows the crystallisation temperatures of various grades of PP as a function of their corresponding MFR's. It can be seen that both T_{eic} and T_{pc} appear to

increase as the MFR increases before MFR=25 g/10min. The data point at PP47 does not follow this trend and have a value slightly lower than that at PP25. The datasheet of PP25 indicates that this grade is nucleated, which allows it to crystallise at higher temperature. The results are qualitatively in agreement with the MW dependence of PP crystallisation reported in the literature [2, 37]. The increase of T_{eic} and T_{pc} with the decrease in MW of PP is attributed to the fact that PP with lower MW has shorter chains and less physical crosslinks (i.e. entanglements), which would both favour the crystallisation.

Figure 2.11(c) shows the heat of fusion of various grades of PP as a function of their corresponding MFR's. For the same material, heat of fusion is proportional to its degree of crystallinity. The results in Figure 2.11(c), thus, can also be interpreted in terms of degree of crystallinity. It can be seen that a decrease in MW tends to increase PP crystallinity, which fits the results for its crystallisation behaviour shown above. However, such effect does not seem significant due to large data scatter, which may be partially attributed to the calculation of the heat of fusion. Broad melting peaks can make it difficult to identify the beginning of melt and small changes can have a significant effect on the values obtained. In this work, the run were started well below the melting region and extended well above the melting area in order to distinguish the flat baseline from the melting region. However, it was down to the operator to select calculation limits.

2.3.2 Thermomechanical properties

Figure 2.12(a) shows storage moduli, E', of three grades of PP as a function of temperature.

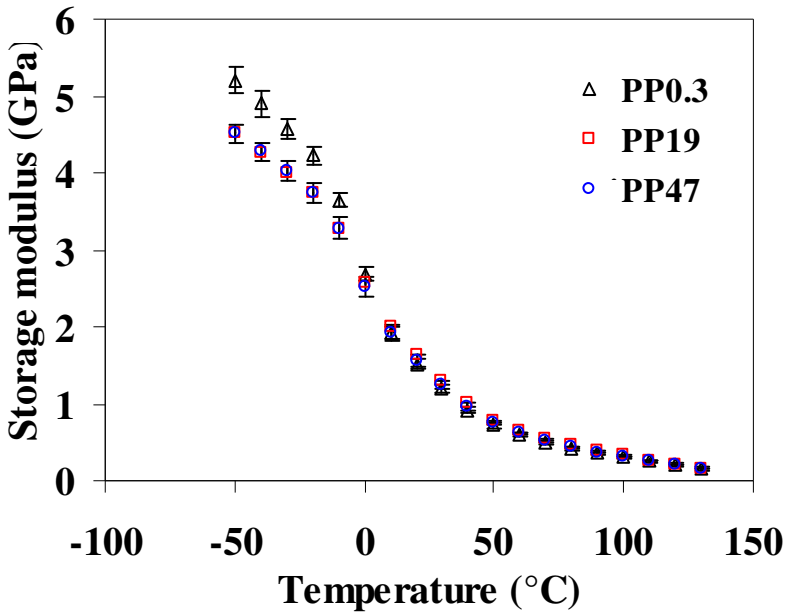
Storage modulus (GPa)
6
5
4
3
2
1
0
-100
-50
0
50
100
150
Temperature (°C)
PP0.3
PP19
PP47

(a)

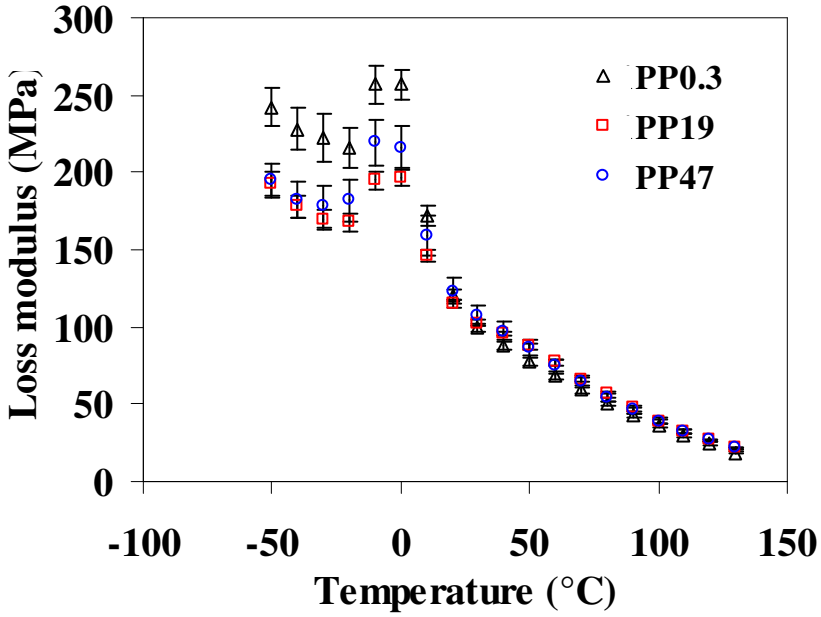
Loss modulus (MPa)
300
250
200
150
100
50
0
-100
-50
0
50
100
150
Temperature (°C)
PP0.3
PP19
PP47

(b)

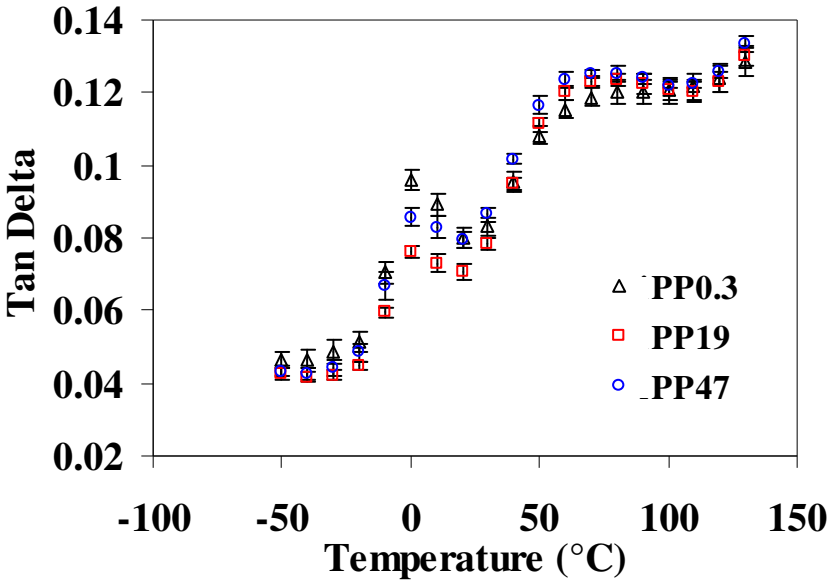

(c)

Fig. 2.12 (a) Storage modulus, (b) loss modulus, and (c) tan Delta of various grades of PP as a function of temperature measured by DMA

It shows significant decrease of E' around T_g, which is about 2°C. Above T_g, the difference in E' among these grades is quite small with E' of PP19 slightly higher than that of PP0.3 and E' of PP47 in between. This seems to agree with the results for their crystallinities as discussed earlier. Below T_g, however, E' of PP0.3 increases more considerably and overtakes E' of other two grades by 15% at -50°C. This may imply the change in a role that the amorphous phase plays in the temperature dependence of mechanical properties of PP. Above T_g, crystallinity of PP mainly accounts for the measured modulus and amorphous phase is in a rubbery state constrained by both molecular entanglements and crystallinites. The number of tie-molecules can also affect the modulus since they are responsible for transferring the load between laminae. Below T_g, crystallinity of PP is still the major contributor to the modulus. However, the amorphous phase is in a glassy state and may affect the modulus more significantly compared to its rubbery state. Thus, PP0.3 with lower

crystallinity and larger number of tie-molecules may have a lower E' above T_g and a higher E' below T_g than other two grades, which have less of this effect probably due to much smaller difference in the MW between PP19 and PP47. Despite the effect of different MW, the results in Figure 2.12(a) clearly shows a rapid change in E' with temperature and slopes of 89.6±3.9, 65.6±4.6, and 67.8±3.7 MPa/°C can be obtained at T_g for PP0.3, PP19, and PP47 respectively.

Figure 2.12(b) shows loss moduli, E'', of three grades of PP as a function of temperature. In general E'' decreases with the temperature and forms a peak around -2°C, which can sometimes be taken as T_g. However, the T_g is determined at the maximum of tanδ as shown below. Furthermore, comparison between different grades shows that the effect of MW on E'' is similar to that on E'. This implies that below T_g the dynamic modulus for PP0.3 should be higher than that of other grades and has a relatively low value above T_g. Figure 2.12(c) shows damping indexes, tanδ, of three grades of PP as a function of temperature. The peaks at a plot of tanδ vs. temperature are normally regarded to correspond to various characteristic relaxation times. T_g can be obtained from the primary peak in each curve of Figure 2.12(c). It shows that there is little different in T_g among these grades, which is a bit surprising since the increasing number of chain ends in PP19 and PP47 is expected to shift the transition region to a much lower temperature from that of PP0.3.

Figure 2.13 shows variation in CLTE of PP47 with temperature. It can be seen that CLTE of PP47 keeps increasing with temperature and develops a step at the glass transition region.

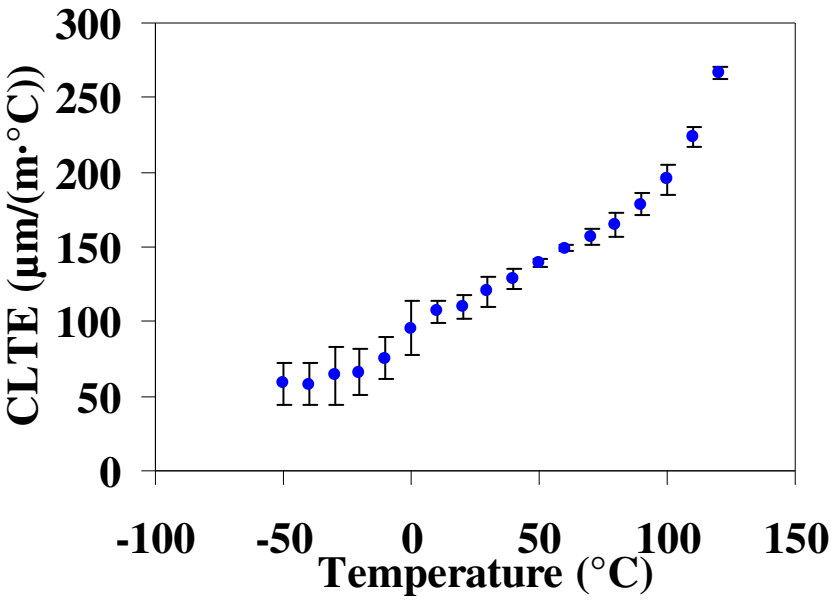

Fig. 2.13 CLTE of PP47 as a function of temperature

The results are in agreement with those found in the literature [20]. Moreover, the curve in Figure 2.13 shows a glass transition temperature similar to that obtained by DMA.

2.3.3 Tensile properties

It is well known that tensile properties at large strain for PP generally are highly variable due to inconsistencies in necking of the gauge section of the specimen. Since properties at yield are more reproducible, the results only for elastic modulus, 0.2% offset yield strength, and tensile strength at yielding are reported here. The average value of elastic modulus of PP47 is 1.20±0.01 GPa, which is lower than the value of 1.45 GPa quoted in the standard test method for tensile properties of plastics [33]. This may be caused by the different conditions for the injection moulding process than those specified in [33]. Particularly, the relatively low mould temperature combined with the overlong mould open time could lead to low

crystallinity of the material. Moreover, relatively low injection and holding pressure may give rise to less oriented polymer molecules. These would all tend to reduce the elastic modulus in a tensile test. The 0.2% offset yield strength and tensile strength at yielding of PP47 at room temperature are 15.93±0.57 MPa and 35.32±0.21 MPa respectively.

2.4 Summary

A series of thermal analyses were carried out on various grades of PP with main focus on PP47. The results from DSC showed that the grades with low MW tended to crystallise at higher temperature and achieved a relatively greater crystallinity, which was the likely cause for their relatively high dynamic moduli above T_g measured by using DMA. Below T_g, however, high MW grade had higher dynamic modulus, which may result from the larger number of tie-molecules. $T_g \approx 2°C$ was obtained for PP47 by both DMA and TMA. The tensile properties of PP47 at small strain were obtained by a set of normal unaxial tensile tests, including elastic modulus, 0.2% offset yield strength, and tensile strength at yielding.

References

[1] Moore EP. Polypropylene Handbook. 1996, New York: Hanser Publisher.

[2] Brydson JA. Plastics Materials. 7th ed. 1999, Oxford: Elsevier Butterworth-Heinemann.

[3] Cheng S, Janimak J,Rodriguez J. Polypropylene: structure and morphology. Polypropylene: structure, blends and composites, ed. Karger-Kocsis J. Vol. 1. 1995, London: Chapman & Hall.

[4] Norton DR,Keller A. The spherulitic and lamellar morphology of melt-crystallized isotactic polypropylene. Polymer 1985;26(5):704-716.

[5] Crawford R. Plastics Engineering. 3rd ed. 1998, Oxford: Elsevier Butterworth-Heinemann.

[6] Greene RG,Prieski ET, Process for degrading stereoregular polymers, Patent US, Editor. 1964.

[7] Azizi H,Ghasemi I. Reactive extrusion of polypropylene: production of controlled-rheology polypropylene (CRPP) by peroxide-promoted degradation. Polymer Testing 2004;23(2):137-143.

[8] Rocha MCG, Coutinho FMB,Balke ST. A study of polypropylene peroxide promoted degradation. Polymer Testing 1995;14(4):369-380.

[9] Kron A, Stenberg B, Reitberger T,Billingham NC. Chemiluminescence from oxidation of polypropylene: Correlation with peroxide concentration. Polymer Degradation and Stability 1996;53(1):119-127.

[10] Berzin F, Vergnes B, Dufossé P,Delamare L. Modeling of peroxide initiated controlled degradation of polypropylene in a twin screw extruder. Polymer Engineering & Science 2000;40(2):344-356.

[11] Richaud E, Farcas F, Fayolle B, Audouin L,Verdu J. Hydroperoxide build-up in the thermal oxidation of polypropylene - A kinetic study. Polymer Degradation and Stability 2007;92(1):118-124.

[12] Fabienne P-E, Bruno C,Jean-Claude B. Modification of isotactic poly(propylene) with a nitrogen plasma; differences in comparison to the treatment with a carbon dioxide plasma. Die Makromolekulare Chemie 1991;192(7):1589-1599.

[13] Garbassi F, Occhiello E,Polato F. Surface effect of flame treatments on polypropylene. Journal of Materials Science 1987;22(1):207-212.

[14] Singh RP. Surface grafting onto polypropylene -- a survey of recent developments. Progress in Polymer Science 1992;17(2):251-281.

[15] Bortolon V, Padua., Savadori T,Pontelagoscuro., Process for modifying polypropylene with maleic anhydride. 2002, P. Group S.r.l., Milan (IT): United States.

[16] Mantia FPL, Morreale M,Ishak ZAM. Processing and mechanical properties of organic filler–polypropylene composites. Journal of Applied Polymer Science 2005;96(5):1906-1913.

[17] Mucha M, Marszalek J,Fidrych A. Crystallization of isotactic polypropylene containing carbon black as a filler. Polymer 2000;41(11):4137-4142.

[18] Tabtiang A,Venables R. The performance of selected unsaturated coatings for calcium carbonate filler in polypropylene. European Polymer Journal 2000;36(1):137-148.

[19] Thomason JL,Vlug MA. Influence of fibre length and concentration on the properties of glass fibre-reinforced polypropylene: 1. Tensile and flexural modulus. Composites Part A: Applied Science and Manufacturing 1996;27(6):477-484.
[20] Thomason JL,Groenewoud WM. The influence of fibre length and concentration on the properties of glass fibre reinforced polypropylene: 2. Thermal properties. Composites Part A: Applied Science and Manufacturing 1996;27(7):555-565.
[21] Thomason JL, Vlug MA, Schipper G,Krikor HGLT. Influence of fibre length and concentration on the properties of glass fibre-reinforced polypropylene: Part 3. Strength and strain at failure. Composites Part A: Applied Science and Manufacturing 1996;27(11):1075-1084.
[22] Thomason JL,Vlug MA. Influence of fibre length and concentration on the properties of glass fibre-reinforced polypropylene: 4. Impact properties. Composites Part A: Applied Science and Manufacturing 1997;28(3):277-288.
[23] Thomason JL. The influence of fibre length and concentration on the properties of glass fibre reinforced polypropylene: 5. Injection moulded long and short fibre PP. Composites Part A: Applied Science and Manufacturing 2002;33(12):1641-1652.
[24] Thomason JL. The influence of fibre length and concentration on the properties of glass fibre reinforced polypropylene. 6. The properties of injection moulded long fibre PP at high fibre content. Composites Part A: Applied Science and Manufacturing 2005;36(7):995-1003.
[25] Thomason JL. The influence of fibre length and concentration on the properties of glass fibre reinforced polypropylene: 7. Interface strength and fibre strain in injection moulded long fibre PP at high fibre content. Composites Part A: Applied Science and Manufacturing 2007;38(1):210-216.
[26] Kantz MR, Newman HD,Stigale FH. The skin-core morphology and structure–property relationships in injection-molded polypropylene. Journal of Applied Polymer Science 1972;16(5):1249-1260.
[27] Fujiyama M, Wakino T,Kawasaki Y. Structure of skin layer in injection-molded polypropylene. Journal of Applied Polymer Science 1988;35(1):29-49.
[28] Nitta K-H,Takayanagi M. Role of tie molecules in the yielding deformation of isotactic polypropylene. Journal of Polymer Science Part B: Polymer Physics 1999;37(4):357-368.
[29] http://plastics.sabic.eu/datasheets/product_datasheets/_en/index.pl
[30] ASTM, Standard Test Method for Plastics: Dynamic Mechanical Properties: In Flexure (Three-Point Bending). 2007.
[31] ASTM, Standard Test Method for Linear Thermal Expansion of Solid Materials by Thermomechanical Analysis. 2006.
[32] ISO, Plastics–Thermomechanical analysis (TMA)–Part 2: Determination of coefficient of linear thermal expansion and glass transition temperature. 1999.
[33] ASTM, D638-03: Standard test method for tensile properties of plastics. 2003, Americian Society of Testing Materials.
[34] Varga J. Crystallization, melting and supermolecular structure of isotactic polypropylene. Polypropylene: structure, blends and composites, ed. Karger-Kocsis J. Vol. 1. 1995, London: Chapman & Hall.

[35] Yang J. Origin of double melting peaks of α-form isotactic polypropylene: Recrystallization and lamellar thickness hierarchy. Journal of Applied Polymer Science 2010;118(3):1520-1526.
[36] Ryu SH, Gogos CG,Xanthos M. Melting behaviour of controlled rheology polypropylene. Polymer 1991;32(13):2449-2455.
[37] Paukkeri R,Lehtinen A. Thermal behaviour of polypropylene fractions: 1. Influence of tacticity and molecular weight on crystallization and melting behaviour. Polymer 1993;34(19):4075-4082.

Chapter 3

Mechanical Characterisation of the GF-PP Interface

3.1 Literature review

3.1.1 Theory of bonding at the fibre-matrix interface

A classic definition of the interface in fibre composites is a surface formed by a common boundary of reinforcing fibre and matrix and maintains the bond in between for the transfer of loads [1]. It has physical and mechanical properties that are different from, but related to, those of the fibres or the matrix. Over the past decades of the research in this subject, this 2D concept has been extended into a more complex 3D interphase, which is considered to be the geometrical surface of the classic fibre-matrix contact as well as the region of finite volume extending on both sides of the interface into both the fibre and matrix. Chemical, physical and mechanical properties of this region can vary either continuously or in a stepwise manner between those of the bulk fibre and matrix material [1]. This means that the interphase is a unique physical region that exists from some point in the fibre through the actual interface into the matrix, embracing all the volume altered during the consolidation or fabrication process from the original fibre and matrix materials. Such concept emphasizes the entity of interphase in fibre composites, particularly with high fibre volume fraction.

The origin of the bonding between fibre and matrix is usually discussed in terms of theories of adhesion with associated mechanisms of bonding. Adhesion in general

can be attributed to mechanisms including adsorption and wetting, electrostatic attraction, interdiffusion and chemical bonding and mechanical interlocking [1, 2]. In most cases, the fibre-matrix adhesion is characterised by a complex blend of the interactions mentioned above. The nature of bonding is therefore not only dependent on the atomic arrangement, molecular conformation and chemical constitution of the fibre and matrix, but also on the morphological properties of the constituents and the diffusivity of elements in each constituent [1]. It follows that the interface is specific to each fibre-matrix system.

It is known that good wetting of fibres by liquid resin material is a prerequisite to ensure a decent interfacial contact between the fibre and the matrix so that a proper consolidation of composites can be achieved. Wetting can be quantitatively expressed in terms of the thermodynamic work of adhesion, W_a, of a liquid to a solid using the Dupre equation

$$W_a = \gamma_{SV} + \gamma_{LV} - \gamma_{SL} \qquad (3.1)$$

where γ_{SV}, γ_{LV}, and γ_{SL} are the surface free energies of the solid-vapour, liquid-vapour, and liquid-solid interfaces, respectively. The above equation can be related to a model of a liquid drop on the flat surface of a solid by Young's equation

$$\gamma_{SV} = \gamma_{SL} + \gamma_{LV} \cos\theta \qquad (3.2)$$

where θ is the contact angle at the contact of three phases. Combining Equations. 3.1 and 3.2 yields the Young-Dupre equation

$$W_a = \gamma_{LV}(1 + \cos\theta) \qquad (3.3)$$

It can be seen from Equation 3.3 that W_a can be experimentally determined by measuring γ_{LV} and θ.

Electrostatic attraction arises from a difference in electrostatic charge between constituents at the interface. It is not regarded as a major contribution to the final bond strength of the interface and can readily be reduced, for example by discharging in the presence of a strongly polar solvent, such as water. Nevertheless, it could be important when the fibre surface is treated with some coupling agent.

Interfacial bonds between two surfaces may be formed by the interdiffusion of atoms or molecules across the interface. The bond strength resulting from the interdiffusion of molecules will depend on the amount of molecular entanglement, the number of molecules involved and the strength of the bonding between the molecules. Interdiffusion can lead to an interpenetrating network in the interface region (i.e. interphase), which may have a substantial thickness and possess different chemical, physical and mechanical properties from those of either the bulk fibre or the matrix [3]. Such networks can sometimes be further mechanically enhanced if chemical reaction occurs in the diffused region [4].

The chemical bonding mechanism is based on the primary bond at the interface between the fibre and the matrix and normally offers a major explanation for a strong adhesive bond across the interface. A variety of coupling agents have been developed to achieve chemical bonding between a chemical group on the fibre surface and another compatible chemical group in the matrix. For instance, a silanol group of a silane coupling agent may react with a hydroxyl group of the glass fibre surface,

while a group such vinyl and amino on the other end of the silane molecule can react with the epoxide group in an epoxy matrix. In most cases the coupling agent as an adhesion promoter is used as a part of chemical package, known as 'size', applied to the fibre surface during the manufacturing (see Literature review in chapter 1).

Mechanical interlocking involves solely mechanical anchoring through surface asperities between two contact surfaces. This concept has been extensively studied in the subject of friction and arises from early attempts to account for Amonton's law, which claims that the friction force that needs to be overcome to cause relative sliding between two contact surfaces is proportional to the normal force across the interface [5]. The proportional constant, defined as coefficient of friction, was related to the maximum slope of the asperity junction in the early analyses based on the idea that one surface must be lifted up a typical slop of the asperity junction determined by roughness on the other surface. It was later argued that asperities on real surfaces do not match as well as envisioned in this model and more advanced models have been established to describe the asperity interaction on a microscopic level [5-8]. Apparently the mechanical interlocking arises from the surface roughness, which exists on nearly all solid surfaces. With the advent of the atomic force microscope (AFM) and lateral force microscopy (LFM), the surface roughness of glass fibres has recently been investigated and it showed that sized glass fibre exhibited heterogeneities in surface roughness, while desized glass fibre (obtained by heating the sized fibre at 600°C for 24 hours) revealed a smooth and homogeneous surface with very small coefficient of friction (approximately equal to 0.04) [9]. In the case of fibre reinforced polymer composites, the quality of mechanical bonding in the interface should depend on the surface roughness of the fibres and wettability of the

matrix to the fibres. The effects are likely to be much more significant under shear loading than in transverse tension unless there are a large number of re-entrant angles on the fibre surface [1]. In addition, mechanical bonds can be further affected by the residual stress built up in the system. For example, the compressive radial residual thermal stress may be formed across the fibre-matrix interface due to the mismatch of coefficient of thermal expansion between the fibre and the matrix. Combined with nonzero coefficient of friction, the compressive residual stress is expected to provide friction resistance against the interfacial sliding.

3.1.2 Mechanical characterisation of the fibre-matrix interface

The ideal technique for measuring interfacial mechanical properties of a composite should have the following characteristics:

(1) Easy to set up and operate the experiment in terms of both sample preparation and testing fixture.

(2) Sensitive to interfacial properties.

(3) Insensitive to the sample and testing conditions such as sample geometry, loading mode, and loading rate etc.

(4) Resemble actual loading configuration of practical composite components.

(5) In-situ observation of the failure process.

(6) Easy to reduce the data.

Over the last four decades a number of experimental techniques have been developed to assess fibre-matrix interface bond quality. In general these techniques can be classified into two different categories depending on the nature of samples used and the scale of testing: on a microscopic scale, microcomposites often involving a single fibre are employed to provide direct measurements of interface properties. In the case of macroscopic level, bulk composite specimens are usually used to measure the interlaminar/intralaminar properties, from which the fibre-matrix interface properties are inferred. Reviews on these techniques and related issues can be found in many fine books and papers [1, 4, 10-12]. Over the years, it has become quite clear that the micromechanical tests serve as the major tools for directly measuring fibre-matrix interfacial properties. The test methods in this category usually include the single fibre pull-out test, microbond test, fragmentation test and single fibre push-out test. In these tests, the bond quality at fibre-matrix interface is measured in terms of the interfacial fracture toughness, G_{ic}, or the interfacial shear strength (IFSS), τ_{ult}. The former is the energy release rate of the composite constituents required to extend a debonded crack and the latter is the shear stress required to produce shear failure locally at a point at the interface. When IFSS is obtained under the assumption that interfacial shear stress is uniformly distributed at debonding, it is usually regarded as apparent IFSS, $\tau_{app.}$ Despite the simplicity and popularity, numerous work has revealed that using the apparent IFSS to characterise the fibre-matrix adhesion without knowing the real shear stress distribution can sometimes considerably underestimate the interface bond strength [13-16]. Moreover, it has been found that the τ_{app} values can be highly contaminated by interfacial friction from the partially debonded interface [17, 18]. Therefore, the local IFSS is

considered by many researchers to more correctly characterise interface strength. The importance of the local IFSS is further emphasised along with the determination of adhesional strength, σ_{ult}, which is another interfacial failure criterion that has been proposed by several authors in recent years [19-21]. In comparison with IFSS, the adhesional strength can also be seen as interfacial normal strength (IFNS), which is the tensile stress component at the fibre-matrix interface at the moment of the debonding onset near the crack tip. It is said to have the following advantages as an interfacial parameter and eventual failure criterion: (a) it corresponds to the actual mechanism of crack initiation in the fibre pull-out test; (b) the σ_{ult} value is directly proportional to the work of adhesion, W_a, between the fibre and the matrix surfaces [21].

The fact that the parameters discussed above can be obtained from either single fibre pull-out test (SFPT) or microbond test (MBT) makes these two methods stand out for the inspection of interfacial bond quality. In both tests, a fibre is partially embedded in a matrix block. While the matrix is constrained, the fibre is loaded under tension. The external force applied to the fibre is recorded as a function of fibre end displacement during the debonding and subsequent pull-out process. In most cases the resin droplet in MBT is much smaller than the matrix block in SFPT. The essential difference between these two tests, thus, lies in their specimen scale and geometry, or in other words, the fibre volume fraction and boundary conditions. In a typical load-displacement curve for SFPT and MBT, the force increases linearly with the fibre end displacement until it reaches the maximum, F_{max}, at which the fibre-matrix interface completely debonds and a sudden drop in the recorded load is normally expected to appear. The fibre is then starting to be pulled out of the matrix

and the interfacial friction force, F_{fr}, recorded in the following stage reflects the interfacial friction strength (IFFS), $\tau_{fr,}$ between the fibre and the matrix due to compressive radial residual stress, $\sigma_{rad.}$ For SFPT, the force will decrease with the reduction in the fibre embedded length, which, on the contrary, remains constant in MBT before the free fibre end enters the matrix block. Depending on the interfacial failure mechanisms (i.e. catastrophic or non-catastrophic interfacial failure at debonding), debonding initiation can occur before F_{max} is reached. This has been both experimentally observed and theoretically predicted [22-25]. A typical force-displacement curve for non-catastrophic interfacial failure can consist of three parts corresponding to the three stages of the test [11]. The fibre-matrix interface remains intact before the applied force reaches initial debonding force, F_d and this part of the curve is nearly linear for a fibre-matrix system whose components considered to be linearly elastic. Once the external load reaches F_d, debonding at the point with the maximum shear stress occurs and interfacial crack propagation is initiated. The applied force continues increasing with the crack length due to the frictional load in the debonded regions being incorporated into the adhesional load from the intact part of the interface. After F_{max} is reached the crack propagation becomes unstable and the whole embedded length fully debonds and the measured force drops from F_{max} to F_{fr}. It has been demonstrated that the value for F_d can be obtained from either direct observation of debonding initiation or the load-displacement curve if the testing system is adequately stiff and the free fibre length, L_{fr} is short [26].

The SFPT and MBT have been extensively studied since they were developed several decades ago [27-30]. The SFPT is more widely used for fibre reinforced thermoplastic composites [17, 31-38] due to its limitations associated with the scale

of the specimen. There exists a maximum embedded length of fibre, L_{max}, which is inversely related to the fibre-matrix adhesion. L_{max} is usually short, which causes experimental difficulties and large data scatter especially for composite systems with strong interface bonding and small fibre diameters. Moreover, an elevated meniscus, which forms around the fibre during sample preparation, causes large stress concentrations and makes the test results often inaccurate. With much in common, the MBT is often seen as a variant of the SFPT. In this test, a small amount of resin is deposited onto the single fibre to form a concentric microdroplet in the shape of an ellipsoid. The stress concentration at the fibre entry can be reduced to a certain extent due to the presence of the smooth curvature at the boundary between the fibre and the microdroplet. This leads to the reduction of the large variation in the experimental data. The MBT is a versatile tool for the mechanical characterisation of the interface in various fibre composites [39-45]. Nevertheless, this technique also suffer limitations related to the nature of the specimen and loading condition as found in experiments [46-48], finite element method [49], and photoelastic analyses [10]. The stress state in the droplet varies significantly with the location and loading modes. In addition, the small size of microdroplet makes the in-situ observation of the failure process rather difficult. Moreover, the meniscus formed around the fibre in MBT specimen can result in inaccuracy in the measurement of the embedded fibre length, which will have a more significant influence on calculated bond strength values than in the SFPT. In the case of thermosetting microdroplets, mechanical properties may also vary with sample size partly because of the variations of concentration of the curing agent [50]. The problems that both tests have to face include the need for a special jig/fixture to fabricate and hold the matrix [40, 51] and

small fibre volume fractions where any effects of interactions between neighbouring fibres cannot be taken into account. In addition, the lack of standardisation makes it difficult to compare the results from the same composite system measured by the same or different tests due to the large scatter in the results [52]. In spite of all these disadvantages, the measured bond strength values appeared to be reasonably sensitive to sample preparation conditions and various fibre surface treatments. Moreover, the IFSS value obtained by these tests for a given system is consistent with the mechanical properties of macrocomposites. A strong correlation has also been found between the IFSS and such thermodynamic parameters as surface free energy or specific enthalpy of adsorption. Therefore, it seems to be possible to obtain useful information about fibre-matrix adhesion from these micromechanical experiments. In the following content, SFPT and MBT will not be distinguished and together referred to be as fibre pull-out test unless otherwise stated.

3.1.3 Theoretical analysis of interfacial failure in fibre pull-out test

In general the fibre-matrix interfacial failure consists of two distinct processes: interfacial debonding and frictional pull-out. Theoretical analysis of interfacial failure has gained significant attention especially for the fibre pull-out test. The theoretical models of interfacial debonding in fibre pull-out test can be classified into three categories: the shear stress controlled approach, energy controlled approach, and the normal stress controlled approach. In the shear strength criterion, when the interfacial shear stress reaches the interfacial shear strength (IFSS), τ_{ult}, debonding occurs. In the fracture mechanics approach, propagation of a debonded crack requires the potential energy release rate of the composite constituents to reach a critical value,

the interface fracture toughness, G_{ic}. Both τ_{ult} and G_{ic} are assumed to be material constants in these two debonding criteria and they are the characteristic interface properties to be determined in experiments. Investigations carried out for several fibre-matrix systems have demonstrated that the stress based and energy based criteria (τ_{ult} and G_{ic}) are not contradictory [53, 54]. More recently, another stress based criterion, adhesional strength, σ_{ult}, has been proposed to more correctly characterise the interfacial bond strength [19-21]. This criterion in cylindrical geometry assumes that an interfacial crack is initiated when the radial stress reaches its critical value, σ_{ult}, which is directly related to the practical adhesion of the system.

3.1.3.1. Shear stress controlled approach (τ_{ult})

Theoretical analyses of interfacial debonding in the fibre pull-out test were initially modelled by Kelly et al for ductile matrices assuming a uniform interfacial shear stress at the fibre-matrix interface [55]. This is based on the matrix yielding over the entire embedded fibre length as a predominant failure mechanism at the interface region. This gives rise to a linear relationship between the fibre debonding stress, σ_d and τ_{ult} through a simple force balance

$$\tau_{ult} = \tau_{app} = \frac{F_{\max}}{A_e} = \frac{D_f \sigma_d}{4L_e} \qquad (3.4)$$

This is thought to be true only in the case of a highly ductile matrix, which allows an extensive rearrangement of the stresses as a consequence of the plastic yielding of the matrix [45, 56]. However, both experimental and theoretical studies have shown that when the fibre embedded length remains small, a linear trend of debonding force

with respect to fibre embedded length can still be noticeable for the composites based on brittle matrices such as epoxy [18, 28, 39, 40, 42]. Nevertheless, it was also found that the interface between glass fibres and a very ductile low density polyethylene could fail in a brittle fashion [17]. Despite the debates on whether $\tau_{ult} = \tau_{app}$, it is generally acceptable to calculate τ_{app} as the first approximation to $\tau_{ult.}$ Furthermore, τ_{app} usually suffices to qualitatively evaluate the bond strength and to estimate the effects of matrix and/or fibre surface modification on the bond strength.

Numerous studies have revealed that in most composites materials, the distribution of interfacial shear stress is not uniform upon interfacial debonding and $\tau_{ult} > \tau_{app}$. The possible reasons for this are summarised below:

(a) In an elastic fibre-matrix system, the value of the interfacial shear stress decrease along the embedded length and its maximum is reached at the point of fibre entry into the matrix.

(b) Thermal shear stress caused by the mismatch of coefficient of thermal expansion between the fibre and the matrix symmetrically varies along the embedded length and will be superposed upon the mechanical-induced interfacial shear stress.

(c) The coexistence of bonded and debonded regions along the interface during the fibre pull-out test.

(d) The functional dependence of the external stress for interfacial debonding is non-linear due to the effect of the Poisson contraction of the fibre, which is subjected to uniaxial tension.

Greszczuk considered the case of an elastic matrix and modified Cox shear-lag model [57] to fit into the fibre pull-out loading geometry, assuming that the tensile stress in the matrix is negligible relative to the fibre while the shear stress in the fibre is small compared to the matrix. He showed that the shear stress distribution was no longer uniform for an elastic composite system and depends on the properties of the elastic matrix. Lawrence and Laws further modified Greszczuk's model by taking into account the effect of frictional resistance of fibre pull-out in the debonded region [24, 58] and identified that the maximum shear stress for complete debonding is dependent on the embedded length and the ratio of the IFSS to IFFS. Takaku et al further considered Poisson contraction of the fibre when subjected to tension and demonstrated its effects on debonding and pull-out stresses [59]. Gray gave a comprehensive review of these theories and concluded that the mixture of adhesive debonding and friction resistance that occurs in a pull-out test specimen depends on the fibre embedded length [60]. Moreover, a so-called 'two-way' debonding model where interfacial shear stress concentration occurs both at the loaded and embedded ends of the fibre, was also developed, suggesting the possibility of debonding propagation from both ends in the context of a shear strength criterion [61, 62]. Despite the difference among the theoretical models above, they all commonly suggest that local IFSS, τ_{ult}, is reached at the fibre entry into matrix in the fibre pull-out test. In practice, τ_{ult} values can be obtained from either graphic methods [42, 51] or analytical methods [13, 20].

3.1.3.2 Energy controlled approach (G_{ic})

The energy-controlled approach is based on the fracture mechanics. In the early work, Outwater and Murphy derived the solution for the constant fibre debonding stress by equating the rate of strain energy released from the fibre for complete debonding of embedded length, L_e, to the incremental interfacial fracture energy, which is the product of interface fracture toughness, G_{ic}, and cylindrical debonded area, $\pi D_f L_e$ [63]. Having reviewed some previous theoretical models, Stang and Shah derived a debonding criterion based on a compliance analysis and applied the analysis to the classical pull-out test to determine the specific work of interfacial cracking, which was then used to predict the uniaxial tensile strength of the composites [64]. Wells and Beaumont considered the effect of the Poisson contraction of the fibre and non-linear friction in the debonded region and derived models for predicting the debonded length and the probability distribution of pull-out lengths of both individual fibres and bundles [65]. Piggott used shear-lag methods to evaluate the stresses and strain energy in pull-out specimens and accounted for the increase in debonded length with the energy changes resulting from the fibre axial tension and matrix shear, assuming that the shear stresses in the fibre and the tensile stresses in the matrix make negligible contributions to the total strain energy. [18]. Gao et al. also presented a relationship between the debonding and post-debonding frictional pull-out stresses versus embedded fibre length [66] and the model has been demonstrated to be able to determine the inherent interfacial properties [67]. A comprehensive theory, which also includes friction and thermal residual stresses, has been developed by Nairn et al [68-70]. They expressed the energy release rate, G, as a function of crack length, with a number of factors including embedded length,

external force, temperature difference between the test temperature and the stress free temperature, interfacial friction and specimen geometry.

3.1.3.3 Normal stress controlled approach (σ_{ult})

Several authors have demonstrated that crack initiation in the fibre pull-out test occurs in normal tension (Mode I) [71]. The variational mechanics analysis carried out by Scheer and Nairn showed that the shear stress is zero at the point where the fibre enters the matrix, and the radial tensile stress is at its maximum instead [69]. Analytical expressions derived by them allow for calculating all stresses in a fibre pull-out specimen including the radial normal stress at the interface. This offers a possibility of identifying the value of this radial normal stress at the moment of crack initiation at the point where debonding starts with σ_{ult}. Based on this method, attempts have been made to correlate the "practical" adhesion, σ_{ult}, with the independently measured "fundamental" adhesion W_a, for several fibre-matrix systems [20].

3.2 Experimental

3.2.1 Material

In order to minimise complexity of the interface, the choice of the materials was limited to uncoated glass fibre and homopolymer polypropylene. The fibres were boron free uncoated E-glass fibres (Ave. diameter = 17.5µm) from Owens Corning-Vetrotex in combination with commercial isotactic homopolymer polypropylene

SABIC®PP 531P (PP0.3), 576P (PP19), and 579S (PP47) with melt flow index = 0.3, 19, and 47 g/10 min at 230°C and 2.16 kg respectively

3.2.2 Design and manufacture of the microvise

In this project a microvise for constraining the matrix block in fibre pull-out test was designed and manufactured in the light of the work done by Craven et al [40]. The technical drawings for individual parts can be found in Appendix (B). The disassembled and assembled microvise models are illustrated in Figure 3.1.

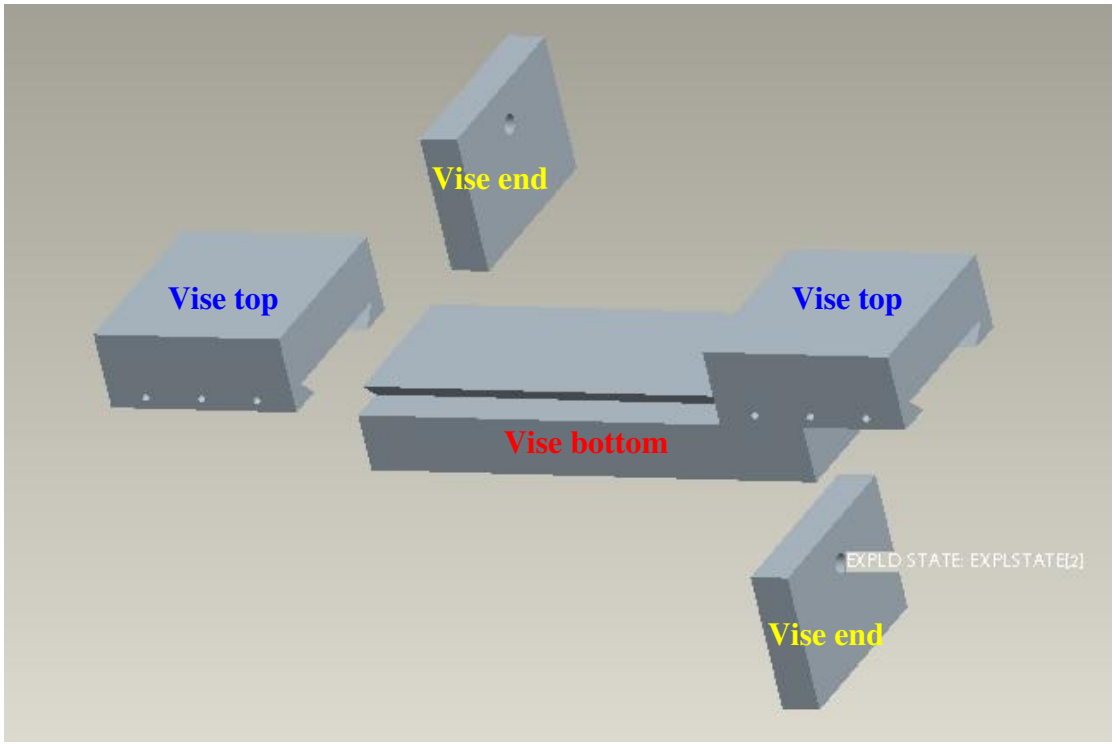

(a)

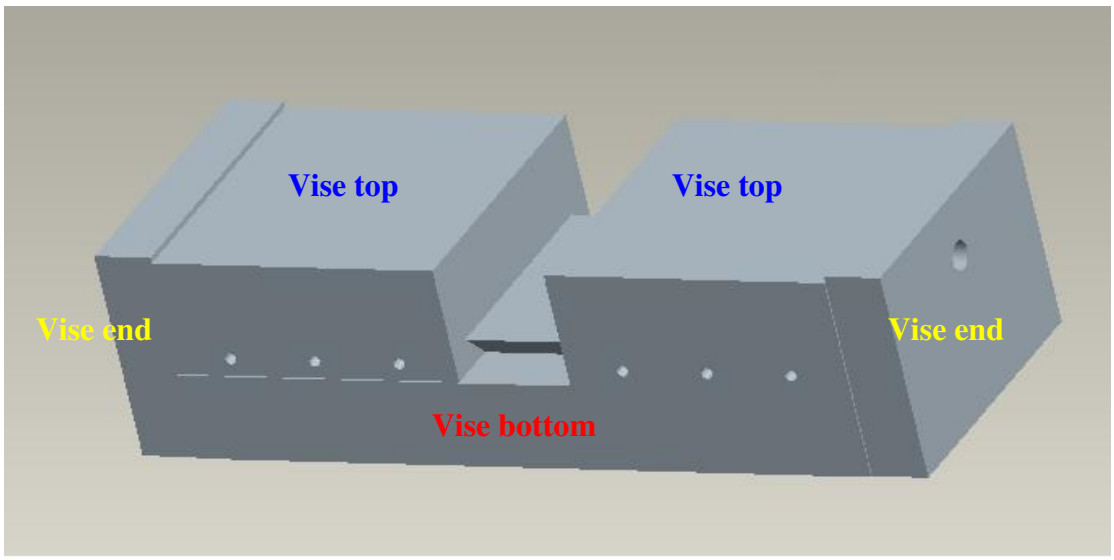

(b)

Fig. 3.1 Microvise model (a) dissembled and (b) assembled

The microvise consists of a vise bottom, two vise tops and two vise ends. The vise tops can be assembled on to the vise bottom through a "dove-tail" joint and connected to the vise ends through a pair of springs at each end. More details can be seen in Figure 3.2.

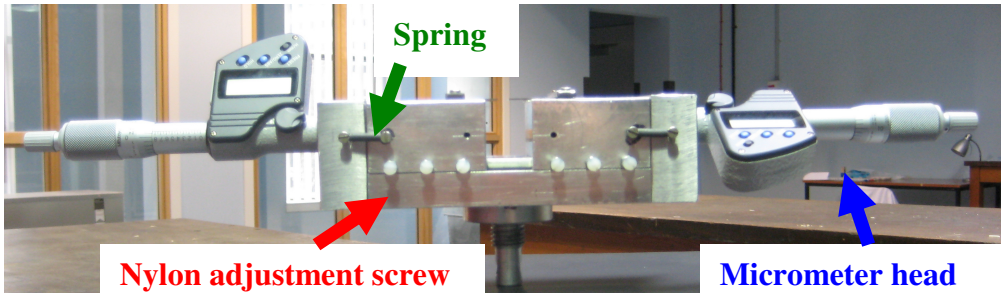

(a)

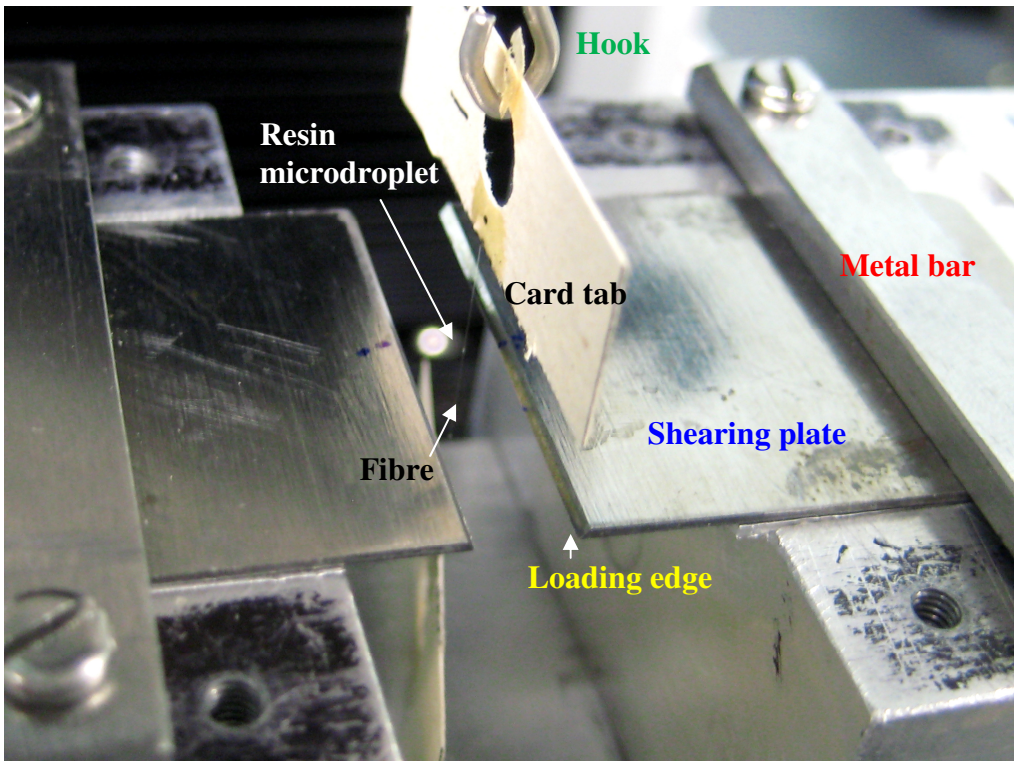

(b)

Fig. 3.2 Photos of self-manufactured (a) microvise and (b) shearing plates

The forth movement (i.e. towards the middle of the micovise) of the vise tops is controlled by a pair of micrometer heads. The back movement (i.e. towards the corresponding vise ends) of the vise tops is achieved by the spring pulling. The resolution of the micrometer heads position is 1μm, which would mainly decide how precisely the movement will be controlled if the resistance to it is insignificant. Nylon adjustment screws can be used to remove any twist in the vise. In order to shear the matrix block off the fibre, a pair of shearing plates were manufactured and installed on the vise tops. Shearing plates play a critical role in the fibre pull-out test because they are responsible for directly applying the load to the matrix and this load will be transferred to the fibre through the fibre-matrix interface. Various shearing plates can be found in the literature and they are schematically illustrated in Figure 3.3 [28, 40, 42, 72].

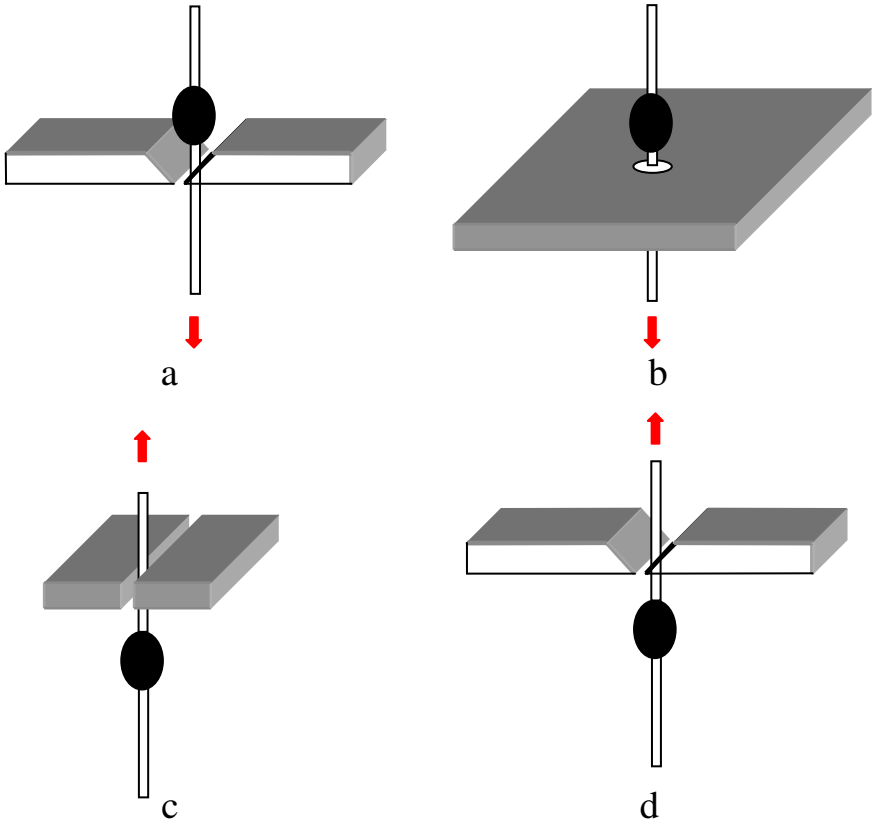

Fig. 3.3 Schematic presentation of common shearing plates

The shearing plates that offer a slope as the contact surface with the microdroplet (see Figure 3.3a) are likely to exert radial compressive stress component at the interface. This can complicate the stress state at the interface and give inaccurate measurements of IFSS. Although such radial compressive stress may also be caused by the flat contact surface due to the curved shape of the resin droplet [46], it could be avoided or at least significantly reduced when the shear plates are brought together to make contact with the fibre. A circular shearing plate was shown to give an axisymmetric geometry, load and stress distribution (see Figure 3.3b) [72]. However, it usually requires highly precise machining such as laser drilling to

produce a very small hole, which could also bring extra difficulties in mounting the specimens into the experiment jig. Moreover, it is almost impossible to maintain a zero gap between the fibre and the edges of the hole since diameter can vary considerably from one fibre to another. The shearing plates that offer a flat contact surface were the early configuration [29] and compared with the droplet-droplet shearing arrangement as shown in Figure 3.4.

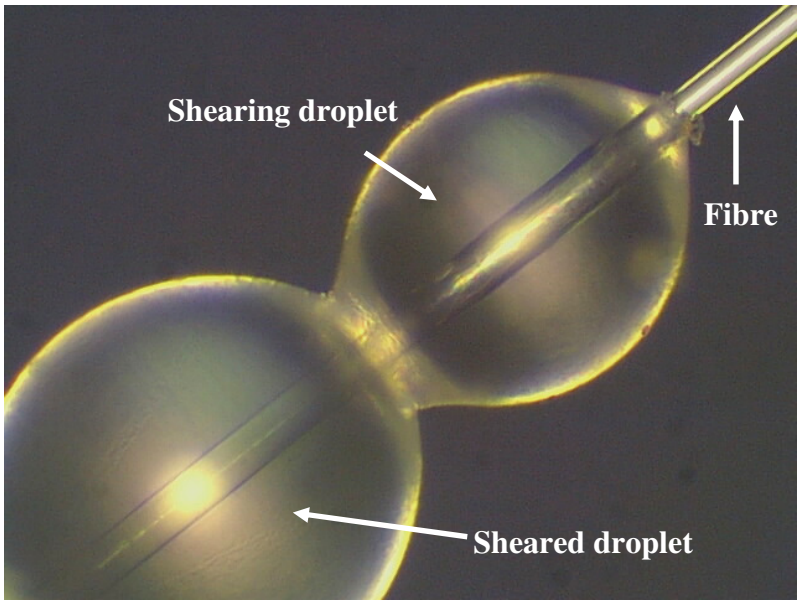

Fig. 3.4 Droplet-droplet shear arrangement

It showed there was no significant difference in measured IFSS for the same fibre-polymer system [29]. Shearing plates shown in Figure 3.3c were initially chosen in this work. A number of modifications to the shearing plates were carried out and described below in the sequence of the occurrence.

(1) The surface area facing the fibre was reduced to leave a very thin edge by polishing as shown in Figure 3.3d. This could minimise the probability for the shearing plates to collide when they were brought extremely close to each other in the case of zero gap between the fibre and the plates.

(2) Instead of aluminium or low carbon steel, high carbon content stainless steel was used to manufacture the shearing plates because this could ensure that after the polishing, there was a perfect finish along the loading edges, which did not have sharp rims and damages as found in the plates made of the aluminium and low carbon steel.

(3) Instead of having the plates screwed to the vise tops, the plates were pressed down on the vise tops by four metal bars. This allows shearing plates to be easily adjusted in order to produce the parallel loading edges with the same height as shown in Figure 3.3d.

3.2.3 Sample preparation

There seems to be no accepted standard way of using thermoplastic polymers to make samples for either the single fibre pull-out (SFPT) or the microbond test (MBT). Every laboratory, thus, has developed their own methods with essentially the same idea and different procedures. The method developed in this work is presented as follows.

For the MBT, a slightly different method from the one that has been adopted in other works to form droplets on a single fibre [73] is illustrated in Figure 3.5.

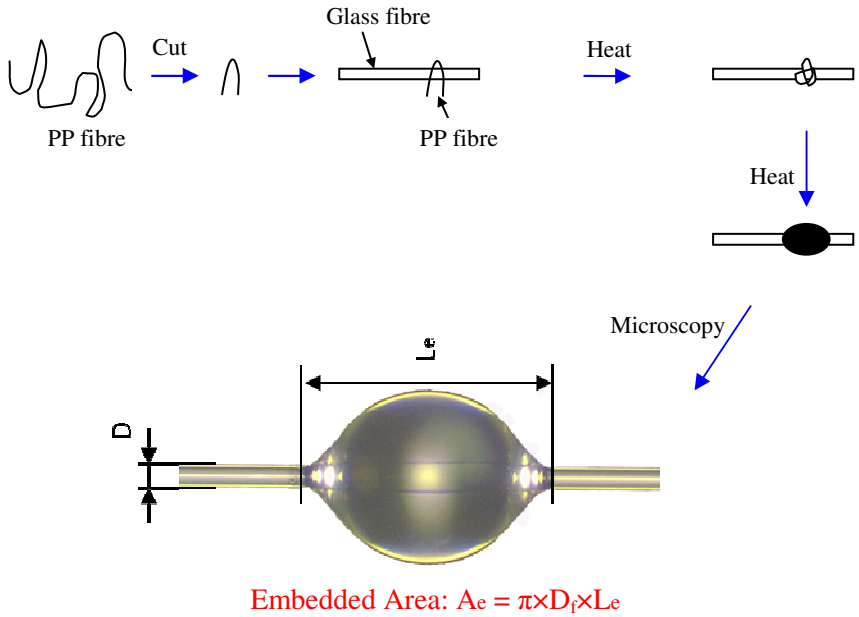

Fig. 3.5 Schematic illustration of sample preparation for the MBT

A single glass fibre (GF) was carefully extracted from a bundle without touching the fibre surface. The fibre was suspended horizontally. Then a small piece of polypropylene (PP) fibre was transferred on the surface of the GF. The PP fibre hung loosely on the GF fibre and could shake off easily. Thus a soldering iron was used to slightly heat the PP fibre so that it could firmly coil itself around the GF. Finally a number of these samples were transferred together into an oven at a temperature of 220ºC, which is well above the melting temperature of this PP (T_{pm}=158°C from DSC in chapter 2) to ensure complete melting and a reasonably low viscosity of the PP melt. The samples were heated either in air or under nitrogen (more about heating under nitrogen can be found in chapter 4). The time for specimens being retained in the oven was set to at least 4 min because 2 and 3 min proved too short a time to form enough testable droplets. The samples eventually cooled down to ambient

temperature and were then screened using a Nikon Epiphot Inverted optical microscope before testing. Only well-shaped, symmetrical droplets were selected for the experiments. The droplet size including droplet length (i.e. fibre embedded length, L_e) and droplet diameter, D_m, and fibre diameter, D_f, were measured to determine the embedded area of the fibre, A_e as shown in Figure 3.5. PP47 was used to prepare the samples for the MBT.

For the SFPT, the method employed by Thomason and Schoolenberg was adopted to make samples [31]. In order to obtain consistent and repeatable results from the fibre pull-out test it was imperative that the techniques used to create and prepare samples for testing were consistent and identical for all samples created. The first step in making the sample was to melt two small pellets of the required PP grade on a glass slide using a hot plate heated to around 230˚C (Figure 3.6a).

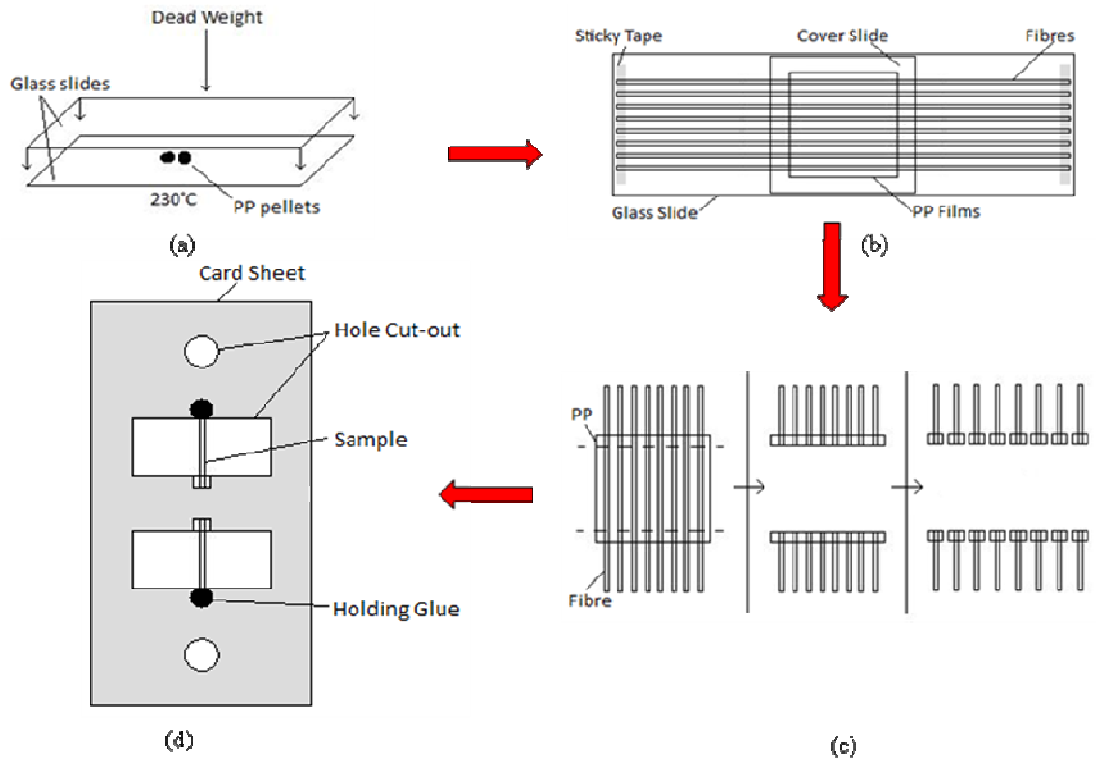

Fig. 3.6 Schematic illustration of sample preparation for the SFPT

Upon melting of the pellets, a further glass slide was positioned on top to create a sandwich configuration; thus creating a thin PP film between the slides. A 1 kg weight (also preheated to 230˚C) was then placed on top of the assembly to apply a holding pressure. This was then left on for 30 seconds, after which the slides and PP film were removed from the hot plate and placed on a glass block to cool down to room temperature. Upon cooling, the PP film was removed from the slide and the thickness of the film measured. The desired thickness of the film was in the range 0.1-0.12mm. The film was then cut with the use of razor blades into a square (13x13mm), ready for the next stage of the preparation. The next stage of the process was to sandwich the glass fibres between a set of the square PP films. This was achieved by laying down one of the films onto a glass slide; the glass fibres were then positioned across the film and secured at either end of the glass slide by sticky tape (Figure 3.6b). Another PP film was then positioned on top of the fibres, square to the film below, thus creating a PP film and glass fibre sandwich assembly. A small glass cover slide was then positioned over the PP films in order to reduce oxidisation during the next heating stage. The next process was to heat the assembly in order to melt the PP films and thus embed the fibres. This was achieved through placing the assembly into a Mettler FP82 hot stage at 220˚C for 2-6 minutes, after which the sample was removed and cooled at ambient room temperature. The PP film (and embedded fibres) was then removed from the glass slide and dissected into individual samples as shown in Figure 3.6c. Care had to be taken when cutting up the samples to ensure that the length of embedded fibre left after cutting was not too long, as the embedded length L_e is limited by the strength and diameter of the fibre, σ_{fu} and $D_{f,}$ respectively and the IFSS, τ_{ult}; according Equation (3.5).

$$L_e < \frac{\sigma_{fu} D_f}{4\tau_{ult}} \qquad (3.5)$$

Given that with a gauge length of 5 mm and diameters in the range 15-21 μm, the average tensile strength of uncoated glass fibre is approximately 1.5 GPa and the average IFSS for neat GF-PP is usually found to be in the range of 3-8 MPa, a maximum testing embedded length of 1.9 mm is possible (most samples tested in this study were actually far shorter than this value due to extra handling weakening GF). It was also important to vary the embedded length to obtain a wide range of embedded areas to test. With the samples mounted on the card as shown in Figure 3.6d, it was then possible to measure the fibre diameter of each sample using the microscope. Three different grades (i.e. PP0.3, PP19, and PP47) were used to prepare the samples for the SFPT.

3.2.4 Fibre pull-out test

Both the SFPT and the MBT were carried out in the same experimental jig as shown in Figure 3.7.

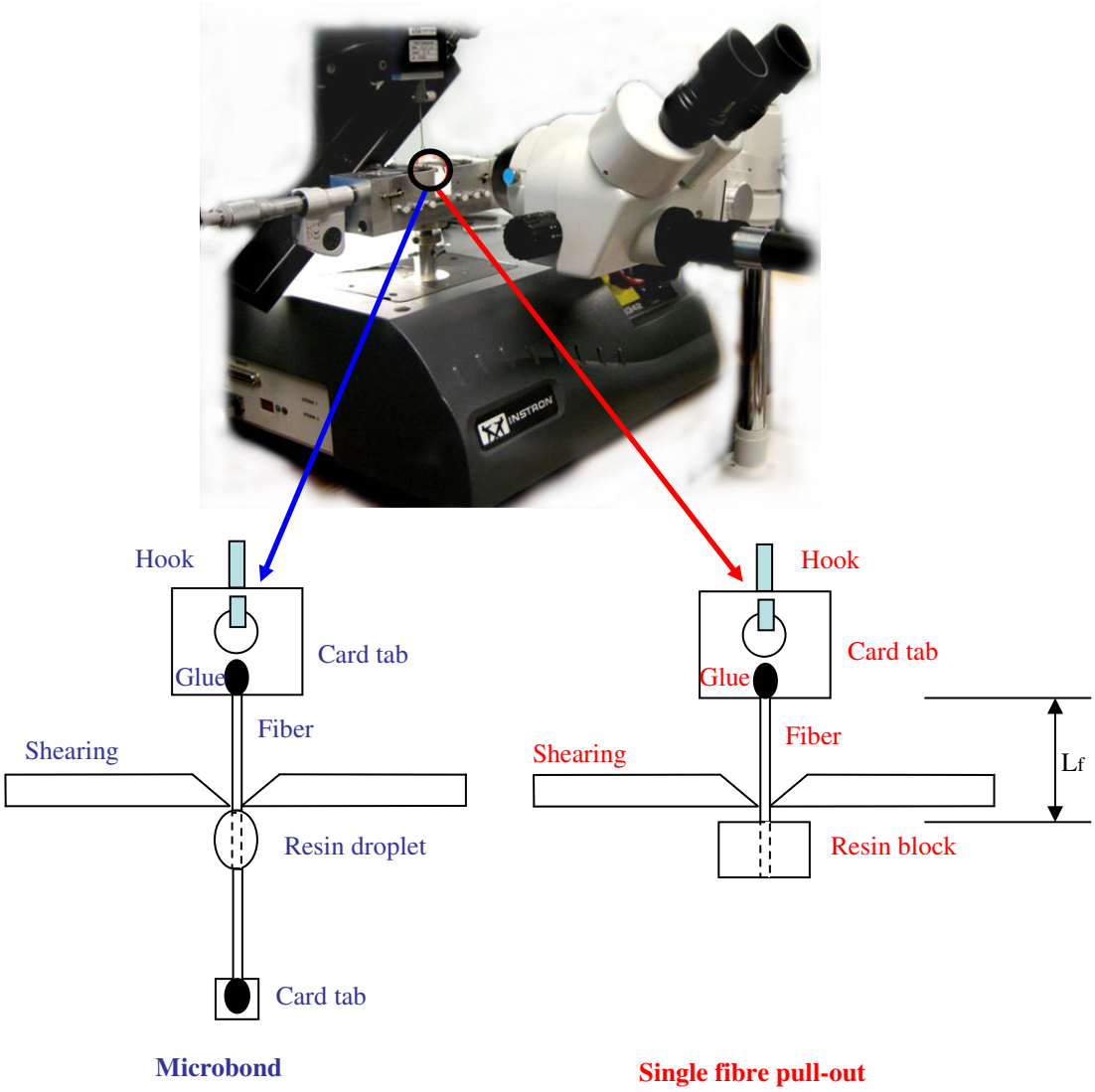

Fig. 3.7 Experimental setup for the fibre pull-out test

To perform the fibre pull-out test the sheets of card were cut to create a tab with the sample hanging off. A hook attached to a 10N load cell on an Instron Model 3342 tensile testing machine was positioned through the circular cut-out section to act as the loading point. In order to aid the setting up of testing and then to be able to observe the debonding and pull-out process, a stereo microscope (45x magnification) with a digital camera attached – feeding real time video to a computer screen – was placed in front of the testing area. The microscope made it possible to accurately position the sample into place and then observe the fibre pull-out occurring during

testing. Due to the small size of resin microdroplets in MBT, some card frame was left taped to the bottom of the fibre to keep it under tension ($\sim$0.5 mN) so that the sample can be perfectly aligned with the loading direction prior to testing. This is apparently not a problem for the specimens in SFPT. The free loaded fibre length, L_{fr}, was kept constant at 5 mm throughout all the tests. The loading edges of the shearing plates were brought to make contact with the fibre. With the sample in place the test could then start and the load cell extended the fibre end at a constant rate of 0.1mm/min. During a period of the test a load vs. displacement plot was produced in real time. These plots helped to identify when debonding had occurred and also when the fibre was complete pulled out. Figure 3.8 represents a typical fibre pull out test plot (although they can vary in shape significantly in some cases) with an initial ramp representing the sample being loaded as the load cell increases the extension, followed by a peak load, F_{max}, where it is thought that the debonding between the fibre and the matrix occurs.

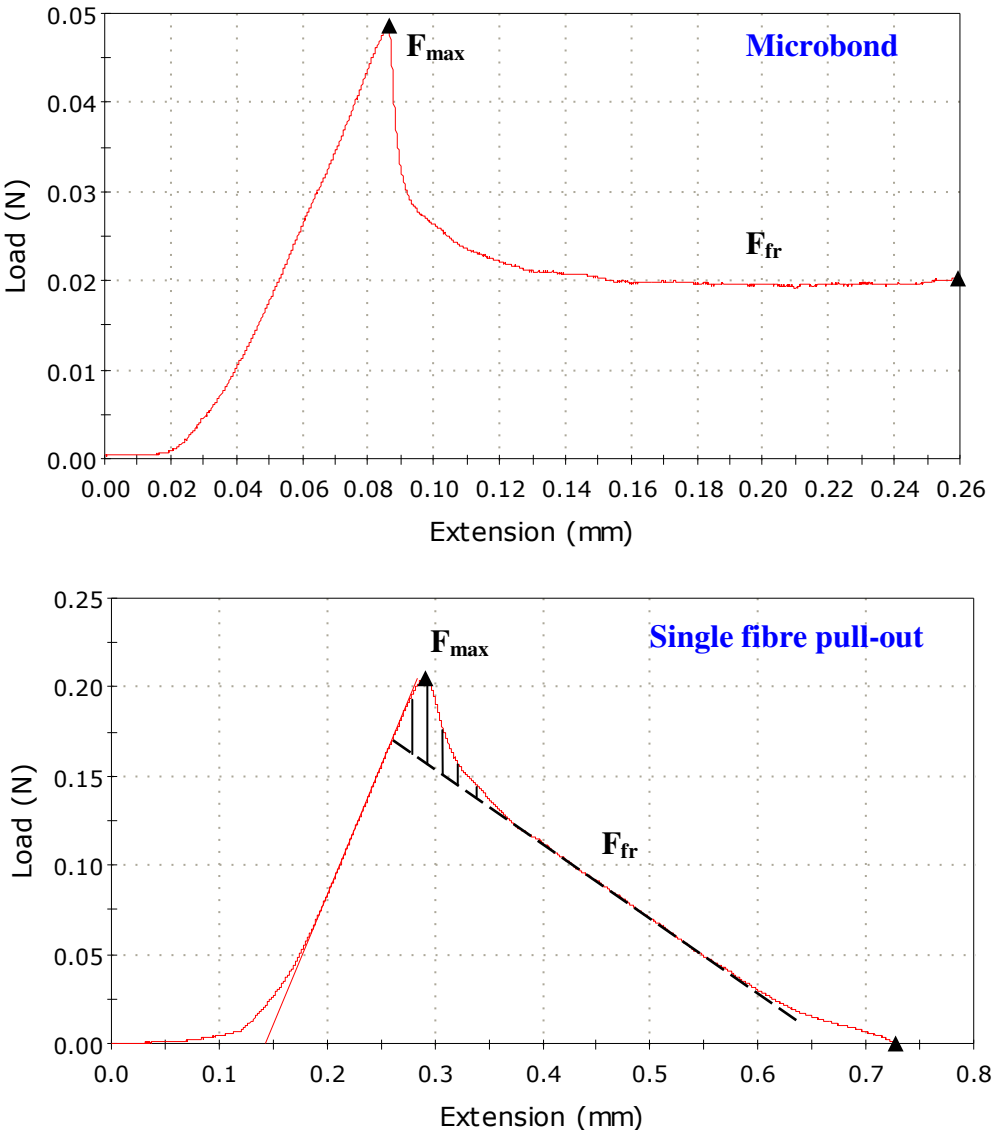

Fig. 3.8 Typical load-extension curves for the fibre pull-out test

In MBT, the load was then found to abruptly drop and gradually proceed into a constant level, which was usually about 50% of F_{max}. In SFPT, it was less likely to observe the sudden load drop, which was found to be about 20% of F_{max} for a number of specimens. The linear downward slope after the peak load indicates the fibre being pulled out of the matrix and overcoming the frictional forces until complete pull-out. In addition, the work energy of the interface can be shown by the area between the experimental curve and extrapolation line of the linear slope as

shown in Figure 3.8. This analysis should be carried out in the future work. There were some difficulties in confidently identifying the actual point of pull out as it was not always completely clear purely through observation. However, using the point of zero load to determine the fibre embedded length may cause larger error because the load could simply not return back to zero when the fibre had been completely pulled out. Alternatively, the embedded length may be determined using the intercept of linear fitting line in pull-out process with the extension axis. The drawback of this method may come from the Poisson effect. After testing, the pulled out fibres were examined under the microscope to confirm the interfacial failure.

Large scatter in the micromechanical results seems to be a common issue and tends to inhibit the development of effective data reduction. Owing to the lack of standardisation, the scatter arises not only from the inherent characteristics of small scale testing but also from the sample preparation and testing procedures. A number of factors that could bring about the scatter in the results from the MBT are listed below (some of them also apply to the SFPT):

a) Inherent heterogeneity of fibre surface

b) Fibre surface contamination

c) The different thermal history in the specimens

d) The measurements of the fibre diameter

e) The size of the droplet (due to the loading edges can never as absolutely high as each other, smaller droplets will be more misaligned with loading direction

than bigger ones during testing).

f) The positioning of the droplet in the shearing microvise

g) The conditions of loading edges including parallelism, vertical interval and contact surface with the matrix

h) The environment (e.g. temperature, humidity, aging) prior to/during the test (see chapter 4 and 5)

Finally, a few basic points are given to help achieve a sound micromechanical test

a) Make a detailed record for the experiment including the dates of sample preparation, measurements and testing, pictures of samples before and after testing, fibre diameter, droplet dimensions, and notes of testing process (e.g. level of misalignment).

b) Keep the tested samples safe and clean so that no artefacts (e.g. damage, scratches or dust) would affect the post-microscopy measurements.

c) Ensure that the numerical label for sample number, test number and the microphotograph is matching, otherwise a lot of confusion in the later analysis of the results could arise.

3.3 Results and discussion

3.3.1 Microbond test (MBT)

When polypropylene (PP) melt is exposed to an oxidative atmosphere, it is subjected to thermo-oxidative degradation as will be discussed in details in chapter 4. It is therefore necessary to avoid such complication by either forming the resin droplet under inert gas such as nitrogen or minimising the exposed sample surface as in making single fibre pull-out specimens. Furthermore, PP may also undergo thermal degradation if the processing temperature is too high. Figure 3.9 shows the results for weight loss of PP melt at 220°C and 250°C under nitrogen by Thermogravimetric analysis (TGA).

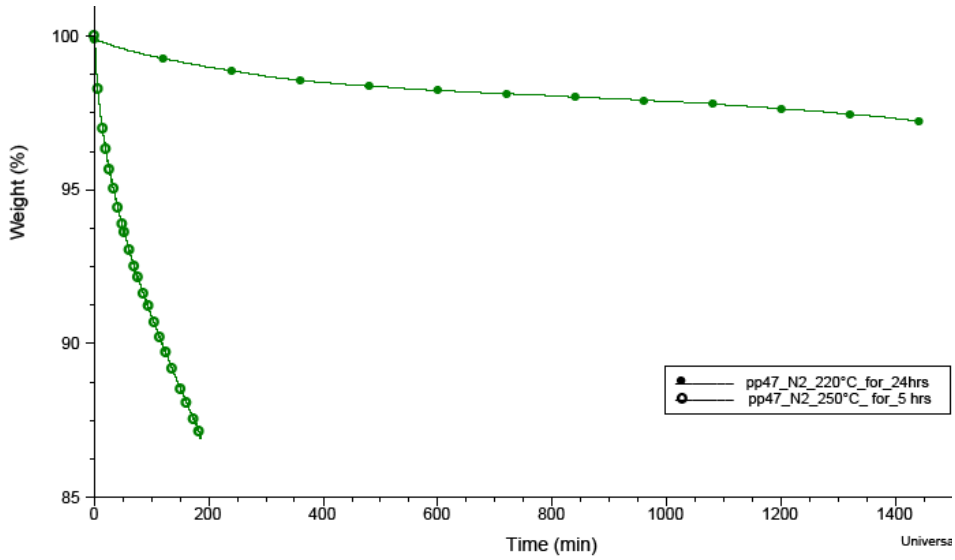

Fig. 3.9 Weight loss of PP47 at 220°C by Thermogravimetric analysis

It clearly shows that under nitrogen thermal degradation of PP can occur at 250°C while it does not appear to be the case at 220°C even after a prolonged period of time. The processing temperature, T_p, for PP composites normally ranges from 200°C to 240°. Thus, 220°C was chosen as T_p to fabricate all the specimens for micromechanical tests in this project. In addition, 4 minutes was chosen as the processing time, t_p, for MBT samples because shorter time proved insufficient to form the axisymmetric PP microdroplets as shown in Figure 3.10.

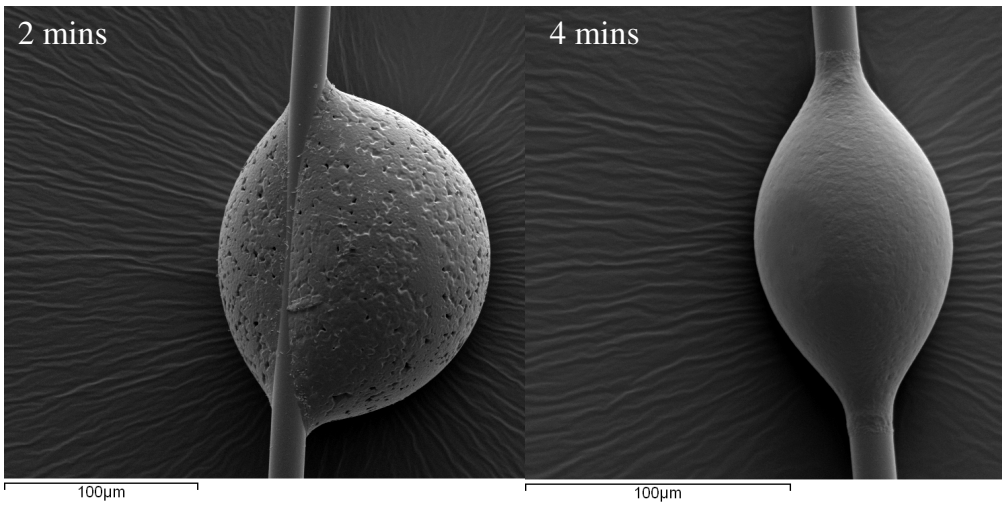

Fig. 3.10 SEM photos of nonaxisymmetrical and axisymmetrical PP microdroplets

Due to the high viscosity of the PP melt, good wetting of glass fibres by the PP melt might require more time than 4 minutes. The effect of t_p on measure IFSS will be discussion in next section.

In practice, the relationship between embedded fibre length, L_e, and droplet maximum diameter, D_m, can be used to inspect the results for droplet dimension measurements [45] and determine the droplet profile [74]. Figure 3.11 shows this relationship for the microdroplets formed in this work.

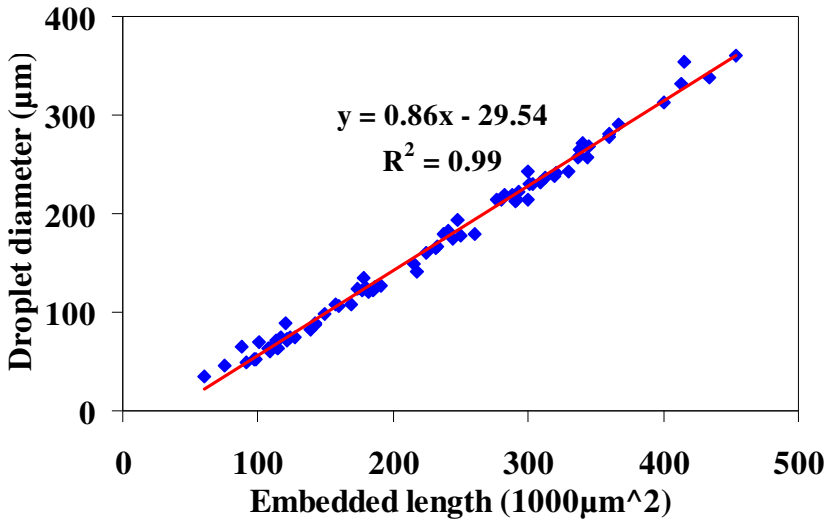

Fig. 3.11 Plot of maximum PP droplet diameter and fibre embedded length

An excellent linear fit can be obtained with R^2 close to 1, yielding $D_m = 0.86L_e - 29.54$ for the relation between fibre embedded length and droplet diameter. It is also noticed that there is an indication of D_m levelling off at the lowest L_e values in Figure 3.11. In fact such behaviour is expected because D_m will not continue to follow the line as L_e decreases, but instead must level off at $D_m \approx D_f$, which is the fibre diameter. This linear relation, therefore, is only valid when $D_m >> D_f$.

The microscopy observation of debonded area (see Figure 3.12) shows a clean surface, indicating an interfacial failure.

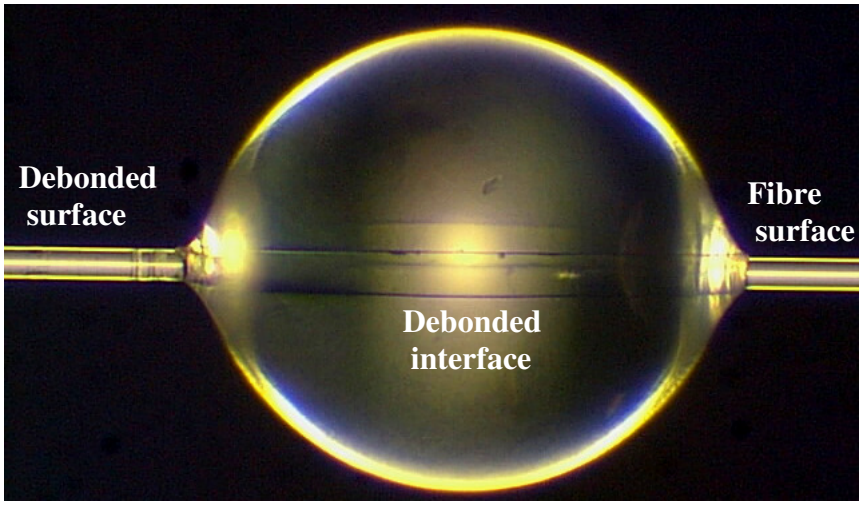

Fig. 3.12 Photo of the MBT sample after fibre pull-out test

The droplets were found too small to visually observe the interfacial debonding as shown in Figure 3.13.

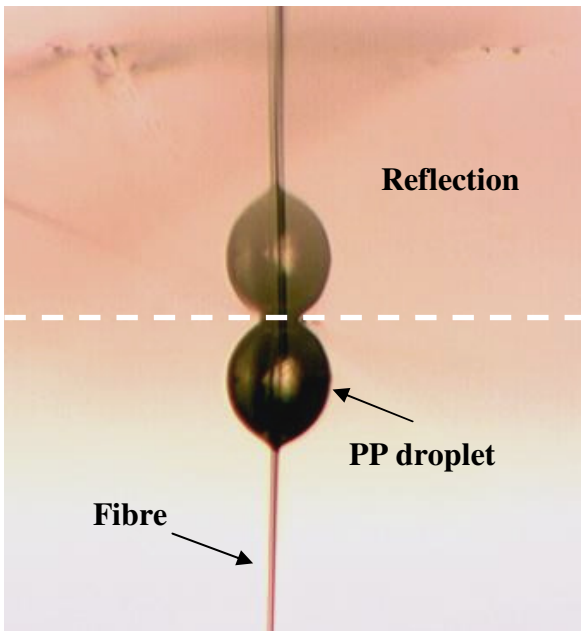

Fig. 3.13 Photo of MBT sample in testing

Results of maximum force, F_{max}, versus fibre embedded area, A_e, obtained for GF-PP47 samples, prepared under nitrogen and tested at room temperature are shown in Figure 3.14.

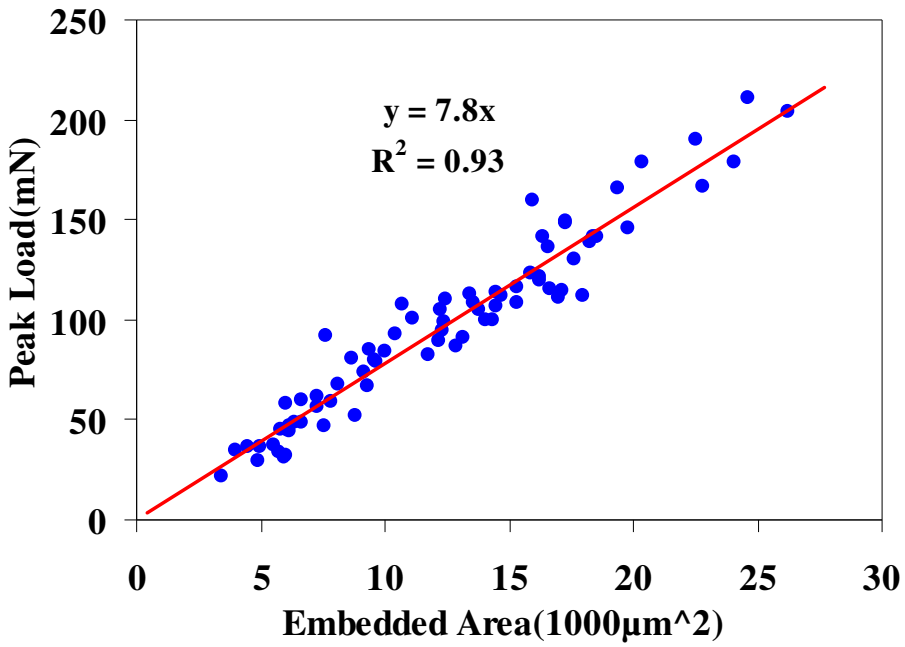

Fig. 3.14 Plot of peak force vs. embedded area measured for neat GF-PP47 using MBT

Almost half of the data points are actually from a different testing fixture (see chapter 5). It will be seen in chapter 5 that the two methods, which are essentially the MBT, yield identical results. It does not make any significant difference to the potential conclusions drawn from the results by pooling the two sets of data. The linear relation expressed by the Equation 3.4 is used to fit the data and it clearly shows from Figure 3.14 that there exhibits a significant linear relationship between F_{max} and A_e. The least-square fitted line gives a value for apparent IFSS, τ_{app} = 7.8 MPa (with a 95% confidence limit = 0.3 MPa) in this system. The exactly same value for τ_{app} is found in some other works with neat GF-PP system (i.e. bare GF and neat PP) [33, 35], although the processing conditions in that work were different and PP weight average molecular weight (M_w) used was M_w=314000 g/mol, which is higher than that of PP47 with estimated M_w=198918 g/mol according to [75]. The relatively low value for the GF-PP IFSS is normally attributed to the weak bonds, resulting from the nonpolar nature of PP homopolymer [31, 33]. Furthermore, the fact that the excellent fit to the data is achieved by Equation 3.4 may justify the validity of the underlying assumption that the interfacial shear stress is distributed uniformly along L_e at F_{max}. This situation is thought to occur if interfacial bonds yield, resulting in extensive redistribution of stresses at the interface. Some examples can be found in the literature [45, 55, 56]. Since a two dimensional interface is normally assumed for neat GF-PP system, the interfacial yielding may be attributed to the yielding of the matrix at the interface. Since the PP47 at the interface may exhibit ductile behaviour at debonding, its shear strength at yielding, τ_y, is estimated by Von Mises criterion (i.e. $\tau_y = \sigma_y / \sqrt{3}$) with tensile strength at yielding, σ_y, which is 35.3 MPa for PP47 according to the results presented in chapter 2. Thus, τ_y

=20.4 MPa is obtained for PP47. This value is significantly higher than measured IFSS. Nevertheless, the matrix is under compression during testing and the compressive yielding stress therefore may be more useful for estimation of τ_y. Figure 3.15 shows the dependence of τ_{app} on L_e for GF-PP47 measured by MBT.

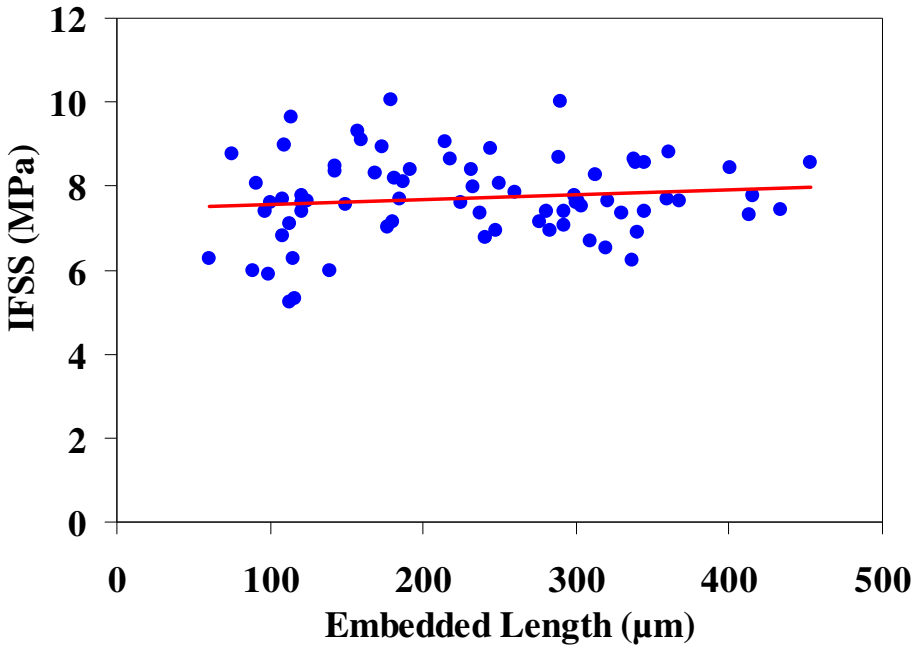

Fig. 3.15 Dependence of IFSS on embedded length for GF-PP47 measured by MBT

The straight line is inserted into the figure to indicate the principal trend of data points and does not represent any data fitting. Unlike the inverse dependence usually found in brittle interfacial failure, τ_{app} obviously does not show any significant correlation with L_e in the case of GF-PP47. In fact, the slightly positive slope of the data in Figure 3.15 can be observed. Similar observation was found in carbon fibre-poly(phenylene sulphide) composite, which was believed to give a ductile interfacial fracture in SFPT [56]. Without giving the references, it was mentioned that slightly positive slope of fitting line for τ_{app} versus L_e can be observed with other material

combinations such as glass fibre-polycarbonate and GF-PP systems [56]. It is therefore reasonable to conclude that for GF-PP47 system $\tau_{ult} = \tau_{app}$.

From the load-displacement curve for MBT in Figure 3.8, one can see that the frictional shear stress, τ_{fr}, may be calculated by

$$\tau_{fr} = \frac{F_{fr}}{\pi D_f L_e} \qquad (3.7)$$

Such stress arises from the compressive radial residual stress, σ_{rad}, by

$$\tau_{fr} = \mu_{dy} \cdot \sigma_{rad} \qquad (3.8)$$

where μ_{dy} is coefficient of dynamic friction. Combing these equations above, μ_{dy} can be evaluated if σ_{rad} is known. Nairn's model is employed in this work to calculate σ_{rad} (see chapter 5 for more details) [76]. The value of μ_{dy} is then estimated for each sample. The average value of τ_{fr} is 2.22 MPa with a 95% confidence limit=0.2 MPa and the average value of σ_{rad} at 20°C is 8.07 MPa with a 95% confidence limit=0.04 MPa. $\mu_{dy} = 0.27 \pm 0.03$ is obtained for neat GF-PP47 system at 20°C. μ_{dy} is likely to be underestimated to some extent since the Poisson effect in the transverse direction of both the fibre and the matrix is not taken into account. Fibre contraction in the lateral direction can occur since the fibre is still under tensile stress during post-debonding pull-out process. This contraction should reduce the σ_{rad} from the matrix. In contrast, the matrix is still under compressive stress in the MBT and Poisson expansion in the lateral direction is also expected. A number of authors have commented on the role of σ_{rad} contributing to the fibre-thermoplastics adhesion

[77-81]. In principle, IFSS should depend on not only the thermal shrinkage but also the physiochemical interactions between the fibre and the matrix (e.g. acid-base interaction, dispersion forces etc.). The two contributors are independent from each other. The former depends on, among various factors, fibre volume fraction, V_f, whereas the latter is independent from V_f. The V_f dependence of thermal shrinkage will be discussed in chapter 5. Although the shrinkage stress is unlikely to fully account for the interfacial bond quality in those systems, the complex interactions at the fibre-matrix interface may be reduced to a single parameter: coefficient of static friction, μ_{st}. Based on the results in Figure 3.14 and 3.15, it may be reasonable to assume that friction mechanism can be used to account for the GF-PP47 adhesion. Or more precisely, interfacial failure of neat GF-PP47 is probably governed by the friction law. One of laws of friction states that friction is independent of the nominal area of contact which suggests that the basic relations $F_{st} = \mu_{st} P$ also apply locally to any element of the contact interface, where F_{st} is static friction, P is normal force across the interface of two rigid bodies, and μ_{st} is considered as a characteristic constant of the interface [82]. If local slipping takes place this leads to

$$\tau_{ult} = \mu_{st} \cdot \sigma_n \qquad (3.9)$$

where σ_n is compressive radial stress (CRS) across the interface. In this case, it could be the sum of σ_{rad} and the adhesive component resulting from molecular interaction between the fibre and the matrix. Therefore, upper boundary of the coefficient of static friction, μ_{st}^*, may be obtained by replacing σ_n with σ_{rad} in Equation (3.9), yielding the value of 0.97±0.01. The value of μ_{st} could therefore lie

in the range of 0.27±0.03 to 0.97±0.01. Further examination on Nairn's model suggests that σ_{rad} is likely to be overestimated in the case of MBT samples, which involve a finite fibre embedded length. Quek has showed an nonuniform radial shear stress distribution in a concentric cylinder model with finite length [83]. Moreover, the maximum resin droplet diameter was used as the input of matrix diameter in the cylinder model. This may lead to the overestimation of $\sigma_{rad.}$ Hence μ_{st} may also be lower in magnitude than the value presented above.

3.3.2 Single fibre pull-out test (SFPT)

Unlike the small MBT samples, SFPT samples are large enough to monitor the pull-out process. However, it proved difficult to capture the debonding initiation due to inadequate magnification and the reflection as shown in Figure 3.16.

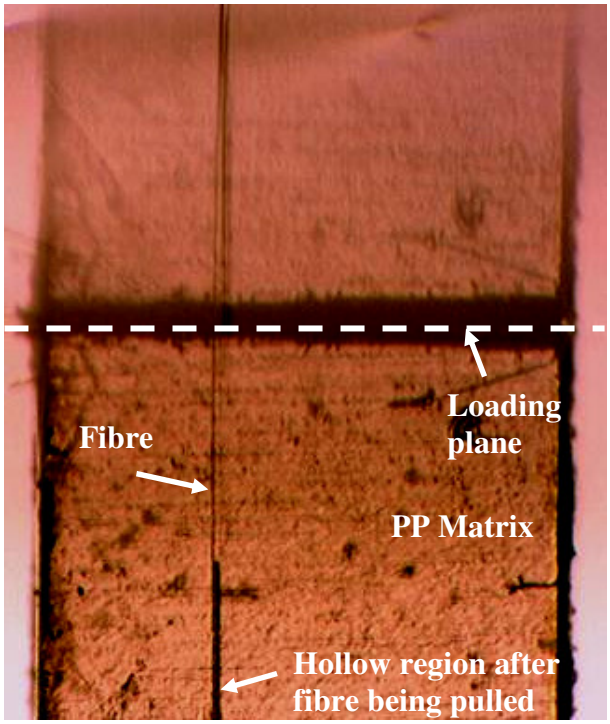

Fig. 3.16 Photo of SFPT sample in testing

The thin samples with rough contact surface often result in misalignment during testing. Microscopy observation of tested samples showed no residual resin left behind on the debonded area, indicating the occurrence of interfacial fracture in SFPT. The influence of processing time on measured IFSS was investigated by varying the processing time at 220°C. Results of maximum force, F_{max}, versus fibre embedded area, A_e, obtained for GF-PP47 samples, heated for 2 minutes – 6 minutes and tested at room temperature are shown in Figure 3.17.

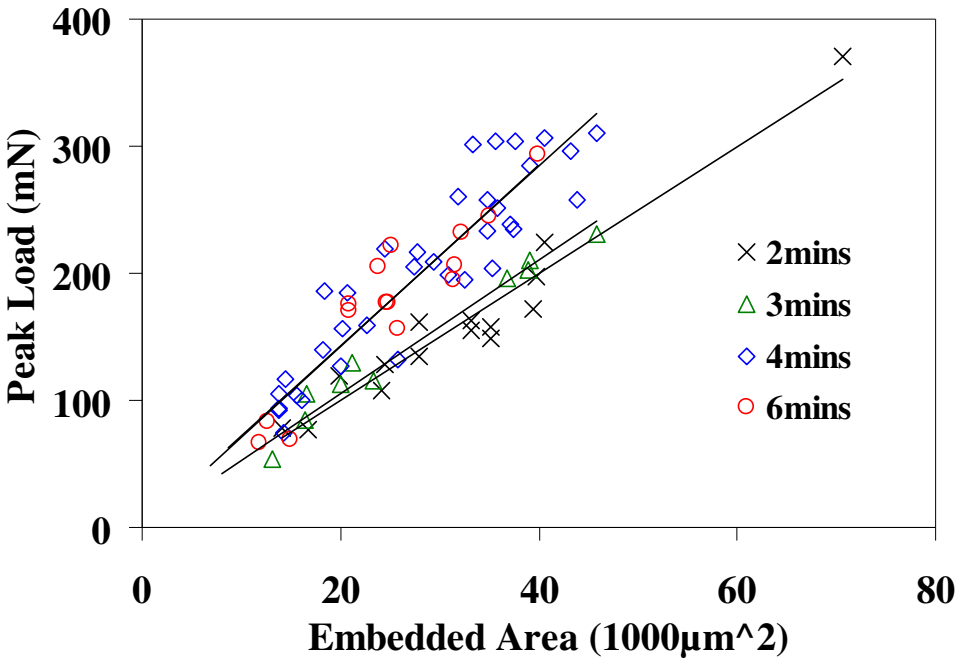

Fig. 3.17 Plot of peak force vs. embedded area measured for neat GF-PP47 with different processing times

It can be seen that each data set displays an excellent linear relation between F_{max} and A_e, indicating the uniform interfacial shear stress distribution at debonding. Thus $\tau_{ult} = \tau_{app}$ is applicable for the results from SFPT as well. The value of IFSS for neat GF-PP47 system, prepared under the same thermal conditions as in MBT, is 7.15

MPa, which is very close to the value of IFSS obtained in MBT. In addition, there is considerable overlapping between 2 minutes and 3 minutes data sets and between 4 minutes and 6 minutes data sets. The effect of t_p on τ_{ult} is summarised in Figure 3.18.

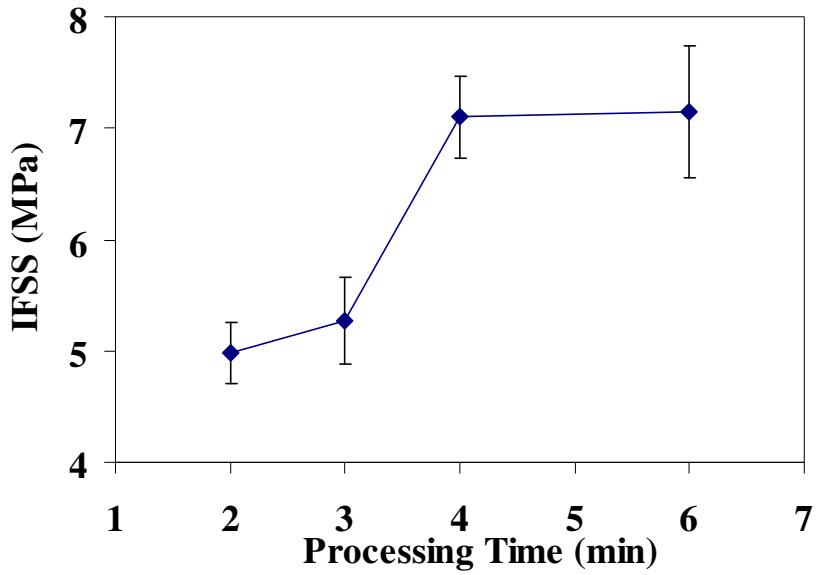

Fig. 3.18 Effect of processing time in SFPT sample preparation on measured IFSS

It shows that within the first 2 minutes the bond strength of GF-PP47 already reaches 70% of its maximum value obtained in this work. It is interesting to see that t_p has much more significant effect on IFSS when $3<t_p<4$ than $2<t_p<3$, although more measurements are required for 3 minutes data set to confirm this. Despite this difference, the measured IFSS generally increases with t_p and levels off after 4 minutes. The results in Figure 3.18 emphasise the importance of wetting in achieving good bond quality for neat GF-PP. 6 minutes appears to be a good choice for a fairly short t_p, from which the measured IFSS is also independent. However, since the samples were fabricated in air, t_p= 4 minutes is more likely to reduce the risk of PP thermo-oxidative degradation and is in preference to t_p=6 minutes.

Figure 3.19 shows a plot of peak force vs. embedded area measured for neat GF-PP0.3, PP19, and PP47 using the SFPT.

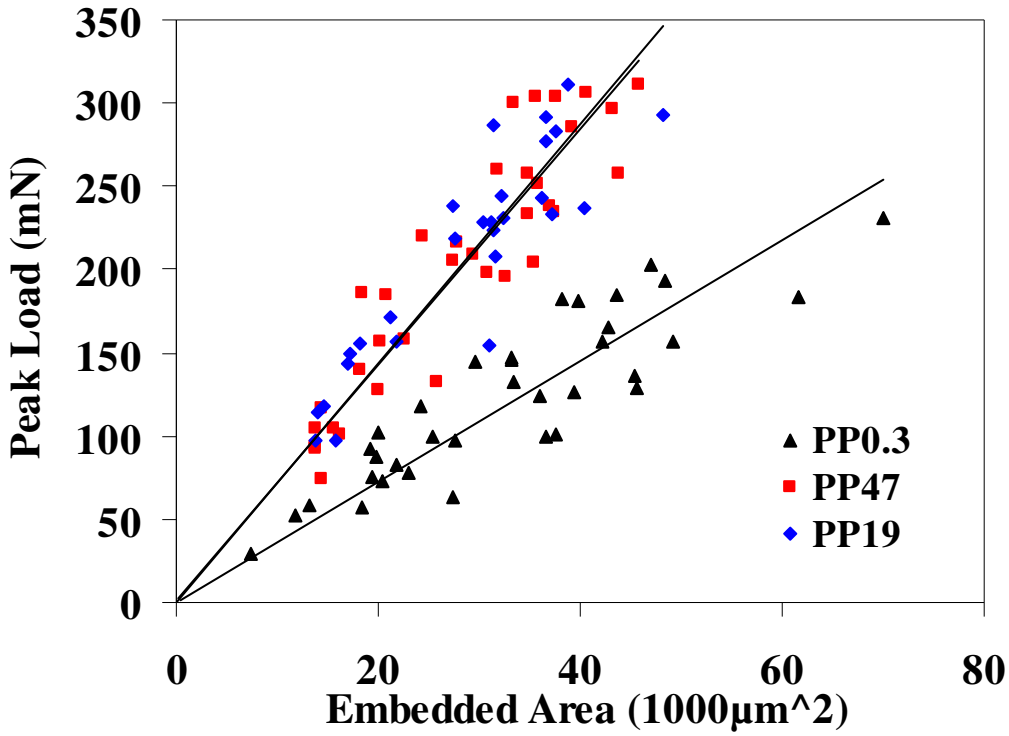

Fig. 3.19 Plot of peak force vs. embedded area measured for neat GF-PP0.3, PP19, and PP47 using the SFPT

It clearly shows that in the same range of embedded area the peak force for PP0.3 is significantly smaller than that obtained from other two grades. There is, however, little difference in the plot between PP19 and PP47 as illustrated in Figure 3.19. The comparison of mean values of measured IFSS for these three grades is shown in Figure 3.20.

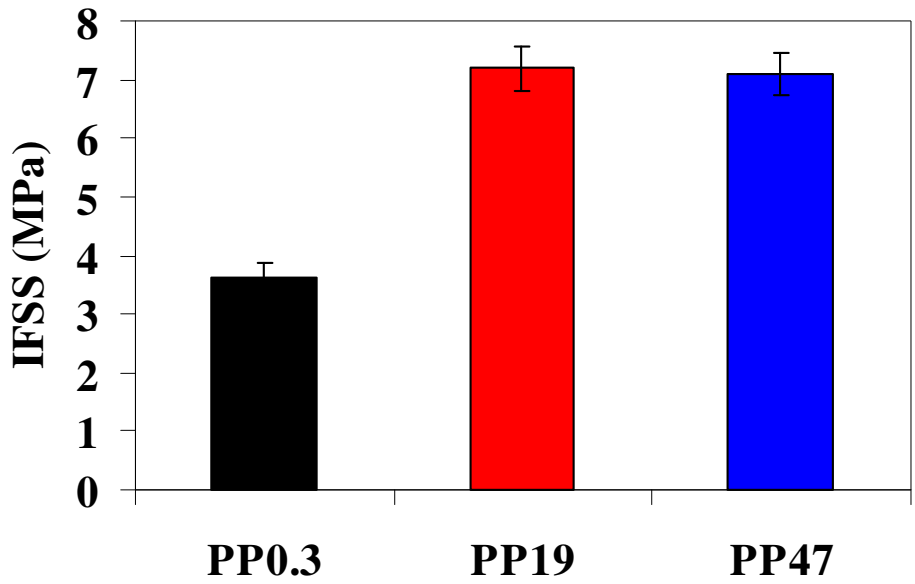

Fig. 3.20 Effect o f molecular weight of PP on measured IFSS for neat GF-PP

It can be seen that PP19 and PP47 give the values almost two fold higher than that of IFSS for PP0.3. These results may well reflect the effect of molecular weight (MW) of PP on measured IFSS. Molecular weight is a measure of the average length of polymer molecules and influences many crucial properties of PP as showed in chapter 2. Low MW (i.e. high MFR) may result in higher mobility of polymer chains than that of long chains under the same thermal conditions. Consequently the matrix melt with lower MW can lead to better wet-out of the fibres and increasing the bond quality between the matrix and the fibre. Furthermore, it has been shown in chapter 2 that both PP19 and PP47 give a higher crystallisation temperature, which is normally accepted as the stress free temperature, at which the thermal residual stress begins to build up in the material. This means that PP19 and PP47 may have a higher compressive radial residual stress, σ_{rad}, at the interface than that of PP0.3. Results related to crystallinity of PP in chapter 2 also indicate that PP19 and PP47 give a higher crystallinity than PP0.3. This implies that the matrix of PP19 and PP47 may lead to greater volume shrinkage than that of PP0.3 during sample cooling. This can

again result in greater $\sigma_{rad.}$ In order to quantitatively evaluate how much difference there is in σ_{rad} among these three PP grades, σ_{rad} is estimated using the cylinder model here. Sample thickness (i.e. 0.1 mm) is taken as the diameter of the matrix cylinder and other inputs are based on the results in chapter 2. Since only PP47 was measured for coefficient of linear thermal expansion (CLTE), CLTE for other grades is set to be the same as that for PP47. The values of calculated σ_{rad} at 20°C for PP0.3, PP19, and PP47 are 7.47 MPa, 8.54 MPa, and 8.28 MPa respectively. Thus among those possibilities mentioned above, better wetting is the most likely cause for the observed increase of measured IFSS in PP19 and PP47. Note that although there is a significant difference in MFR between PP19 and PP47, the difference in MW is much smaller than that between any of them and PP0.3 since MFR is exponentially related to MW of PP [75].

3.3.3 Comparison between MBT and SFPT

Figure 3.21 and 3.22 show the comparison between MBT and SFPT of IFSS and fibre embedded length dependence of IFSS for the same neat GF-PP47 system.

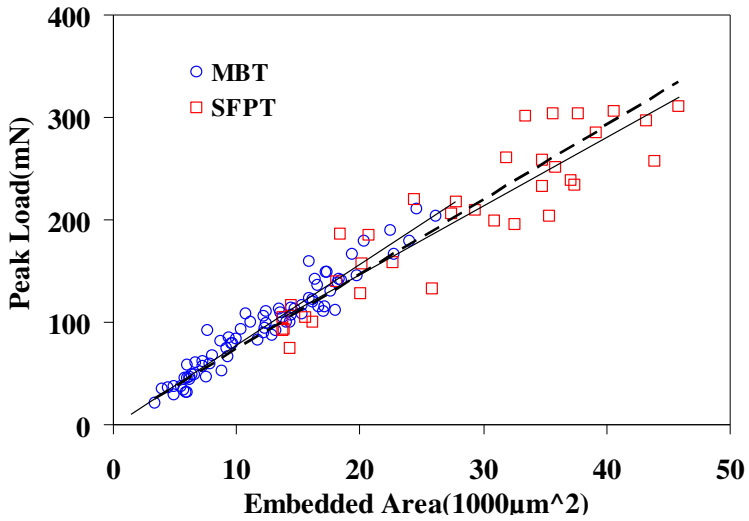

Fig. 3.21 Peak load vs. embedded area from both MBT and SFPT on neat GF-PP47

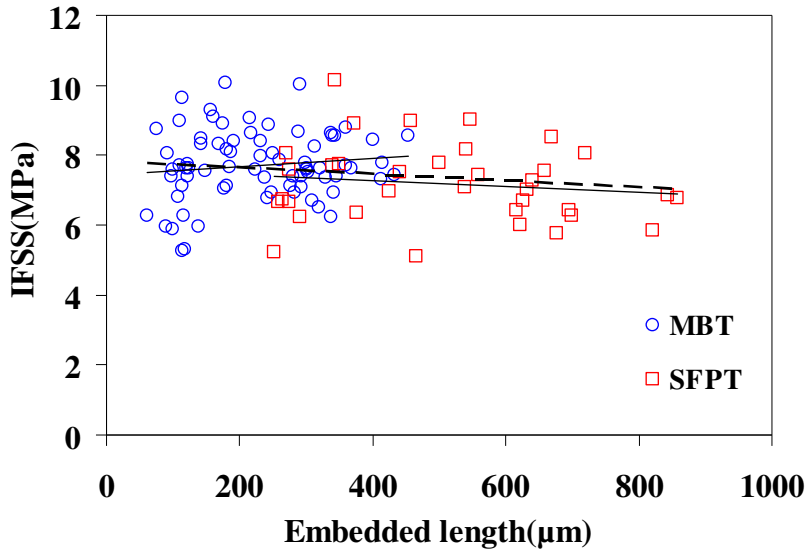

Fig. 3.22 Dependence of IFSS on embedded length for GF-PP47 measured by the MBT and the SFPT

Solid lines are linear least square fits for MBT and SFPT data points respectively and dotted line is the linear fit for all the data in Figure 3.21 and 3.22. It can be observed that the linear relation between F_{max} and A_e explains the entire data as well as it does for the separate data sets. There might be a slight tendency of the data deviating from the linear relation at the large embedded area (i.e. long fibre embedded length). The decrease of apparent IFSS with increase in L_e is regarded as a common feature in brittle interfacial fracture [13, 16, 18, 25, 28, 42, 68, 70, 84]. More recently, Piggott also observed this in a composite with very ductile low density polyethylene and fit the results using an energy-based model, in which the tensile strain energy in the matrix and the shear strain energy in the fibre are neglected. This model is also employed here to fit the L_e dependence of F_{max} as shown in Figure 3.23.

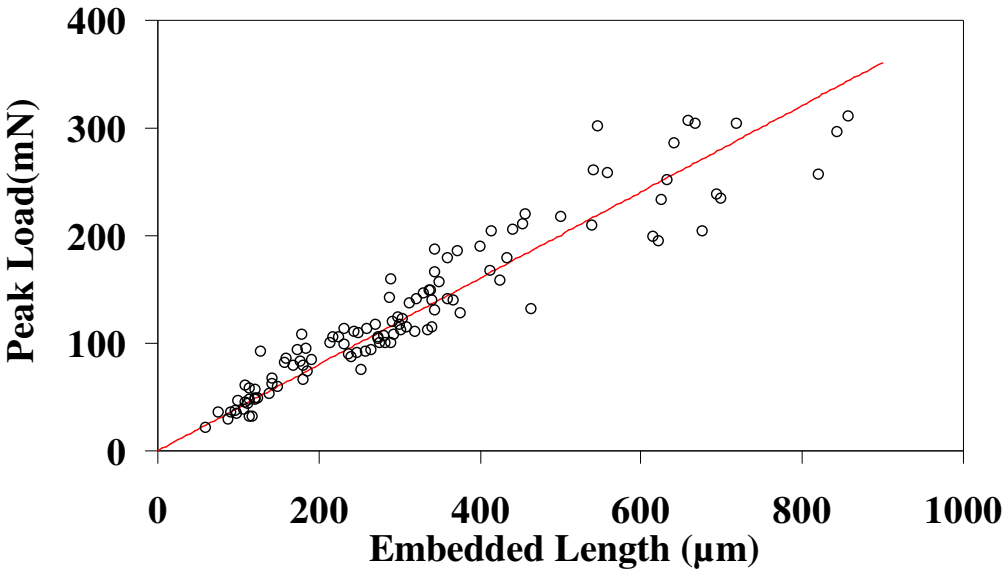

Fig. 3.23 Dependence of Peak load on embedded length with fit by Piggott's model

The effective matrix radius, R_m, was adjusted until the fitting line lies on top of linear regression line. However, this requires an almost infinite value for R_m, which is completely unacceptable. Thus, it is confirmed from this that neat GF-PP47 interfacial failure is governed by a ductile fracture mechanisms and that the adhesion between the two materials can be evaluated by Equation 3.4. The excellent agreement between MBT and SFPT results also implies that the SFPT samples did not experience any significant degradation.

Transcrystallisation is a nucleation-controlled process taking place under quiescent conditions in a semicrystalline polymer such as PP in contact with other material such as fibres [85]. It occurs at the fibre surface when closely spaced nuclei at a foreign surface hinder the lateral extension and force growth in one direction, namely perpendicular to the fibre surface as illustrated in Figure 3.24.

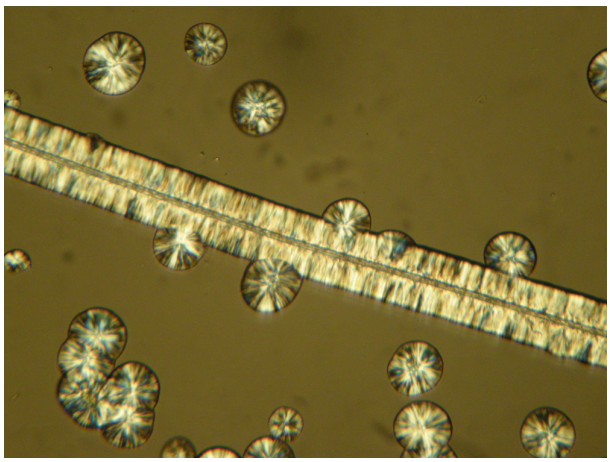

Fig. 3.24 Transcrystallisation of PP47 on Kevlar fibre

Transcrystallisation in GF-PP system and its effect on GF-PP adhesion have been extensively studied [37, 86-93]. It has been shown that the application of stress at the interface between a glass fibre and a supercooled PP melt (by mechanical pulling of the fibre) can result in PP transcrystallisation at the interface [87]. The thermal residual shear stress formed during the sample cooling might give rise to such interfacial morphology. To confirm this, Both MBT and SFPT samples were inspected under polarised light as shown in Figure 3.25.

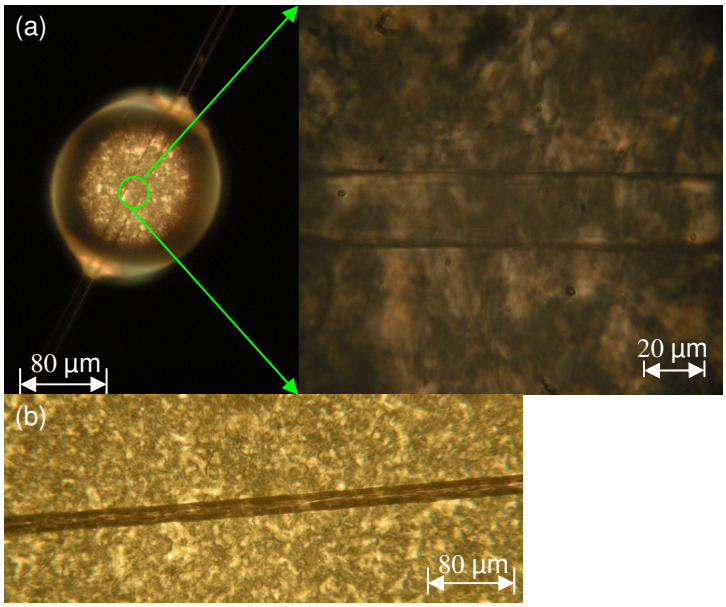

Fig. 3.25 MBT and SFPT samples under polarisation microscope

No transcrystalline zone around the fibre could be observed in any of these samples under the polarisation microscope.

3.4 Summary

Fibre pull-out tests (i.e. MBT and SFPT), were developed in our laboratory, including design and manufacture of a microvise and shearing plates. The protocols for both MBT and SFPT sample preparation were established and no transcrystalline zone at the interface was observed under polarisation microscopy. Samples were monitored by the stereo-microscope during the test and the pull-out process was followed until the fibres were pulled out of the matrix.

MBT results for IFSS exhibited a significant linear relation between the maximum load and fibre embedded area, giving IFSS value, 7.8 MPa for neat GF-PP47 system. The possible range from 0.27±0.03 to 0.97±0.01 for coefficient of static friction was estimated by measuring dynamic friction from MBT loading-displacement curves and assuming a friction mechanism for neat GF-PP47 adhesion respectively.

SFPT results also showed an excellent linear relation between the maximum load and fibre embedded area, giving an IFSS value of 7.2 MPa for the same GF-PP47 system. In addition, the effect of processing time in sample preparation on the measured IFSS was investigated and the results indicated that approximately 70% of the bond strength in neat GF-PP47 could be achieved within the first 2 minutes at 220°C. The measured IFSS increased significantly within the first 4 minutes and levels off afterwards.

The results for IFSS obtained from the MBT and the SFPT were in good agreement and the data as a whole can be well fit by linear least square method, yielding the value of 7.3 MPa for the IFSS of neat GF-PP47. Moreover, the data was also fit by the model based on brittle interfacial failure and unrealistic input had to be adopted to achieve the same fit as the least square method. Consequently ductile interfacial fracture was concluded to be the most probable interface mode of failure for the composite system studied in this work.

References

[1] Kim J,Mai Y. Engineered Interfaces in Fiber Reinforced Composites. 1998, Oxford: Elsevier Science Ltd.

[2] Hull D,Clyne TW. An Introduction to Composite Materials. 2nd ed. Cambridge Solid State Science Series, ed. Clarke PDR, Suresh PSFRS PIMW. 1996: Cambridge Univerisity Press.

[3] Plueddemann EP. Interfaces in Polymer Matrix Composites. Composite Materials, ed. Broutman LJRichard HK. Vol. 6. 1974, New York: Academic Press.

[4] Jones FR. Handbook of Polymer-Fibre Composites. Polymer Science And Technology, ed. Brewis DMBiggs D. 1994, Essex and New York: Longman Scientific and Technical.

[5] Gao J, Luedtke WD, Gourdon D, Ruths M, Israelachvili JN,Landman U. Frictional Forces and Amonton's Law: From the Molecular to the Macroscopic Scale. The Journal of Physical Chemistry B 2004;108(11):3410-3425.

[6] Persson BNJ,et al. On the origin of Amonton's friction law. Journal of Physics: Condensed Matter 2008;20(39):395006.

[7] Prasanta S,Atanu B. Asperity interaction in elastic–plastic contact of rough surfaces in presence of adhesion. Journal of Physics D: Applied Physics 2005;38(16):2841.

[8] uuml, ser MH, Wenning L,Robbins MO. Simple Microscopic Theory of Amonton's Laws for Static Friction. Physical Review Letters 2001;86(7):1295.

[9] Behary N, Ghenaim A, El Achari A,Caze C. Tribological analysis of glass fibers using atomic force microscopy (AFM)/lateral force microscopy (LFM). Journal of Applied Polymer Science 2000;75(8):1013-1025.

[10] Herrera-Franco PJ,Drzal LT. Comparison of methods for the measurement of fibre/matrix adhesion in composites. Composites 1992;23(1):2-27.

[11] Zhandarov S,Mäder E. Characterization of fiber/matrix interface strength: applicability of different tests, approaches and parameters. Composites Science and Technology 2005;65(1):149-160.

[12] Gray RJ. Experimental techniques for measuring fibre/matrix interfacial bond shear strength. International Journal of Adhesion and Adhesives 1983;3(4):197-202.

[13] Dutschk VP, E.; Mäder, E.; Schneider, K. Can the results obtained by microtension and pull-out techniques be compared? Composite Interfaces 1998;6(121-134.

[14] Zhandarov SF,Pisanova EV. Two interfacial shear strength calculations based on the single fiber composite test. Mechanics of Composite Materials 1996;31(4):325-336.

[15] Gorbatkina YA. Adhesive Strength In Fibre-Polymer Systems. 1992: KHIMIYA PUBLISHERS

[16] Day RJ,Rodrigez JVC. Investigation of the micromechanics of the microbond test. Composites Science and Technology 1998;58(6):907-914.

[17] Piggott MR,Dai SR. Fiber pull out experiments with thermoplastics. Polymer Engineering & Science 1991;31(17):1246-1249.
[18] Piggott MR. Debonding and friction at fibre-polymer interfaces. I: Criteria for failure and sliding. Composites Science and Technology 1987;30(4):295-306.
[19] Dutschk V, Pisanova E, Zhandarov S,Lauke B. “Fundamental” and “practical” adhesion in polymer-fiber systems. Mechanics of Composite Materials 1998;34(4):309-320.
[20] Pisanova E, Zhandarov S,Mäder E. How can adhesion be determined from micromechanical tests? Composites Part A: Applied Science and Manufacturing 2001;32(3-4):425-434.
[21] Zhandarov S, Gorbatkina Y,Mäder E. Adhesional pressure as a criterion for interfacial failure in fibrous microcomposites and its determination using a microbond test. Composites Science and Technology 2006;66(15):2610-2628.
[22] Piggott MR,Xiong YJ. Direct observation of debonding in fibre pull-out specimens. Fibre, matrix, and interface properties ASTM STP 1290 1996;84-91.
[23] Pisanova E, Zhandarov S, Mäder E, Ahmad I,Young RJ. Three techniques of interfacial bond strength estimation from direct observation of crack initiation and propagation in polymer-fibre systems. Composites Part A: Applied Science and Manufacturing 2001;32(3-4):435-443.
[24] Lawrence P. Some theoretical considerations of fibre pull-out from an elastic matrix. Journal of Materials Science 1972;7(1):1-6.
[25] Piggott MR. Failure processes in the fibre-polymer interphase. Composites Science and Technology 1991;42(1-3):57-76.
[26] Piggott MR,Xiong Y. Visualization of debonding of fully and partially embedded glass fibres in epoxy resins. Composites Science and Technology 1994;52(4):535-540.
[27] Broutman LJ. Measurement of the fibre-polymer matrix interfaical strength. Interfaces in Compoistes ASTM STP 452 1969;27-41.
[28] Miller B, Muri P,Rebenfeld L. A microbond method for determination of the shear strength of a fiber/resin interface. Composites Science and Technology 1987;28(1):17-32.
[29] Gaur U,Miller B. Microbond method for determination of the shear strength of a fiber/resin interface: Evaluation of experimental parameters. Composites Science and Technology 1989;34(1):35-51.
[30] Miller B, Gaur U,Hirt DE. Measurement and mechanical aspects of the microbond pull-out technique for obtaining fiber/resin interfacial shear strength. Composites Science and Technology 1991;42(1-3):207-219.
[31] Thomason JL,Schoolenberg GE. An investigation of glass fibre/polypropylene interface strength and its effect on composite properties. Composites 1994;25(3):197-203.
[32] Mäder E,Freitag KH. Interface properties and their influence on short fibre composites. Composites 1990;21(5):397-402.
[33] Mäder E, Jacobasch HJ, Grundke K,Gietzelt T. Influence of an optimized interphase on the properties of polypropylene/glass fibre composites. Composites Part A: Applied Science and Manufacturing 1996;27(9):907-912.

[34] Mäder E, Moos E,Karger-Kocsis J. Role of film formers in glass fibre reinforced polypropylene -- new insights and relation to mechanical properties. Composites Part A: Applied Science and Manufacturing 2001;32(5):631-639.
[35] Mäder E,Pisanova E. Characterization and design of interphases in glass fiber reinforced polyproplyene. Polymer Composites 2000;21(3):361-368.
[36] Mäder SZE. Determination of interfacial parameters in fiber-polymer systems from pull-out test data using a bilinear bond law. Composite Interfaces 2004;11(361-391.
[37] Pompe G,Mäder E. Experimental detection of a transcrystalline interphase in glass-fibre/polypropylene composites. Composites Science and Technology 2000;60(11):2159-2167.
[38] Zhuang RC, Burghardt T,Mäder E. Study on interfacial adhesion strength of single glass fibre/polypropylene model composites by altering the nature of the surface of sized glass fibres. Composites Science and Technology 2010;70(10):1523-1529.
[39] Biro DA, McLean P,Deslandes Y. Application of the microbond technique: Characterization of carbon fiber-epoxy interfaces. Polymer Engineering & Science 1991;31(17):1250-1256.
[40] J.P. Craven RC, C. Viney. Evaluating the silk/epoxy interface by means of the Microbond Test. Composites: Part A 2000;31(653-660.
[41] Mandell JF, Chen JH,McGarry FJ. A microdebonding test for in situ assessment of fibre/matrix bond strength in composite materials. International Journal of Adhesion and Adhesives 1980;1(1):40-44.
[42] Wagner HD, Gallis HE,Wiesel E. Study of the interface in Kevlar 49-epoxy composites by means of microbond and fragmentation tests: effects of materials and testing variables. Journal of Materials Science 1993;28(8):2238-2244.
[43] Straub A, Slivka M,Schwartz P. A study of the effects of time and temperature on the fiber/matrix interface strength using the microbond test. Composites Science and Technology 1997;57(8):991-994.
[44] Yang L,Thomason JL. Interface strength in glass fibre-polypropylene measured using the fibre pull-out and microbond methods. Composites Part A: Applied Science and Manufacturing 2010;41(9):1077-1083.
[45] Gonon L, Momtaz A, Van Hoyweghen D, Chabert B, Gérard JF,Gaertner R. Physico-Chemical and micromechanical analysis of the interface in a poly(phenylene sulfide)/glass fiber composite—a microbond study. Polymer Composites 1996;17(2):265-274.
[46] Chou CT, Gaur U,Miller B. The effect of microvise gap width on microbond pull-out test results. Composites Science and Technology 1994;51(1):111-116.
[47] Hann LP,Hirt DE. Simulating the microbond technique with macrodroplets. Composites Science and Technology 1995;54(4):423-430.
[48] Heilhecker H, Cross W, Pentland R, Griswold C, Kellar JJ,Kjerengtroen L. The vice angle in the microbond test. Journal of Materials Science Letters 2000;19(23):2145-2147.

[49] Ash JT, Cross WM, Svalstad D, Kellar JJ,Kjerengtroen L. Finite element evaluation of the microbond test: meniscus effect, interphase region, and vise angle. Composites Science and Technology 2003;63(5):641-651.
[50] Rao V, Herrera-franco P, Ozzello AD,Drzal LT. A Direct Comparison of the Fragmentation Test and the Microbond Pull-out Test for Determining the Interfacial Shear Strength. The Journal of Adhesion 1991;34(1):65 - 77.
[51] Pitkethly MJ,Doble BJ. Characterizing the fibre/matrix interface of carbon fibre-reinforced composites using a single fibre pull-out test. Composites 1990;21(5):389-395.
[52] Pitkethly MJ, Favre JP, Gaur U, Jakubowski J, Mudrich SF, Caldwell DL, Drzal LT, Nardin M, Wagner HD, Di Landro L, Hampe A, Armistead JP, Desaeger M,Verpoest I. A round-robin programme on interfacial test methods. Composites Science and Technology 1993;48(1-4):205-214.
[53] Zhandarov SP, E.; Lauke, B. Is there any contradiction between the stress and energy failure criteria in micromechanical tests? Part I. Crack initiation: stress-controlled or energy-controlled? Composite Interfaces 1997;5(387-404.
[54] Hsueh C-H. Strength versus energy debonding criteria at fiber/matrix interfaces. Composites Engineering 1992;2(8):665-675.
[55] Kelly A,Tyson WR. Tensile properties of fibre-reinforced metals: Copper/tungsten and copper/molybdenum. Journal of the Mechanics and Physics of Solids 1965;13(6):329-338, in1-in2, 339-350.
[56] Meretz S, Auersch W, Marotzke C, Schulz E,Hampe A. Investigation of morphology-dependent fracture behaviour with the single-fibre pull-out test. Composites Science and Technology 1993;48(1-4):285-290.
[57] Cox HL. The elasticity and strength of paper and other fibrous materials. British Journal of Applied Physics 1952;3(3):72.
[58] Laws V,et al. Reinforcement of brittle matrices by glass fibres. Journal of Physics D: Applied Physics 1973;6(5):523.
[59] Takaku A,Arridge RGC. The effect of interfacial radial and shear stress on fibre pull-out in composite materials. Journal of Physics D: Applied Physics 1973;6(17):2038.
[60] Gray RJ. Analysis of the effect of embedded fibre length on fibre debonding and pull-out from an elastic matrix. Journal of Materials Science 1984;19(3):861-870.
[61] Hsueh C-H. Embedded-end debonding during fiber pull-out. Materials Science and Engineering: A 1993;163(1):L1-L4.
[62] Banbaji J. On a more generalized theory of the pull-out test from an elastic matrix Part I--Theoretical considerations. Composites Science and Technology 1988;32(3):183-193.
[63] Outwater JD,Murphy MC. On the fracture energy of unidirectional laminates 24th Annual Technical Conference, Reinforced Plastics/Composites Division, Washington, D.C. 1969;Section 11-C(1-8):
[64] Stang H,Shah SP. Failure of fibre-reinforced composites by pull-out fracture. Journal of Materials Science 1986;21(3):953-957.
[65] Wells JK,Beaumont PWR. Debonding and pull-out processes in fibrous composites. Journal of Materials Science 1985;20(4):1275-1284.

[66] Gao Y-C, Mai Y-W,Cotterell B. Fracture of fiber-reinforced materials. Zeitschrift für Angewandte Mathematik und Physik (ZAMP) 1988;39(4):550-572.
[67] Kim J-K, Baillie C,Mai Y-W. Interfacial debonding and fibre pull-out stresses Part I Critical comparison of existing theories with experiments. Journal of Materials Science 1992;27(12):3143-3154.
[68] Liu C-H,Nairn JA. Analytical and experimental methods for a fracture mechanics interpretation of the microbond test including the effects of friction and thermal stresses. International Journal of Adhesion and Adhesives 1999;19(1):59-70.
[69] Scheer RJ,Nairn JA. A Comparison of Several Fracture Mechanics Methods for Measuring Interfacial Toughness with Microbond Tests. The Journal of Adhesion 1995;53(1):45 - 68.
[70] Nairn JA. Analytical fracture mechanics analysis of the pull-out test including the effects of friction and thermal stresses. Advanced Composite Letters 2000;9(6):373-383.
[71] Piggott MR. A new model for interface failure in fibre-reinforced polymers. Composites Science and Technology 1995;55(3):269-276.
[72] Hodzic AK, S.; Lowe, A.; Stachurski, Z.H. The microdroplet test: experimental and finite element analysis of the dependance of failure mode on droplet shape. Composite Interfaces 1998;6(375-389.
[73] Gaur U, Desio G,Miller B. Measuring fiber/matrix adhesion in thermoplastic composites. Plastics Engineering 1989;(Oct 1989)(43-45.
[74] Nishikawa M, Okabe T, Hemmi K,Takeda N. Micromechanical modeling of the microbond test to quantify the interfacial properties of fiber-reinforced composites. International Journal of Solids and Structures 2008;45(14-15):4098-4113.
[75] Bremner T, Rudin A,Cook DG. Melt flow index values and molecular weight distributions of commercial thermoplastics. Journal of Applied Polymer Science 1990;41(7-8):1617-1627.
[76] Nairn JA. Thermoelastic analysis of residual stresses in unidirectional, high-performance composites. Polymer Composites 1985;6(2):123-130.
[77] Thomason JL. Dependence of interfacial strength on the anisotropic fiber properties of jute reinforced composites. Polymer Composites 2010;31(9):1525-1534.
[78] Thomason JL. Interfaces and interfacial effects in glass reinforced thermoplastics. in 28th Risø International Symposium on Materials Science. 2007. Risø National Laboratory, Roskilde, Denmark.
[79] Thomason JL. Interfacial strength in thermoplastic composites - at last an industry friendly measurement method? Composites Part A: Applied Science and Manufacturing 2002;33(10):1283-1288.
[80] Di Landro L,Pegoraro M. Evaluation of residual stresses and adhesion in polymer composites. Composites Part A: Applied Science and Manufacturing 1996;27(9):847-853.
[81] Nairn JA,Zoller P. Matrix solidification and the resulting residual thermal stresses in composites. Journal of Materials Science 1985;20(1):355-367.
[82] Savkoor RA, Models of friction based on contact and fracture mechanics, in Fundamentals of friction: macroscopic and microscopic processes (NATO

ASI Series E: Applied Sciences Vol 220, Singer LLPollock MH, Editors. 1992, Kluwer Academic: Dordrecht.
[83] Quek MY. Analysis of residual stresses in a single fibre-matrix composite. International Journal of Adhesion and Adhesives 2004;24(5):379-388.
[84] Chua PS,Piggott MR. The glass fibre-polymer interface: II--Work of fracture and shear stresses. Composites Science and Technology 1985;22(2):107-119.
[85] Billon N,Haudin J. Influence of transcrystallinity on DSC analysis of polymers. Journal of Thermal Analysis and Calorimetry 1994;42(4):679-696.
[86] Thomason JL,Van Rooyen AA. Transcrystallized interphase in thermoplastic composites. Journal of Materials Science 1992;27(4):889-896.
[87] Thomason JL,Van Rooyen AA. Transcrystallized interphase in thermoplastic composites. Journal of Materials Science 1992;27(4):897-907.
[88] Misra A, Deopura BL, Xavier SF, Hartley FD,Peters RH. Transcrystallinity in injection molded polypropylene glass fibre composites. Die Angewandte Makromolekulare Chemie 1983;113(1):113-120.
[89] Wang K, Guo M, Zhao D, Zhang Q, Du R, Fu Q, Dong X,Han CC. Facilitating transcrystallization of polypropylene/glass fiber composites by imposed shear during injection molding. Polymer 2006;47(25):8374-8379.
[90] Yue CY,Cheung WL. Some observations on the role of transcrystalline interphase on the interfacial strength of thermoplastic composites. Journal of Materials Science Letters 1993;12(14):1092-1094.
[91] Li Y, Chen L,Zhou X. Interfacial crystalline behavior in glass-fiber/polypropylene composites modified by block copolymer coupling agents. Journal of Materials Science 2008;43(15):5083-5091.
[92] Nagae S, Otsuka Y, Nishida M, Shimizu T, Takeda T,Yumitori S. Transcrystallization at glass fibre/polypropylene interface and its effect on the improvement of mechanical properties of the composites. Journal of Materials Science Letters 1995;14(17):1234-1236.
[93] Hoecker F,Karger-Kocsis J. Effects of crystallinity and supermolecular formations on the interfacial shear strength and adhesion in GF/PP composites. Polymer Bulletin 1993;31(6):707-714.

Chapter 4

Effect of Thermo-oxidative Degradation on IFSS for GF-PP

4.1 Literature review

4.1.1 Introduction to polymer degradation

Degradation of polymers is a process where changes in the physical properties and/or chemical structure of the polymers occur due to external chemical or physical stresses caused by chemical reactions, involving bond scissions in the backbone of the macromolecules that lead to materials with characteristics different from (usually worse than) those of the starting material [1]. Polymer degradation in broader terms can be classified as biodegradation, thermal degradation, oxidative degradation, mechanical degradation, photodegradation and high energy degradation (radiolysis), ultrasonic degradation and catalytic degradation. Each type of degradation has its own mechanism and kinetics of the reactions, following specific pathways. The modes, extent and/or mechanism of degradation are strongly dependent on the intensity and duration of the physical and chemical stresses, to which the polymer is exposed, including environmental pollutants, heat, light etc., which may be experienced individually or, more often, in multiple combinations [1]. Therefore, countermeasures in stabilisation need to be developed to protect polymers from these harmful effects. The most commonly used method is to add effective stabilisers into the materials, in which the stabilisers are consumed in sacrificial reaction so as to

inhibit the unwanted reactions that would lead to the degradation. Figure 4.1 also summarises other different types of degradation and corresponding stabilisation.

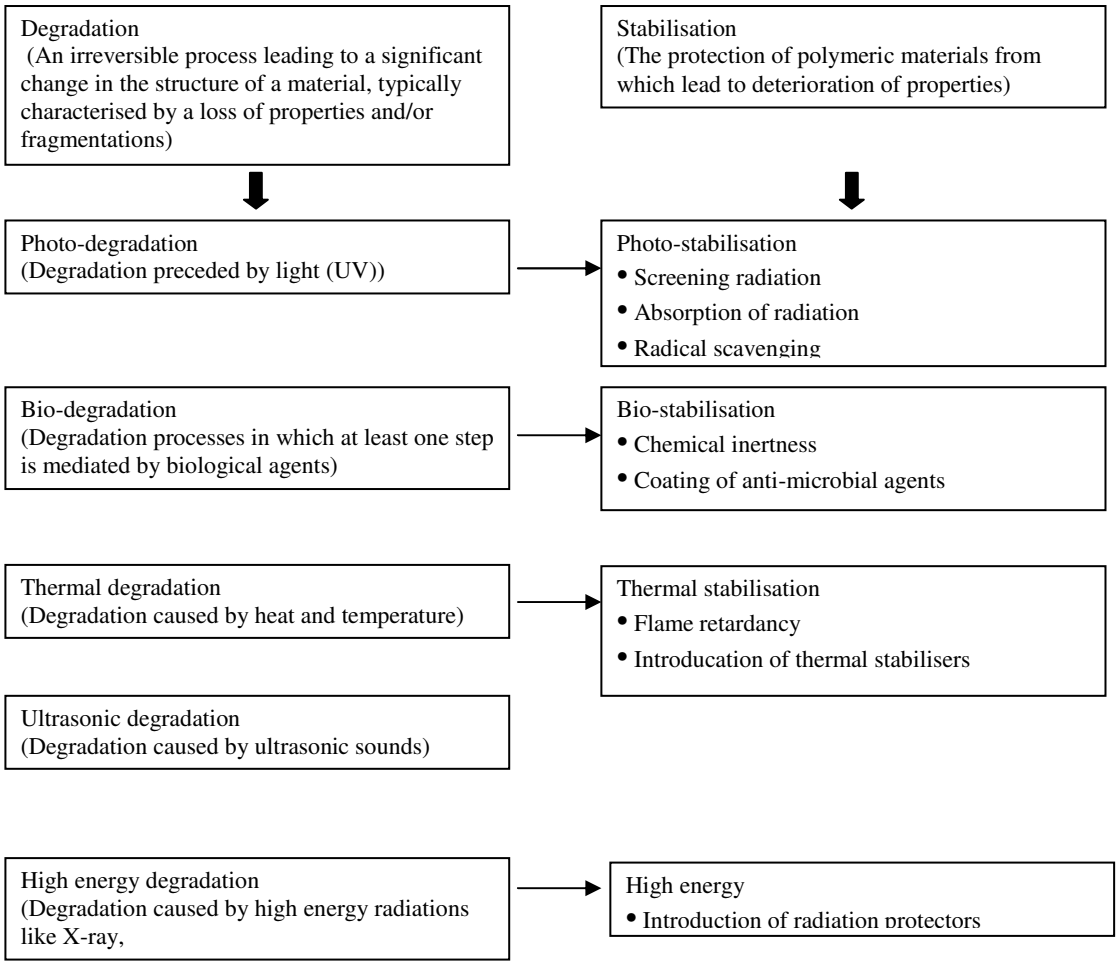

Fig. 4.1 Schematic representation of different degradation and stabilisation processes in polymers [2]

Degradation of polymers has been studied extensively with the aid of various analytical techniques. These methods have proved useful not only in defining suitable processing conditions for these polymers and drawing up useful service guidelines for their application, but also in obtaining information on the relationships between thermal properties and polymer chain structure. Factors generally used to characterise polymer degradation include changes in rheology, changes in loss and

storage moduli, molecular weight characteristics and polydispersity index. Additional measurements include branching, content of new functional groups (unsaturation, oxygenated groups), loss (consumption) of stabilisers and discoloration (yellowness index, YI). The techniques that can measure these factors are summarised in Figure 4.2.

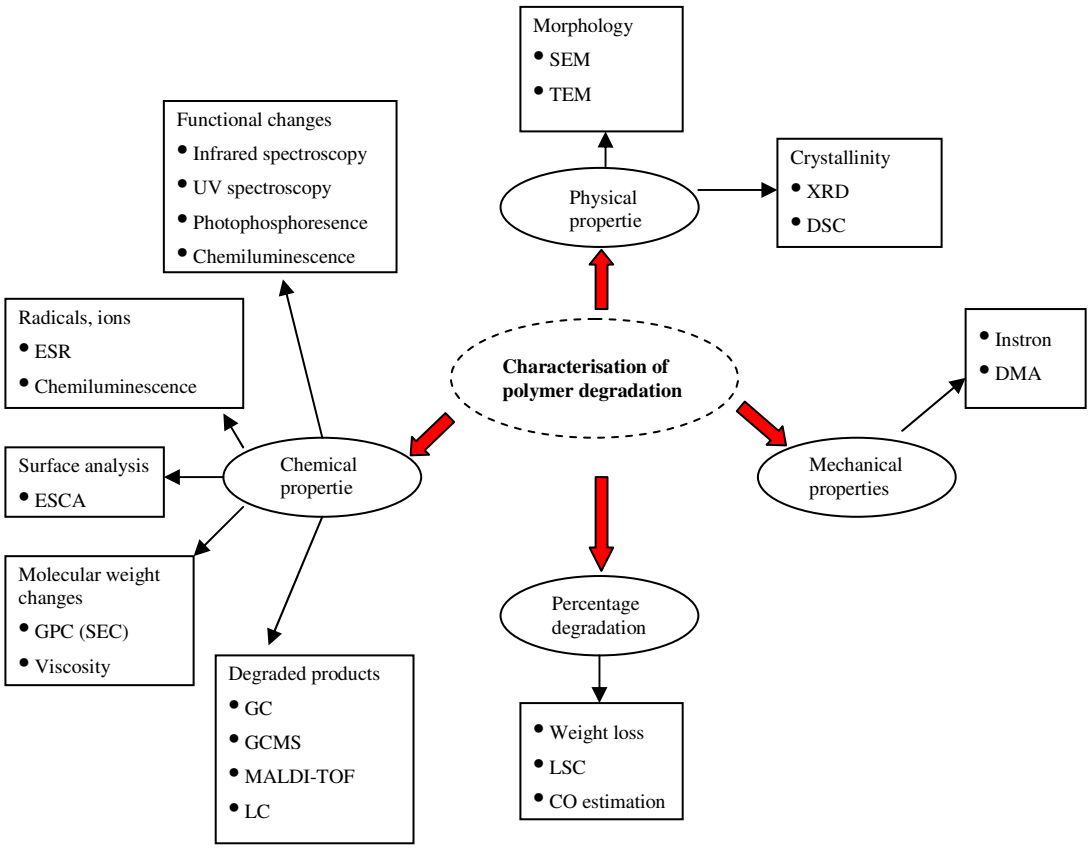

Fig. 4.2 Different analytical techniques to analyse the polymer degradation [2]

Different aspects of polymer degradation and stabilisation have been the object of numerous investigations [1, 3-7]. The importance of study in this field cannot be understated since polymers have become an indispensable ingredient of human life. There is often a natural concern regarding the durability of polymeric materials. Studies of degradation mechanisms can serve as a basis for prolonging the lifetime of polymers and reducing maintenance and replacement. On the other hand, their

enormous use is a matter of great environmental and economic concern, which has motivated the researchers and technologists to induce different degrees of degradations in the polymers. Therefore, controlled stability of the polymers for specific product applications is the ultimate goal through various research activities.

4.1.2 Mechanism for thermo-oxidative degradation

To control polymer stability, understanding of the degradation mechanisms is a primary requisite. Degradation involves very complex mechanisms, occurring by several simultaneous and successive reactions. The individual reactions and even the elementary steps are affected by chemical composition, molecular structure, molecular weight, morphology, etc [8]. Various factors, such as impurities, additives, oxygen, light, temperature, and humidity, also act simultaneously under practical conditions. Despite this complexity, there is a well-established mechanism of polymer degradation and stabilisation due to the tremendous research effort. Thermal degradation of polymers can follow three major pathways: side-group elimination, random scission, and depolymerisation [1, 8]. Random scission involves the formation of a free radical at some point on the polymer backbone, producing small repeating series of oligomers usually differing in chain length by the number of carbons [1]. If such random scission events are repeated successively in a polymer and its degradation products, the result is initially a decrease in molecular weight and ultimately weight loss, as degraded products, with a broad range of carbon numbers, become small enough to evaporate without further cleavage. Unlike thermal degradation, where polymer scission can occur randomly and/or at the chain end, thermo-oxidative degradation is characterised by random scission in the polymer

backbone [1]. Polypropylene (PP) is known to be very vulnerable to oxidative degradation under the influence of elevated temperature and sunlight because of the existence of tertiary carbon atoms. PP degradation chemistry has been very extensively studied and recognised as a free-radical chain reaction, which leads to chain scission [9-13]. The free-radical degradation of PP consists of initiation, propagation, chain branching and termination leading to non-radical products [3]. Initiation results from thermal dissociation of chemical bonds, whereas the key reaction in the propagation is the reaction of the polymer alkyl radicals (P•) with oxygen to form polymer peroxy radicals (POO•) in a very fast reaction. The next propagation step is the abstraction of a hydrogen atom by the polymer peroxy radical to yield hydroperoxide polymer (POOH) and new alkyl radical. The chain branching of POOH results in the formation of very reactive polymer alkoxy radicals (PO•) and hydroxyl radicals (HO•). The polymer oxy radicals can react further to form in-chain ketones or can be involved in termination reactions. The termination of PP radicals occurs by various bimolecular recombinations. The key reactions in the process of PP oxidation are illustrated in Figure 4.3. Once the carbon-based radical is formed, intramolecular hydrogen abstraction will tend to occur. The act of intramolecular abstraction will cause the radical site to migrate down the polymer chain. This migration provides a mechanism for radicals to “find” another radical or antioxidant molecule which can terminate the chain reaction. If termination does not occur, then a mechanism exists for the buildup of hydroperoxide concentration in the polymer. During this migration, the free radical has a choice of hydrogens to abstract: primary, secondary, or tertiary, forming the corresponding radical. A teriary sterically

hindered carbon radical is thermodynamically favoured and becomes the one of the most common locus for chain scission termed as β-scission [3].

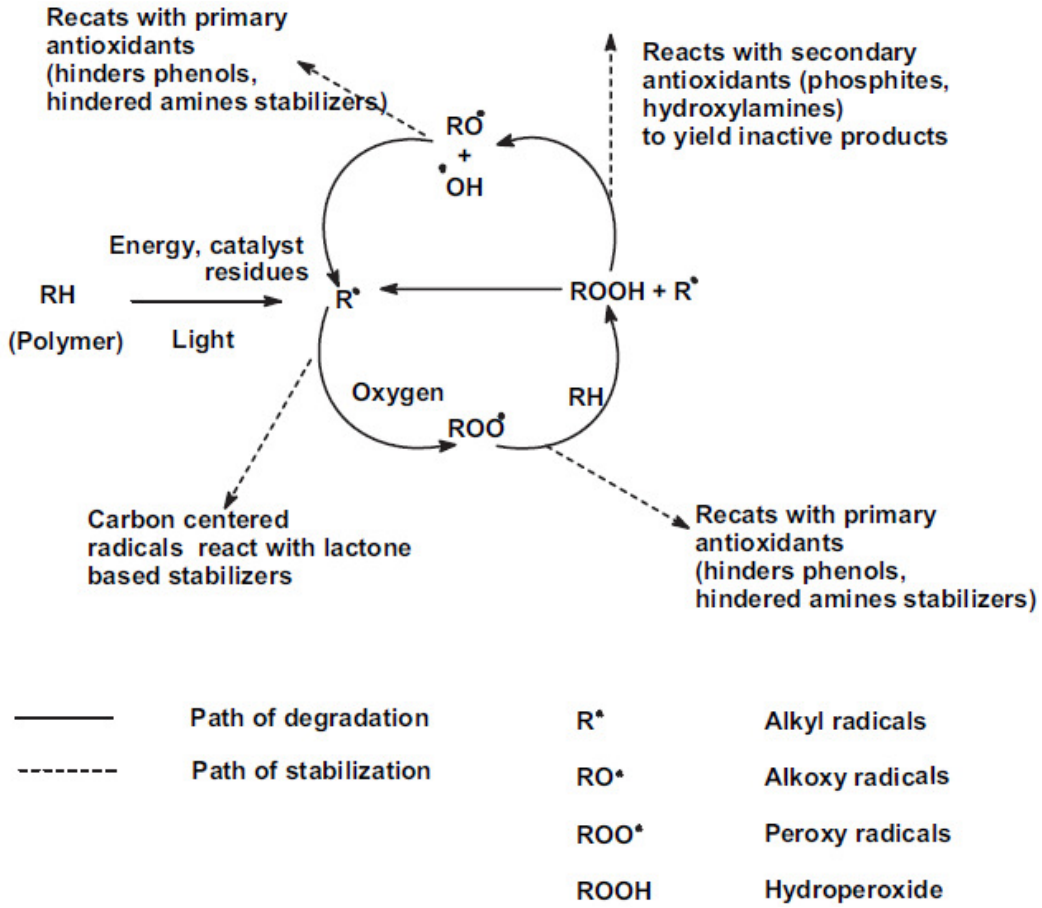

Fig. 4.3 Schematic presentation of mechanism of PP oxidation and degradation [3]

The oxidative degradation of PP can occur in its different physical forms (i.e. solid or molten). Many studies have been carried out with PP in these forms to evaluate the effects of a variety of factors on oxidation and degradation. In the solid form, PP is a semicrystalline polymer with a crystalline content that is normally between 40% and 60%. The crystalline regions are essentially impervious to oxygen, so the oxidation only occurs in the amorphous region [5, 14-16]. Furthermore, it has been shown that the initiation of the oxidation starts specifically in the interface of the crystallites since it can be reasonably assumed that most of the anomalous groups are

placed in this region [17]. Unlike in the solid form, morphology is no longer a concern for molten PP. The stereoregularity of PP was found to be a rather influential factor. The relative stability of PP was found to decrease in the following order: syndiotactic PP > atactic PP >> isotactic PP [11, 18]. Other factors, such as molecular weight, chemical composition, and catalyst residue, have also been studied [19-21]. Regardless of different physical forms, the temperature and availability of oxygen are key factors in the thermo-oxidation degradation of PP. High temperature can accelerate the oxidation and affect the effectiveness of antioxidant in the material. At PP processing temperatures of 200°C to 300°C, the oxidative reaction rates are extremely rapid [3]. Fortunately, a very limited amount of air has access to the melt during the extrusion or moulding of PP. It has been reported that PP under repetitive processing (e.g. multiple extrusion) shows an absence of changes in the chemical structure but an increase of melt flow rate (MFR) [22]. This suggests that chain scission is not dominated by oxidation but mechanical stresses, namely mechanical degradation, where the polymer is subject to very powerful shearing force that will break the molecules and reduce the average molecular weight. In practice, however, oxidation of PP or other polymers during extrusion may occur if there is a considerable amount of impurities, such as hydroperoxide [23]. Oxidation may also be deliberately induced in the process of reactive extrusion, where peroxide is added to change the rheological properties or even the durability of the polymers [24, 25].

4.1.3 Effect of degradation

Like any other types of degradation, thermo-oxidative degradation tends to worsen the different mechanical properties of the polymers to the different extents. The study

of degradation of PP during multiple extrusions showed that small strain properties (e.g. yield stress and modulus) were slightly affected, whereas break properties (e.g. tensile strength and energy to break) demonstrated a considerable reduction, which makes initially ductile material become practically brittle [22, 26]. Thermo-oxidation induced embrittlement was also reported for the solid PP [27]. The influence of degradation of PP by multiple processing on coefficient of thermal expansion (CTE) was studied during the development of a new position sensor used in the measurement of CTE. It showed that the first three cycles reduced the CTE by about 6–22% within the temperature range up to 100°C and CTE increased again in the subsequent cycles [28].

An advantageous aspect of having PP oxidised involves adhesion improvement by surface modification. It is well understood that oxidised polypropylene shows an increase in surface energy relative to its unoxidised counterpart [13]. Surface oxidation of PP by various means (e.g. thermal and flame) has been adopted to polarise the polymer surface and improve the adhesion of PP to other materials with polar surface as well [29, 30]. However, it should be mentioned that this adhesion enhancement is mainly evident in the applications such as painting coating and printability, where the wetting characteristics of PP is the dominating factor for the adhesion. In addition, it seems that the surface oxidation needs to be mild enough not to lead to severe degradation, which appears to have an adverse effect on adhesion [29]. A direct attempt at evaluating the effect of thermal degradation of several thermoplastic polymers on the interface strength to a steel wire can be found in [31]. In this work, single wire pull-out samples of LLPE, HDPE, and PP were tested and the fabrication temperature was varied from 150°C to 220°C combined with the

variation in fabrication time from 5 h to 24 h. It was concluded that both prolonged heating at low temperature and short periods of time at high temperature can reduce the strength of the adhesive joints to a certain extent.

4.2 Experimental

4.2.1 Material

In order to minimise complexity of the interface to be investigated, the choice of the materials was limited to uncoated glass fibre and homopolymer polypropylene. Boron free uncoated E-glass fibres (Ave. diameter = 17.5µm) were supplied by Owens Corning-Vetrotex and commercial isotactic homopolymer polypropylene PP 579S (PP47) with melt flow index = 47 g/10 min at 230°C and 2.16 kg was supplied by Saudi Basic Industries corporation (SABIC).

4.2.2 Single fibre composites

The interfacial shear strength (IFSS) of GF-PP47 was measured by using laboratory-developed microbond and single fibre pull-out techniques. The specific procedure to prepare the samples for microbond and pull-out tests and details of how to conduct both tests have been described in chapter 3. Initially unaware of the severity of PP degradation during sample preparation, the formation of PP microdroplets for the microbond test was originally carried out in air. Various factors, including knife edges, microvise gap, glue type and effect of solder iron, had been investigated previously to account for inconsistent results with large scatter in them and residual resin left around the debonded area on some fibres. None of these

factors seemed to show a marked effect on the measured IFSS in a single set of data. For instance, PP droplets sheared off by knife edges vs. PP droplets above them, gel superglue vs. liquid superglue, use of solder iron vs. without using it. Further review of the results gathered from all sets of data suggested that PP droplets may experience severe thermo-oxidative degradation under the applied conditions for their formation.

To verify this hypothesis, PP droplets were also formed under nitrogen. Owing to lack of a nitrogen purged oven for making microbond samples under nitrogen, we used a small metallic chamber and drilled a hole on its lid to let the nitrogen flow into the chamber, where the samples were kept. The chamber was then transferred into the oven and heated at 220°C. The temperature inside the chamber was continuously monitored by a thermocouple and the nitrogen flow was controlled by a flow regulator. This experimental setup is schematically presented in Figure 4.4.

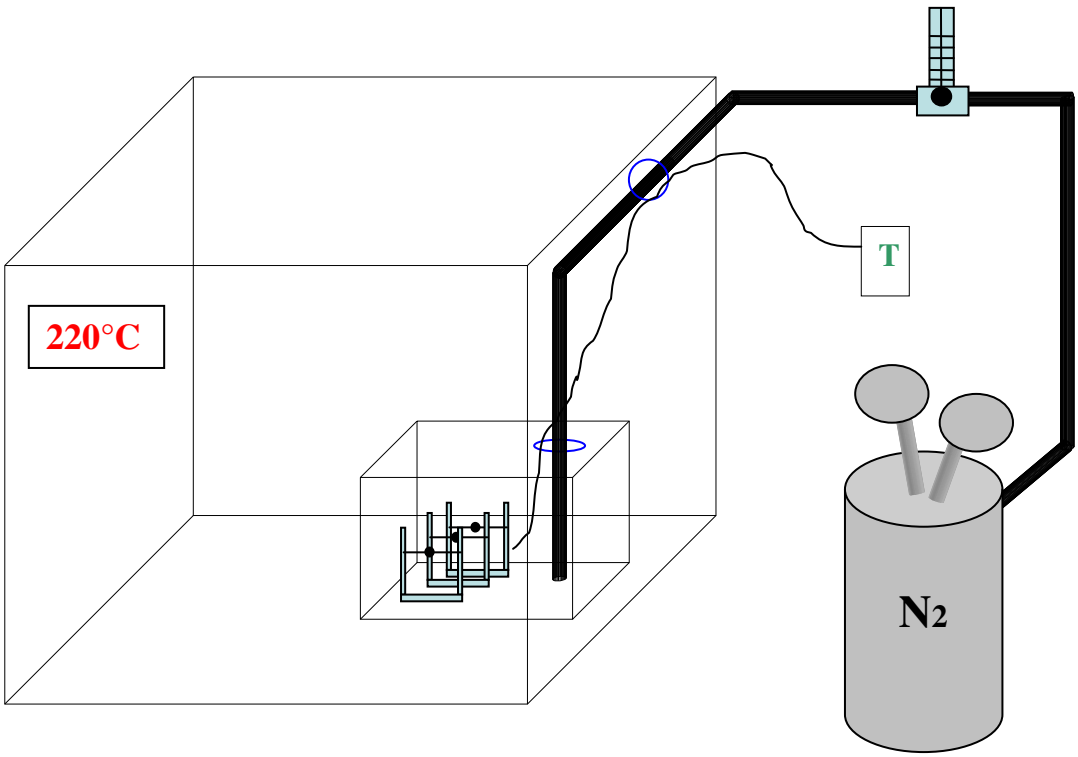

Fig. 4.4 Illustration of the setup for droplet formation under nitrogen

In order to avoid any unexpected complexity, a group of metal frames were made to replace the cardboard as the sample holder, which is shown in Figure 4.5 together with other details about this sample preparation. Rapid cure Araldite epoxy was applied on the metal frame to secure the multiple fibres, on which a number of isolated PP resin droplets could be formed. The chamber could accommodate 10 of these metal frames. To seal the chamber, sealing tape was wound around the joint line between the box and the lid. The lid had two holes. One was located in the centre as the inlet of the gas and the other was at one of the corners to allow the thermocouple to stick into the chamber. Before the chamber was heated in the oven, it had been fully purged with nitrogen to make sure there was no air trapped inside the chamber as seen in Figure 4.5(c). The nitrogen travelled into the chamber through a copper pipe, which was coiled to enable the nitrogen to sufficiently heat up before it entered the chamber as shown in Figure 4.5(d). The nitrogen flow rate was maintained at 150ml/min and samples were heated in the chamber until some droplets were formed. It was found that it became very difficult to form symmetrical PP droplets around the fibres under nitrogen at 220°C even after a prolonged period of heating. This will be discussed in the Results and discussion section. The samples cooled down at ambient temperature immediately after the chamber was moved out of the oven. Single fibres with PP droplets on them were retrieved from the metal frame and secured on to standard cardboard test frames. The process for the measurement of sample dimensions and IFSS via the microbond test remained the same as described in chapter 3.

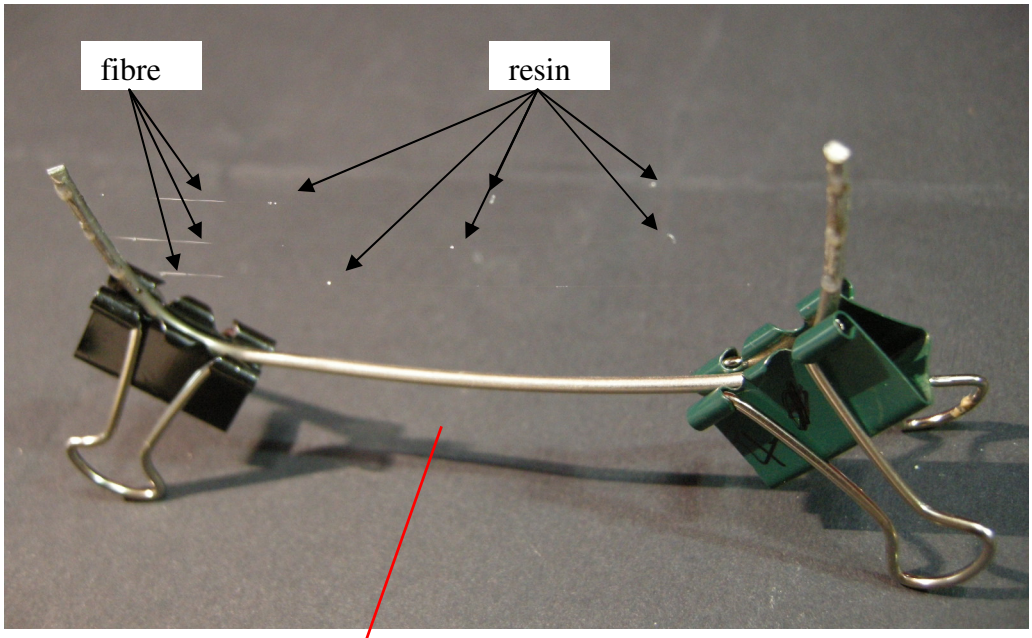

(a)

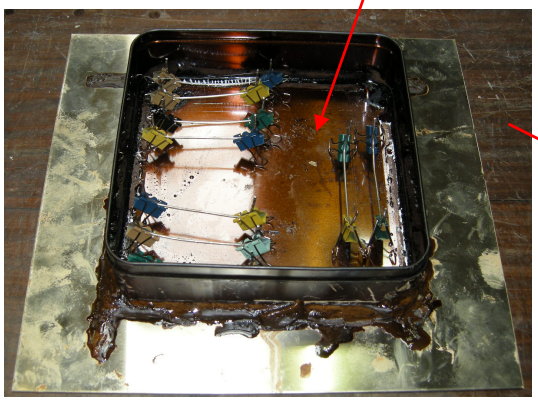

(b)

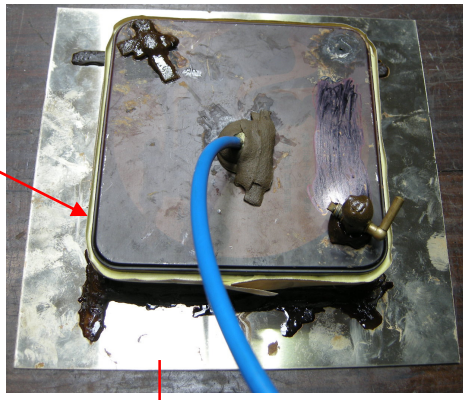

(c)

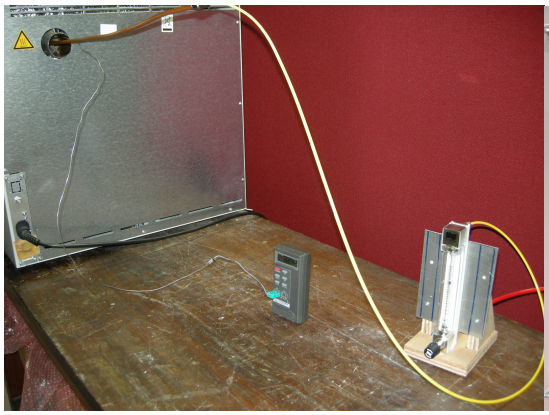

back view

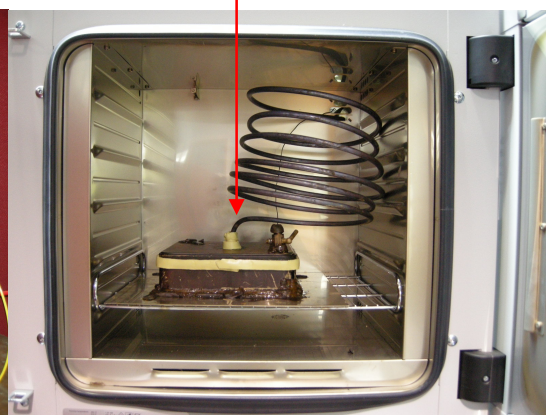

front view

(d)

Fig. 4.5 Photos for presenting the procedure of forming PP microdroplets on glass fibres under nitrogen

4.2.3 Hot stage microscopy

In order to better understand PP microdroplet formation and degradation, a transmitted light optical microscope equipped with a Mettle FP 82 hot stage was employed to visualise the formation of PP microdroplet on a single glass fibre and the dimensional change of the droplet during heat treatment. A single glass fibre was suspended slightly above a glass slide and secured with the aid of plaster. A PP fibre was then deposited on the surface of the glass fibre as seen in Figure 4.6(a). The sample was inserted into the hot stage, where it was heated rapidly from ambient temperature up to 220°C in air as shown in Figure 4.6(b). Time started to be registered when the temperature reached 218°C. For those droplets whose formation had completed within the first minute, a series of photographs of the droplets were then taken by the digital camera connected with the microscope at time interval of 30 sec for 60 min. The fibre embedded length and diameter of the PP droplet in each picture were then measured using the image analysis software, Image-Pro Plus as shown in Figure 4.6(c).

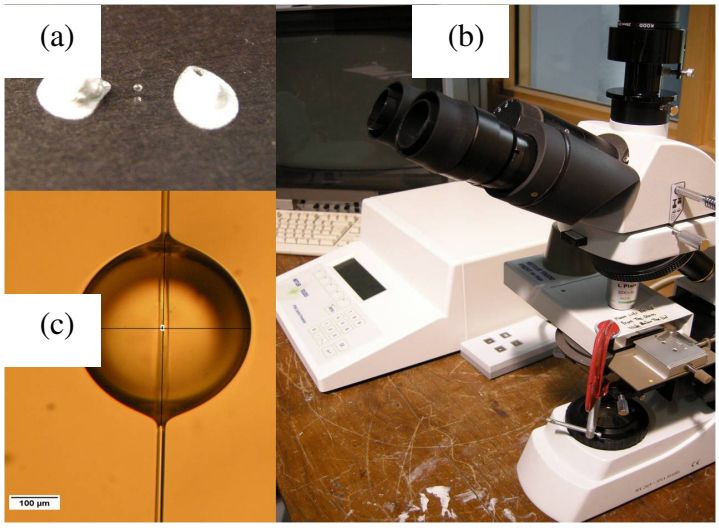

Fig. 4.6 Photos of (a) coiled PP fibre on a glass fibre secured by plaster on a cover slip, (b) hotstage setup, and (c) formed PP microdroplet with the measurement of its dimension

4.2.4 Nanoindentation test

GF-PP47 microbond samples with PP microdroplets that had different initial dimensions were heated at 220°C in air and nitrogen respectively. The mechanical properties of these droplets were then measured by an Agilent Nano Indenter G200 equipped with the continuous stiffness measurement (CSM) technique. In the conventional nanoindentation test, the measurement of contact stiffness is made just at the point of unloading, whereas the CSM technique offers a direct measure of dynamic contact stiffness at any point during the loading portion of an indentation test by imposing a small sinusoidally varying force, which is added to the nominally increasing load, on the indenter as illustrated in Figure 4.7 [32].

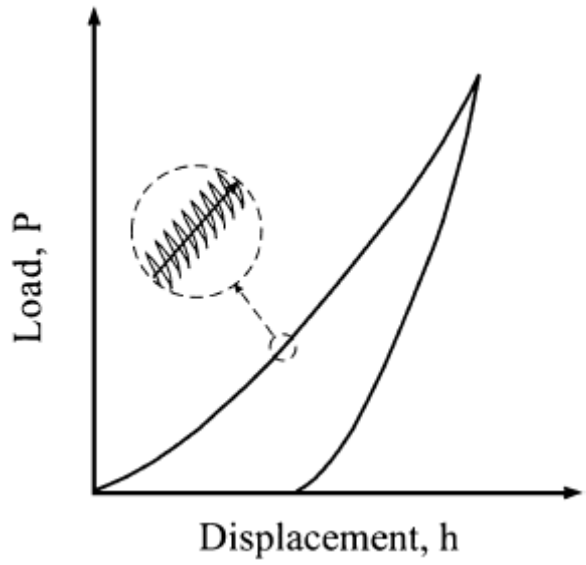

Fig. 4.7 Schematic of the CSM loading cycle [32]

The force oscillation and the relevant displacement response of the indenter allow Young's modulus and viscoelastic properties of the resin droplet to be continuously probed as a function of indentation depth. If the oscillating force is $P(t) = P_0 e^{i\omega t}$, in which P_0 is the force amplitude and ω is the harmonic frequency, the assumed

particular solution for the displacement is $h(t) = h_0 e^{i(\omega t - \theta)}$, in which θ is the phase angle between the applied force and resultant displacement. The ratio of these two can be written as

$$\frac{P(t)}{h(t)} = E_1 + iE_2 \qquad (4.1)$$

and

$$\frac{P_0}{h_0} = \left(E_1 \cos\theta + E_2 \sin\theta\right) + i\left(E_2 \cos\theta - E_1 \sin\theta\right) \qquad (4.2)$$

where $E_1 = K_s + S - m\omega^2$ and $E_2 = \left(C_i + C_s\right)\omega$ deduced from the mechanical model for nanoindentation as shown in Figure 4.8 [33].

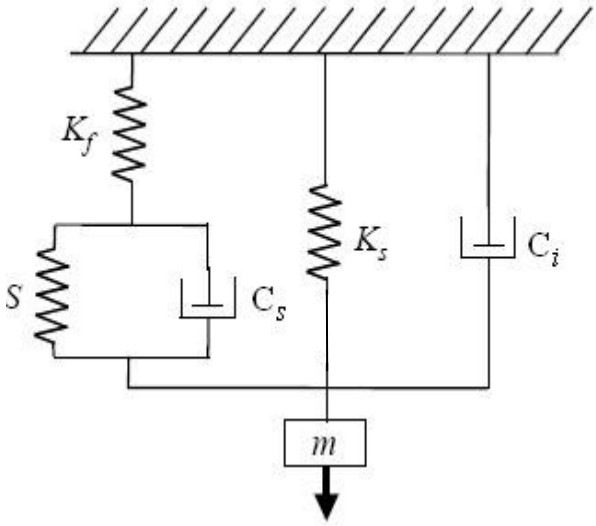

Fig. 4.8 Mechanical model for nanoindentation [33]

From Equation (4.1), we have

$$\tan\theta = \frac{E_2}{E_1} \qquad (4.3)$$

and

$$\left|\frac{P_0}{h_0}\right| = \sqrt{E_1^2 + E_2^2} \qquad (4.4)$$

From the equations above, the contact stiffness, S, can be obtained by

$$S = \left|\frac{P_0}{h_0}\right| \cos\theta + m\omega^2 - K_s \qquad (4.5)$$

The storage modulus of the polymer determined through nanoindentation is

$$E' = \frac{S}{2\beta}\sqrt{\frac{\pi}{A}} \qquad (4.6)$$

where β is a constant that depends on the geometry of the indenter and A is the projected contact area, which is determined as a function of contact depth [33].

In this work, the microbond samples were first secured on a highly stiff substrate. The specimen was then placed into the indenter and the top area of each droplet was located as the testing field seen in Figure 4.9(a).

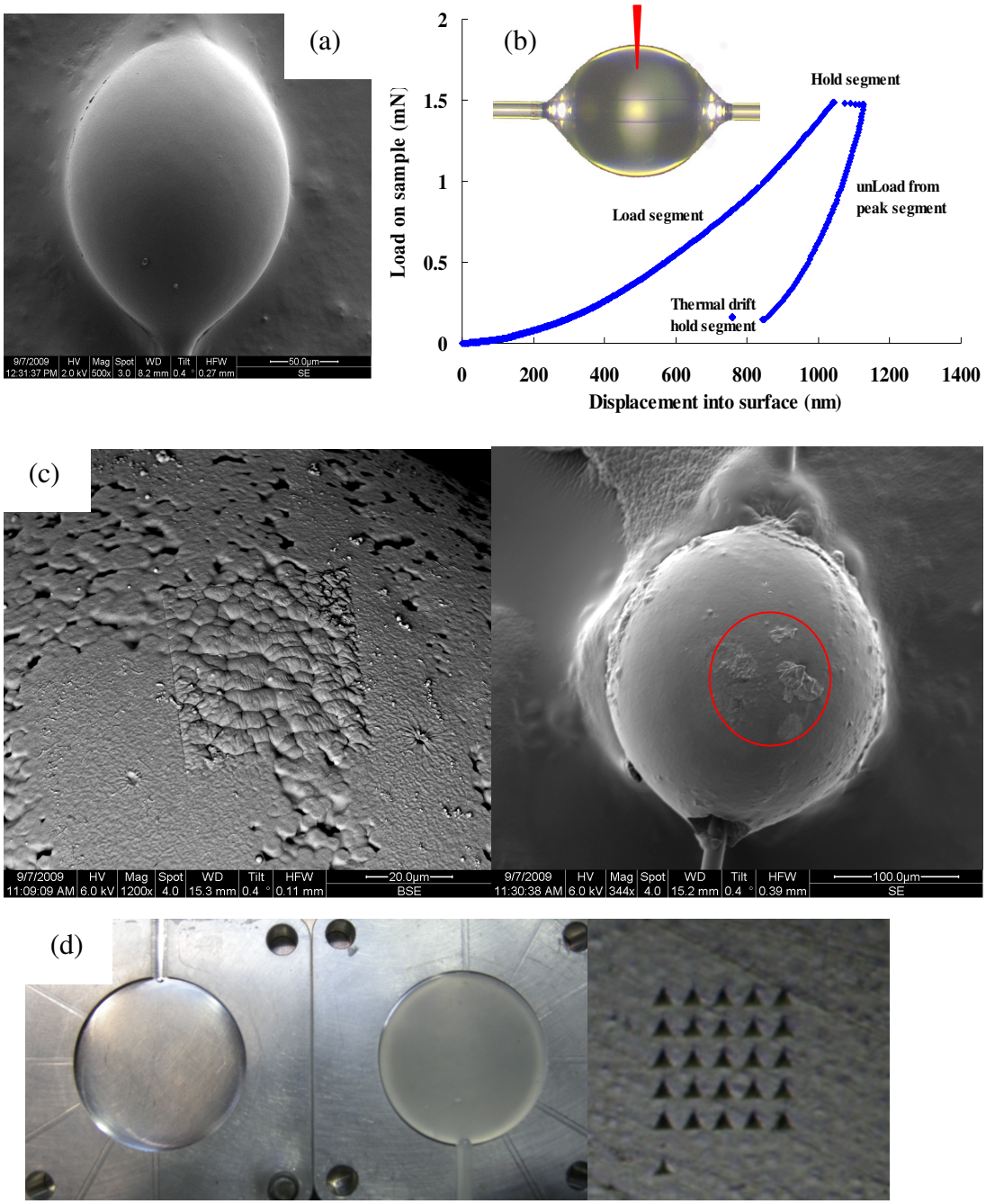

Fig. 4.9 (a) SEM photo of a sample for the nanoindentation test, (b) load vs. displacement curve during testing, (c) samples with porous and contaminated surface, and (d) injection moulded PP47 disc and indents after the nanoindentation test

The indentation test was conducted with maximum indentation depth and spacing division set to 1µm and 20 µm respectively throughout all the samples. The force oscillation had the frequency of 45 Hz. Figure 4.9(b) shows a typical load-

displacement curve for the nanoindentation test, which exhibits the following test segments:

1. Load until the penetration depth reaches 1µm.

2. Hold the peak load constant for 10 seconds.

3. Unload the force on the indenter until the applied force becomes 10% of the peak force.

4. Hold the load on the indenter constant for 100 seconds

5. Withdraw the indenter completely.

Prior to the test, samples were carefully chosen to offer a smooth surface. Figure 4.9(c) presents an example of samples that should not be used in the nanoindentation test because of surface porosity and contamination. Complexity could arise from the curved surface of PP microdroplets and nonhomogeneity in their mechanical properties from the surface to the core. Therefore, the data in the defined depth range from 600 µm to 1000 µm were chosen to calculate the mean values. At least 6-9 measurements were carried out on each PP microdroplet to obtain the average values for its mechanical properties. The same measurements were also made on the injection moulded PP samples with flat smooth surface to establish reference values. The sample and indents can be seen in Figure 4.9(d). The tested samples were then examined using ISAAC Quanta 200F field-emission environmental scanning electronic microscope (SEM) to observe the indents. With SEM in combination with

energy dispersive X-ray spectroscopy (EDX), quantitative elemental analyses were also conducted on the tested samples.

4.2.5 Thermo-oxidative degradation of PP

To understand how the thermo-oxidative degradation of PP would affect the measured IFSS, the effect of degradation on thermo-mechanical properties of PP needs to be evaluated. It was not possible to do this with degraded PP microdroplets by using normal thermal analysis techniques (e.g. DMA and TMA). Thus, a number of PP rectangular bars were treated under a thermo-oxidative environment. These samples were oxidised and degraded to different extents by varying the duration of the treatment. The thermo-oxidative treatment was carried out on a hotplate at approximately 220°C. The sample dimensions were determined by the channel formed by 5 pieces of microscope glass slides as shown in Figure 4.10.

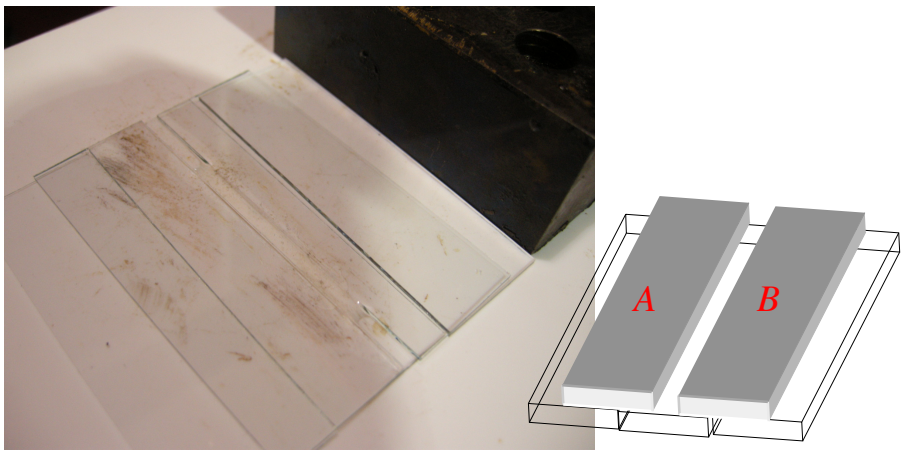

Fig. 4.10 Arrangement of glass slides for making PP sample bars

The injection moulded PP bars were used as the initial material rather than PP pellets because PP pellets could cause many air bubbles to be trapped in the sample bars and

these air bubbles may have adverse effect on thermo-mechanical characterisation. The PP bars first melted in the channel with an opening wider than expected sample width. This was because as the degradation proceeded the exposed upper surface gradually sank due to the evaporation of degraded material and formed a concave because of the adhesion between the melt and inner sides of both top glass slides *A* and *B*. This could strongly affect the three-point bending test in DMA and thermal expansion measurement in TMA since in both cases having a pair of parallel flat surfaces was a critical requirement for the sample geometry. Although a flat surface may also be obtained through polishing away the material from the top, removal of this part of the material can disrupt the basis of comparison established by the heat treatment due to the fact that the degraded PP samples may no longer be homogeneous after thermo-oxidative treatment and a gradient of severity of oxidation and degradation through the thickness of the sample might exist. In this work a flat surface was created simply by slowly push the glass slides *A* and *B* towards each other (i.e. reducing the melt width). This forced the PP melt move towards the middle of the channel and in turn raised the concave surface. The flat surface was then obtained by putting the sixth glass slide on the top of the melt. Another advantage of having a flat surface in such way was to produce samples with exactly the same thickness, which was an important parameter for a three-point bending test. The samples made by this method had dimensions of width= 4.00±0.32 mm and thickness= 1.01±0.03 mm. The treatment duration varied from 0 min to 60 min and after that the PP melt cooled down at ambient temperature. The sample was weighed using the Mettler Toledo analytical balance before and after the treatment to yield the weight loss due to the polymer degradation. Each sample was further

subdivided into 3 pieces for the three-point bending test in DMA Q800 as shown in Figure 4.11(a), the measurement of CLTE in TMA Q400, and crystallinity measurement in Mettler Toledo TGA/DSC 1 respectively.

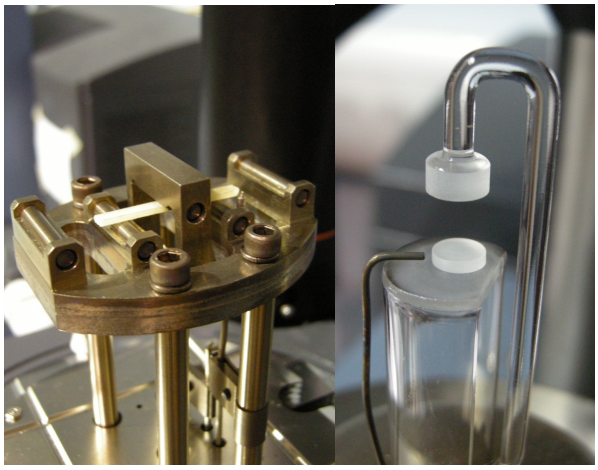

(a) (b)

Fig. 4.11 Photos of experimental setup in DMA and TMA

The experimental settings for these tests were the same as those adopted in the measurement of non-degraded PP in chapter 2. The preload in TMA was set to be 0.04 N to minimise the influence of exerted force on the measurement of CLTE. Even with this small load the elastic strain of PP samples with different levels of degradation would vary from 1 to 31 μm/(m·°C) in the course of scan.

Apart from producing degraded PP samples on the hotplate, thermo-oxidative degradation of PP was induced also in TGA Q50, which gave a much better control of the thermo-oxidative environment and accurate evaluation of the weight loss. Initial weight of each sample was kept the same and degradation was controlled based on the weight loss this time. To obtain the sample with the consistent shape, Mettler Toledo standard Aluminium crucibles with diameter of 6 mm and depth of 1.6 mm were used as the sample holder. Non-degraded samples were made at 220°C

under nitrogen and degraded samples were treated at 220°C in air. The samples were tested in TMA Q400 to obtain the CLTE of PP as shown in Figure 4.11(b). TGA-treated samples gave the curved surface, which would reduce the contact area between the surface and the TMA probe and in turn increase the localised stress around the edge. As the temperature increases, the edge could go through a significant deformation, which would cause a great error in the measured thermal expansion. Therefore, these samples had to be polished to obtain the flat smooth surface.

4.3 Results and discussion

4.3.1 IFSS measurement of GF-degraded PP

Figure 4.12 contains all the microbond data before realising occurrence of the thermo-oxidative degradation to PP in microbond samples made in air. In other words, all the data in Figure 4.12 come from thermo-oxidative degraded microbond samples made and tested under various conditions as mentioned in the figure caption.

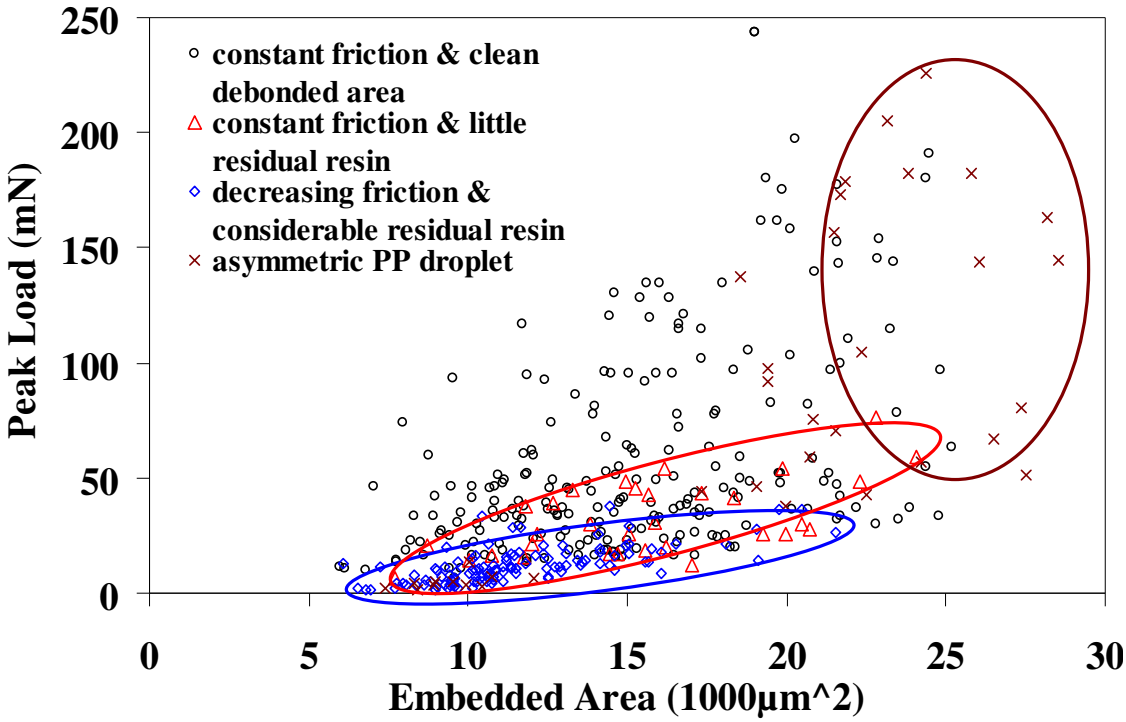

Fig. 4.12 Plot of peak load vs. embedded area of microbond samples made and tested under different conditions involving microvise modification, the use of solder iron, gap between the fibre and knife edges, and types of super glue

Although the entire data look like a messy cloud, some interesting implications may still worth being pointed out in this plot. First of all, the measured IFSS in Figure 4.12 lies in a very wide range of values stretching from 1 MPa up to 8 MPa. Such a big uncertainty suggests that the factors that dominatingly affect the results were actually not under the control during the experiment. Second of all, the data points represented by the green cross indicate that the largest symmetrical PP droplets that could be formed on a single glass fibre under the experiment conditions had an embedded length ~460µm. Thirdly, it can be seen that there is an overall tendency of increasing IFSS with the increase of the embedded area (i.e. the droplet dimension) and the data can be divided by whether the dynamic friction after debonding is constant or decreasing and whether there is residual PP left behind on the debonded

area. In fact, the decreasing friction was expectedly accompanied by obvious residue resin on the fibre. In most cases constant dynamic friction means a clean debonded area left on the fibre, although in some cases tiny amount of residue resin does not seem to necessarily correspond to decreasing friction. Residual resin is usually regarded as an indication of good adhesion between the fibre and the matrix as it implies that the intrinsic shear/tensile strength of the matrix is actually lower than the interfacial shear/tensile strength and the matrix fractures before the interface/interphase. Thus, the matrix strength is usually considered as the practical limit to the adhesion enhancement for a given composite. However, the results in Figure 4.12 show the opposite situation, where the data related to the matrix failure actually forms the lower boundary of the plot. Since many microbond samples with small resin droplets failed cohesively, this might arise from different load projection at fibre entry to the matrix due to different contact angle as schematically shown in Figure 4.13

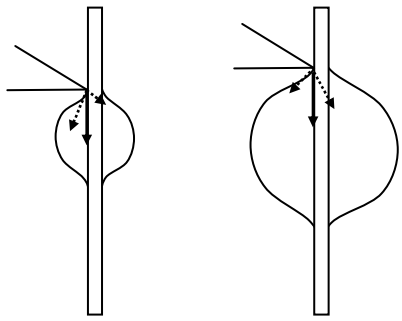

Fig. 4.13 Schematic presentation of load projection at fibre entry to resin droplet with different size

It seems more likely for a small droplet to fail in a mixed mode and for a big droplet to fail in interfacial shear. In practice, however, the very top part of meniscus should experience highest stress concentration in this work and may undergo considerable

deformation. Consequently the shape edge of shearing plate may no long apply a point load as it does in the beginning but a line or even area load. This would make little difference in the load projection for different resin droplets. Another interpretation to the data in Figure 4.12 is that PP droplets have undergone severe thermo-oxidative degradation during the sample preparation and that the mechanical properties of PP have seriously deteriorated.

In order to further confirm the effect of thermo-oxidative degradation of PP on the measured IFSS, we carried out the microbond test on the samples with the 4 min and 6 min heating at 220°C in air. A plot of peak force vs. embedded area obtained from 4 min set is shown in Figure 4.14.

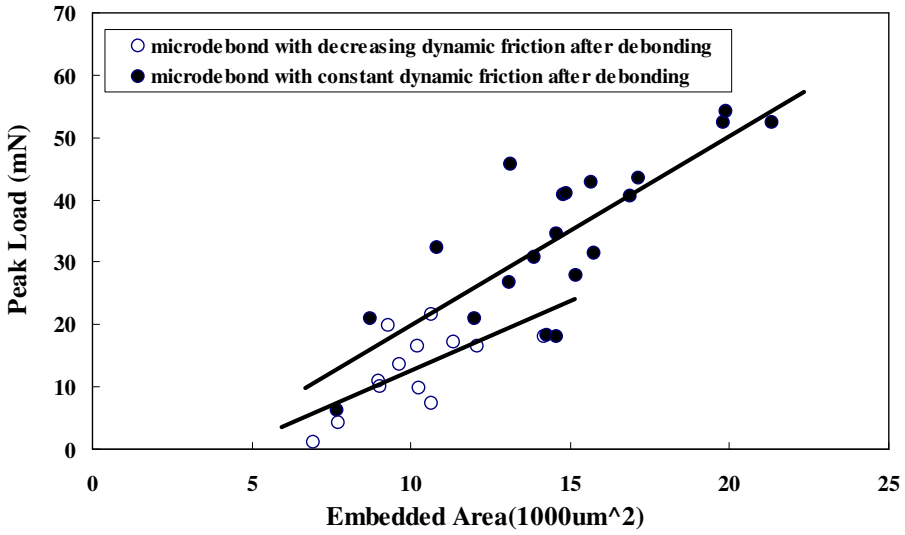

Fig. 4.14 Plot of peak force vs. embedded area measured for bare GF in PP47 using microbond test

Apparently the data can also be divided into two groups according to whether there is constant or decreasing dynamic friction after debonding. This division seems to be related to the droplet size. Relatively small resin droplets are more likely to give

decreasing dynamic friction whereas larger droplets exhibit constant friction after debonding. Interestingly these two groups also appear to fall on similar trend lines as shown by the solid fitting lines, neither of which go through the origin. Further microscopy observation of tested specimens from microbond tests has divided these two distinctive situations into two categories (A and B) as shown in Figures 4.15 and 4.16.

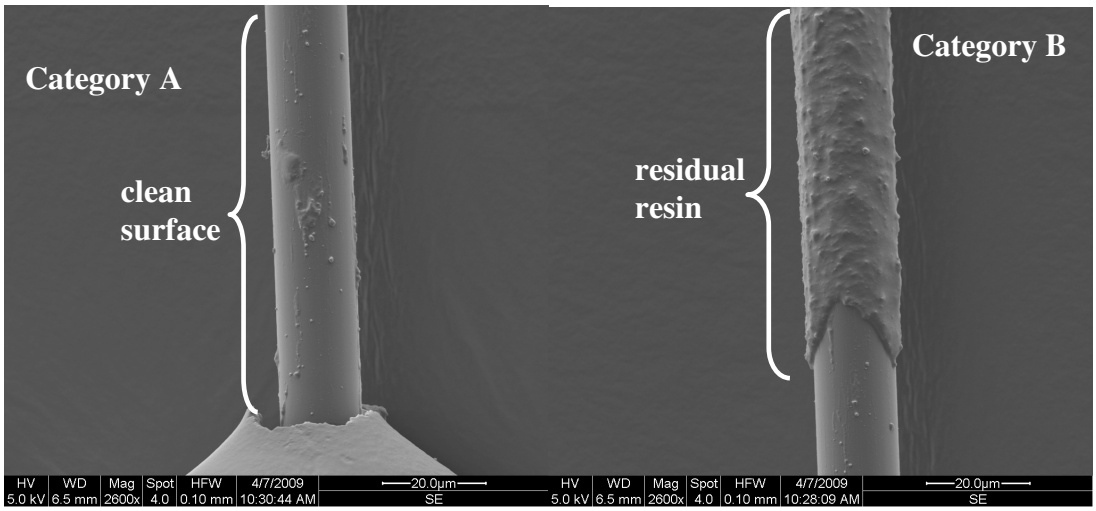

Fig. 4.15 SEM photograph of different debonded fibre surfaces

About 2-7 µm thickness of residual resin was observed around the debonded area of the fibres in group B, which corresponds to decreasing friction after the peak load as seen in Figure 4.16.

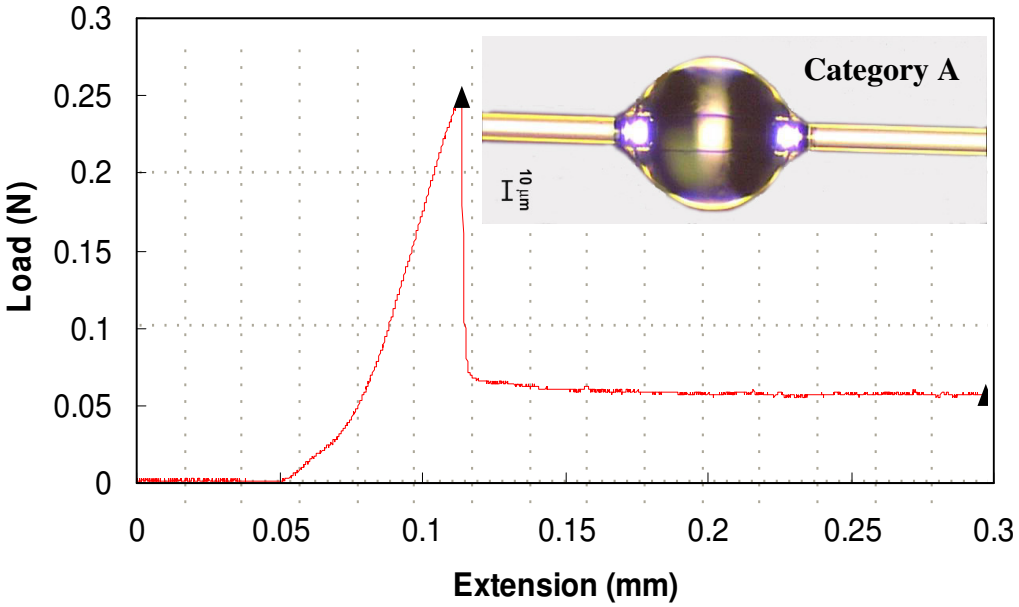

(a)

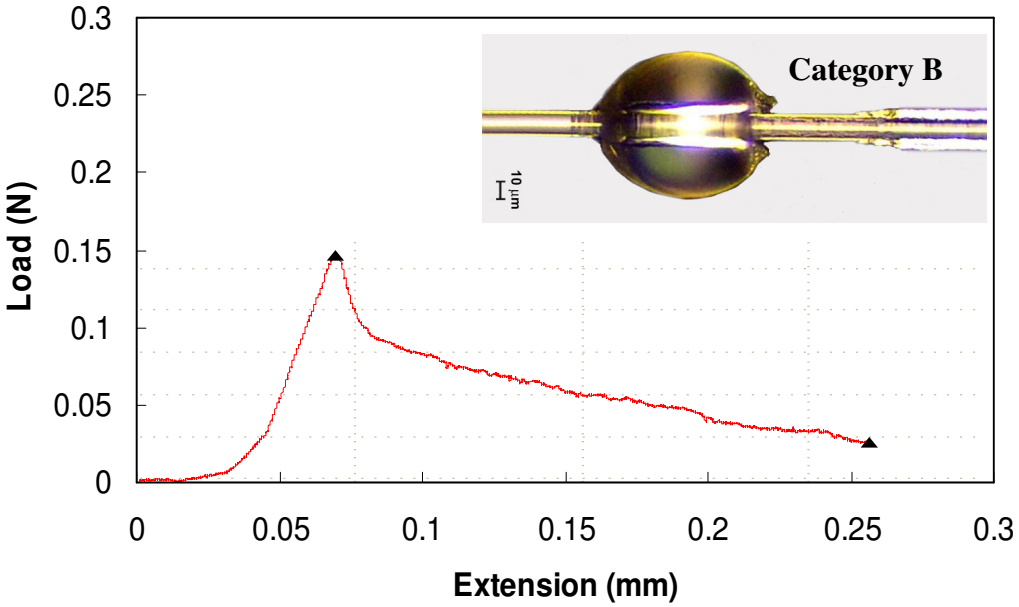

(b)

Fig. 4.16 Typical load vs. extension plots of tested samples of (a) category A and (b) category B recorded in the microbond test

Very occasionally tested samples exhibiting category A behaviour were also observed with residual resin but at a much lower level. Most samples in the category A exhibited a clean debonded fibre surface after the test. The observation of matrix

indentations caused by knife edges (see Figure 4.17) suggests that such a difference did not arise from the knife edges, which were spaced 20 μm away from each side of the fibre in these tests.

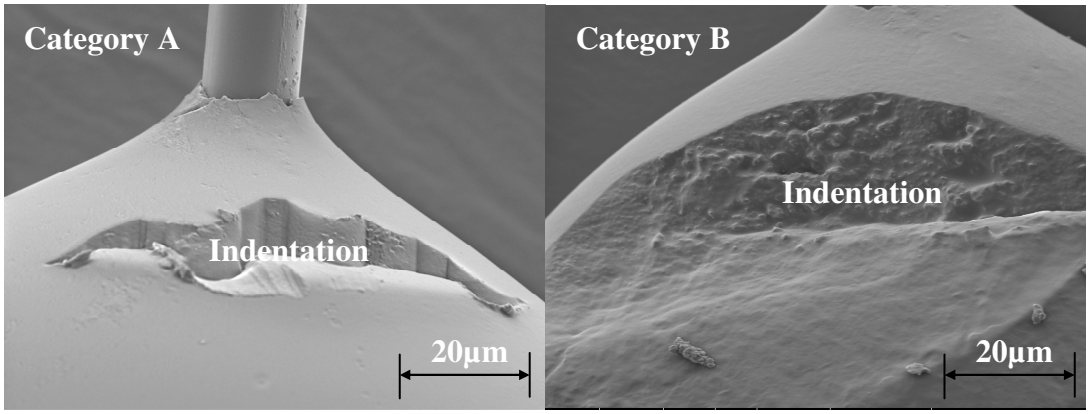

Fig. 4.17 SEM photograph of different indentations caused by knife edges

In addition, the fracture surfaces exposed via the indentation are different between the two categories. Samples in category A undertaking a higher peak load exhibited a less severe indentation compared to those in category B with the similar embedded area. These observations may imply that the difference between these two groups is caused by a difference in the mechanical properties of the matrix. The failure mode in B is usually referred to as cohesive matrix failure while in A it is termed as adhesive interfacial failure. The former is generally considered to be clearly indicative of good adhesion relative to the latter due to interfacial modification deliberately made in same work [34]. However, in this case there had been no modification of the interface in any case, implying all samples should exhibit a similar level of adhesion. Cohesive matrix failure may also be caused by deterioration of mechanical properties of the matrix, from which good adhesion with fibres could hardly be expected. Thus we must seek an explanation for these different behaviours of the test parameter.

Consequently another set of microbond tests was conducted with variation of the thermal history in matrix by changing its duration of stay in the oven from 4 min to 6 min at the same temperature (i.e. 220°C). The results are shown in Figure 4.18.

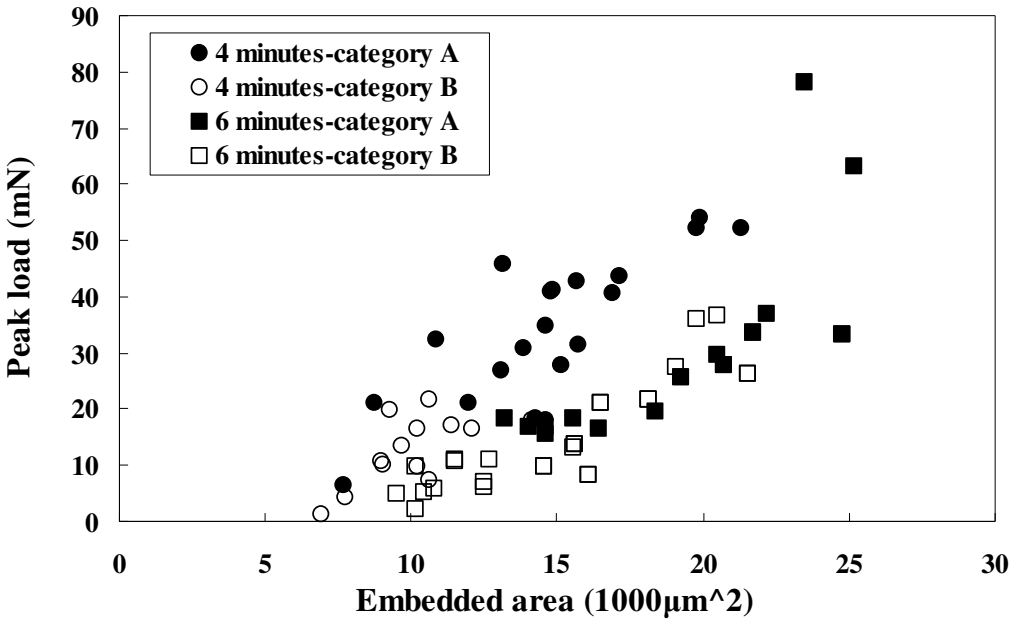

Fig. 4.18 Comparison of effect of different thermal loads on the IFSS of bare GF-PP47 measured using microbond method

It can be seen that the extra 2 min heating has made a significant impact on the IFSS value obtained for bare GF and neat PP47 studied in the present work. The 6 min set has an overall lower peak load than the 4 min in the same range of droplet size. Few tested samples in category B could be found in the 4 min data set, while about half of tested samples appears as category B in the 6 min group. In both data sets the tested samples in the category B tend to emerge from relatively small droplets. As droplet size increases it becomes more likely to have tested samples in category A. In comparison with two data sets, such a tendency has also been modified by different thermal loads. It should be noticed in the 6 min group that the peak load seems to

non-linearly increase with the embedded area and the data from the largest droplets tend to join into the 4 min data set trend. It can be seen that the additional thermal load has not only changed adhesive interfacial failure into cohesive matrix failure but also considerably reduced the value of IFSS. The average values of sum of individual IFSS for different categories of microbond specimens in both 4 and 6 min sets are shown in Figure 4.19.

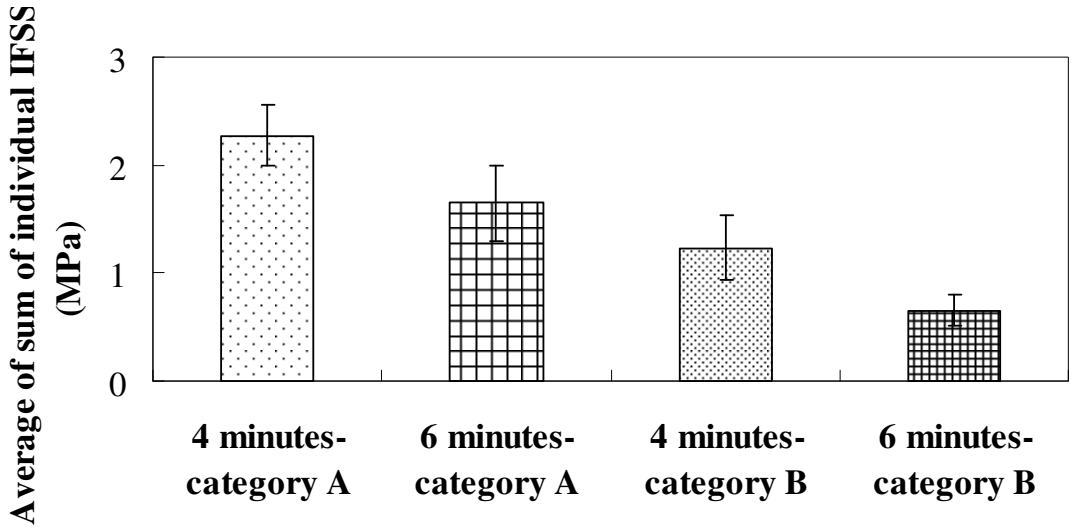

Fig. 4.19 Comparison of average values of sum of individual IFSS between different categories of microbond samples in 4 and 6 min groups

It can be seen that the additional 2 min heating has lowered the average value in the 4 min category A set from 2.3 MPa down to 1.6 MPa in the 6 min category A and the value in the 4 min category B from 1.2 MPa to 0.7 MPa in the 6 min category B. Statistic analysis of the data in Figure 4.18 using the Two Sample *t*-test indicated that the reduction in average IFSS by both increased treatment time (4 min vs 6 min with fixed category) or a change of category (A vs B at fixed treatment time) was statistically significant at the 95% confidence level. Tested samples in category B of both sets generate the values in Figure 4.19 around the shear yielding strength (~1

MPa) for atactic polypropylene [35], exhibit residual resin on the tested fibres, and apparently possess a weaker region in the matrix with respect to the interface.

The results of the IFSS and microscopy observation indicate that the variation in thermal conditions has strongly influenced the properties of the matrix. To examine this possibility, the embedded length normalised maximum slopes of load-extension curves recorded in microbond tests were estimated. Individual IFSS values vs. maximum slopes of corresponding load-displacement curves are plotted in Figure 4.20.

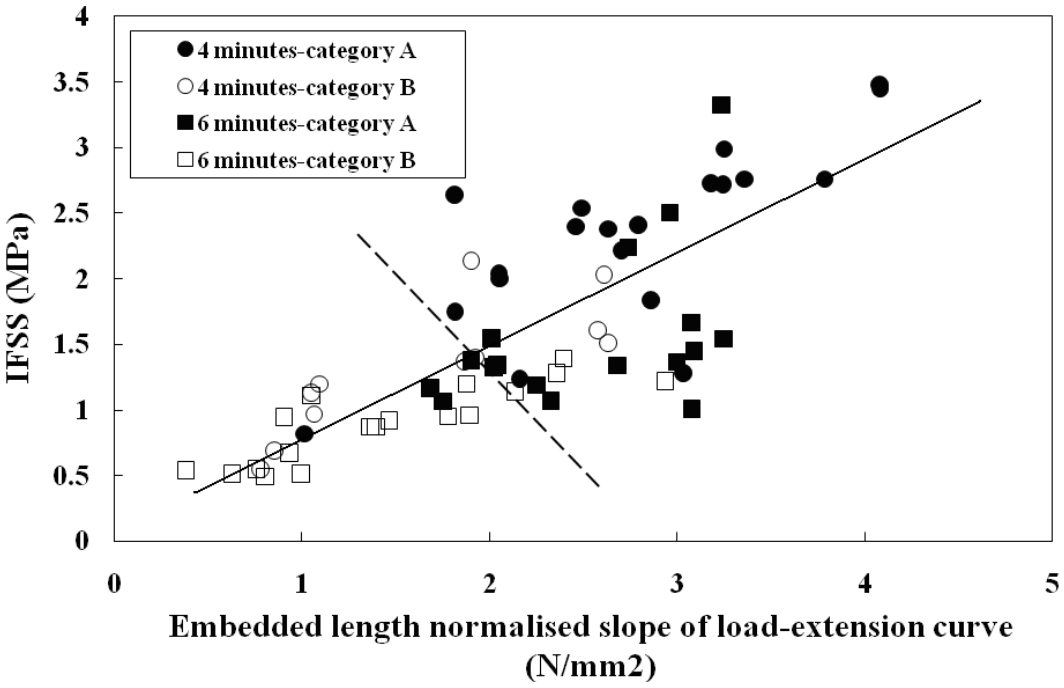

Fig. 4.20 Comparison of correlation between IFSS and slope of load-extension curve in microbond tests for 4 min and 6 min sets respectively. Dotted and solid lines are drawn to visually distinguish category A & B and 4 min & 6 min data sets respectively

The free fibre length was kept approximately the same throughout all tests. Thus the variation in slope of the load-extension curve should, to some extent, reflect changes in matrix stiffness, assuming the compliance of all other parts in the testing fixture

remain the same. It can be seen in Figure 4.20 that the measured IFSS tends to rise as the slopes of load-extension curves increase in both groups and overall, samples in category A of two groups with higher IFSS values also have higher slopes than those in category B. It is noticed that the situation in Figure 4.20 is analogous to that in Figure 4.18. Indeed, the fact that the data in Figure 4.18 clearly deviate from the origin and tend to intersect the positive axis of embedded area means that apparent IFSS increases as the increase in embedded area, or droplet size if neglecting the relative small variation in fibre diameter. Thus the combination of these two observations implies that the slope of load-extension curve increases as the droplet becomes bigger as shown in Figure 4.21. Consequently it appears that there may be a correlation between the IFSS and the PP stiffness.

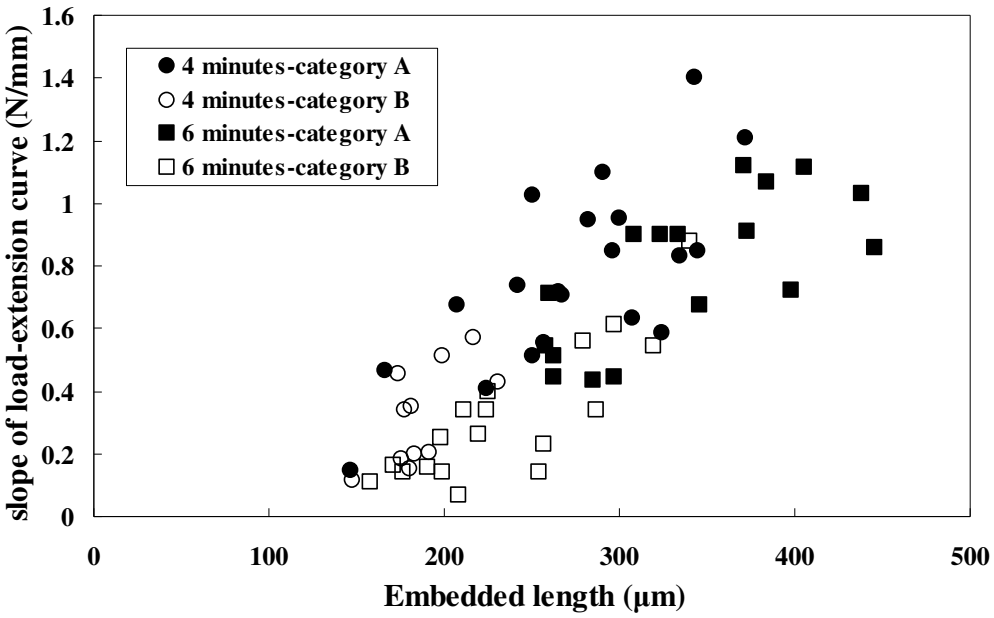

Fig. 4.21 Slope of load-extension curve vs. embedded length from the microbond test on bare GF-PP47

One possible explanation for these observation can be found in terms of a variation in matrix mechanical properties due to thermal oxidation and degradation. Small

polypropylene droplets are naturally more vulnerable to thermal degradation and more sensitive to oxidative attack at elevated temperature due to their relative high surface to volume ratio. Thus when the droplets with various sizes undergo the same thermal loads, the small ones may suffer from more severe thermo-oxidative degradation. As the tacticity along the polymer chain is reduced by either the addition of oxygen atoms on polymer chains or chain breakage, the degree of crystallinity can be expected to decrease. As a result, in both the 4 min and the 6 min sets the decrease in crystallinity caused by thermo-oxidative degradation during sample fabrication could lead to the degradation of PP47 mechanical properties. For relatively small droplets, this deterioration of mechanical properties was so severe that PP47 shear strength could be less than its interface strength with glass fibre, and cohesive matrix failure would then occur. As the droplets become bigger, it would be more possible for them to maintain sufficient crystallinity and in turn mechanical properties, which would provide a matrix shear strength higher than its interface strength with fibre. Interfacial failure would then have a higher probability to occur. When the thermal process was relatively mild (e.g. 4 min at 220°C), those droplets that would have failed in the matrix under a severe condition (e.g. 6 min at 220°C) were able to maintain sufficient mechanical properties and prevent the matrix failure during the test. Unlike most glass fibre-thermosetting systems, there may be little or no chemical reaction across the interface between the bare GF and neat PP. The compressive radial residual stress (CRRS) built around the interface during fabrication of thermoplastic composites is regarded as the major contribution to the stress transfer capability at the interface. The level of this radial stress at the interface depends on processing conditions and physical properties of the fibre and the matrix

such as their stiffness and thermal expansion coefficients. Although it is known that for most crystalline polymers, thermal expansion is depressed by crystal lattice constraints, in a thermoplastic polymer thermal expansion is strongly influenced by the strength of the secondary bonds between molecules [36]. For instance, thermoplastic polymer molecules held together by strong hydrogen bonds generally expand less than those held by dispersion bonds [36]. Therefore if more severe thermal degradation had happened to samples in the 6 min group, there would be much more amount of oxygen atoms in polymer molecules held together by strong hydrogen bonds between those polar atoms. This could lead to relative small CRRS at the interface of samples in the 6 min group and in turn lower IFSS values than those in the 4 min group. In addition less crystallinity in the 6 min group may lead to potential relaxation of CRRS in the matrix, which does not favour high IFSS.

4.3.2 Thermo-oxidative Degradation of PP and its effect on IFSS

In order to provide direct evidence of thermo-oxidative degradation of PP during the sample preparation for the microbond test, hot-stage microscopy was used to establish a degradation profile of PP microdroplets with different initial dimensions. Figure 4.22 shows a series of micrographs following the dimensions of a GF-PP47 microbond sample held at 220°C in air for 30 minutes.

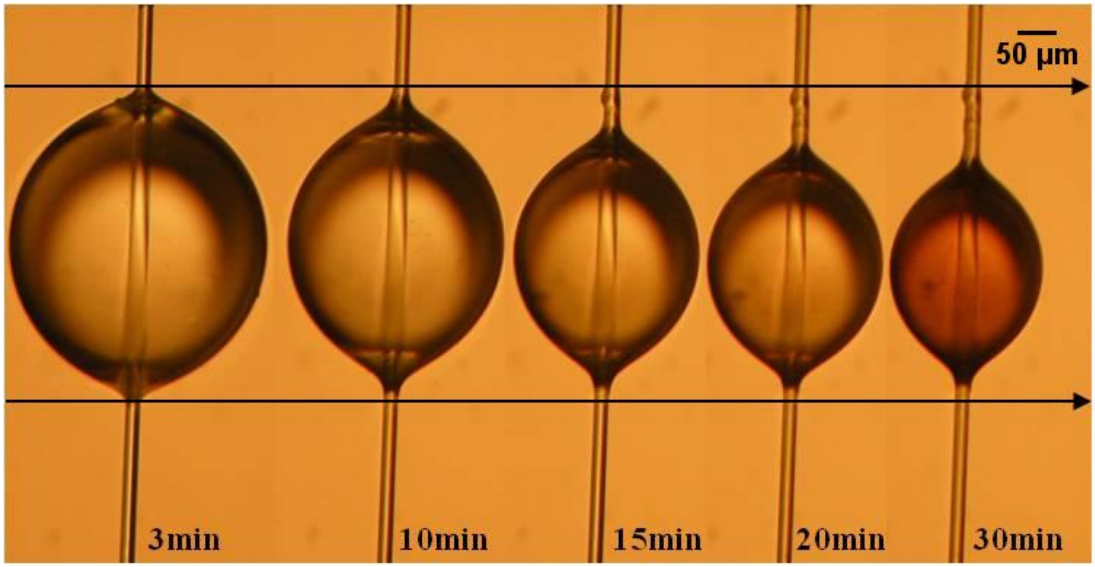

Fig. 4.22 Photographs of the GF-PP47 microbond sample heated at 220°C in air

It can be clearly seen that there is a considerable reduction in the volume of the PP droplet over this time. Even in the first 10 minutes the volume loss is significant. This evidently indicates that the PP droplet undergoes severe degradation during the sample preparation process, since this volume reduction can only be attributed to large scale evaporation of volatile products yielded from the degraded PP. It is well known that the thermal oxidation of PP leads to a step termed as chain scission, which involves the formation of a free radical at some point on the polymer backbone [3]. The chain scission produces small series of oligomers with a broad range of the number of carbons in the backbone. If this process is repeated successively in a polymer, the resultant products will become small enough to evaporate without further bond cleavage. Thus, thermo-oxidative degradation of PP initially leads to a decrease in molecular weight and ultimately weight and volume loss. Furthermore, the sample shows a marked colour change with time, which is also a typical sign of significant polymer degradation. It can be expected that such high levels of polymer degradation will also result in significant changes (reduction) in

the mechanical properties of the droplet. It is noticed in Figure 4.22 that the decrease in the transverse dimension of the droplet appears to proceed symmetrically with respect to the fibre, while the decrease along the droplet length (i.e. fibre embedded length) proceed to much greater extent on the upper part of the droplet than the lower portion. A small resin bump also emerges from the upper end of the droplet and remains on the fibre as the droplet length decreases. The observation of other samples indicates that the asymmetrical length reduction exists in each sample but preference to which part decreases faster does not seem to be consistent and the appearance of the resin bump is not consistent from sample to sample. The sensitivity of the droplet degradation to the initial droplet dimensions is examined in Figure 4.23 where the droplet dimensions were measured regularly during isothermal treatment at 220ºC in air.

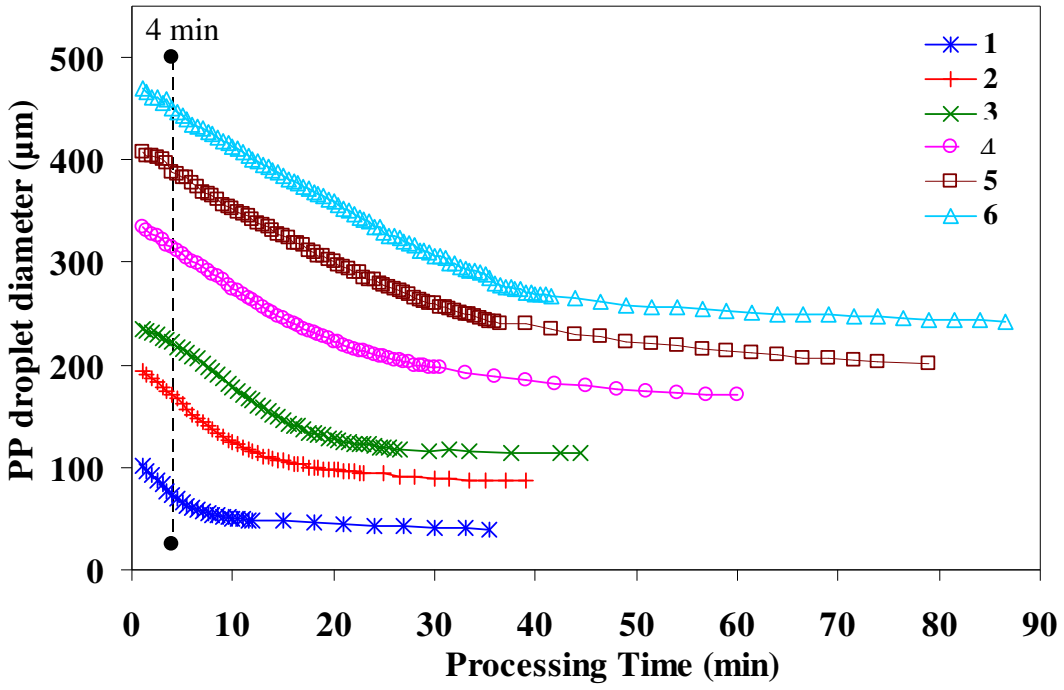

(a)

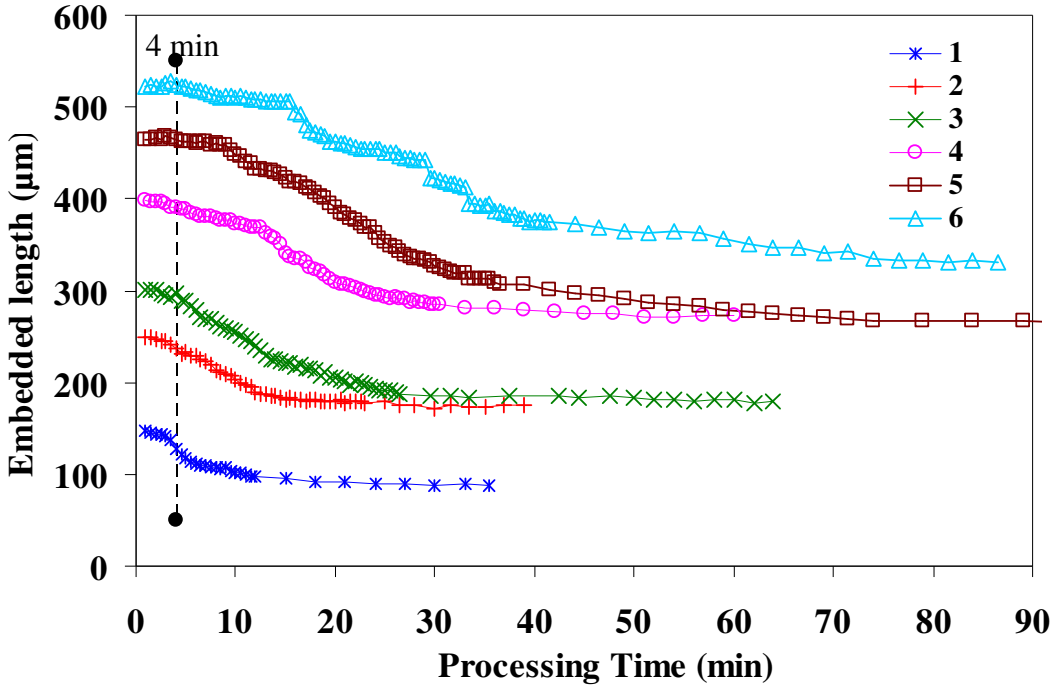

(b)

Fig. 4.23 Maximum diameter of PP microdroplet (a) and fibre embedded length (b) as function of time as PP microdroples are heated at 220°C in air

It can be seen in Figure 4.23(a) that the droplet diameter decreases immediately when time registration commences. Oxidation induction time cannot be observed in these data despite the fact that this commercial polymer contains a full anti-oxidant package. Diameter decreases linearly as function of time and gradually levels out. The reduction rate can be obtained from the slope of the linear segment in each curve and it varies with the initial dimension from 9.3 µm/min for the smallest droplet down to 5.3 µm/min for the largest one. This normalised initial rate as a function of initial droplet diameter is presented in Figure 4.24.

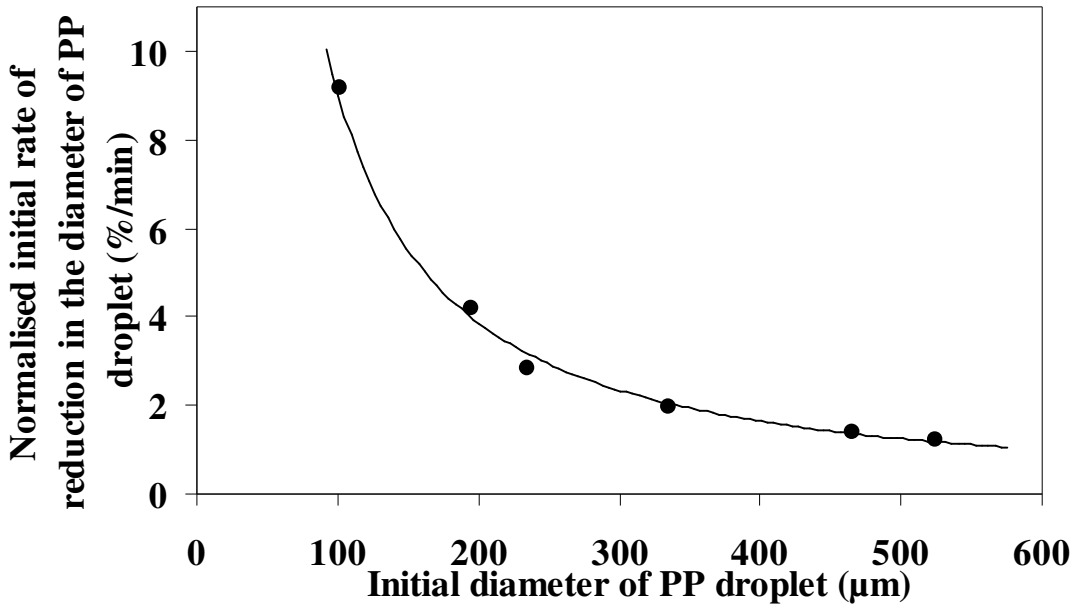

Fig. 4.24 Rate of reduction in the diameter of PP microdroplet as a function of its initial diameter

It is clearly seen that diameter loss in the PP microdroplet accelerates as the initial droplet diameter decreases and the relationship can be fit perfectly by the power law in the dimensional range of PP droplets studied in this work. If we consider the diameter loss as a reliable indication of degradation severity, the results in Figure 4.24 then suggest that relatively small PP droplets degrade faster than large ones. One explanation for this is surface-to-volume ratio (S/V). Small droplets possess a higher S/V and offer a greater percentage of polymer molecules exposed to the hot air. Consequently they are more susceptible to oxidative attack at elevated temperature and undergo more severe thermal oxidation and degradation within a given time. It is because the fast degradation rate that it takes less time for the diameter loss in small PP droplets to reach the plateau, where the degradation may be close to its maximum. Apparently such effective degradation time is related to the initial droplet diameter as well and can be obtained at the intersection of the tangent

at the inflection point with the plateau line in Figure 4.23(a). The linear correlation between the initial droplet diameter and the effective degradation time is presented by the fitting line that passes the origin in Figure 4.25.

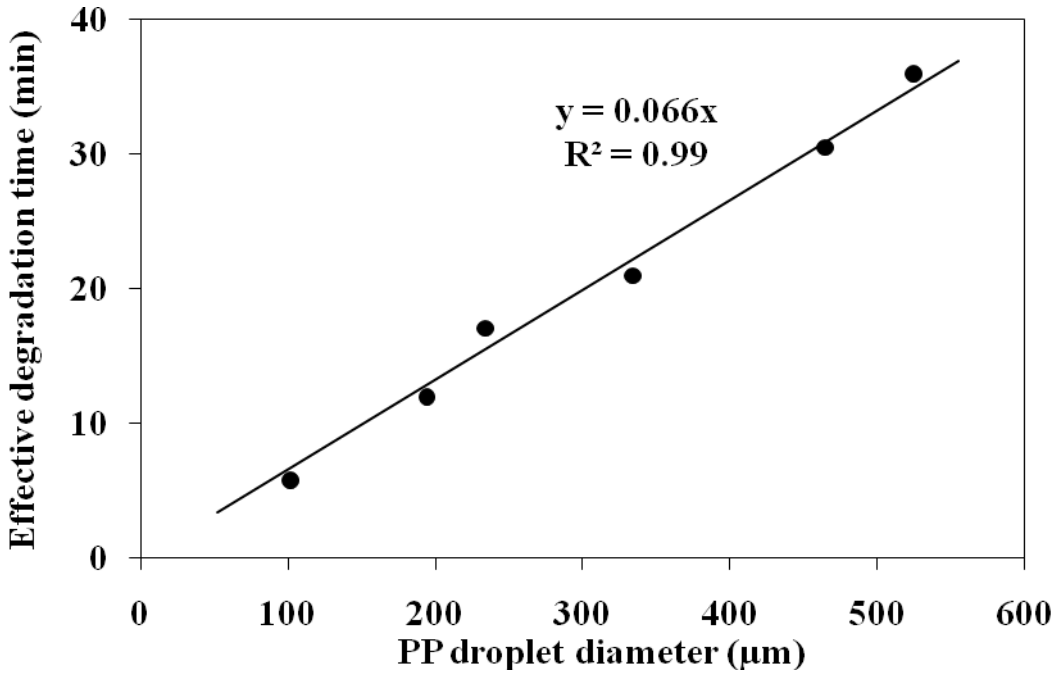

Fig. 4.25 Effective degradation time at 220°C as a function of initial diameter of PP microdroplet

This suggests that for a PP microdroplet with the diameter of 100 µm the completion time for its degradation at 220 ºC in air is only 6.6 min. It can be expected that as the temperature or oxygen concentration increase the effective degradation time for a given PP microdroplet will decrease further.

The change in the embedded length is apparently complicated by the presence of the glass fibre as seen in Figure 4.23(b). Unlike a uniform rate of the diameter loss, the reduction in the embedded length is inhibited in the beginning, showing a much slower decrease compared to the diameter loss. In addition, most curves exhibit kinks,

after which the reduction of embedded length increases to a rate comparable with diameter loss. The kink in each curve is found to coincide with the emergence of the resin bump in the corresponding sample. The example for such resin bump has been shown in Figure 4.22. This phenomenon may be explained by a combination of contact angle hysteresis and the effect of degradation. Contact angle hysteresis arises from the existence of energy barriers at the liquid front, manifesting the difference between advancing and receding angles. For example, removal of liquid from a drop on a horizontal planar surface will initially make the drop become flatter without moving its periphery, and the contact angle will become smaller. When enough liquid is removed, the drop front will suddenly retract. The angle at the onset of this sudden retraction is the minimum receding contact angle. In the case of the degradation of a PP droplet on a cylindrical fibre, the fast dimensional decrease in the transverse direction means a decrease of the droplet-fibre contact angle. It seems reasonable to assume that the surface tension of the glass fibre and interfacial tension between the fibre and the molten PP remain constant at least in the early stage of the heating process. It is also known that the oxidation of PP increases the surface tension of PP [13]. Therefore, the contact between three phases (i.e. air, PP melt, and solid glass) is in a nonequilibrium state. To attain the mechanical and thermodynamic equilibrium, the meniscus of the PP melt tends to move inwards along the fibre surface. Such movement will be impeded by the energy barriers at the melt front. Taking the melt elasticity into account, a shear stress could also arise from this tendency of fluid/fibre motion and the melt in the meniscus is in tension. While the contact angle continues decreasing, the PP in the meniscus degrades so rapidly that it gradually loses its mobility due to either good adhesion caused by polarising PP or

charring. The meniscus part that undertakes the most severe degradation is also expected to possess the lowest tensile strength. When the stress reaches this criterion, the movable PP melt then breaks with the meniscus followed by the fast retraction along the fibre axis. If degradation-induced shear stress does exist, it is very likely to be incorporated into the thermal residual stress formed during the cooling process. Consequently, it may slightly affect the absolute level of measured IFSS and it will certainly contribute to the scatter in the data. In order to examine the discussion above, the variation of calculated contact angle, θ, of the PP microdroplets, whose dimensional change is shown in Figure 4.23, is investigated in Appendix C.

In contrast with dimensional change in microbond samples made in hot air, Figure 4.26 presents the different behaviour of the samples made under nitrogen at the same temperature.

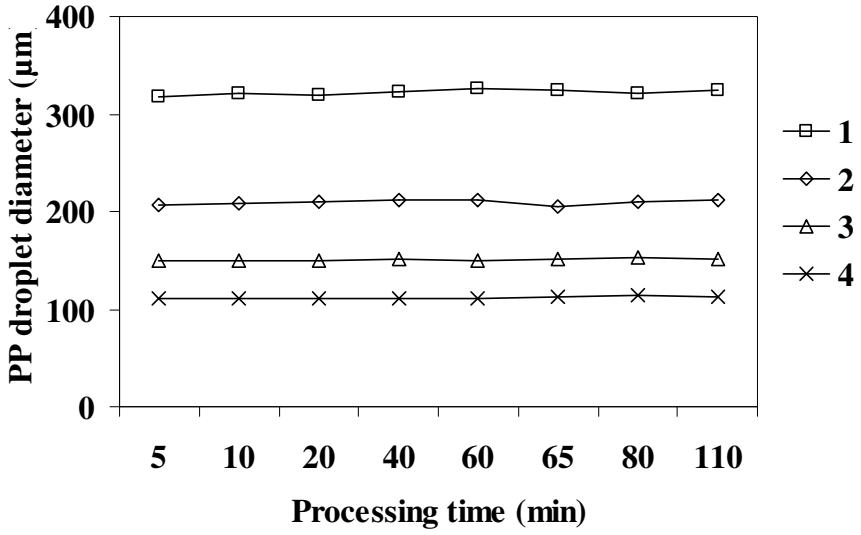

Fig. 4.26 Diameter of PP microdroplet as a function of its processing time at 220°C under nitrogen

It can be clearly seen that the PP microdroplets formed under nitrogen do not show any decrease in their dimensions even after a very prolonged heat treatment, indicating no degradation occurs to these samples under the applied processing conditions.

Dynamic nanoindentation test was carried out directly on the PP microdroplets. This technique allows for measuring mechanical properties as a function of depth in the sample for a single load-depth cycle. Figure 4.27 demonstrates how the elastic modulus is continuously measured as the indenter is penetrating into the droplet.

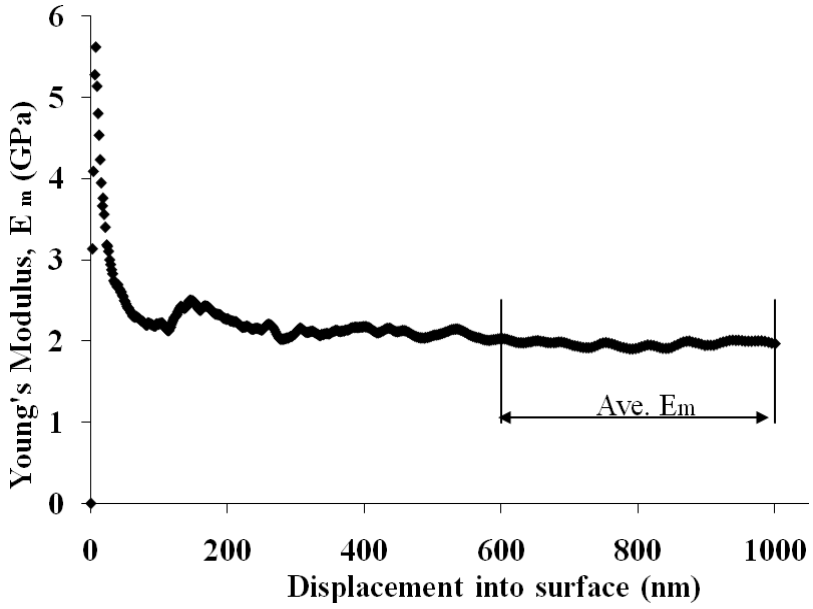

Fig. 4.27 Plot of Young's modulus against displacement into surface of PP microdroplet in nanoindentation test

To minimise the influence of curved surface on the measurement, the average value for the modulus obtained from each individual sample is calculated in a defined range of 600 nm to 1000 nm below the surface. The nanoindentation results for storage moduli of PP microdroplets prepared for 4 min and 6 min at 220°C in air and under nitrogen are presented in Figure 4.28.

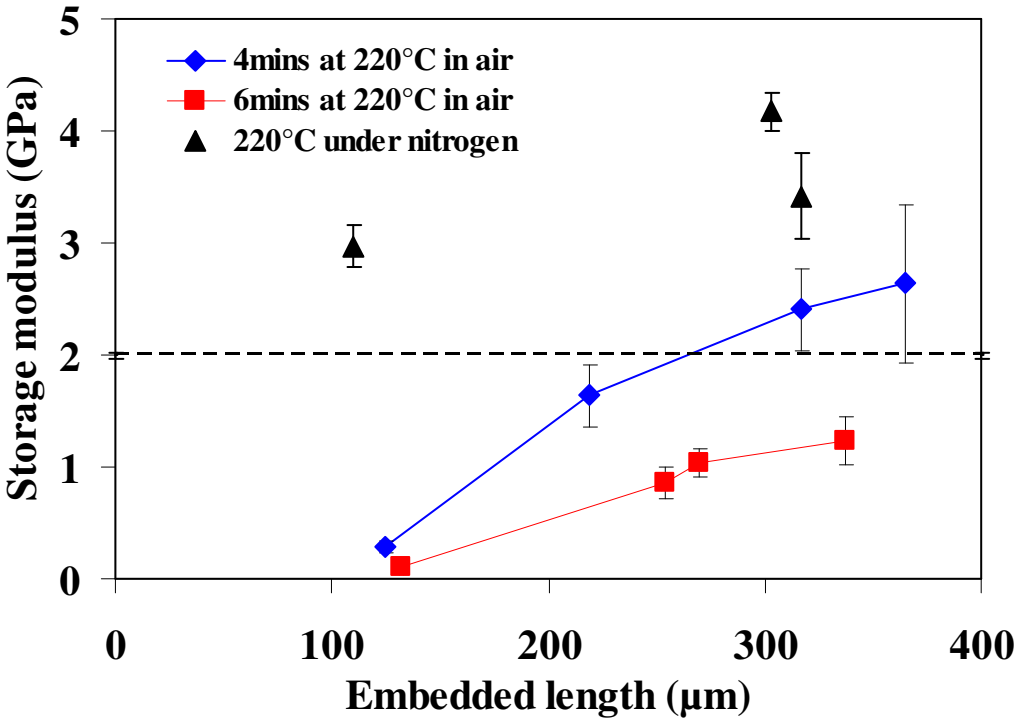

(a)

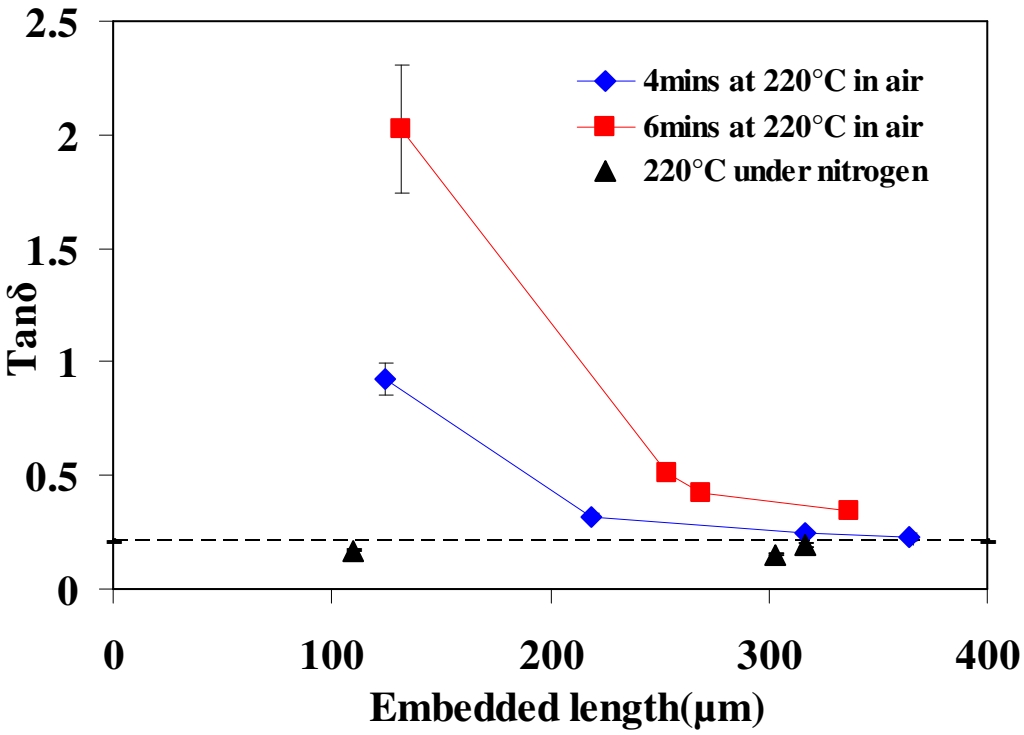

(b)

Fig. 4.28 (a) Storage modulus and (b) tanδ of degraded and non-degraded PP microdroplets with different initial dimensions

It can be seen from Figure 4.28(a) that the PP storage modulus for a given thermal load is also strongly related to the initial dimensions of the droplet and this correlates well with the above analysis on the levels of degradation in the droplets. In contrast, microdroplets prepared under nitrogen show no such loss in the modulus. Young's moduli of PP microdroplets present the same relationship with sample dimensions. Furthermore, damping index, tanδ, clearly indicates that elasticity loss in the material is significantly dependent on the dimension of PP microdroplets made in air. Non-degraded samples, on the contrary, maintain a rather constant low damping performance. The dotted lines in these plots indicate the average values for the corresponding properties of injection moulded PP samples. The error bars can be found at the ends of each line. These average values are obtained from many measurements on a flat smooth surface and may, thus, serve as the reference to the results made on the droplets. It is noticed that the storage moduli (elastic moduli as well) of non-degraded PP droplets are considerably higher than the reference value. This may be due to the cold metal quench during the injection moulding and the molecular orientation along the direction of injection. The former may lead to relatively low crystalline content in the surface of the moulded samples.

The tested PP microdroplets had been unintentionally stored for almost 1-2 months before they were examined by SEM. No indents could be found even in low vacuum mode, where non-conductive samples can be inspected without prior coating. Chemical analysis of the elements in the samples was also carried out by SEM-EDX. The results are summarised in Table 4.1.

Table 4.1 Results for the surface composition of degraded PP microdroplets

Sample	4mins at 220 in air			6mins at 220 in air	
Initial embedded length(μm)	179	280	393	233	340
C wt%	84.36	85.89	87.52	86.16	87.84
O wt%	15.64	14.11	12.48	13.84	12.16

High vacuum mode 20kv

Although the single measurement on each sample may not be adequate to generate any conclusive results, it does seem to show that larger droplets tend to have a less oxygen content. It is unexpected to see that the oxygen content in samples treated for 6 mins is less than that for 4 mins. It may be due to further oxidation during the storage time, which is one month longer for 4 mins set. Nevertheless, it should be quite confident to say that oxidation process dose occur to the PP droplets prepared in air and more than 10 wt% oxygen can be incorporated into the polymer chains.

To further investigate how thermo-oxidative degradation in the polymer affects the measured IFSS with glass fibre, thermo-mechanical properties of degraded material need to be measured. The samples were isothermally treated at 220°C in air in an open system for different times. Figure 4.29 shows the relationship between the normalised weight percent of PP samples and the time for heat treatment.

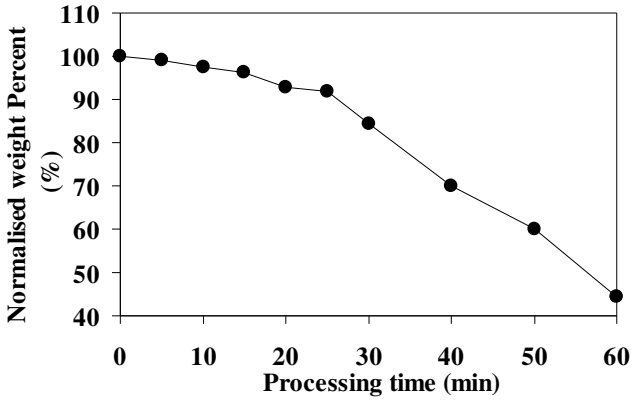

Fig. 4.29 Normalised weight percent of macroscopic PP samples at 220°C in air as a function of processing time

Significant weight loss can be seen in the course of degradation. Although each data point is representative of one individual specimen, it may be acceptable to regard this behaviour in weight loss as that anyone of those samples would have if it was treated continuously for 60 min. Figure 4.30 presents dynamic mechanical properties of these degraded samples.

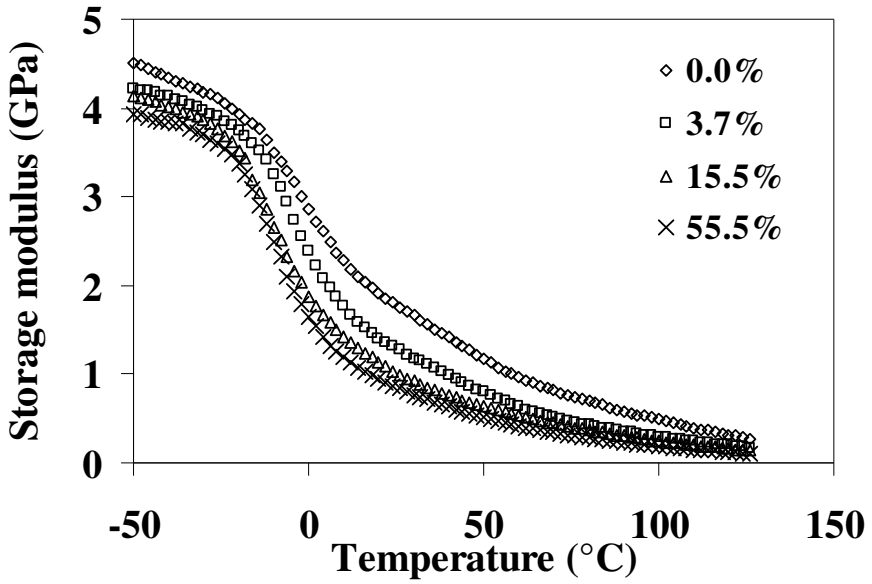

(a)

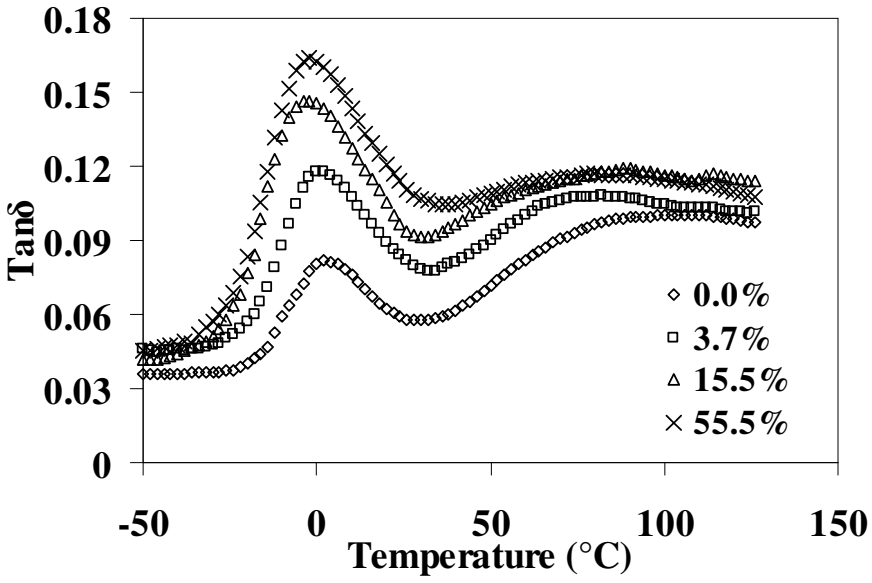

(b)

Fig. 4.30 (a) Storage modulus and (b) tanδ of macroscopic PP samples with different weight losses caused by the degradation

It can be seen in Figure 4.30(a) that storage modulus of PP decreases as the degradation increases in the temperature range of -60°C to 130°C. Particularly during the first 15% weight loss, which occurs within the first 30 minutes heat treatment under the thermal conditions applied in this study. Less significant decrease in the modulus with further weight loss may be due to the fact that three-point bending test mainly characterises the mechanical properties of exposed surface layer, which may tend to vary to a less extent as the degradation increases after 15% weight loss. The correlation between the degradation and the modulus obtained from macroscopic PP samples by three-point bending test is qualitatively in agreement with the above nanoindentation analysis on the PP microdroplets at room temperature. Furthermore, it should be pointed out that although the macroscopic samples were treated at the same thermal conditions as those for PP microdroplets, results from the same processing time in both preparations are not comparable due to significantly different S/V between PP microdroplets and injection moulded samples. The former is believed to suffer much more severe degradation than the latter for a given processing time. The effect of thermo-oxidative degradation of PP microdroplets on their damping property is further confirmed by the results shown in Figure 4.30(b) with the fact that tanδ increases as the degradation increases. It is also noticed that the peak in the curve gradually shifts towards lower temperatures as the degradation increases until it reaches 55.5% weight loss. This implies that degradation can depress the glass transition temperature (T_g) of PP. This can be attributed to the increasing number of flexible chain ends caused by a decrease in molecular weight during the degradation and entrapped low-molecular weight products, which may act as plasticisers. The rise of T_g at 55.5% weight loss certainly needs to be confirmed by

more measurements. Despite this, the similar trend for the relationship between the weight loss and T_g was also observed in other work on a different polymer[37]. The results for T_g of PP with different levels of degradation are presented in Figure 4.31.

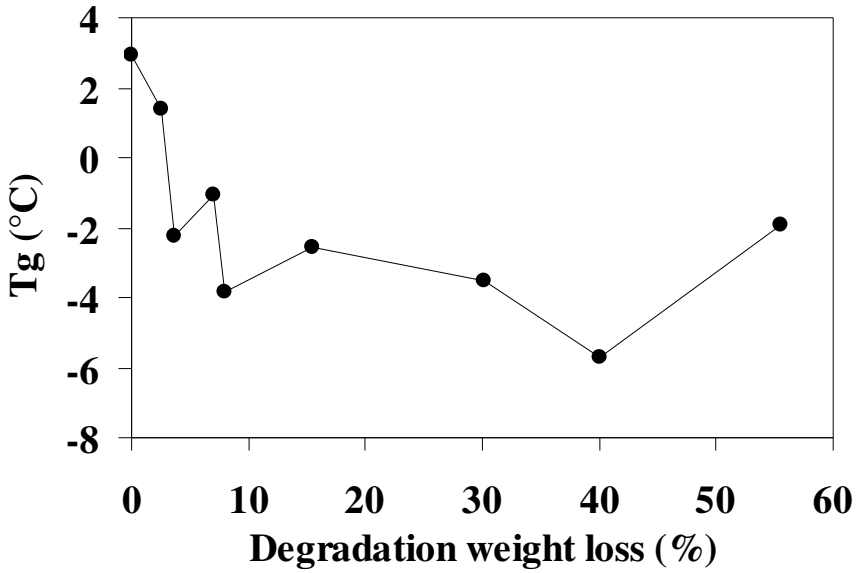

Fig. 4.31 Glass transition temperature (T_g) of PP with different level of degradation

The measurements of CLTE of degraded samples were carried out by using TMA with macro-expansion probe. The samples include both hotplate-treated PP bars and TGA-treated PP tablets (see Figure 4.32).

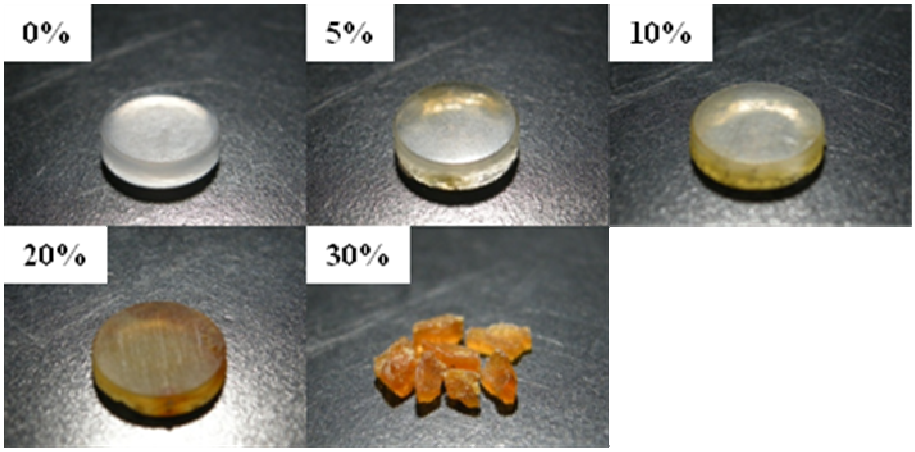

Fig. 4.32 PP47 samples treated to various levels of degradation in TGA

The sample with 30% weight loss became so brittle that it could not be taken out of the DSC pan without breaking it. The results for CLTE of degraded PP are rather irreproducible, which is the same problem with both types of specimen. This is thought to be mainly attributed to inadequate thickness of the samples. It is recommended in ISO 11359–1 that the plastic samples for the measurement of CLTE in TMA should have a thickness of a few millimetres [38]. The thickness of most samples made in this work is approximately 1 mm. Moreover, hotplate-treated samples tend to have a porous surface, which also results in increased imprecision [38]. The results obtained from these samples are together presented in Figure 4.33.

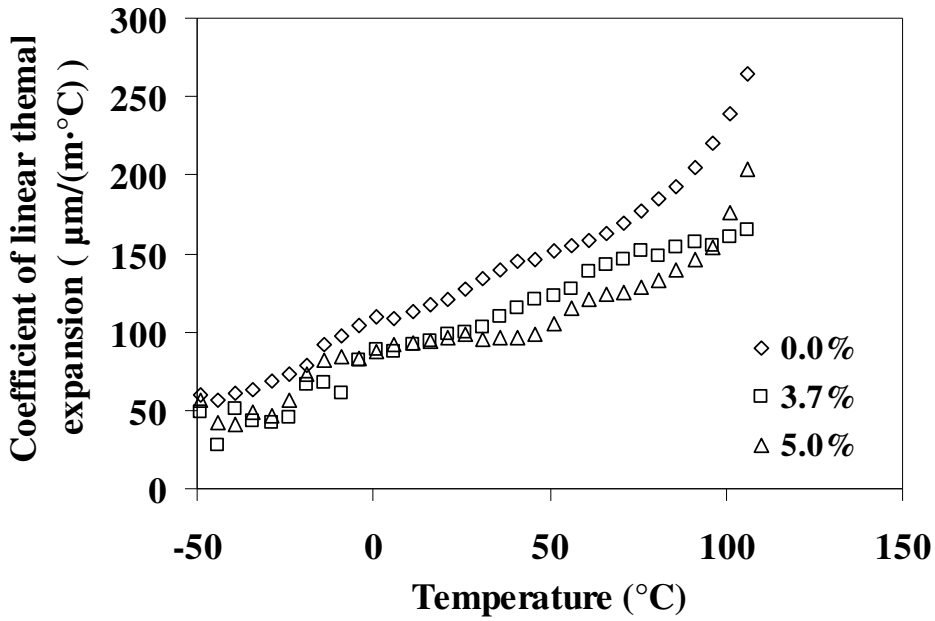

Fig. 4.33 Temperature dependence of coefficient of linear thermal expansion for non-degraded and degraded samples

Only the curves that have been repeated from two individual specimens are presented in Figure 4.33. It is found that samples with no or little degradation (< 5% weight loss) tend to give more repeatable results of CLTE as function of temperature. The results for non-degraded samples agree well with the typical values found in the

literature [39]. Within the first 5% weight loss, degraded PP exhibits a smaller CLTE at the same temperature. Other work has reported the 6–22% reduction in PP CLTE in the case of the first three times of reprocessing [28]. This was attributed to the decreased amount of free volume caused by the growth of spherulites. Nevertheless, the growth of spherulites does not necessarily mean a rise in crystallinity. In addition, it has been stated that the CLTE of a thermoplastic polymer can be reduced by intermolecular hydrogen bonds, which may be formed by oxygen atoms added to the PP chains via thermal oxidation [36]. Another factor that needs to be considered is the molecular weight, whose reduction means the decrease in the length of polymer chains and in the number of molecular entanglements. These changes could lead to the increase of PP CLTE. The CLTE of degraded PP may therefore be controlled by the result of the competition between these factors.

DSC analysis was carried out on degraded PP bars since the microdroplets contain much too little material for a standard analysis. Figure 4.34 shows melting peaks in the second heating cycle with different levels of degradation weight loss.

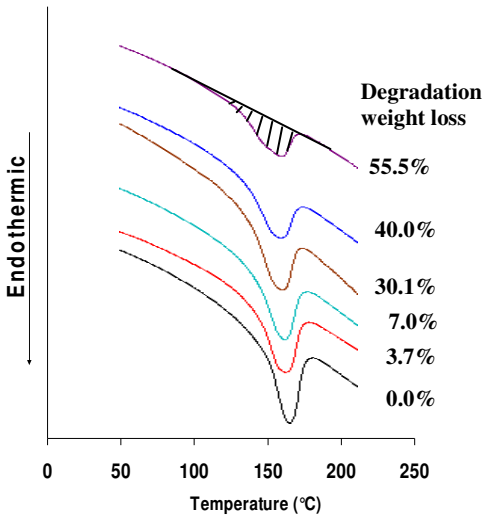

Fig. 4.34 Melting peaks in the second heating cycle in DSC analysis

It certainly indicates that the melting peak is broadened and progressively shifted to lower temperatures as the weight loss increases. Reduction in the onset melting temperature is expected since polymer chains tend to repel oxidised segments from the crystals, leading to the increase of surface free energy of the crystals [15]. As for the decrease of melting temperature, it is known that the melting temperature of PP decreases with reduction in molecular mass [40], with random copolymerisation [41] and with increase in stereo-irregularities [42]. Moreover, the entrapped low-molecular products could act as impurities in the crystal and in turn depress the melting temperature. Similar melting behaviour associated with degraded PP can be found in other work [15]. This melting behaviour of PP together with onset of crystallisation associated with thermo-oxidative degradation is illustrated in Figure 4.35(a).

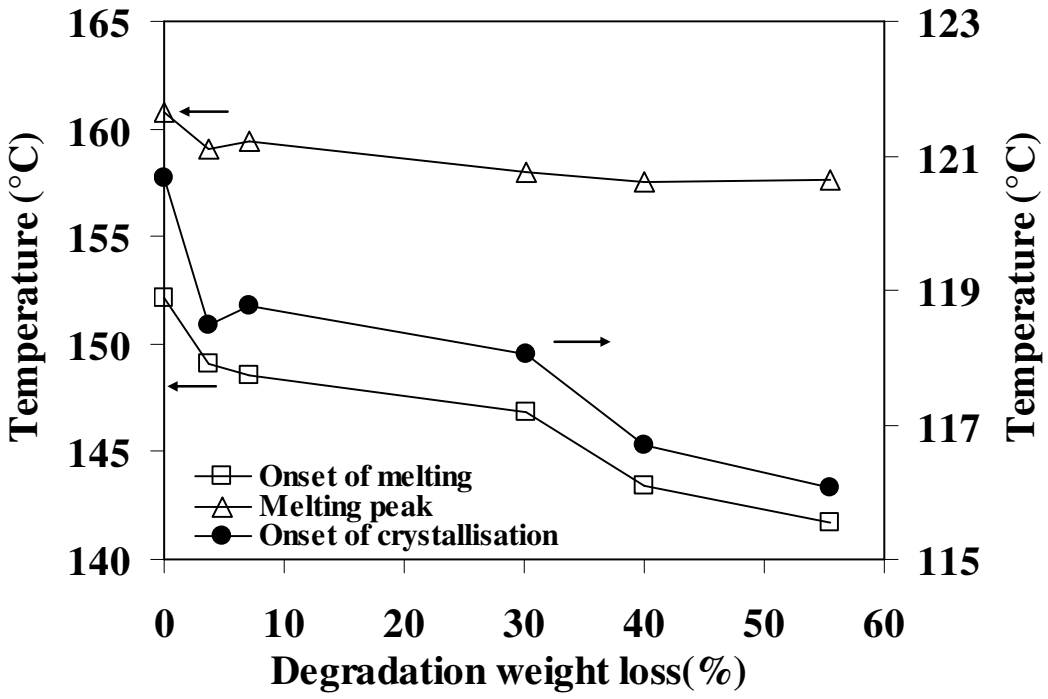

(a)

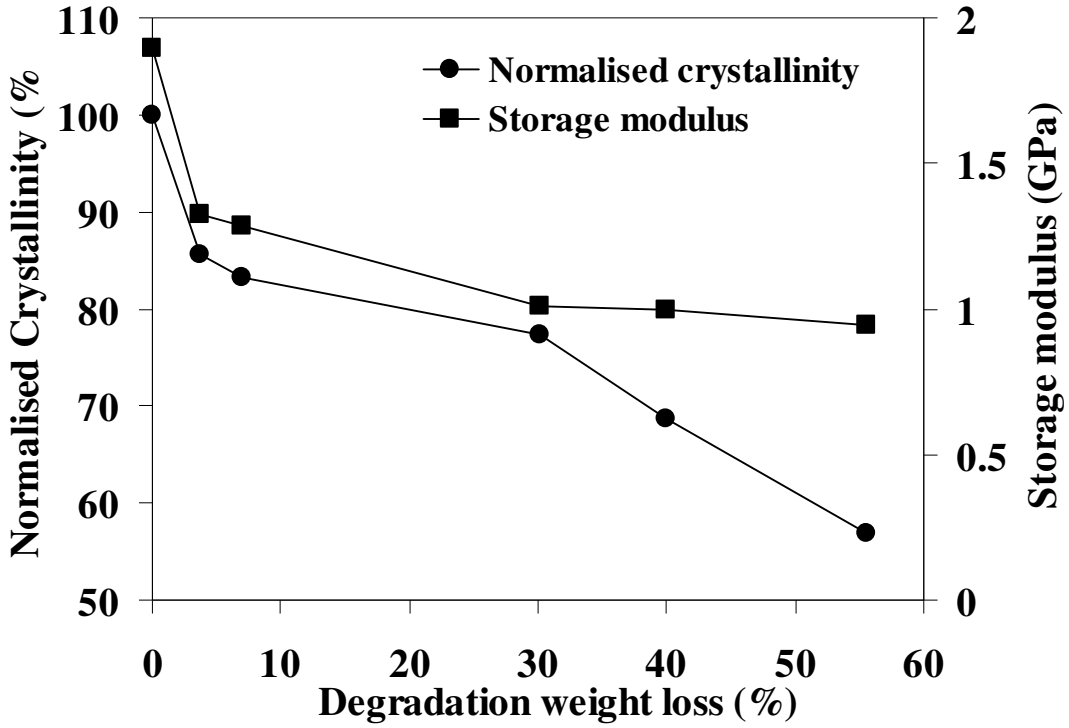

(b)

Fig. 4.35 (a) Melting and crystallisation behaviour of degraded PP and (b) normalised crystallinity of PP samples and their corresponding storage moduli as a function of degradation weight loss

The onset crystallisation temperature was found to be lowered by approximately 5°C up to 55.5% weight loss. The crystallinity of PP is known to be proportional to the integration of the area between the melting peak and the baseline as shown by an example in Figure 4.34. Figure 4.35(b) presents the results for normalised crystallinity and corresponding storage moduli at 20°C of degraded PP samples. It can be seen that the degradation gives rise to a significant decrease in PP crystallinity with 44% reduction for the most degraded sample. The storage modulus follows the similar trend with the degradation weight loss until it reaches 30%, after which the decrease of storage modulus becomes much less significant. This may be due to the stiffness compensation resulting from the cross-linked polymer chains at the late stage of degradation. Regardless of this complication, the results in Figure 4.35(b)

suggest that the decrease of PP crystallinity is the most likely cause of the drop in modulus observed in both degraded PP microdroplets and macroscopic samples.

The results and discussion above not only support the findings from the earlier work on the measurement of IFSS for GF-PP47, but also provide evidence that could account for a mechanism by which the degradation affects measured IFSS. These possibilities are summarised as follows:

- Thermo-oxidative degradation of PP reduces PP crystallinity. This leads to the decrease of PP modulus and in turn decreases CRRS at the interface. In addition, lowering crystallinity can give rise to the reduction in thermal shrinkage related to the densification, which normally is considered to account for large residual stress built up in a semi-crystalline matrix [43]. Decrease of crystallinity may also mean potential stress relaxation.

- Thermo-oxidative degradation of PP reduces the onset temperature for PP crystallisation. This temperature is commonly adopted as stress free temperature, at which the residual stress is thought to begin accumulating around the interface. In most theoretical models, residual stress is found to be proportional to the difference between stress free temperature and test temperature [43, 44].

- The CLTE of PP microdroplets is reduced by thermo-oxidative degradation. This reduction in CLTE will depress thermal shrinkage upon cooling of a thermoplastic polymer and consequently reduce CRRS at the interface.

To better elucidate the points made above, compressive radial stress at the interface was calculated using the concentric cylinder model [43, 44] and experimental results obtained in this work. The model assumes that the solid cylindrical fibre is concentrically assembled with the hollow cylindrical interphase (if there is one) and the matrix. It is also assumed that all components are linearly elastic and possess perfect bonding between them. In the case of this work, we assume there is no interphase between the glass fibre and PP matrix and both components are isotropic. The physical and mechanical properties of the glass fibre are assumed to be independent of the temperature in this study. The elastic modulus and CLTE of the glass fibre has been measured by the standard single fibre tension test in chapter 1. The radii for internal and external cylinders were set to be 9 μm and 160 μm, which are average values of the fibre and the PP microdroplet respectively. The temperature dependence of elastic modulus of PP was obtained from the thermo-mechanical characterisation of PP and some of the results have been shown in Figure 4.30(a). The input for the stress free temperature was based on the results in Figure 4.35(a). Since the results for the CLTE of PP were not available for most degraded samples, the temperature dependence of the CLTE of PP was taken to be independent of the PP degradation level throughout the calculation. The results for CRRS are shown in Figure 4.36.

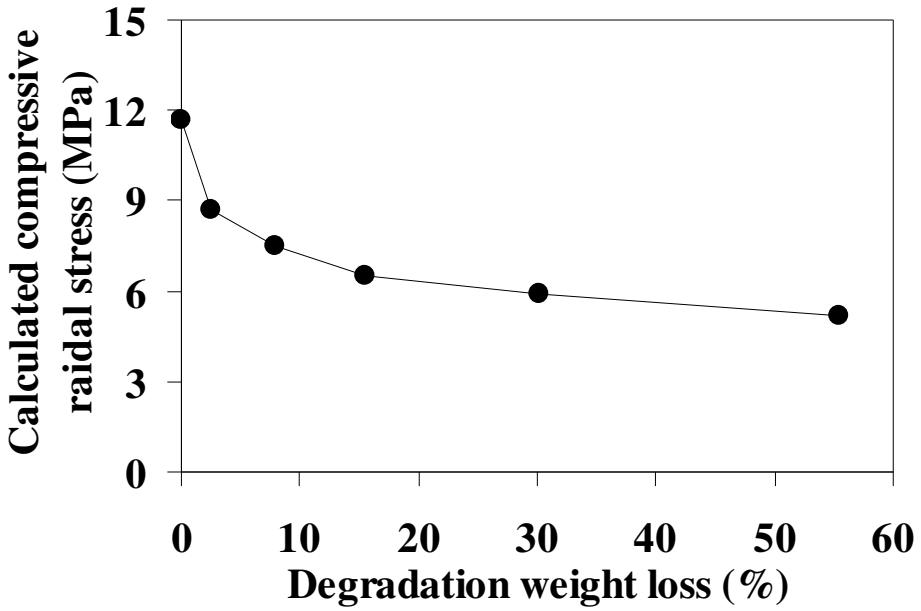

Fig. 4.36 Calculated compressive residual thermal stress at the GF-PP47 interface at 20°C exerted by the PP matrix with different degradation weight loss

It can be seen that degradation of the PP matrix does lead to lower CRRS at the interface. In particular, the first 2.5% degradation weight loss results in the most significant decrease in CRRS. This should be expected from the results in Figure 4.30(a).

4.3.3 Comparison of IFSS between GF-degraded PP and GF-non-degraded PP

Results for IFSS of samples prepared in air and under nitrogen are presented in Figure 4.37.

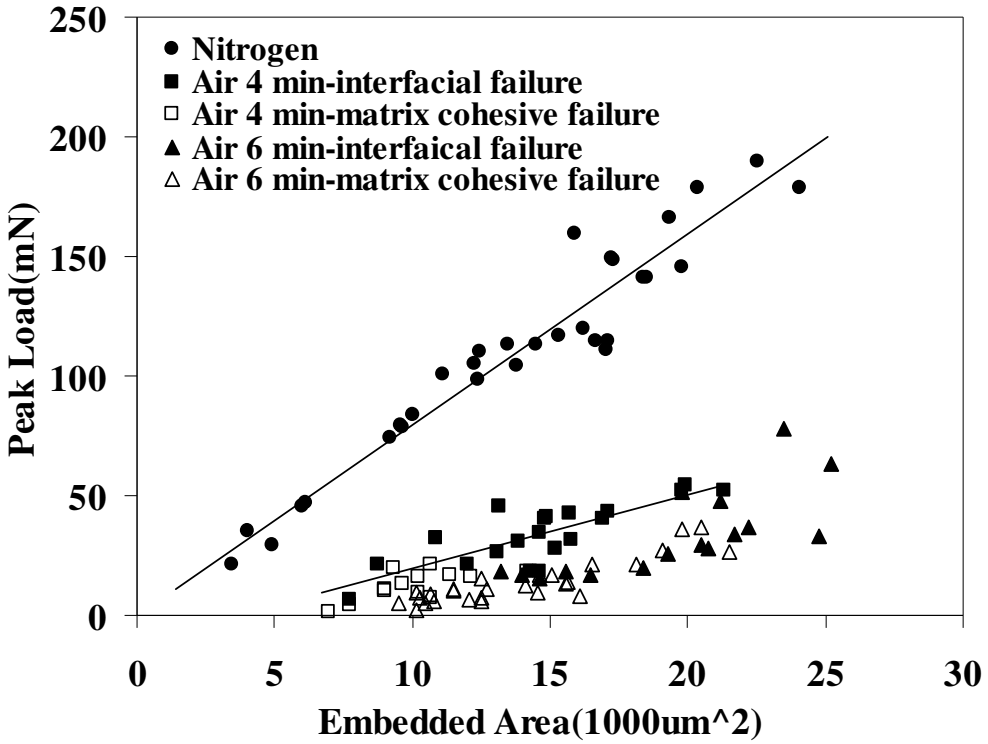

Fig. 4.37 Effect of thermo-oxidative degradation of PP on the microbond measured apparent IFSS of GF-PP47

The simple calculation of IFSS is via the ratio of peak load to embedded area with the assumption of uniform distribution of interfacial shear stress. It can be clearly seen in Figure 4.37 that measured IFSS for GF-PP47 is significantly affected by the thermal load (temperature and time) and the atmosphere (air or nitrogen) in terms of thermo-oxidative degradation in PP matrix. Without degradation of the PP microdroplet the measured average IFSS is over twice the magnitude obtained from degraded PP samples. The fact that the linear fitting lines of the data from non-degraded samples goes through the origin and lines for the degraded samples do not indicate that thermal degradation of PP may be one of the reasons why the regression lines in some microbond studies of IFSS do not pass through the origin. Note that the data points with hollow symbols in the 4 and 6 minutes sets correspond to the microbond samples that were previously observed to undergo the matrix cohesive

failure due to severe degradation and therefore should not be involved in the comparison of IFSS with non-degraded samples. However, other samples did undergo the interfacial failure with clean debonded area left behind after testing and yet they gave much lower values for IFSS than those obtained from non-degraded samples.

Finally it is worth pointing out that it has been reported in the literature that the use of degraded/recycled PP in fibre (mainly natural fibres) reinforced composites can give rise to the good retention or even improvement in some mechanical properties [45, 46]. In most cases this is attributed to the enhanced compatibility and resultant higher IFSS between the fibre and the matrix. The results presented in this study do not necessarily challenge these ideas since the method and scale of sample preparation are different. In composite preparation by extrusion and moulding, functional groups resulting from a relatively mild thermo-oxidative degradation of PP are likely to find the fibre surface directly. However, in the process of formation of a PP droplet on a single fibre, the degradation takes place in-situ and by the time PP immediately adjacent to the fibre is functionalised the whole droplet has likely degraded and become too weak to transfer the applied load to the interface to cause interfacial debonding in the microbond test. Consequently, the degraded droplet experiences a matrix shear failure and leaves behind residual resin on the fibre surface as shown earlier in this chapter.

4.4 Summary

The effect of thermo-oxidative degradation of homopolymer isotactic PP47 on the measured IFSS with uncoated E-glass fibre is reported. It was found that PP micrdroplets employed in the standard microbond test suffered considerable thermo-oxidative degradation when they were formed in air. Degradation of the PP droplets proved very detrimental to the apparent level of adhesion of GF-PP47. It is therefore strongly recommended that PP microbond samples should be formed in an inert atmosphere, such as nitrogen. Studies on both PP microbond and macroscopic samples showed that the change in their thermo-mechanical properties is mainly responsible for the decrease of IFSS in terms of a decrease in the radial residual thermal stress at the interface. A qualitative correlation between PP degradation and measured IFSS has been generated in this study. Further work should extend to investigating how this degradation in PP affects the mechanical properties of macroscopic GF-PP47 composites.

References

[1] Pielichowski K,Njuguna J. Thermal Degradation of Polymeric Materials 2005, Shawbury: Rapra Technology Ltd.

[2] Pandey JK, Raghunatha Reddy K, Pratheep Kumar A,Singh RP. An overview on the degradability of polymer nanocomposites. Polymer Degradation and Stability 2005;88(2):234-250.

[3] Moore EP. Polypropylene Handbook. 1996, New York: Hanser Publisher.

[4] Gugumus F. Thermooxidative degradation of polyolefins in the solid state: Part 1. Experimental kinetics of functional group formation. Polymer Degradation and Stability 1996;52(2):131-144.

[5] Gugumus F. Thermooxidative degradation of polyolefins in the solid state. Part 2: Homogeneous and heterogeneous aspects of thermal oxidation. Polymer Degradation and Stability 1996;52(2):145-157.

[6] Gugumus F. Thermooxidative degradation of polyolefins in the solid state--4: Heterogeneous oxidation kinetics. Polymer Degradation and Stability 1996;53(2):161-187.

[7] Hinsken H, Moss S, Pauquet J-R,Zweifel H. Degradation of polyolefins during melt processing. Polymer Degradation and Stability 1991;34(1-3):279-293.

[8] Singh B,Sharma N. Mechanistic implications of plastic degradation. Polymer Degradation and Stability 2008;93(3):561-584.

[9] Bertin D, Leblanc M, Marque SRA,Siri D. Polypropylene degradation: Theoretical and experimental investigations. Polymer Degradation and Stability 2010;95(5):782-791.

[10] Gugumus F. Thermooxidative degradation of polyolefins in the solid state--6. Kinetics of thermal oxidation of polypropylene. Polymer Degradation and Stability 1998;62(2):235-243.

[11] Hatanaka T, Mori H,Terano M. Study of thermo-oxidative degradation of molten state polypropylenes with a variety of tacticities. Polymer Degradation and Stability 1999;64(2):313-319.

[12] Canevarolo SV. Chain scission distribution function for polypropylene degradation during multiple extrusions. Polymer Degradation and Stability 2000;70(1):71-76.

[13] Calhoun AA, Nicholson PD,Barnes AB. The use of inverse gas chromatography to study surface thermal oxidation of polypropylene. Polymer Degradation and Stability 2006;91(9):1964-1971.

[14] Gugumus F. Thermooxidative degradation of polyolefins in the solid state. Part 3: Heterogeneous oxidation model. Polymer Degradation and Stability 1996;52(2):159-170.

[15] Rabello MS,White JR. Crystallization and melting behaviour of photodegraded polypropylene -- I. Chemi-crystallization. Polymer 1997;38(26):6379-6387.

[16] Rabello MS,White JR. Crystallization and melting behaviour of photodegraded polypropylene -- II. Re-crystallization of degraded molecules. Polymer 1997;38(26):6389-6399.

[17] Hoyos M, Tiemblo P, Gómez-Elvira JM, Rychlá L,Rychlý J. Role of the interphase dynamics in the induction time of the thermo-oxidation of isotactic polypropylene. Polymer Degradation and Stability 2006;91(7):1433-1442.
[18] Kato M,Osawa Z. Effect of stereoregularity on the thermo-oxidative degradation of polypropylenes. Polymer Degradation and Stability 1999;65(3):457-461.
[19] Chan JH,Balke ST. The thermal degradation kinetics of polypropylene: Part I. Molecular weight distribution. Polymer Degradation and Stability 1997;57(2):113-125.
[20] Kron A, Stenberg B, Reitberger T,Billingham NC. Chemiluminescence from oxidation of polypropylene: Correlation with peroxide concentration. Polymer Degradation and Stability 1996;53(1):119-127.
[21] Xiang Q, Xanthos M, Patel SH,Mitra S. Comparison of volatile emissions and structural changes of melt reprocessed polypropylene resins. Advances in Polymer Technology 2002;21(4):235-242.
[22] da Costa HM, Ramos VD,Rocha MCG. Rheological properties of polypropylene during multiple extrusion. Polymer Testing 2005;24(1):86-93.
[23] Gijsman P, Kroon M,van Oorschot M. The role of peroxides in the thermooxidative degradation of polypropylene. Polymer Degradation and Stability 1996;51(1):3-13.
[24] Rocha MCG, Coutinho FMB,Balke ST. A study of polypropylene peroxide promoted degradation. Polymer Testing 1995;14(4):369-380.
[25] Azizi H,Ghasemi I. Reactive extrusion of polypropylene: production of controlled-rheology polypropylene (CRPP) by peroxide-promoted degradation. Polymer Testing 2004;23(2):137-143.
[26] da Costa HM, Ramos VD,de Oliveira MG. Degradation of polypropylene (PP) during multiple extrusions: Thermal analysis, mechanical properties and analysis of variance. Polymer Testing 2007;26(5):676-684.
[27] Fayolle B, Audouin L,Verdu J. Oxidation induced embrittlement in polypropylene -- a tensile testing study. Polymer Degradation and Stability 2000;70(3):333-340.
[28] El-Tonsy MM. Automatic measurement of the absolute CTE of thin polymer samples: I--effect of multiple processing on thermal expansion of polypropylene films. Polymer Testing 2004;23(3):355-360.
[29] Garbassi F, Occhiello E,Polato F. Surface effect of flame treatments on polypropylene. Journal of Materials Science 1987;22(1):207-212.
[30] Mathieson I,Bradley RH. Improved adhesion to polymers by UV/ozone surface oxidation. International Journal of Adhesion and Adhesives 1996;16(1):29-31.
[31] Gorbatkina YA. Adhesive Strength In Fibre-Polymer Systems. 1992: KHIMIYA PUBLISHERS
[32] Li X,Bhushan B. A review of nanoindentation continuous stiffness measurement technique and its applications. Materials Characterization 2002;48(1):11-36.
[33] Odegard GM, Bandorawalla T, Herring HM, Gates TS. Characterization of viscoelastic properties of polymeric materials through nanoindentation. SEM Annual Conference and Exposition on Experimental and Applied Mechanics 2003

[34] Mäder E,Pisanova E. Characterization and design of interphases in glass fiber reinforced polyproplyene. Polymer Composites 2000;21(3):361-368.
[35] Hoecker F,Karger-Kocsis J. Effects of crystallinity and supermolecular formations on the interfacial shear strength and adhesion in GF/PP composites. Polymer Bulletin 1993;31(6):707-714.
[36] ASM I. Characterization and failure analysis of plastics. 2003, OH: ASM International.
[37] Wondraczek K, Adams J,Fuhrmann J. Effect of Thermal Degradation on Glass Transition Temperature of PMMA. Macromolecular Chemistry and Physics 2004;205(14):1858-1862.
[38] ISO, Plastic–Thermomechanical analysis (TMA)–Part 1: General principles. 1999.
[39] Thomason JL,Groenewoud WM. The influence of fibre length and concentration on the properties of glass fibre reinforced polypropylene: 2. Thermal properties. Composites Part A: Applied Science and Manufacturing 1996;27(7):555-565.
[40] Lehtinen A,Paukkeri R. Fractionation of polypropylene according to molecular weight and tacticity. Macromolecular Chemistry and Physics 1994;195(5):1539-1556.
[41] Oliveira MJ,Hemsley DA. The microstructure of polypropylene welds as a guide to processing history. British Polymer Journal 1985;17(3):269-274.
[42] Cheng SZD, Janimak JJ, Zhang A,Hsieh ET. Isotacticity effect on crystallization and melting in polypropylene fractions: 1. Crystalline structures and thermodynamic property changes. Polymer 1991;32(4):648-655.
[43] Nairn JA. Thermoelastic analysis of residual stresses in unidirectional, high-performance composites. Polymer Composites 1985;6(2):123-130.
[44] Wagner HD,Nairn JA. Residual thermal stresses in three concentric transversely isotropic cylinders: Application to thermoplastic-matrix composites containing a transcrystalline interphase. Composites Science and Technology 1997;57(9-10):1289-1302.
[45] Miyazaki K, Okazaki N, Terano M,Nakatani H. Preparation and Characterization of Cellulose/Polypropylene Composite Using an Oxidatively Degraded Polypropylene. Journal of Polymers and the Environment 2008;16(4):267-275.
[46] Abu-Sharkh BF,Hamid H. Degradation study of date palm fibre/polypropylene composites in natural and artificial weathering: mechanical and thermal analysis. Polymer Degradation and Stability 2004;85(3):967-973.

Chapter 5

Effect of residual thermal stress on IFSS for GF-PP

5.1 Literature review

5.1.1 Introduction to residual thermal stress

Residual stress can be defined as a self-equilibrated stress that persists in a material that is free of external forces or temperature gradients. It has its root in the inhomogeneity of a system such as composites in general. It is regarded that residual stress is inherently present in virtually all composite materials whether they are based on polymer, metal or ceramic matrices and yet it is often ignored or underestimated in both design and analytic modelling [1]. Over the last several decades, material research, particularly in the composite field, has proved that residual stress plays a significant in role in the properties of the composite structures such as dimensional stability, structural integrity, and mechanical performance. The oversight of residual stress may lead to incorrect interpretations of material characteristics and mechanical behaviour [1]. It is therefore of utmost importance that the residual stress should be taken into account in both design and analytic modelling of composite structures. This accordingly requires a good understanding of the role of residual stress in composite. The ultimate goal of studies on the residual stress is to control and utilise it to our advantage.

5.1.2 Formation of residual thermal stress

The residual stress may be classified into three categories based on the different origin. They are thermal, mechanical, and phase transformation [1]. The last two are mainly concerned in composites based on metallic and ceramic matrices, while the thermal origin is the most prevalent and arises from the different coefficient of thermal expansion (CTE) of the composite constituents. Residual thermal stress (RTS) can be defined as a residual stress introduced within a body resulting from a change in temperature. Composites in general achieve their structural integrity by being cured as in thermosetting composites or processed at elevated temperature as in thermoplastic composites. This process invariably induces the residual thermal stress to build up in the composite when it is at a temperature different from its process temperature. Favre gave the first review of the RTS in both thermosetting and thermoplastic composites [2] and more recently the available literature on the RTS in thermoplastic composites has been reviewed by Parlevliet *et al* in a series of published papers [3-5]. They firstly described the sources and mechanisms of formation of RTS in thermoplastic composites, related to material properties and processing conditions. Experimental techniques developed for determination of the RTS in polymer matrix composites were then reviewed. Finally, the effects of RTS on the composite material properties were also reviewed.

The magnitude of RTS in fibre reinforced composite structures is considered to primarily depend on four parameters: temperature difference between use temperature and stress free temperature, at which the residual stress is thought to begin accumulating, CTE of the composite constituents or plies, thermo-elastic

properties of these constituents or plies, and fibre volume fraction. Apparently these parameters vary with different types of fibres and matrices used in composites. For instance, glass fibres normally show isotropic thermal expansion behaviour, whereas both carbon and aramid fibres are highly anisotropic with small shrinkage in the fibre longitudinal direction upon heating [1]. Despite this difference, the CTE for the reinforcing fibres is in general much lower than for the polymer matrices especially for the thermoplastic matrices, whose CTEs are normally at least one order of magnitude higher than those fibres [1]. More significant effect on the RTS comes from the variation in types of polymer matrices, which are mainly responsible for the relative shrinkage difference, stress free temperature (in turn, temperature difference) and sensitivity to the processing conditions. For example, the amount of volume shrinkage upon the same amount of cooling is believed to follow the order: semi-crystalline thermoplastic polymer > amorphous thermoplastic polymer > thermosetting polymer [3]. In addition, the corresponding stress free temperatures are observed to be the crystallisation, glass transition and cure temperature respectively [3, 6-8]. Both crystallisation and glass transition temperature are known to be affected by processing conditions such as cooling rate or atmosphere [9, 10]. For amorphous polymer matrices, it was concluded that the faster the cooling rate in the glass transition region, the higher the RTS due to higher stress free temperature. For semi-crystalline polymer matrices, however, fast cooling may result in lower crystallisation temperature and crystallinity levels, which all lead to a lower RTS. Thus, the RTS is considered to be the result of these two competing mechanisms. When the fibres and the matrix are brought together under certain conditions, an interface or interphase may be formed, which can affect the RTS. For example,

higher fibre-matrix interfacial bond strength by chemical treatment will increase the RTS [11, 12]. That is because during the cooling process, both constituents shrink but the full contraction of the matrix is constrained as a consequence of being bonded to the fibre. On the other hand, the fibre is not only shortened by its own thermal shrinkage, but is also compressed by the constrained shrinkage of the matrix. As a result, residual axial compressive stresses, which decrease from a maximum at mid-length to zero at the fibre ends, are induced in the fibre. At the same time, the matrix is constrained by the fibre from fully shrinking, and as a result, is stressed in tension in a direction parallel to the fibre axis. Stress transfer from fibre to matrix takes place. A weak interfacial strength may allow for some extent of fibre-matrix slippage in the longitudinal fibre direction and in turn relieving partially the stress build-up.

Depending on the geometry and scale of the composites concerned, RTS has been examined on both micro- and macroscopic levels. RTS on the micromechanical level directly arises from the mismatch in CTE between the fibres and the matrix. Analytical studies on this level were mainly carried out on a representative volume element or unit cell, which usually involves a single fibre completely coaxially embedded in certain amount of matrix material in a shape of cylinder [13-15]. Recently Shokrieh *et al* investigated the effect of different representative volume elements on RTS in fibre-reinforced composites using finite element method and showed slight difference between different configurations [16]. These models can serve as the basis of determination in anisotropic thermo-elastic properties of a long fibre unidirectional lamina. It is this lamina anisotropy that gives rise to a RTS present on a ply-to-ply scale. The RTS in each ply depends on the specific lay-up in the laminate. Furthermore, a gradient in cooling rate, temperature or moisture

conditions throughout the thickness of the composite laminate or structure may lead to a RTS through the thickness of the composite [8, 17]. Finally, the RTS formed during processing may also be a function of time if the visco-elastic behaviour of the polymer matrix is pronounced.

5.1.3 Techniques for characterisation of residual thermal stress

Various experimental techniques have been developed to characterise RTS in both micro and macroscopic level of different composites. Techniques that use inherent material properties of the constituents of composites usually include Photo-elasticity, Micro-Raman spectroscopy and electrical conductivity of carbon fibre reinforcement.

Photo-elasticity is applied to materials that exhibit the property of birefringence when subjected to the stress and the value for the index of refraction (IR) varies as a function of the stress applied. When a ray of polarised light passes through such materials, the light resolves into two components, each of which is oriented into a direction of principal stress in the material and travelling at different velocity with the other (i.e. having different IR).This difference in the IR results in a relative phase retardation between these two light vectors. The magnitude of retardation is correlated with principal stress by the stress-optic law (also called Brewster's law). Photo-elasticity requires a transparent or translucent matrix and has been used to examine the RTS distribution in the both thermoplastic and thermosetting matrices [6, 18].

Micro-Raman spectroscopy relies on the Raman effect that occurs when there is the energy transfer between the photons of the incident monochromatic light and the

molecules of the material during their interaction. Such interaction is inelastic and known as Raman scattering. The difference in energy between the incident photon and the Raman scattered photon is equal to the energy of a vibration of the scattering molecule. This technique is based on the stress (strain) sensitivity of most Raman vibrational modes of crystalline phases and has been widely used in carbon fibre reinforced composites [19, 20].

Strain dependence of electrical resistance has enabled the carbon fibre to be used as intrinsic strain sensor in carbon fibre reinforced composites, where the strain of carbon fibre can be measured by electrical resistance measurement [21, 22]. The electrical resistance of carbon fibre increase almost linearly with increasing fibre length before about 0.7% strain [22].

When the carbon fibre is used in the composites with different reinforcements, it can serve as an extrinsic embedded strain sensor, which refers to another group of techniques for RTS determination. The commonly used sensors include strain gauges, fibre optic sensors, and embedded metallic particles in combination with X-ray diffraction. Among them, the fibre Bragg grating sensor is most often applied to monitor RTS formation during processing due to its small diameter and accuracy [4]. A Bragg grating is a permanent periodic change of the IR in the core of an optical glass fibre, which enables the fibre to reflect a narrow spectral component of a broadband light source. The central wavelength of the reflected component λ_{refl} is related to the grating period Λ and the mean effective IR n_{eff} through Bragg condition: $\lambda_{refl} = 2n_{eff}\Lambda$. Any change of the fibre length will modify the grating

period and the effective IR and in turn leads to a modification of the Bragg wavelength.

A common manifestation of RTS in composites with unsymmetrical lay-up is out-of-plane deformation, which partially relieves the RTS. Therefore, warping can be measured to indicate the magnitude of the RTS [4]. In addition, the methods based on interferometry can measure in-plane deformation as well as out-of-plane deformation.

The methods mentioned above are based on non-destructive evaluation of the RTS in composites. A number of destructive RTS measurement techniques are also available. These include first ply failure, layer removal, hole drilling and crack compliance techniques [4]. Destructive techniques are known to have advantage of determining the RTS distribution through the thickness.

5.1.4 Effect of Residual thermal stress

In unidirectional lamina, RTS often leave fibres in a state of compression and the matrix under tension in the fibre longitudinal direction. It implies that the stress transfer between the fibre and the matrix takes place through the interface. In the radial direction, RTS often put both the fibres and the matrix under compression. However, close packing of fibres can result in “tricorn” regions which can change the compressive radial stresses to tensile stresses [13]. This implies that the normal stress at the interface can be compressive or tensile. Furthermore, compressive and tensile hoop stresses are also induced in the fibre and the matrix respectively. Consequently, these stresses will affect the properties of constituents and their

interface. In general, when the residual stresses and the stresses resulting from external loads are equal in sign the maximum allowable external stress decreases. For example, the compressive residual stress in the fibre may give rise to an increased tensile strength in the fibre direction [7] but also means a reduced compressive strength. Although the interfacial shear stress induced by the RTS may result in interfacial debonding, it can also augment the fibre debonding stresses arising from mechanical loading [15]. Moreover, it was found that with increasing radial compressive RTS the fibre-matrix interfical bond became stronger due to mechanical locking [11, 23]. Effects of RTS on the mechanical properties of laminates are more complicated and generally observed to be detrimental. Much work thus has been dedicated to minimise the RTS in the composites.

If the RTS is sufficient enough, some defects may be introduced in composite laminates and structures. Compressive stress in the fibre may give rise to fibre waviness, which can be defined as fibres deviating from the mean direction of the laminate and forming a pattern that is often represented mathematically as a sine wave [5]. Alone or combined with stresses caused by external forces, the interfacial thermal stresses may initiate an interfacial crack resulting in fatigue failure and deterioration in material properties. Tensile hoop stress tends to craze or crack the matrix around the fibre. Voids tend to aggravate the condition at the interface. When the fibre-matrix interface bond is weak, cracks can propagate along the interface. When a strong interface is present, cracks may propagate into the matrix. This fibre-matrix debonding/matrix cracking can grow to form microcracks, which may further develop into transverse ply cracks. In a laminate, the ply with transverse cracking can initiate delamination and subsequently leads to the ultimate failure of the laminate.

Delamination can also be caused by the high interlaminar stresses developed due to property discontinuities through the thickness at a free edge.

Effects of RTS on fibre-matrix adhesion have been commented through both analytical analyses and experimental studies. Nairn et al experimentally determined the RTS in fibre reinforced thermoplastic and thermosetting matrices by means of photoelasticity [6] Although direct comment on the effect of RTS on fibre-matrix adhesion was not given in that work, they showed the RTS at the interface could be significant for most composites and must be taken into account. Based on classic elasticity theory, Nairn also developed a theoretical model, which clearly showed significant normal compressive stresses at the interface could be developed upon cooling [13]. This model was later employed in some other works to mainly account for the adhesion level in the composites with little or no chemical bonds at the interface [12, 24, 25]. Di Landro et al. incoporated stress relaxation in the matrix and Poisson effect into Nairn's model and found the RTS at the interface was smaller than that predicted by Nairn's model. Nevertheless, they carried out the microfragmentation test at different temperatures for amophous, semicrystalline and thermosetting matrices and proved that radial compressive stress at the interface strongly affected the fibre-matrix adhesion in all the microcomposites studied. Particularly for amophous and semicrystalline thermoplastic matrices, the radial compressive stress was likely to be mainly responsible for the fibre-matrix adhesion. More recently, Quek derived closed-form solutions for the thermal stresses in a fibre of finite length embedded in a definite elastic matrix with the total complementary energy principle approach and carried out a parametric study on the effects of fibre length, matrix radius, Young's modulus, CTE and Poisson's ratio of the matrix on

the residual stress distribution [26]. It was found that the thermal stresses in composites are dependent on the material properties of the constituents as well as geometry. For a given fibre/matrix system, the thermal stress fields will augment the fibre debonding stresses caused by mechanical loading, and influence the analysis of interfacial properties in fibre pull- and push-out tests [26]. Despite various models being established, they have not been experimentally verified to account for the adhesion. The main missing requirement in converting these residual stresses into IFSS is an accurate estimation of the coefficient of static friction (CSF) for any particular system. A better understating of the role of wetting and interfacial interaction on CSF is also required.

5.2 Experimental

5.2.1 Material

In order to minimise complexity of the system to be studied, the choice of the materials was limited to uncoated glass fibre and homopolymer polypropylene. The fibres were uncoated boron free E-glass fibres (Ave. diameter = 17.5µm) from Owens Corning-Vetrotex in combination with commercial isotactic homopolymer polypropylene (PP47) SABIC®PP 579S with melt flow index = 47 g/10 min at 230°C and 2.16 kg.

5.2.2 Instron-microbond test (I-MBT)

Fibre pull-out tests (i.e. microbond test and single fibre pull-out test) have been developed in our laboratory and the details on sample preparation and testing procedures for both tests have been discussed in chapter 3. The processing temperature, T_p=220°C, and processing time, t_p=4 minutes were adopted as the appropriate conditions for producing specimens for fibre pull-out tests. It has also been demonstrated in chapter 4 that PP melt will undergo significant thermo-oxidative degradation when it is exposed to oxidative atmosphere (e.g. air) during sample preparation and concluded that samples have to be fabricated under inert atmosphere (e.g. nitrogen). Effects of residual thermal stress (RTS) on GF-PP adhesion is the main focus in chapter 5 and other factors mentioned above should be kept identical in order not to cause other complication to the work carried out in this chapter. Therefore, the conditions listed in Table 5.1 will be maintained for the sample preparation and the microbond test in Instron tensile testing machine (I-MBT).

Table 5.1 Conditions for sample preparation and MBT

	sample preparation				testing conditions			
	T_p (°C)	t_p (min)	atmosphere	cooling	L_{fr} (mm)	loading mode	loading rate	gap between edges (μm)
I-MBT	220	4	N_2	air	5	strain ramp	0.1 mm/min	$=D_f$
TMA-MBT	220	4	N_2	air	5	force ramp	0.15 N/min	$=D_f$

The specific procedure to form a PP microdroplet on a glass fibre in hot air and details for the room temperature I-MBT can be found in chapter 3 and will not be described here again. The formation of PP microdroplets under nitrogen has been

described in chapter 4 and will not be repeated. However, one of things worth mentioning is that the success rate of forming axisymmetric PP droplets under nitrogen is actually much lower than that in air, with only ~15% for the former and ~90% for the latter. This will be discussed in section 5.3. Only well-shaped, symmetrical droplets were selected for the experiments.

5.2.3. TMA-Microbond test (TMA-MBT)

In order to quantitatively correlate RTS with the GF-PP bond quality, the measurement of GF-PP adhesion needs to be carried out with different level of RTS. One of ways to vary RTS is to change the temperature of samples in testing (i.e. testing temperature, T_t). Assuming the stress free temperature is the same for all the samples, the temperature range, within which the RTS builds up, can be either increased by reducing T_t or decreased by increasing T_t. Considering the MBT described in chapter 3, this would at least require the sample and the microvise to be accommodated in a temperature-controlled chamber, which was not directly available with the facilities housed by the department. An alternative is to adapt the MBT configuration to fit into a well controlled temperature environment, which is routinely produced by some thermal analytical instruments. The possibility for such combination was recognised after examining a Thermomechanical Analyzer (TMA Q800EM from TA Instruments). Its film/fibre probe has been used in chapter 1 to successfully measure the coefficient of thermal expansion of a single glass fibre. This probe also has the potential to carry out the fibre pull-out test as shown in Figure 5.1.

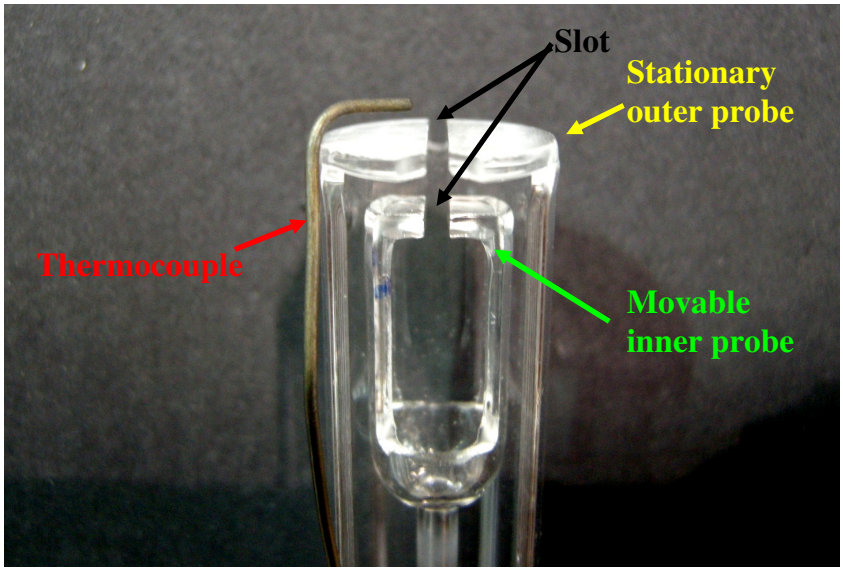

Fig. 5.1 Photo of TMA fibre/film probe

This system consists of two concentrically installed probes. The outer one is fixed on a flat stage, while the inner probe is driven up and down by a shaft. Both of them have a 1.2 mm slot on the top for supporting two clamps normally used at each end of the specimen when measuring the sample expansion coefficients as shown in chapter 1. Such a fixture provides the potential of conducting the MBT in TMA, where the resin droplet could sit on the outer stationary probe and the fibre could thread through both slots and end up with some attachment that can just fit under the slot of the inner movable probe. This leads to three main challenges that have to be overcome in carrying out the MBT in a TMA:

1. Sample mounting - how to connect the fibre to the inner movable quartz probe.

2. Droplet restraint - the width of the upper slot in the stationary quartz probe is approximately 1.2 mm which is much too large to engage the resin droplets with a normal diameter range of 40-400 μm.

3. Development of an appropriate TMA testing protocol for an instrument not initially designed for quasi-static tensile testing.

These challenges were met with the following solutions:

1. The TMA Q800 fibre/film probe is supplied with a pair of stainless steel clamps for gripping thin film samples and cleaved aluminium balls for gripping fibre samples. This clamping mechanism works quite well with tough materials such as polymer films and natural fibres. However, brittle 17μm diameter glass fibres do not survive such severe clamping. In addition, heavy clamps could give rise to underestimation of the maximum load for interfacial failure or premature sample failure because the weight of the clamps could excessively pre-strain the sample. Thus, the fibre was glued to the card tab as used in fibre pull-out samples. The card tab with one fibre end attached could be positioned under the slot of the inner probe, which was then able to pull the fibre downwards. It was found that two card tabs actually had to be used to sandwich the fibre end so that the fibre would not break because of bending at the joint during testing. Approximately 0.5 mN was applied on the fibre by the card tab, which is negligible in comparison to the normal debonding forces (e.g. 25–300 mN for neat GF-PP47 obtained in chapter 3).

2. To support the resin droplet in the TMA, a small shearing plate with a narrow slot was manufactured as presented in Figure 5.2. The shearing plate was machined using high carbon content stainless steel and consisted of three separate parts, as shown in Figure 5.2(a). The bar on the top was used to integrate other two bars in the same plane. The shearing edges were created in

the same way as the shearing plates in the microvise. Two plates had been polished to form a sharp edge along one of the surfaces. Instead of having a pair of parallel loading edges, a small angle of approximately 1.2° was deliberately left between these knife plates to facilitate sliding of the fibre (i.e. the sample) into the gap. Moreover, this arrangement gave a varying distance between two loading edges from 95µm–0µm, which completely covered the range of fibre diameters (i.e. 15.5µm–22.5µm) encountered in this work. This ensured that the contact between the fibre and the loading edges could always be achieved for any fibres. Compared to parallel shearing plates, this small angle leads to the difference of 0.33% in the fibre perimeter in loading points around the fibre on each side. For the maximum fibre diameter in, approximately 22 µm, the difference in the arc length between two loading points of the parallel plate and that of the angled plate is only 0.23 µm. Consequently, this slight non-parallel alignment of the shearing plate edges was not expected to make any significant difference in the loading pattern of the resin droplet in comparison with the conventional parallel slot. The TMA-shearing plate was small enough to be positioned on the top of the stationery quartz probe. No clamp is required to hold the plate on the probe.

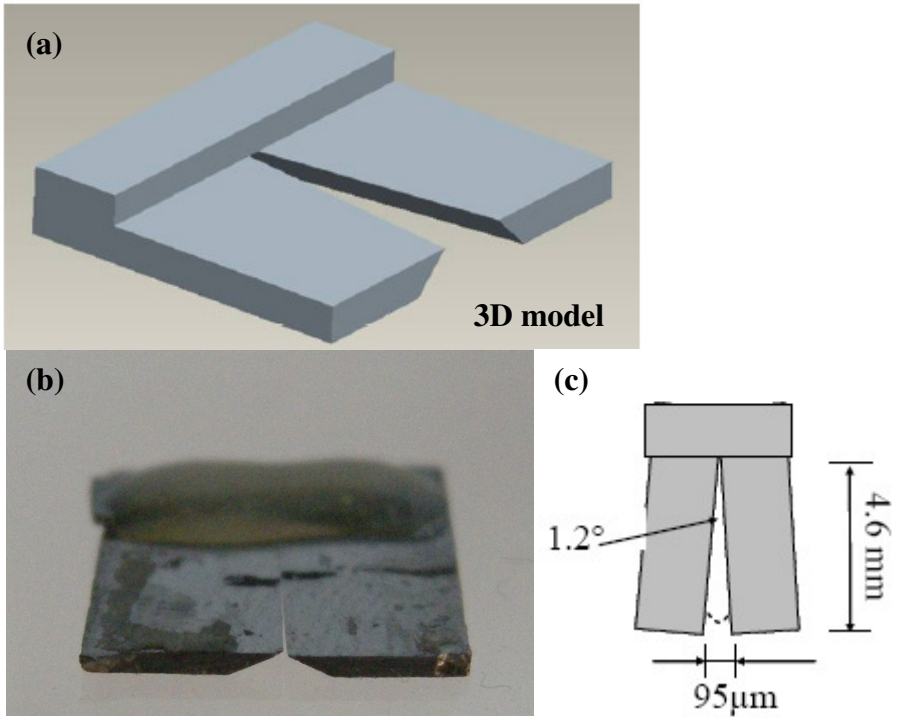

Fig. 5.2 TMA-MBT shearing plate (a) model, (b) photo, and (c) dimensions

3. The TMA configuration proved to be a tricky part in the process of achieving TMA-MBT since this instrument was intended for the measurement of length change with the temperature not for conducting the MBT. In a normal TMA test with the film/fibre probe in use, two steps have to be programmed to allow an experiment to run. They are zero initiation and initial length measurement. In zero initiation, the inner probe rises until it makes contact with the bottom of the outer probe. The screen then displays the thickness of the two stages of the probes. In initial length measurement, the inner probe drops until it makes contact with the sample (i.e. the card tab in TMA-MBT) and applies a static pre-load on the sample to remove the slack of the fibre or film and put them under slight tension. The choice of this parameter mainly depends on mechanical properties of materials to be tested. In the case of

TMA-MBT, the pre-load should be significantly smaller than the maximum load for interfacial failure, even though it will be automatically incorporated into the applied force upon the start of testing. In fact, it is desirable to set the pre-load to be as small as possible because, firstly, the loading process should be free of pre-loading for the sake of comparison between I-MBT and TMA-MBT; secondly, significant creep may be caused by a long period of static loading, especially when the test is carried out at elevated temperatures; and thirdly, sudden loading may cause damage to the sample and lead to a premature failure. However, it was found that a small load was not enough to register the presence of the sample and stabilise the probe on the card tab because the probe could be readily bounced away while it was trying to press down the card tab to carry out the initial length measurement. Furthermore, the vibration resulting from the movement of closing the furnace tends to disturb the inner probe with the small pre-load and makes it move up again. In order to completely solve this problem, the process of the length measurement was tricked by providing an artificial resistance to the inner probe movement as shown in Figure 5.3. After zero initiation, the sample was amounted into the shearing plate. A piece of string was attached to the probe-locking lever, which moves along with the inner probe. The string was gently strained and kept under a metal block as shown in Figure 5.3. In this way the inner probe would stay at the zero initiation position when carrying out length measurement. In other words, after the length measurement the TMA would "think" that the initial sample length was equal to the thickness of the two stages of the probes. The furnace was then closed and the set temperature was

reached while the inner probe was still being held. It was not until 30 seconds before the load was going to be applied to the sample that the inner probe was slowly released by relaxing the string. The inner probe would then gently land on the card tab and apply the pre-load on the sample. The advantages of using this method includes:(a) easy to use, (b) no modification to TMA, (c) free of potential damage caused by the length measurement process and (d) free of pre-load until a few seconds before testing. The minimum pre-load of 1 mN was used in TMA-MBT.

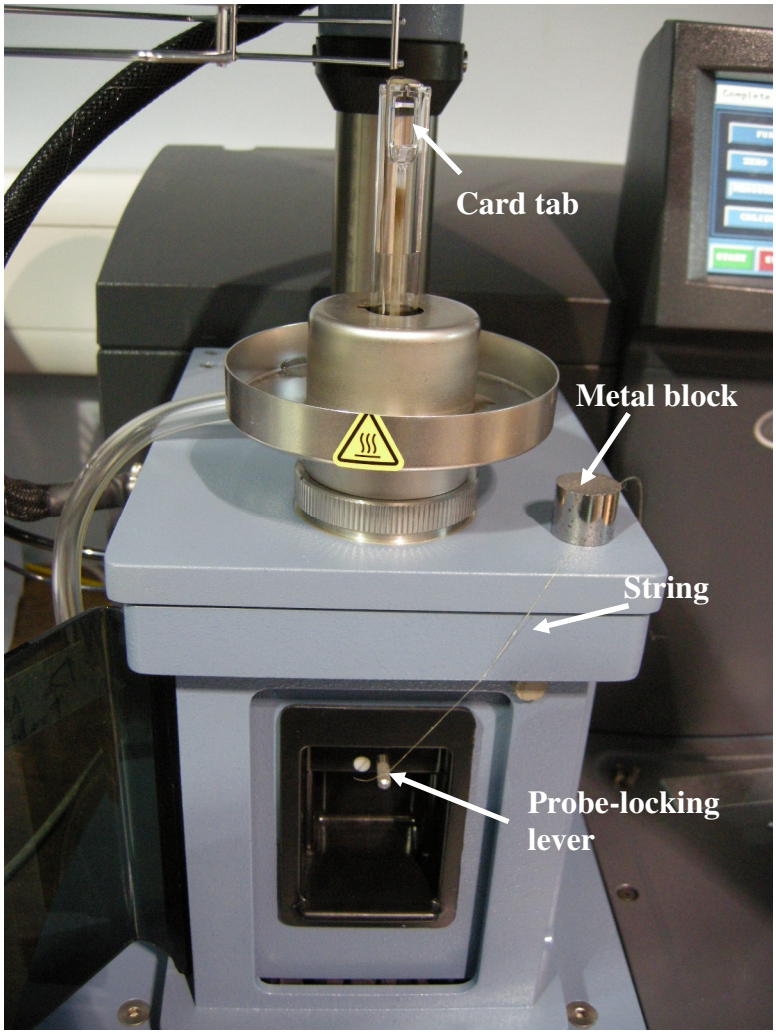

Fig. 5.3 Setup for length measurement in TMA-MBT

The I-MBT is carried out by measuring the load generated during the displacement of the free fibre end at constant rate (i.e. linear strain ramp), however, this mode could not be employed in TMA-MBT because the load generated during strain ramp with the same rate as in I-MBT somehow could not be recorded continuously, but in a stepwise manner as shown in Figure 5.4. This unexpected behaviour was not associated with the data readout speed. No real solutions were provided after consulting the technical service of the TMA manufacturer. Consequently, the TMA had to be configured to measure sample displacement during a linear force ramp. It can be seen from Figure 3.8 in chapter 3 that the rate of force increase in I-MBT force-displacement plot is approximately linear during most of the strain ramp up to the debonding force. The loading rate can be obtained from the slope of the force-displacement, which depends on extension rate and the stiffness of the entire fixture. The average value of the slope of the force-displacement curve for the measurements on MBT samples made under nitrogen was found to be 0.15 N/min. In order to keep the TMA-MBT as comparable as possible to the I-MBT we therefore adopted 0.15 N/min as the applied force ramp rate in the TMA-MBT.

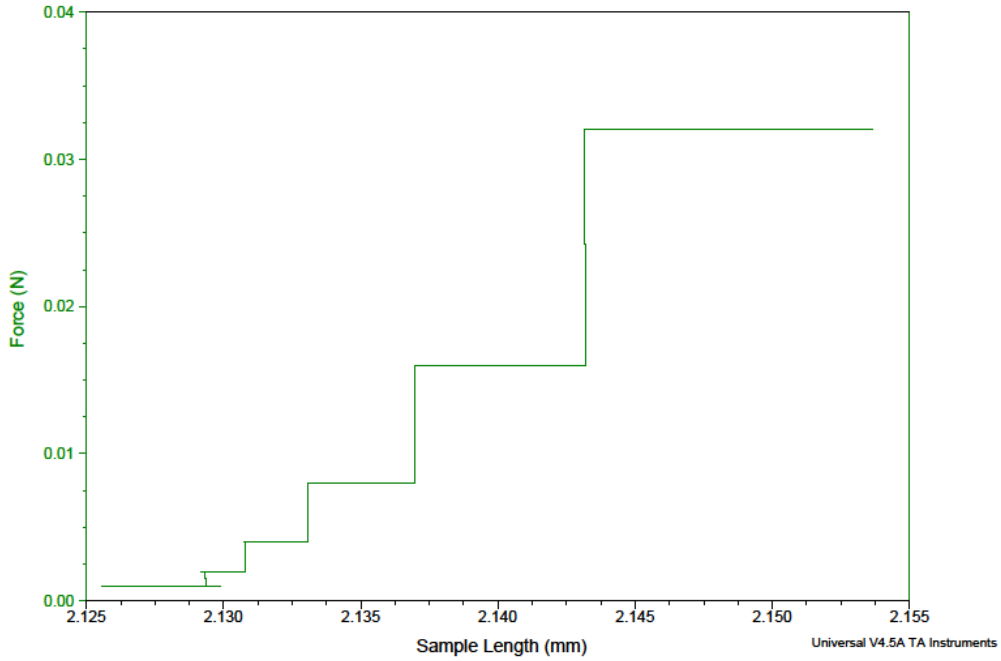

Fig. 5.4 Plot of force vs. sample length in TMA-MBT under strain ramp

The measurement protocol then proceeded as follows (see Figure 5.5).

(1) The probe displacement was electronically zeroed.

(2) The single fibre microdroplet sample was loaded into the shearing plate with the lower card tab hanging freely below the movable quartz probe.

(3) With the movable probe immobilised above the card tab, the furnace was closed. The initial sample length and probe position was recorded.

(4) The sample temperature was equilibrated at the desired test temperature (in the -40ºC to 100ºC range) with an addition 3-5 minutes isothermal segment to ensure a constant equilibrium temperature was attained.

(5) The movable inner probe was then lowered very gently to contact the card tab and the force ramp was initiated at 0.15 N/min.

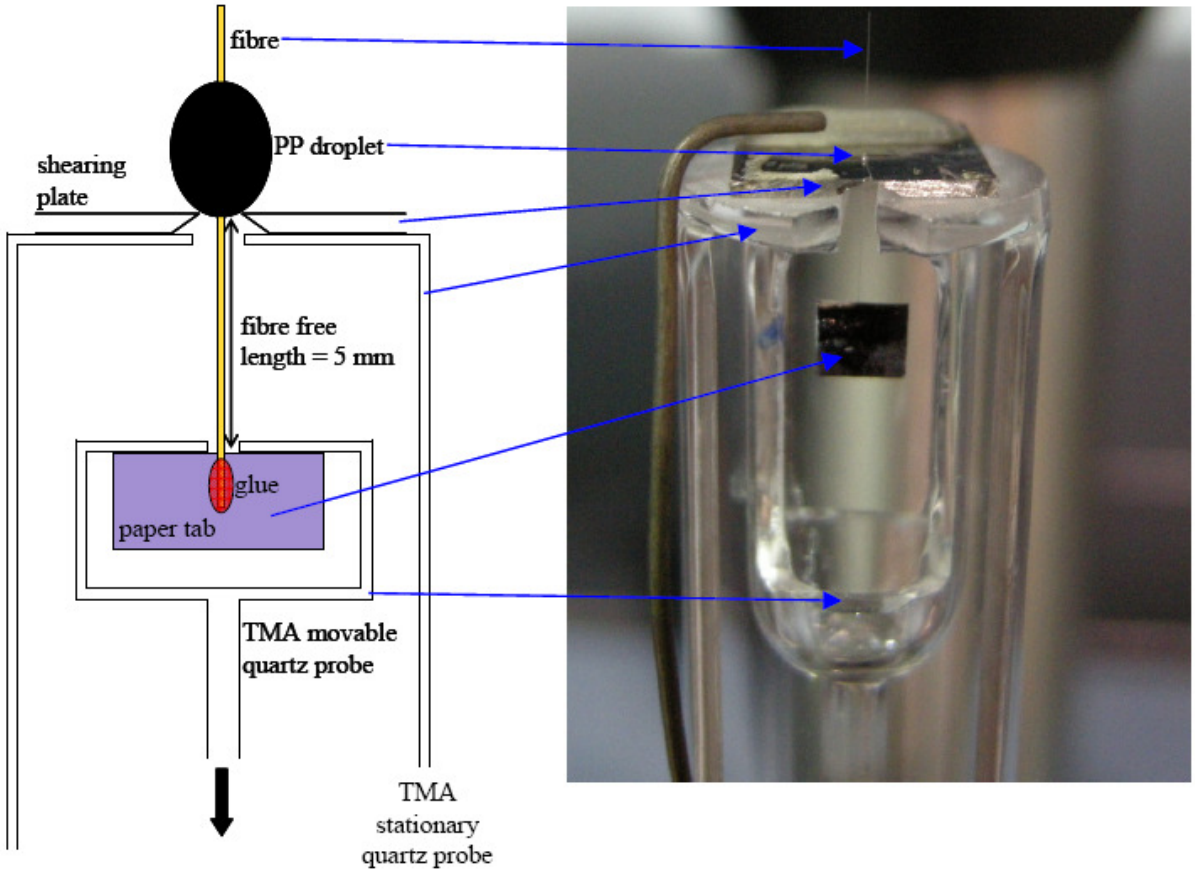

Fig. 5.5 Schematic and close up photograph of the TMA-MBT test configuration

The increasing probe displacement was then recorded until debonding occurred. A typical result obtained from a TMA-MBT test is plotted as a force-displacement curve in Figure 5.6.

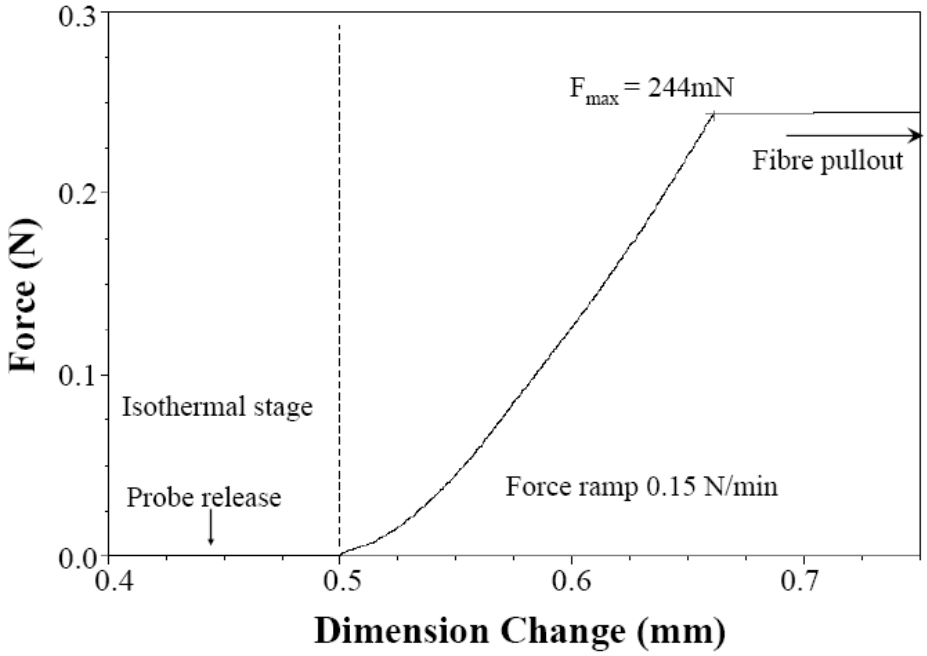

Fig. 5.6 Load-displacement curve from a typical TMA-MBT test

The general form of the curve is clearly different than that obtained in I-MBT. However, the maximum value of force required to obtain a full debonding event is still obtained. The major difference is what occurs after debonding. Since the TMA continues to attempt to increase the applied force above F_{max} after debonding there is a rapid downward displacement of the debonded fibre, which is approximately 2 mm. Consequently, in this test configuration, there can be no further information obtained on post-debonding dynamic friction in a similar manner to I-MBT.

The TMA-MBT was carried out at five different temperatures (-40°C, 0°C, 20°C, 40°C, and 100°C) and ~30 data points were collected for each set. The uncoated glass fibres became more fragile after extra handling from sample preparation. Fibre breakage often occurred during testing especially when TMA-MBT was performed under subambient temperatures due to the increase of fibre-matrix adhesion. Many samples had to be wasted to obtain the decent number of data points. What made the

test even much more time-consuming was the extremely low success rate of droplet formation under nitrogen. It was because of these disadvantages that we decided to use the specimens repeatedly. The nature of thermoplastic polymer allowed debonded PP microdroplets to be reshaped at elevated temperature. Additional thermal treatment under the conditions applied in this work was unlikely to alter the results for measured interfacial shear strength (IFSS), τ_{ult}, as indicated by the results in chapter 3. The bond between the fibre and the matrix was formed at the new fibre surface, which was ~2 mm away from the debonded surface. After test, the free fibre length, L_{fr}, was enlarged up to 7 mm and readjust back to 5 mm by detaching the fibre from the card tab and re-gluing it on the card tab.

5.3 Results and discussion

5.3.1 PP Droplet formation under nitrogen

It proved extremely difficult to actually form an axially symmetric PP47 microdroplet on a glass fibre under nitrogen. Only a few out of dozens of samples treated at 220°C under nitrogen for 4 minutes could offer the axisymmetric droplets for the MBT. Considerable time extension for heating process did not seem to bring about any improvement to the droplet yield. Figure 5.7 presents the photos of various axially asymmetric PP47 microdroplets after total 270 minutes heat treatment, which was stopped at 4, 15, 30, 60, 120, and 270 minutes respectively to examine the droplet yield.

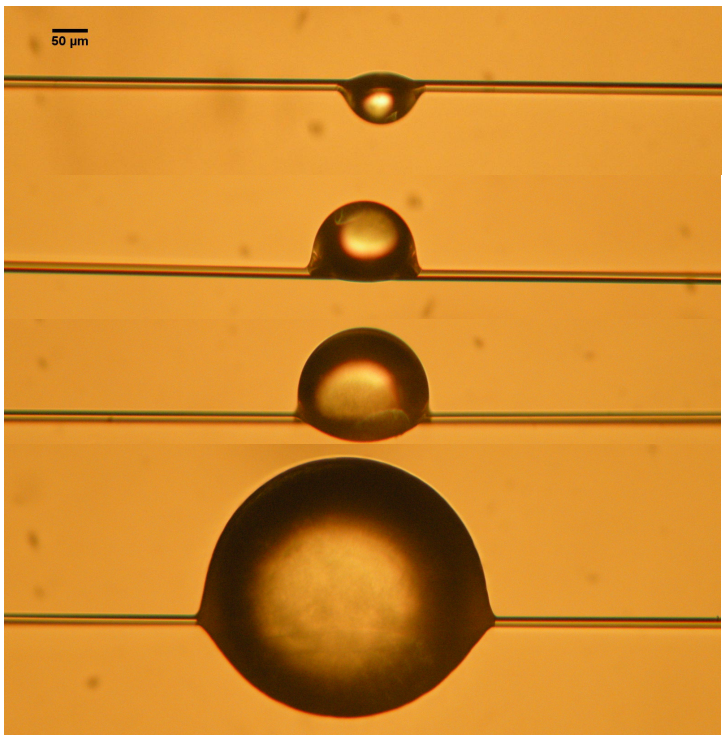

Fig. 5.7 Micrographs of various axially asymmetric PP47 microdroplets after 270 minutes heat treatment

It was found that there were 5 droplets formed out of 42 samples in 4 minutes and no droplet formed afterwards. It raises the question that if such a prolonged period of heating did not produce any more droplets, why any droplet should be formed at all in the first 4 minutes and whether those testable PP microdroplets represent the PP47 matrix.

It has been known that there are two types of equilibrium conformations of a small liquid drop on a cylindrical fibre: barrel shape and clam-shell shape [27-31]. For a given system, the transition between these two shapes, also called roll-up process, depends on the reduced volume, which is the ratio of the droplet volume to the fibre radius. Large reduced volume favours the barrel shape and clam-shell shape is the preferred conformation when the reduced volume is small [28]. The critical value of this reduced volume for the shape transition to occur is dependent on the equilibrium

contact angle [28]. However, it can be seen from Figure 5.7 that axially asymmetric droplets on fibres in this case may not be related to such shape transition since it occurred to the droplets with various volumes. It may not be attributed to the wettability of PP melt to glass fibre either due to the fact that zero equilibrium contact angle is normally found for this system [32, 33].

In chapter 3, Figure 3.10 exhibits a clam-shell shaped droplet, which appears not to fully wrap up the fibre. Physically the droplet will tend to form the barrel shape if the fibre surface is completely included in a liquid droplet. However, it is impossible to see these details in Figure 5.7. Nevertheless, let us assume some fibre surface is fully included in asymmetric liquid droplet as shown in Figure 5.8.

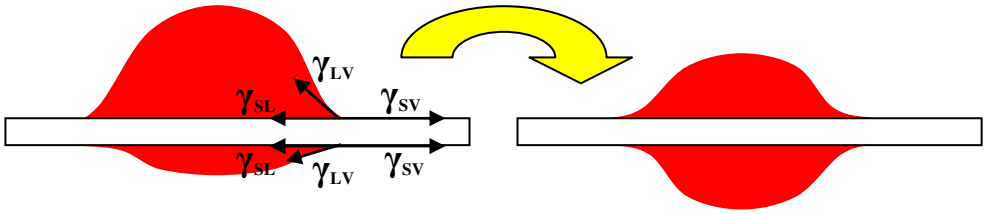

Fig. 5.8 Schematic illustration of the formation of the axisymmetric droplet

The contact line of the larger resin volume will correspond to a contact angle greater than the equilibrium one, while a contact angle smaller than the equilibrium one will be found at the contact line of the smaller resin volume. To achieve the mechanical equilibrium around the entire contact line, excessive liquid resin will flow into the other side to form a symmetric droplet shape with respect to the fibre axis as shown in Figure 5.8. For a given system and thermal conditions, the time for such transformation will be strongly affected by the polymer viscosity. The higher viscosity is, the more time is required to form symmetric droplet on a fibre. Figure 5.9 displays two PP47 microdroplets on the same glass fibre heated at 220°C in air.

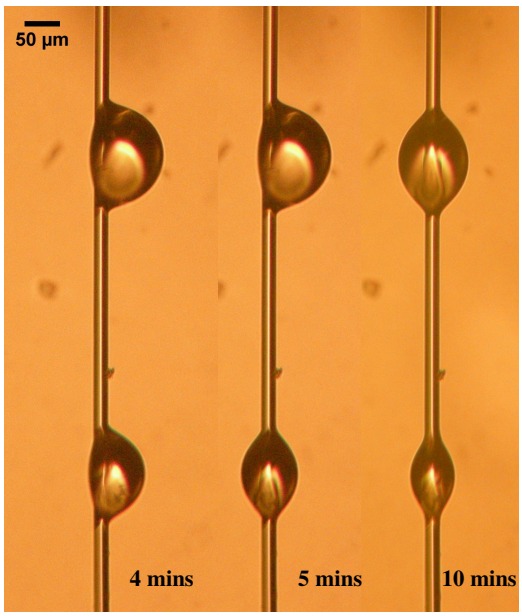

Fig. 5.9 Micrographs of two PP47 microdroplets heated at 220° in air

As discussed in chapter 4, the smaller droplet degraded faster than the larger one due to different surface to volume ratio. Therefore, the molecular weight and in turn the viscosity of the smaller droplet decreased faster and form the axially symmetric shape significantly earlier than the opponent. It is therefore reasonable to state that the shape of PP47 droplet on a fibre could be strongly affected by the polymer viscosity. Note that PP47 is actually a relatively low molecular weight polymer.

From the discussion above, the possibilities for those droplets formed under nitrogen within 4 minutes may involve (a) some of fibre surface had been fully included in the PP melt upon melting and (b) the PP samples had contained some residual peroxides, which oxidised the polymer and led to polymer degradation and reduction in viscosity. The former may depends on how the PP fibre deforms upon melting and can be affected by the way the PP fibre coils up and wraps up the fibre. Such behaviour is influenced by the dimensions of PP fibres. Raising processing

temperature may give higher droplet yield. However, to maintain the same conditions in sample preparation throughout this project, this change was not made in this work.

5.3.2 Comparison between I-MBT and TMA-MBT

Results of F_{max} versus embedded area, A_e obtained for GF-PP47 samples, prepared under nitrogen, using the I-MBT and the TMA-MBT at room temperature are shown in Figure 5.10.

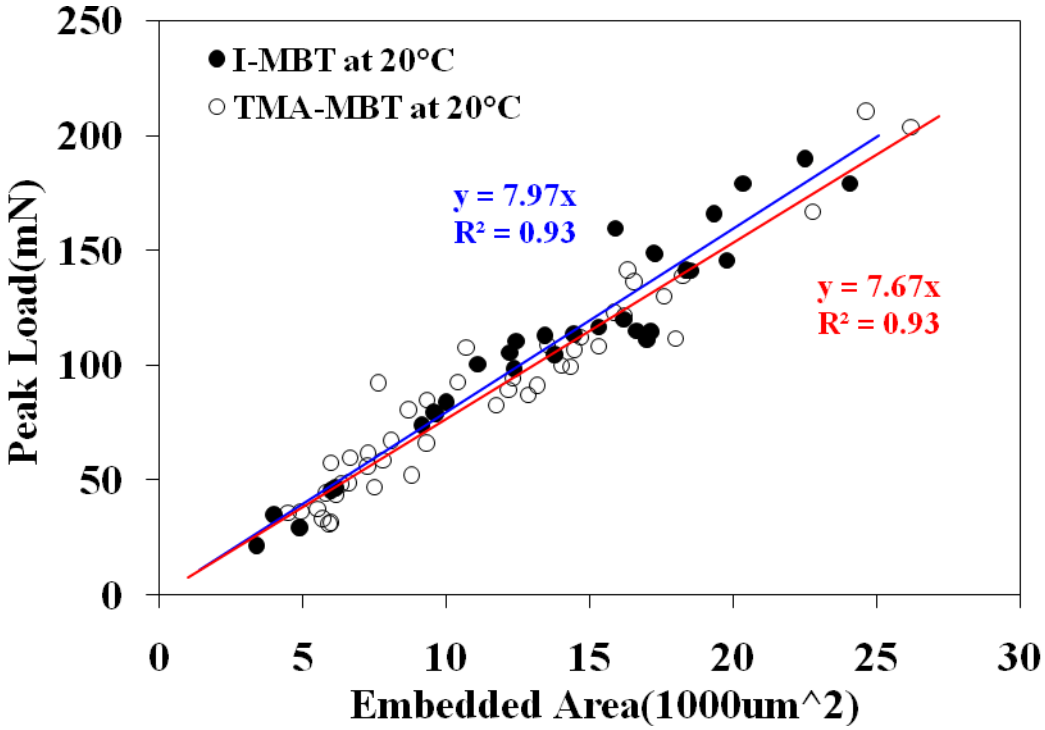

Fig. 5.10 Comparison of results for GF-PP obtained from I-MBT and TMA-MBT

It is noticeable that the two data sets completely overlap with each other and both data sets clearly exhibit a significant linear relationship with a low level of scatter and high value of R^2. The linear least square fitted lines illustrated give a value for apparent IFSS, τ_{app}, equal to 8.0 and 7.7 MPa respectively in GF-PP47 system. It can be seen that the comparison of the two test configurations indicates an excellent level

of reproducibility of the measured IFSS of PP with bare glass fibres. Therefore, the results from two techniques have been pooled and presented in chapter 3. Both extrapolated lines pass through the origin as predicted from Equation 3.4 and the frictional mechanism may account for the GF-PP47 adhesion as discussed in chapter 3. Thus, $\tau_{ult=} \tau_{app}$ for the GF-PP47 system.

5.3.3 Temperature dependence of measured IFSS

Due to the significant inefficiency in forming the axisymmetric PP47 droplet for MBT, the tested specimens were reused as described in section 5.2. TMA-MBT was carried out from high temperature (100°C) to low temperature (-40°C) in sequence in order to maximise the use of the samples. Newly made samples were also added to gradually increase the total number of the testable samples because it became more likely to encounter fibre fracture during testing as the test temperature, T_t, decreased. Many samples tested at subambient temperatures failed to produce interfacial failure before the fibre breakage, which led to relatively less data points than expected.

The TMA-MBT results for F_{max} versus embedded area obtained for this system at five different T_t in the range -40°C to 100°C are shown in Figure 5.11.

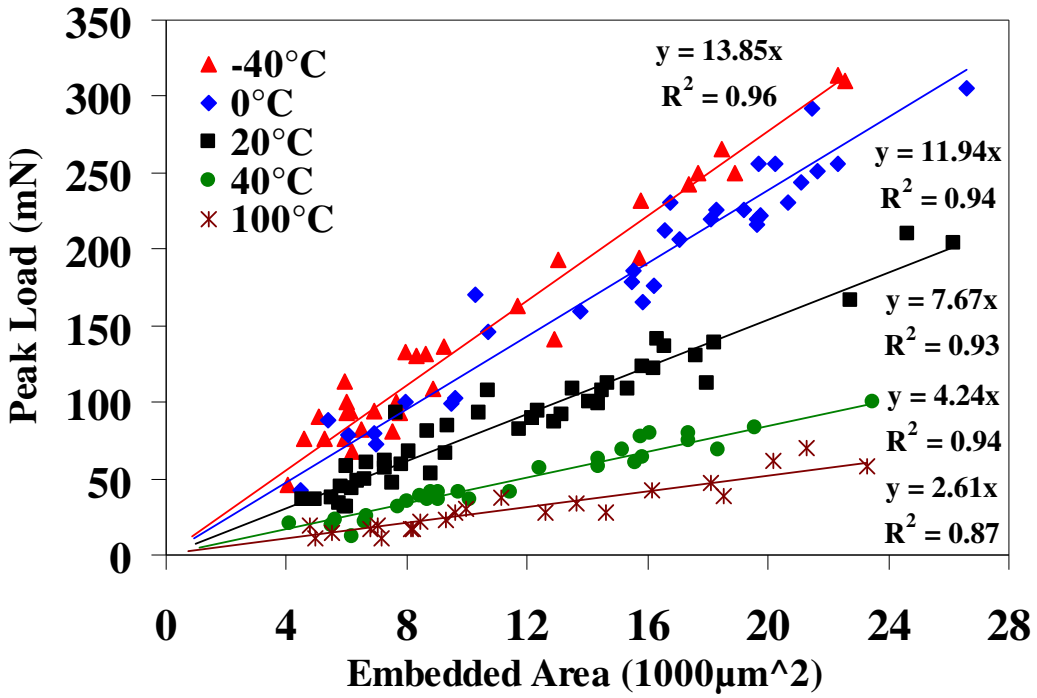

Fig. 5.11 TMA-MBT peak load versus embedded area for GF-PP47 at various test temperatures

Once again the data for each T_t exhibit a strong linear relationship with a low level of scatter, high values of R^2, and all extrapolated lines pass through the origin as predicted from Equation 3.4. It is a bit surprising to see that the high values of R^2 were also obtained at subambient temperatures (i.e. 0°C and -40°C), which lie below PP glass transition temperature ($T_g \approx 2$°C) as reported in chapter 2. Ductile interfacial fracture during I-MBT at room temperature was assumed in chapter 3, although the estimated matrix yielding strength appeared to be much higher than measured IFSS for GF-PP47. However, the mechanical properties of the interface may be different from the bulk matrix. Below T_g, the polymer matrix becomes more brittle and jeopardise the validity of the assumption of uniform shear stress at the interface. Nevertheless, simple linear least square technique seems to be the best fit to the results obtained from TMA-MBT at all test temperatures as seen in Figure 5.11.

The results for IFSS obtained for this system at five different T_t in the range -40°C to 100°C are summarised in Figure 5.12, which shows the average values of apparent IFSS (with 95% confidence limits) plotted versus the testing temperature.

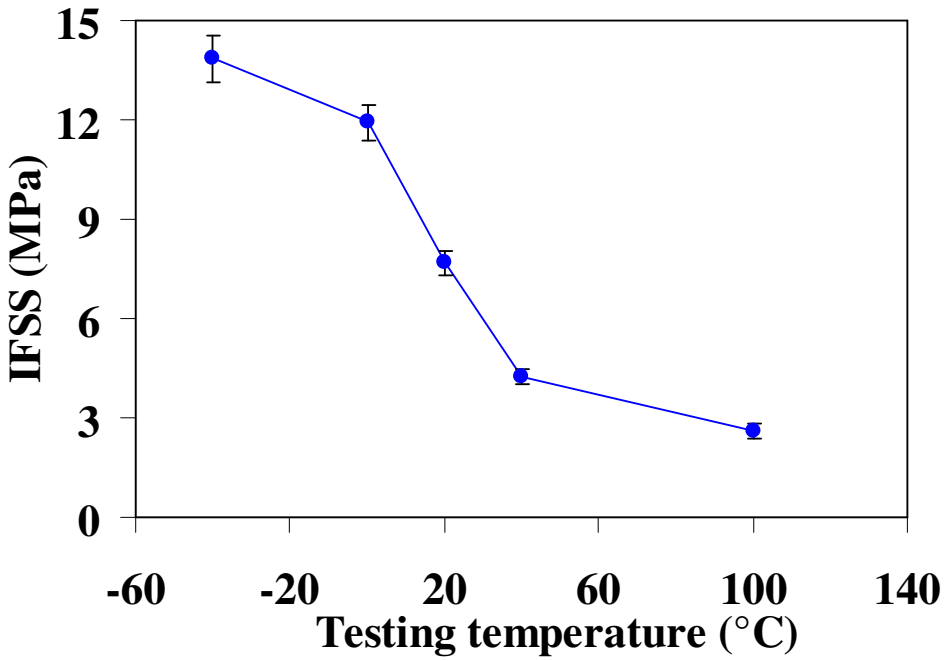

Fig. 5.12 Dependence of IFSS of GF-PP47 on test temperature

It is clear that the IFSS of GF-PP is significantly dependent on testing temperature. It is worth noting that the rate of change of IFSS with temperature is highest around room temperature (approximately 0.2 MPa/°C at 20°C). It is well known that the scatter in the measurement of IFSS using the MBT can often be quite high. The results in Figure 5.12 indicate that, at least with PP matrices, small variations of the sample test temperature could contribute significantly to observed scatter in the results for IFSS. Although no measurements of IFSS have been carried out at the stress free temperature (120°C for GF-PP47 based on DSC results in chapter 2), at which the residual thermal stress starts building up, the trend seems to show the contribution mainly from actual adhesion component between the bare glass fibre

and the PP47 may account for almost 30% of measured IFSS at room temperature. Consequently the value of 2.1 MPa is assumed for the IFSS of GF-PP47 at 120°C.

Varying sample temperature through controlling T_p can change the magnitude of residual thermal stress (RTS) in the sample. From the results above, one can see that RTS does play a significant role in stress transfer capacity of the fibre-matrix interface. One of possibilities is related to the compressive radial residual stress (CRRS), σ_{rad}, acting perpendicularly across the interface. Analytical studies of the distribution of σ_{rad} in a unit composite have been carried out by a number of authors and have been reviewed in section 5.1. Based on experimental results obtained in this work, a simple linear model is first used to estimate σ_{rad} [34-36]:

$$\sigma_{rad} = \frac{(\alpha_m - \alpha_f)(T_t - T_{ref})E_m}{1 + \nu_m + \frac{1-\nu_f}{E_f}} \quad (5\text{-}1)$$

where α_f and α_m are coefficient of thermal expansion of the fibre and the matrix respectively; ν_f and ν_m are Poisson's ratio of the fibre and the matrix respectively. When the magnitude of E_f is very high, Equation (5.1) is normally reduced to

$$\sigma_{rad} \approx (\alpha_m - \alpha_f)(T_t - T_{ref})E_m \quad (5.2)$$

The situation in which the materials have temperature dependent mechanical properties can be handled by

$$\sigma_{rad} = \int_{T_{ref}}^{T_t} \sigma_{rad}(T)dT \quad (5.3)$$

The above equations do not take into account the dependence of σ_{rad} on fibre volume fraction, V_f.

In addition, the concentric cylinder model is also employed to calculate the RTS in GF-PP47. The model assumes that infinitely long solid cylindrical fibre is concentrically assembled with the infinitely long hollow cylindrical interphase (if there is one) and matrix. It is also assumed that all components are linearly elastic and possess perfect bonding between them. In this work, we assume there is no such interphase between the glass fibre and PP matrix and both components are isotropic. Glass fibre properties are temperature dependent but on an insignificant scale and can be considered constant in the temperature range studied in this work. The elastic modulus of the glass fibre was measured by the standard single fibre tension test at room temperature and the coefficient of linear thermal expansion (CLTE) of the glass fibre was also obtained in chapter 1. The temperature dependence of elastic modulus and CLTE of PP47 was obtained from the thermo-mechanical characterisation of non-degraded PP47 in chapter 2. The stress free temperature was set to be the crystallisation temperature determined by DSC analysis in chapter 2, which showed the matrix solidification process of PP began when the temperature dropped below 120°C. This may be indirectly supported by the observation of contraction behaviour of the PP microdroplet during cooling process shown in Figure 5.13.

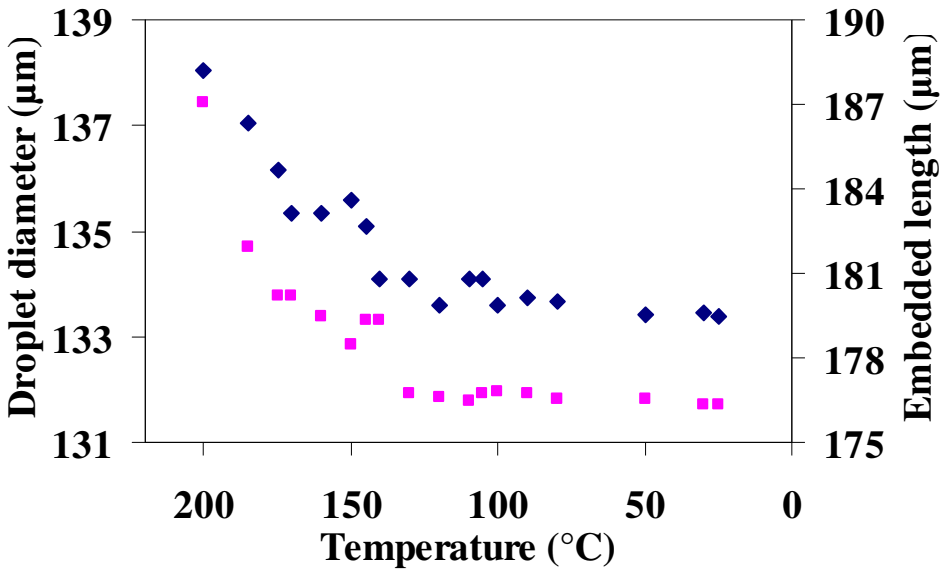

Fig. 5.13 Contraction behaviour of PP microdroplet during cooling process at 20°C/min

This PP droplet was formed on a single glass fibre in the hot-stage as described in chapter 4 and cooled down at 20°C/min. It can be seen from Figure 5.13 that the contraction proceeds rapidly above 120°C and gradually levels out after that. It indicates that the matrix starts to gain solid-like character early in the crystallisation region and implies that constrained shrinkage is likely to be large, resulting in large residual stresses. Otherwise, dimensional changes may still be significant after 120°C. Finally, the radii for internal and external cylinders were set to be 9 µm and 160 µm, which are average values of the fibre diameter and the maximum diameter of PP microdroplet respectively. These inputs for the calculation of CRRS in GF-PP47 are summarised in Table 5.2.

Table 5.2 Properties of glass fibre and polypropylene

Property	Glass Fibre	Polypropylene
Young's modulus (GPa)	78.70	Dependent on T_t
Poisson's ratio	0.22	0.35
CLTE (µm/(m·°C)	4.8	Dependent on T_t
Volume fraction (%)	0.3	99.7

The calculation derivation for the cylinder model can be found in Appendix (E). The calculation was carried out in Matlab®R2010b software and the code can be found in Appendix (F).

As discussed in chapter 3, the combination of σ_{rad} and physiochemical interaction at the interface (i.e. adhesive component) may fully account for the measured IFSS on a basis of the coulomb friction law. For the sake of simplicity, we first assume that these two components are independent from each other and the Equation 3.9 can then be extended into

$$\tau_{ult} = \mu_{st}\sigma_n = \mu_{st}(\sigma_0 + \sigma_{rad}) = \tau_{ult}(T_{ref}) + \mu_{st}\sigma_{rad} \qquad (5.4)$$

where μ_{st} is the coefficient of static friction (CSF) and σ_0 is the interfacial normal stress purely resulting from molecular interaction between the fibre and the matrix. In this sense, $\tau_{ult}(T_{ref}) = \mu_{st}\sigma_0$ when the test temperature is equal to the reference temperature, at which σ_{rad} is expected to be zero.

Figure 5.14 shows the comparison between the measured IFSS using TMA-MBT and the calculated IFSS using Equation (5.4), in which σ_{rad} is determined by Equation (5.3), different values μ_{st} are used to fit the results, and $\tau_{ult}(T_{ref})$=2.1 MPa.

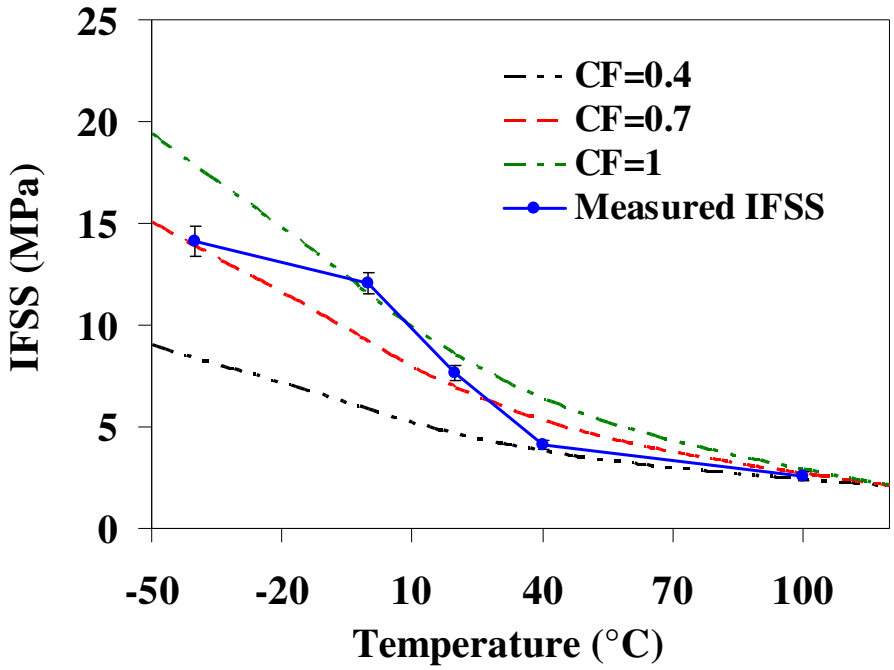

Fig. 5.14 Comparison between measured IFSS using TMA-MBT and calculated IFSS based on the linear model

It can be seen that the calculated IFSS builds up significantly as the temperature is lowered. Furthermore, the experimental IFSS data fall well within the range of calculated IFSS for μ_{st}=0.4-1.0, which almost lies in the CSF range of 0.27±0.03 to 0.97±0.01 estimated in chapter 3. The detailed dependence of the IFSS on temperature will clearly require further investigation; however it is clear that there is a strong dependence of the IFSS in GF-PP on the test temperature. As indicated in Equation (5.4), this could be interpreted as direct evidence of the importance of σ_{rad} on the stress transfer capabilities of the interface.

Figure 5.15 displays the comparison between the measured IFSS using TMA-MBT and the calculated IFSS based on the cylinder model.

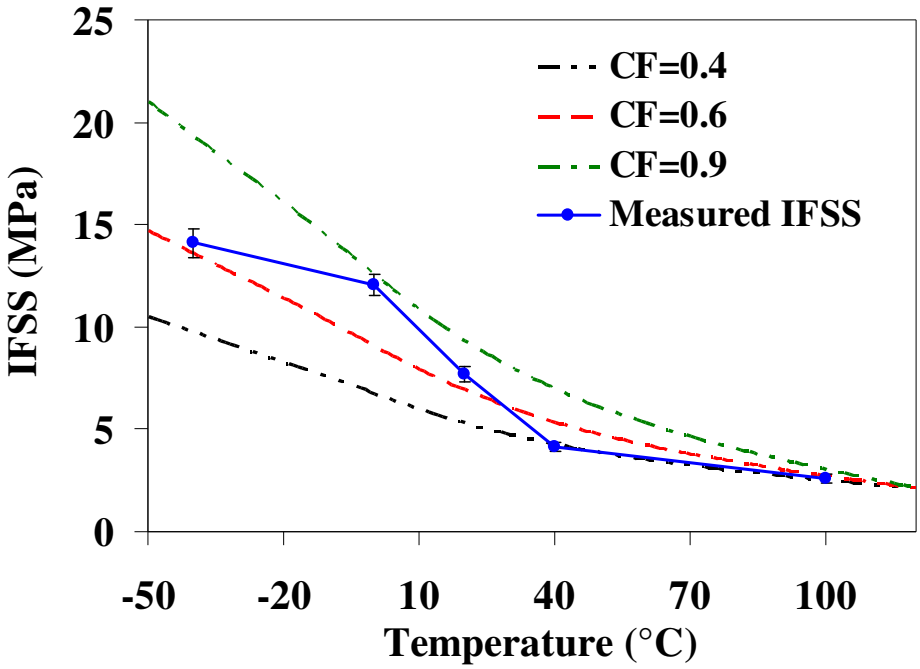

Fig. 5.15 Comparison between measured IFSS using TMA-MBT and calculated IFSS based on the cylinder model

The model shows the significant increase in calculated IFSS as the temperature decreases. Measured IFSS data fall well within the range of calculated IFSS for μ_{st}=0.4-0.9, which completely lies in the CSF range estimated in chapter 3. This is not surprising since the upper boundary of μ_{st} is actually obtained based on the cylinder model too. From the results presented in Figure 5.14 and Figure 5.15, it is reasonable to say that the simple linear model can fit the experimental results as well as the more complex cylinder model. Nevertheless, the cylinder model allows us to easily examine the effects of V_f on the rate of σ_{rad} build-up and cumulated σ_{rad} as a function of temperature (see Figure 5.16 and Figure 5.17).

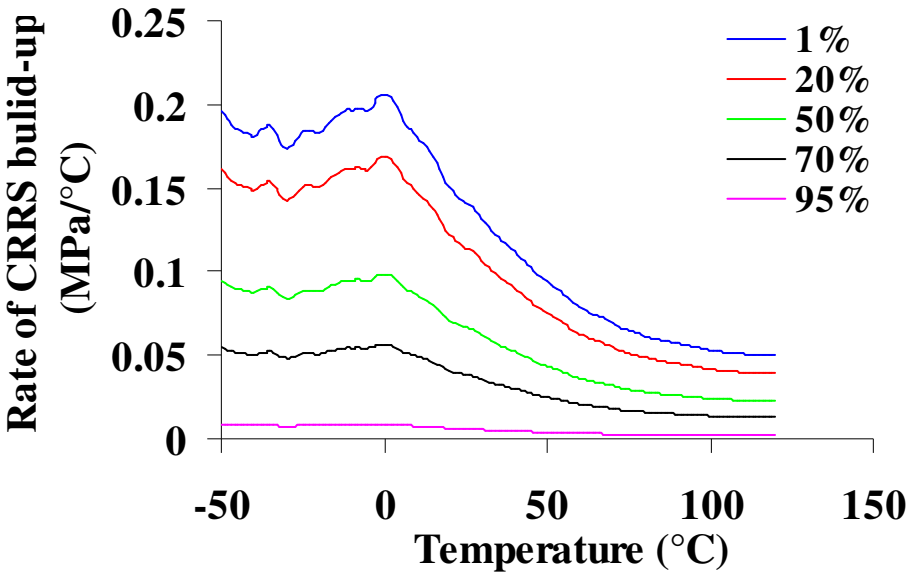

Fig. 5.16 Rate of compressive radial residual stress (CRRS) as a function of temperature in GF-PP47 with various fibre volume fraction

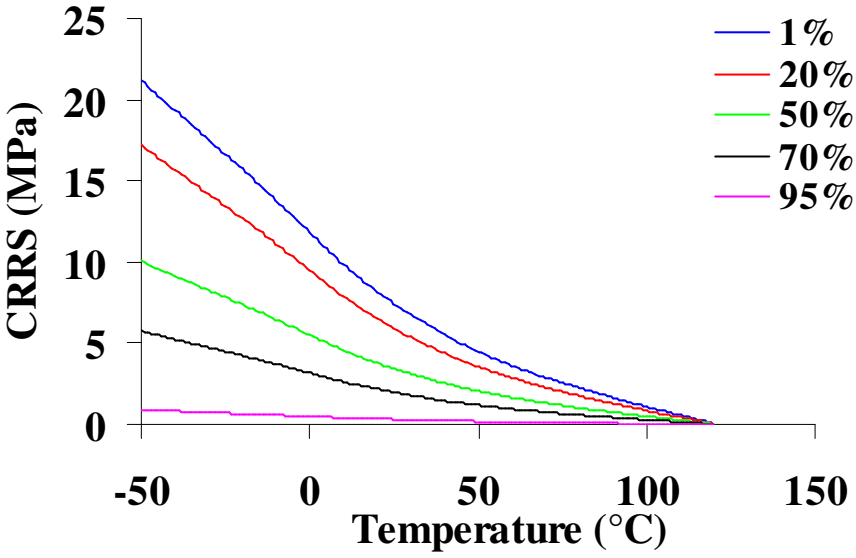

Fig. 5.17 CRRS as a function of temperature in GF-PP47 with various fibre volume fraction

The overall trend of each curve in Figure 5.16 is the same, with the rate increasing with the increase of temperature before T_g and dramatically decreasing after T_g. Thus, the highest rate for σ_{rad} build-up per degree appears at T_g. This is the result of

opposite dependence of E_m and CLTE on the temperature as shown in Figure 5.18 for PP47. It is also clear that the rate is strongly affected by V_f, with high rate corresponding to low V_f. The same dependence of σ_{rad} on V_f can be found in Figure 5.17. The effect of V_f on σ_{rad} in GF-PP47 at various temperatures can be more directly seen in Figure 5.19 with V_f presented in the logarithmic scale.

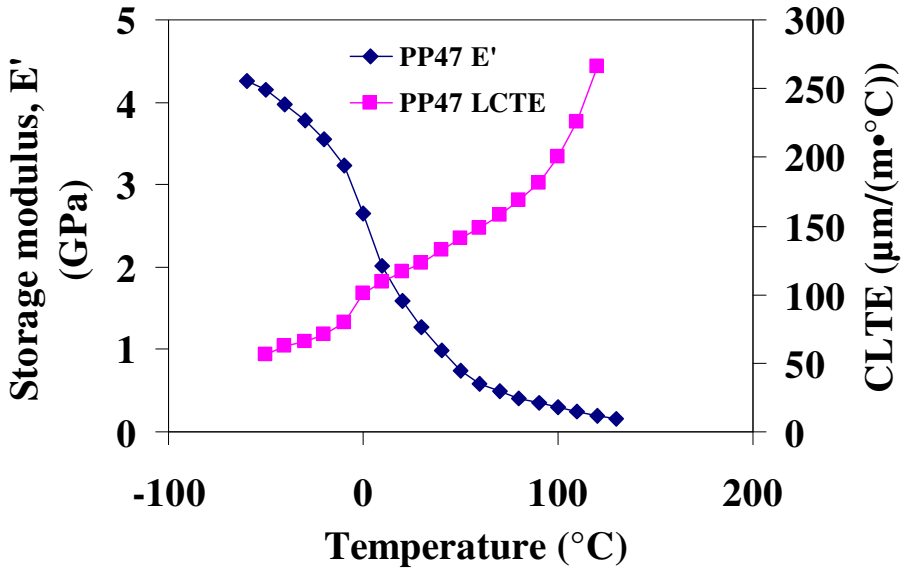

Fig. 5.18 Dependence of storage modulus and coefficient of linear thermal expansion of PP47 on temperature measured by DMA and TMA respectively

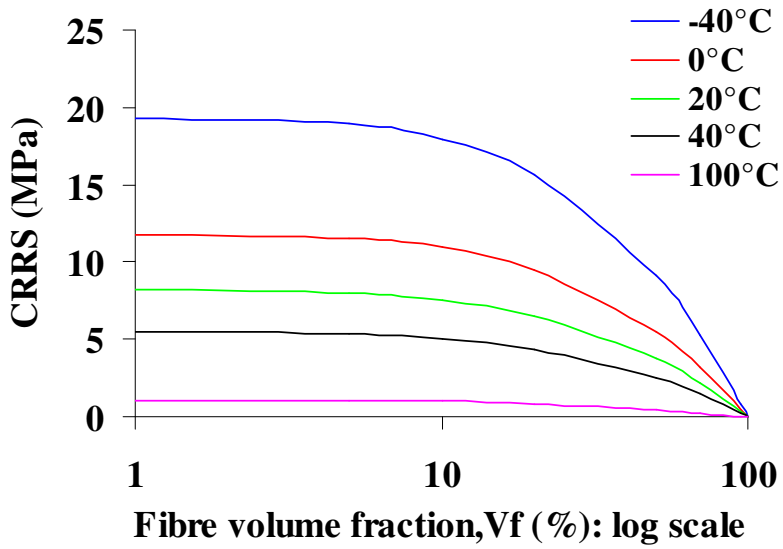

Fig. 5.19 Dependence of CRRS on fibre volume fraction at various temperatures

It shows that σ_{rad} will decrease as V_f increases but this effect is insignificant until V_f reaches approximately 10% at various test temperatures applied in this work. V_f in most of microbond samples used in TMA-MBT is even less than 5%. This means that the variation of σ_{rad} caused by different V_f in microbond samples may be negligible. Although it is not obviously presented in Figure 5.19, σ_{rad} actually linearly decrease with V_f after 10%. The slope of linear fitting line to each curve gives the amount of reduced σ_{rad} due to 1% increase of V_f. It is can be seen from Figure 5.19 that the value of this slope should also be significantly influenced by temperature. The relation between them is presented in Figure 5.20.

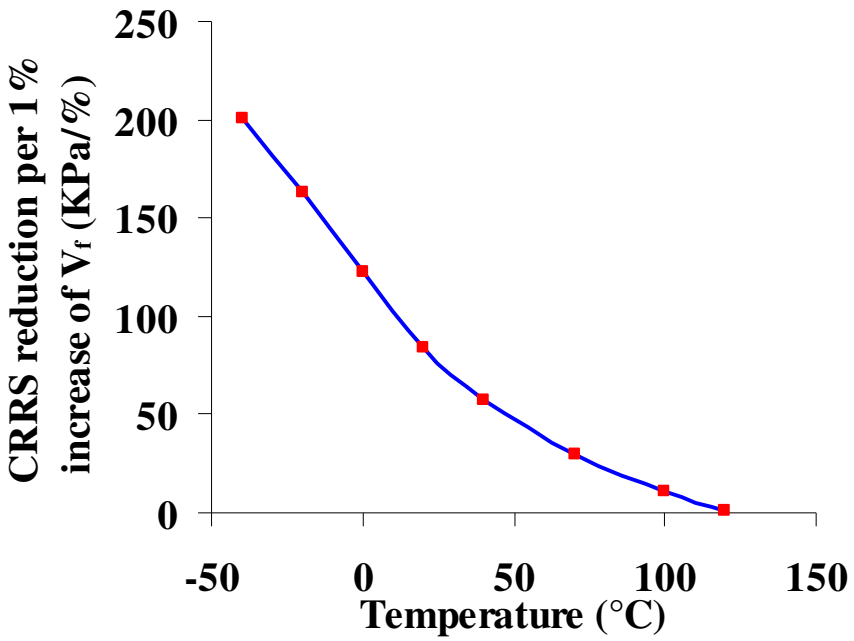

Fig. 5.20 Reduction per 1% increase of fibre volume fraction of CRRS as a function of temperature

The dependence of σ_{rad} on V_f is inversely related to temperature. In other words, σ_{rad} becomes more sensitive to the change of V_f at lower temperature.

In the case of the MBT samples, the fibre volume fraction in each cross-section constantly varies from the mid-span of the droplet length to both ends. This could result in different CRRS distribution at the interface compared to that based on the cylinder model. However, to the author's best knowledge, there seem to be no analytical models currently available to directly deal with such droplet geometry. An indirect approach is to replace the matrix region surrounding the embedded fibre with an equivalent cylinder of matrix in terms of matrix volume by choosing the diameter of the matrix cylinder to preserve the total amount of matrix material [37]. If the droplet of MBT samples is assumed to have an ellipsoid shape, the total volume, V, will be

$$V = \frac{4\pi}{3}\left(\frac{D_m}{2}\right)^2\left(\frac{L_e}{2}\right) \qquad (5.5)$$

The volume fraction of the fibre is then

$$V_f = \frac{\pi D_f^2 L_e}{4V} = 1.5\left(\frac{D_f}{D_m}\right)^2 \qquad (5.6)$$

The diameter of the converted matrix cylinder is then

$$D_m^{'} = D_m \Big/ \sqrt{1.5} \qquad (5.7)$$

In fact, whichever value is adopted as the diameter of the matrix cylinder does not significantly affect the calculated σ_{rad} since σ_{rad} is ultimately dependent on V_f as shown in Appendix (E). As long as the droplet is not too small, σ_{rad} can always be regarded to be independent of the converted droplet diameter as demonstrated above.

The discussion above may justify use of the average droplet diameter of 320 μm in the calculation of σ_{rad}. This may be further checked by examining the V_f dependence of measured IFSS for neat GF-PP47. According to Equation (5.4), if μ_{st} and $\tau_{ult}(T_{ref})$ remain constant at a given temperature, τ_{ult} will change with V_f in MBT samples due to the variation in σ_{rad}. Figure 5.21 presents a plot of measured IFSS against V_f of MBT samples at various temperatures.

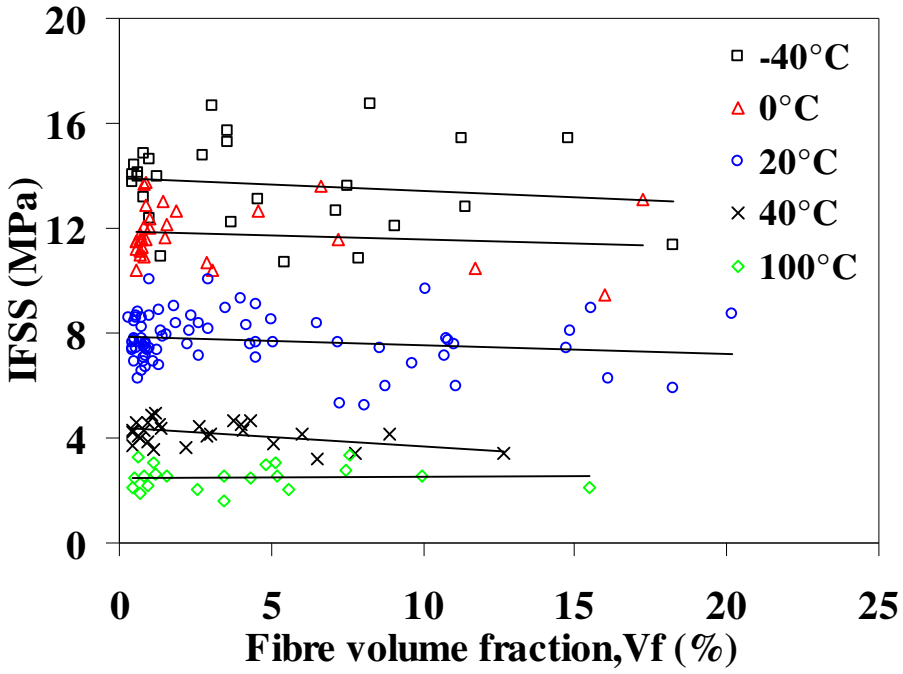

Fig. 5.21 Plot of measured IFSS versus V_f in MBT samples at various temperatures

The straight lines are inserted into the figure to indicate the principal trend of data points and do not represent any data fitting. They do seem to indicate that the measured IFSS tends to slightly decrease as V_f increases. However, if this was the case, such tendency would become more obvious at lower temperature as suggested by the results shown in Figure 5.20. Nevertheless, this does not seem to be the case in the results in Figure 5.21.

From analysis above, one can see that neither the linear model nor the cylinder model can fit the IFSS data with a single value of CSF. It is said that CSF may be expressed by molecular (adhesion) component of the frictional force and the deformation component caused by the introduction of microroughnesses into the softer of the two working bodies and their deformation of the surface layer [38]. The former implies that the CSF is associated with the adhesive interaction at the interface and is said to normally decrease with temperature, while the latter is said to monotonically increase with temperature. The overall correlation between CSF and temperature depends on the result of superimposition of these two components and in turn the materials that come into contact, surface state and processing conditions. Therefore, it is not reasonable to assume a constant CSF in the calculation of IFSS at different temperatures. Wróbel et al showed in temperature range of 25°C to 60°C CSF for low density polyethylene can vary significantly [39]. Clearly, investigation of temperature dependence of CSF between the glass and the polypropylene should be recommended in future work.

Apart from temperature dependence of CSF, it is also worth noting that the cylinder model assumed infinitely long cylinders with definite elastic behaviour. This leads to the situation that no shear stress develops at the interface. This might not be true with finite-length cylinders, in which interfacial shear stress will develop near the cylinders' ends as shown by Quek's model [40]. In addition, Quek's model also showed the residual radial stress at the ends of the single fibre composite is actually tensile. Analysis of stress distribution in the single fibre pull-out test has revealed that the radial stress at the interface changes from tensile to compressive along the fibre length [40]. This tensile stress caused by the Poisson effect, together with the

tensile stress resulting from RTS, could weaken the interface in the vicinity of the loaded free fibre and even give rise to premature failure during the pull-out test.

Neither of these models took into account polymer viscoelasticity, which could lead to relaxation of RTS. The stress relaxation to the CRS can be very dramatic for the semicrystalline matrix as shown in [41]. Such relaxation is expected to become more significant above glass transition temperature (T_g) and lead to lower level of CRS. The stress state is probably also strongly perturbed by the presence of inhomogeneous cooling stresses in the polymeric droplet, and in the embedded portion of the fibre. These stresses must be accounted for in the calculation of the interfacial shear strength.

It can be seen from the results presented in Figure 5.15 that at room temperature the fibre-matrix adhesion only makes up of 29% of measured IFSS, while the CRRS is responsible for 71% of measured IFSS, which supports the hypothesis that the principal contribution to apparent IFSS in GF-PP results from a combination of CRRS and static friction at the fibre-matrix interface. Moreover, there is a very interesting correlation between this percentage and the results in Figure 3.18. For the first 2 minutes, the measured IFSS already reaches 5 MPa, which coincides with 71% of the highest IFSS measured in this work. This could be mainly attributed to the CRRS since wet-out of the fibre surface by molten resin has a time dependence whereas the same magnitude of CRRS will be introduced as long as the fibre-matrix system is equilibrated at the elevated temperature during heating. This implies that the sequent increase in measured IFSS after 2 minutes may solely arise from improvement of wetting.

5.4 Summary

It proved very difficult to form testable PP microdroplet under nitrogen at given thermal conditions due to high viscosity of the polymer. In order to investigate the temperature dependence of the measured IFSS of neat GF-PP47, the microbond test has been successfully adapted to be carried out in the temperature controlled environment of a thermo-mechanical analyser. Excellent comparability was obtained for the IFSS of GF-PP47 measured at room temperature by the TMA-microbond and the Instron-microbond test configurations. TMA-microbond test was carried out in the range -40°C up to 100°C and an excellent linear relationship between the debonding force and embedded area was held for the results obtained from TMA-microbond test at all chosen temperatures. The temperature dependence of IFSS of neat GF-PP47 showed a highly significant inverse dependence on testing temperature.

Both simple linear model and classic concentric cylinder model were used to obtain the compressive radial residual stress (CRRS) and little difference was found in the calculation. The measured IFSS at different temperatures was fit by a simple coulomb friction law combined with different values for coefficient of static friction (CSF) and estimated CRRS.

The IFSS at stress free temperature was estimated to be 2.1 MPa, which, together with the combination of CRRS and CSF may fully account for the measured IFSS for GF-PP. CRRS proved to be mainly responsible for the stress transfer capacity at the interface, making up of 71% of measured IFSS at room temperature. This supports the hypothesis that the principal contribution to apparent IFSS in GF-PP results from

a static friction resulting from the combination of CRRS and CSF at the fibre-matrix interface.

Finally one can see that the results from micromechanical tests carried out in chapter 3–5 address different aspects of PP-GF microcomposites, which involve only a single fibre embedded in the matrix. One of the obvious differences between a microcomposite and a macrocomposite is the fibre volume fraction and gross interfacial area. The PP-GF macrocomposite with very high fibre volume fraction may lead to low CRRS and in turn low IFSS. Regardless of the different scales, the optimal processing time for PP47-GF appears to be at least longer than 4 minutes when the processing temperature is set to be 220°C. The influence of thermo-oxidative degradation of PP in macrocomposite is likely to be less concerned than in microcomposite since the oxygen availability is normally quite low during composite processing and S/V is very low for the former.

References

[1] Kim J,Mai Y. Engineered Interfaces in Fiber Reinforced Composites. 1998, Oxford: Elsevier Science Ltd.

[2] Favre J. Residual thermal stresses in fibre reinforced composite materials - A review Journal of the Mechanical Behavior of Materials 1988;1(1-4):37-53.

[3] Parlevliet PP, Bersee HEN,Beukers A. Residual stresses in thermoplastic composites--A study of the literature--Part I: Formation of residual stresses. Composites Part A: Applied Science and Manufacturing 2006;37(11):1847-1857.

[4] Parlevliet PP, Bersee HEN,Beukers A. Residual stresses in thermoplastic composites--A study of the literature--Part II: Experimental techniques. Composites Part A: Applied Science and Manufacturing 2007;38(3):651-665.

[5] Parlevliet PP, Bersee HEN,Beukers A. Residual stresses in thermoplastic composites - a study of the literature. Part III: Effects of thermal residual stresses. Composites Part A: Applied Science and Manufacturing 2007;38(6):1581-1596.

[6] Nairn JA,Zoller P. Matrix solidification and the resulting residual thermal stresses in composites. Journal of Materials Science 1985;20(1):355-367.

[7] Detassis M, Pegoretti A, Migliaresi C,Wagner HD. Experimental evaluation of residual stresses in single fibre composites by means of the fragmentation test. Journal of Materials Science 1996;31(9):2385-2392.

[8] Barnes JA,Byerly GE. The formation of residual stresses in laminated thermoplastic composites. Composites Science and Technology 1994;51(4):479-494.

[9] Young RJ,PA L. Introduction to polymers. 1991, London: Chapman & Hall.

[10] Kim KS, Hahn HT,RB C. The effect of cooling rate on residual stress in a thermoplastic composite. Journal of Composite Technology and Research 1989;11(2):47-52.

[11] Youssef Y,Denault J. Thermoformed glass fiber reinforced polypropylene: Microstructure, mechanical properties and residual stresses. Polymer Composites 1998;19(3):301-309.

[12] Di Landro L,Pegoraro M. Evaluation of residual stresses and adhesion in polymer composites. Composites Part A: Applied Science and Manufacturing 1996;27(9):847-853.

[13] Nairn JA. Thermoelastic analysis of residual stresses in unidirectional, high-performance composites. Polymer Composites 1985;6(2):123-130.

[14] Wagner HD,Nairn JA. Residual thermal stresses in three concentric transversely isotropic cylinders: Application to thermoplastic-matrix composites containing a transcrystalline interphase. Composites Science and Technology 1997;57(9-10):1289-1302.

[15] Quek MY,Yue CY. Axisymmetric stress distribution in the single filament pull-out test. Materials Science and Engineering: A 1994;189(1-2):105-116.

[16] Shokrieh MM,AR GM. Finite element modeling of residual thermal stresses in fibre-reinforece compoistes using different representative volume elements. in The World Congress on Engineering. 2010. London.

[17] Unger WJ,Hansen JS. The Effect of Cooling Rate and Annealing on Residual Stress Development in Graphite Fibre Reinforced PEEK Laminates. Journal of Composite Materials 1993;27(2):108-137.
[18] Kim BW,Nairn JA. Experimental verification of the effects of friction and residual stress on the analysis of interfacial debonding and toughness in single fiber composites. Journal of Materials Science 2002;37(18):3965-3972.
[19] Filiou C,Galiotis C. In situ monitoring of the fibre strain distribution in carbon-fibre thermoplastic composites1. Application of a tensile stress field. Composites Science and Technology 1999;59(14):2149-2161.
[20] Filiou C, Galiotis C,Batchelder DN. Residual stress distribution in carbon fibre/thermoplastic matrix pre-impregnated composite tapes. Composites 1992;23(1):28-38.
[21] Chung DDL. Continuous carbon fiber polymer-matrix composites and their joints, studied by electrical measurements. Polymer Composites 2001;22(2):250-270.
[22] Zhang B, Yang Z,Sun X. Measurement and analysis of residual stresses in single fiber composite. Materials & Design 2010;31(3):1237-1241.
[23] Kim K-Y,Ye L. Interlaminar fracture toughness of CF/PEI composites at elevated temperatures: roles of matrix toughness and fibre/matrix adhesion. Composites Part A: Applied Science and Manufacturing 2004;35(4):477-487.
[24] Thomason JL. Dependence of interfacial strength on the anisotropic fiber properties of jute reinforced composites. Polymer Composites 2010;31(9):1525-1534.
[25] Thomason JL. Interfaces and interfacial effects in glass reinforced thermoplastics. in 28th Risø International Symposium on Materials Science. 2007. Risø National Laboratory, Roskilde, Denmark.
[26] Quek MY. Analysis of residual stresses in a single fibre-matrix composite. International Journal of Adhesion and Adhesives 2004;24(5):379-388.
[27] Carroll BJ. Equilibrium conformations of liquid drops on thin cylinders under forces of capillarity. A theory for the roll-up process. Langmuir 1986;2(248-250.
[28] McHale G, Newton MI,Carroll BJ. The Shape and Stability of Small Liquid Drops on Fibers. Oil & Gas Science and Technology 2001;56(1):47–54.
[29] McHale G, Käb NA, Newton MI,Rowan SM. Wetting of a High-Energy Fiber Surface. Journal of Colloid and Interface Science 1997;186(2):453-461.
[30] McHale G,Newton MI. Global geometry and the equilibrium shapes of liquid drops on fibers. Colloids and Surfaces A: Physicochemical and Engineering Aspects 2002;206(1-3):79-86.
[31] McHale GR, S.M.; Newton, M.I.; Käb, N.A. Estimation of contact angles on fibers. Journal of Adhesion Science and Technology 1999;13(1457-1469.
[32] Mäder E, Jacobasch HJ, Grundke K,Gietzelt T. Influence of an optimized interphase on the properties of polypropylene/glass fibre composites. Composites Part A: Applied Science and Manufacturing 1996;27(9):907-912.
[33] Grundke K, Uhlmann P, Gietzelt T, Redlich B,Jacobasch HJ. Studies on the wetting behaviour of polymer melts on solid surfaces using the Wilhelmy balance method. Colloids and Surfaces A: Physicochemical and Engineering Aspects 1996;116(1-2):93-104.

[34] Biro DA, McLean P,Deslandes Y. Application of the microbond technique: Characterization of carbon fiber-epoxy interfaces. Polymer Engineering & Science 1991;31(17):1250-1256.
[35] Biro DA, Pleizier G,Deslandes Y. Application of the microbond technique: Effects of hygrothermal exposure on carbon-fiber/epoxy interfaces. Composites Science and Technology 1993;46(3):293-301.
[36] Di Landro L,Pegoraro M. Carbon fibre thermoplastic matrix adhesion. Journal of Materials Science 1987;22(6):1980-1986.
[37] Nairn JA. Analytical fracture mechanics analysis of the pull-out test including the effects of friction and thermal stresses. Advanced Composite Letters 2000;9(6):373-383.
[38] Mikhin NM,Amosov NI. Experimental investigation of the dependence of the coefficient of external static friction on temperature. 1974;
[39] Wróbel G,Szymiczek M. Influence of temperature on friction coefficient of low density polyethylene. Journal of Achievements in Materialsand Manufacturing Engineering 2008;28(1):31-34.
[40] Quek MY. Analysis of residual stresses in a single fibre-matrix composite. International Journal of Adhesion and Adhesives 2004;24(5):379-388.
[41] Di Landro L,Pegoraro M. Evaluation of residual stresses and adhesion in polymer composites. Composites Part A: Applied Science and Manufacturing 1996;27(9):847-853.

Chapter 6

Summary and Further work

It is well known that the fibre-matrix interface has great importance to the mechanical performance of fibre reinforced composite materials. The aim of this project was to supply sufficient experimental data to test the hypothesis that the principal contribution to the IFSS in glass fibre reinforced polypropylene comes from the static friction resulting from the combination of compressive radial residual stress (CRRS) and coefficient of static friction (CSF) at the fibre-matrix interface. Towards accomplishing this aim, three major work programmes have been conducted:

1) Estimation of the level of thermal residual stresses in glass fibre reinforced polypropylene (GF-PP). The measurement of the axial fibre stiffness at room temperature and thermal expansion coefficient of a single glass fibre in axial direction over a wide temperature range were carried out. Similar data were also obtained for the matrix PP. This work was covered in chapter 1 and 2 respectively. The data obtained in chapter 1 and 2 then fed into a theoretical model to calculate the thermal residual stress for GF-PP at different temperatures.

2) Estimation of the interfacial strength of GF-PP. This led to the construction of an appropriate experimental rig and establishment of protocols for the sample preparation for the direct characterisation of the interfacial shear strength (IFSS) of GF-PP. This work formed chapter 3 and 4.

3) Evaluation of temperature dependence of IFSS for GF-PP. A novel technique was developed to carry out the microbond test in a well-controlled temperature environment provided by TMA. The results were then fit on a basis of the hypothesis mentioned above. This work was described in chapter 5.

The summary of the main results presented in each chapter is given below:

In chapter 1, the mechanical characterisation of the reinforcement glass fibres was carried out at room temperature. The standard single fibre tension test was employed to measure the tensile properties of both uncoated and APS-coated glass fibres over a gauge length range from 5 mm to 80 mm. The measured Young's modulus for uncoated fibres was found to be 3 GPa higher than that for APS-coated fibres. Further confirmation on this result is required by using more accurate techniques such as the ultrasonic method. The data for the tensile strength was fit by the classic two parameter Weibull analysis. The results obtained from uncoated fibres were found to be reasonably explained by unimodal Weibull distribution whereas the APS-coated fibres show a multiple flaw distribution, which requires the maximum likelihood method to estimate the unknown parameters of Weibull analysis in the future. Compared to uncoated fibres, APS-coated fibres showed considerably higher strength controlled by less severe flaws but no significant effect on the strength controlled by the most severe flaws. This result is contrary to that found in the literature and subject to further verification by conducting the same tests on in house-coated fibres.

Axial CLTE of a single uncoated glass fibre was measured in TMA with the aid of plaster as the sample holder material. Temperature range covered low operating temperature up to processing temperature (approximately -40°C to 240°C) of GF-PP composites in most applications. The preliminary results showed that the CLTE of the uncoated E-glass fibre was found to be fairly constant in the temperature range of 20°C–300°C with the value close to 5 μm/(m·°C), which is usually assumed in various calculations associated with the CLTE of E-glass fibre. The protocol for the procedure to this characterisation needs improving through further more measurements.

In chapter 2, the thermal and thermo-mechanical characterisation of the matrix PP with different molecular weights (MW) was described. The results from DSC showed that PP grades with low MW tended to crystallise at higher temperature and gave rise to a relatively greater crystallinity. This was in agreement with the DMA results, which suggested that PP with low MW tended to give relatively high dynamic moduli above T_g. Below T_g, however, high MW grade had higher dynamic modulus, which might be related to the larger number of tie-molecules. $T_g \approx 2$°C was obtained for PP47 by both DMA and TMA. In addition, the tensile properties of PP47 at small strain were obtained by a set of normal unaxial tensile tests, including elastic modulus, 0.2% offset yield strength, and tensile strength at yielding, which was used in chapter 3 to estimate the shear strength at yielding for PP47.

In chapter 3, the microvise with controllable shearing plates was manufactured from scratch in the laboratory. The protocols for sample preparation for both microbond and single fibre pull-out tests were established. The testing process could

be monitored by a stereo-microscope until the fibre was pulled out the matrix. Excellent compatibility was obtained for these two methods and the results for IFSS exhibited a significant linear relation between the maximum load and fibre embedded area, giving a value of 7.3 MPa for IFSS of neat GF-PP47. Consequently a ductile interfacial fracture was concluded to be the most probable interfacial failure mode for the composite system studied in this work. The CSF was estimated to be in the range from 0.27±0.03 to 0.97±0.01 for neat GF-PP47.

In addition, the effects of processing time in sample preparation and molecular weight on the measured IFSS were also investigated. The results indicated that approximately 70% of the bond strength in neat GF-PP47 could be achieved within the first 2 minutes of heating at 220°C. The measured IFSS increased significantly within the first 4 minutes and levelled off afterwards. Lower MW PP tended to yield higher IFSS. These results emphasised the important role of wetting in interfacial adhesion of GF-PP.

In chapter 4, the effect of an originally unexpected variable, thermo-oxidative degradation of PP matrix, on the measured IFSS for GF-PP was studied. It was found that PP microdroplets in the standard microbond test suffered considerable thermo-oxidative degradation when they were fabricated in air. Degradation of the PP droplets proved very detrimental to the measured IFSS of GF-PP47. Studies on thermo-mechanical properties of both degraded PP microbond and macroscopic samples showed that the change in these properties was likely to be the cause for the decrease of IFSS in terms of a decrease in CRRS at the interface. Further work may extend to investigating how this degradation in PP would affect the mechanical

properties of macroscopic composites of GF-PP47 and how this would be related to the use of recycled PP in PP composites.

In chapter 5, the microbond test was successfully adapted to be carried out in a temperature controlled environment provided by a TMA. Excellent comparability was obtained for the IFSS of GF-PP47 measured at room temperature by the TMA-microbond and the Instron-microbond test configurations. TMA-microbond test was carried out in the temperature range -40°C up to 100°C and results showed a highly significant inverse dependence of measured IFSS on testing temperature, particularly at the PP glass transition region.

The IFSS at stress free temperature was estimated to be 2.1 MPa, which, together with the static friction resulting from the combination of CRRS and CSF may fully account for the measured IFSS for GF-PP. CRRS proved to be mainly responsible for the stress transfer capacity at the interface, making up of 71% of measured IFSS at room temperature. This supports the hypothesis mentioned earlier.

The measured IFSS at different temperature was fit by a simple coulomb friction law combined with different CSF values and estimated CRRS based on both simple linear model and classic concentric cylinder model. The experimental IFSS data fall well within the range of calculated IFSS for CSF values obtained in chapter 3. Further work would involve studies on the temperature dependence of CSF for the interface of GF-PP by measuring the dependence of debonding force on an externally applied hydrostatic pressure at different temperatures.

The accuracy of predicted CRRS will be improved if compressive properties of the polymer matrix and stress relaxation are used. It is therefore recommended that a thermo-mechanical characterisation of compressive properties and the temperature dependence of (compressive) stress relaxation in the polymer matrix should be carried out.

The methodology developed in this work can also be applied to different material systems such as carbon, aramid, and natural fibres combined with other thermoplastics. Note these fibres are known to be anisotropic and thermo-mechanical characterisations should be carried out in both axial and transverse directions. This may also be the case for the matrix when anisotropy is introduced by the presence of transcrystallisation. The measurement of interfacial strength in these systems do not have to be carried out at various temperature as done for GF-PP in this work, if an experimental jig is available to determine the CSF. However, one of merits in the TMA-microbond technique is to evaluate the contribution from adhesive component to the interfacial bond quality by measuring IFSS at the stress free temperature.

The mechanical performance of the fibre-matrix interface has been the main focus throughout this work and this makes the mechanical characterisation of the interface become an essential routine. Therefore, the integration of this work can also be reflected in terms of the mechanical characterisation of the fibre-matrix interface as illustrated in Figure 6.1.

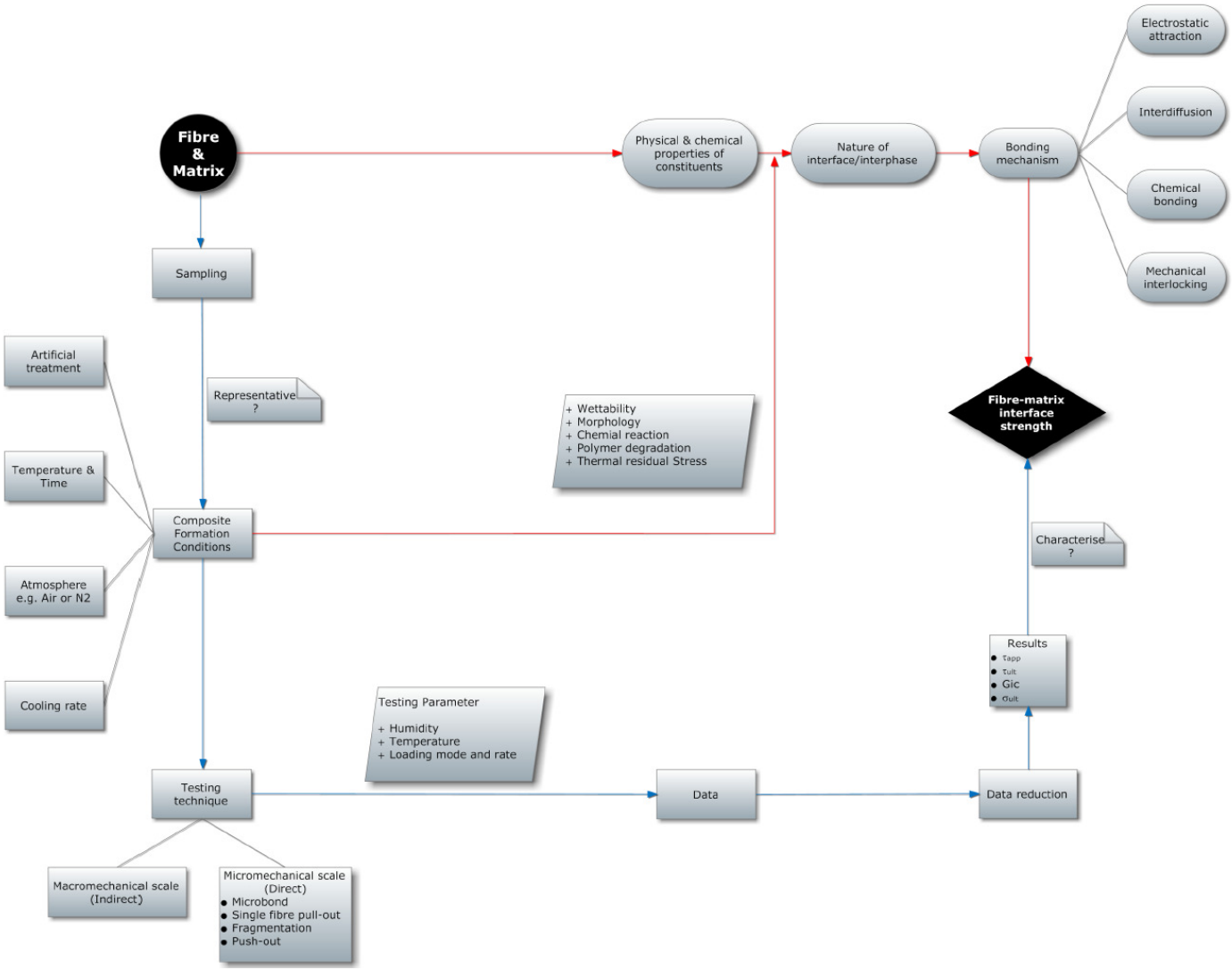

Fig. 6.1 Mechanical characterisation of the fibre-matrix interface

From material's point of view, for a given combination of the reinforcement fibre and the matrix their physical and chemical properties decide the intrinsic nature of the fibre-matrix interface (chapter 1 and 2). The practical characteristics of the interface, however, can be highly altered by the composite formation conditions, including processing time, temperature, and atmosphere (chapter 3 and 4), cooling rate, and various artificial treatments such as surface coating and additives. These factors could strongly influence the nature of the interface through effects on wettability (chapter 3), morphology, degradation (chapter 4), chemical reaction and thermal residual stress (chapter 5). The ultimate nature of the interface decides what bonding mechanisms (usually multiple) will take place across the interface and what level of ultimate interfacial strength should be expected.

From mechanical characterisation's point of view, the first thing that comes to mind should be whether the material selected will be a representative sample and indicative of the properties of bulk material (chapter 1 and 2). This becomes extremely important when it comes to the micromechanical characterisation since only a tiny amount of material may be required to meet the entire sample demand for a study. The composite formation conditions must be strictly controlled throughout the study since they can strongly affect the nature of the fibre-matrix interface (chapter 3), otherwise the additional complexities (i.e. variables) could be introduced (chapter 4). It is desirable to have a mechanical characterisation technique that is free from the influence of sample geometry and can generate direct information on the fibre-matrix interface (chapter 3). It must also put a strict control on parameters for testing such as humidity, temperature, and loading mode and rate, unless one of these variables is intended to be studied (chapter 5). The obtained data should be reduced

with appropriate methods, whose underlying assumptions have a high probability to be valid and theories can well account for the process of interfacial failure in the test. The reduced data should give rise to some type of characteristic parameters, which are able to truly characterise the strength of the fibre-matrix interface.

Appendix (A)

Statistical Strength Of Analysis Of The Glass Fibres

The results for E-glass fibre strength and Weibull distribution are presented according to ASTM C1239-07, which suggests that the Weibull plot (i.e. $\ln\left[-\ln\left(1-P_L(\sigma)\right)\right]$ vs. $\ln(\sigma)$ plot) should have the ordinate axis and abscissa labelled as probability of failure and failure stress respectively. Figure A-1 present these Weibull plots for uncoated and APS-coated glass fibres tested at a variety of gauge lengths.

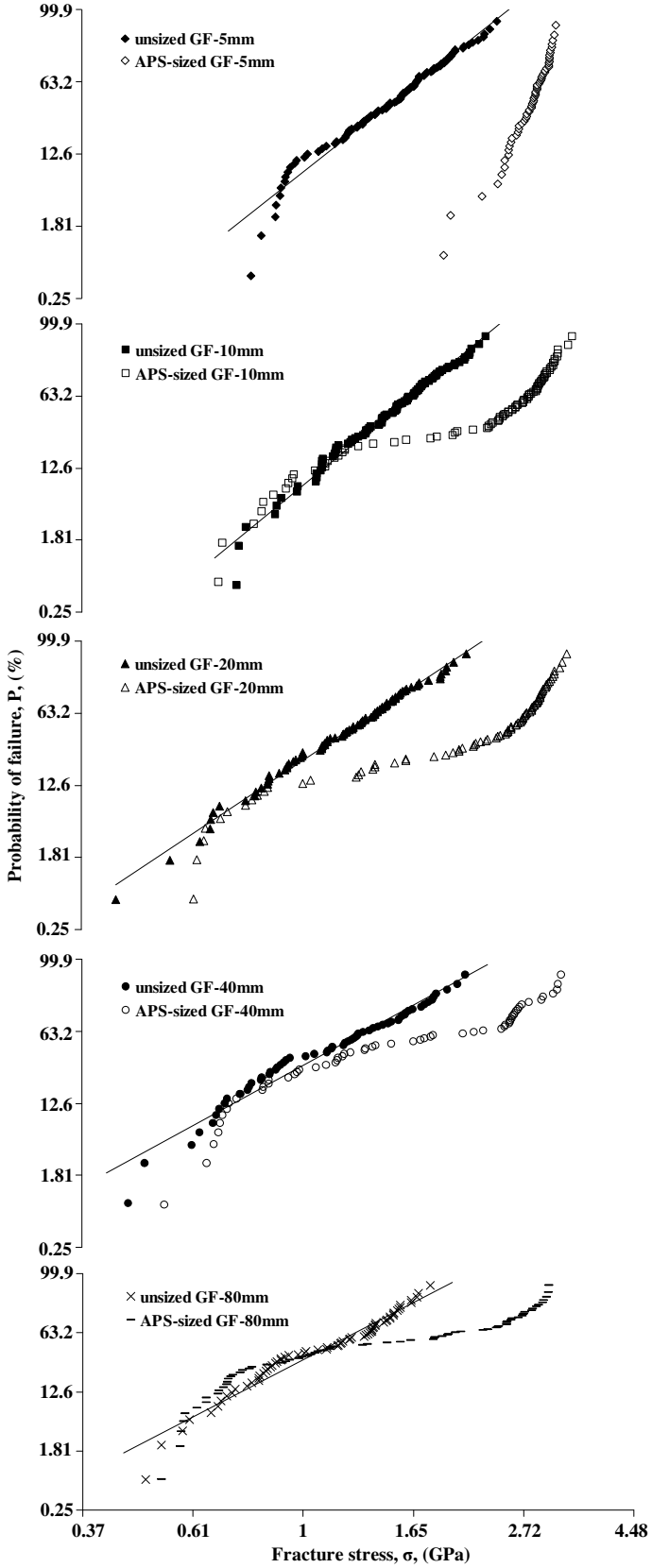

Fig. A-1 Comparison of Weibull plots of uncoated and APS-coated glass fibres

It can be seen in Figure A-1 that the measured strength for uncoated E-glass fibres is quite low compared with the intrinsic fatigue strength, 3.5 GPa, indicating there must have been damage resulting from subsequent processes (e.g. roving) after fibre formation and/or extra handling in sample preparation. In addition, the experimental data obtained from the uncoated glass fibres appear to show linear trends in the Weibull plots for each gauge length. This implies that the failure of the uncoated glass fibres may be dominated by one flaw population, which can be described by unimodal Weibull distribution. It also means that the graphic method can be used to estimate the unknown parameters for the Weibull distribution. Table A-1 contains estimated parameters, correlation coefficient, R^2 of linear fitting, and mean strength, $\overline{\sigma}$ for uncoated E-glass fibre at various gauge lengths.

Table A-1 Fibre strength and Weibull analysis of uncoated glass fibre

Gauge length (mm)	Number of sample	Mean strength, $\overline{\sigma}$, (GPa)	Weibull modulus	Characteristic strength, σ_0', (GPa)	R^2
5	107	1.55	4.8	1.69	0.97
10	97	1.51	5.0	1.64	0.98
20	89	1.26	4.1	1.38	0.99
40	60	1.19	3.3	1.34	0.96
80	72	1.14	3.9	1.26	0.96

It is found that the experimental data are well approximated by the unimodal Weibull distribution except for the weakest fibres. This discrepancy is likely to be caused by the damage done to the fibres in the specimen preparation process. R^2 coefficients are very close to 1, indicating a good degree of linearity. The values of 3-5 for Weibull modulus are obtained from the slopes of the fitting lines in the Weibull plot and agree with typical values found in the literature. Such low values indicate that the strength of uncoated E-glass fibres statistically vary a great deal due to flaw

heterogeneity in terms of flaw size, shape, and orientation. Weibull characteristic strength corresponds to a failure probability of 63.2% and is found to decrease as the gauge length increases. This is the manifestation of dimension effect, which leads the Weibull plot to completely shift towards lower stress with increase of the gauge length as seen in Figure A-1. It means that it is more probable to encounter more severe flaws as the fibre length increases. Despite the fact that the data at each gauge length can be well fit by the unimodal Weibull distribution, it seems unsafe to claim that the failure at gauge lengths from 5 to 80 mm is controlled by just one type of flaw distribution, since the Weibull modulus varies quite significantly with the gauge length. Particularly for the data obtained from 40 and 80 mm fibres the Weibull modulus is much lower than others. Carefully inspecting their Weibull plots in Figure 1.22 further reveals that the data may be fit better using multimodal Weibull distribution. Thus, the Weibull modulus may have been underestimated in a way as pointed out by Beetz. This implies that the conclusion that the linear regression plots are linear only by judging from the R^2 coefficients can be misleading. In fact, it is said that a more robust statistical analysis of linear regression revealed that in all cases the assumption of linearity is disputable.

The APS-coated E-glass fibre, on the other hand, clearly presents nonlinear Weibull plots except the one at 5 mm gauge length. These nonlinear curves are likely to be fit with three linear lines. This suggests that the failure of APS-coated glass fibres at gauge length from 10 mm to 80 mm is controlled by three distinct types of flaw populations *A*, *B*, and *C* in the order of severity. The overall failure distribution is the result of a competition between these flaw populations, which may be described by the multimodal Weibull distribution. It also means that the graphic

method is no long valid to estimate the Weibull parameters and numerical methods are required. One of the most commonly used methods is maximum likelihood technique, in which multiple flaw distributions are assumed to coexist in a certain way, the corresponding likelihood function is then derived, and finally the numerical procedures are required to yield independent sets of parameter estimates for respective flaw distributions. This work should be carried out in the future to further analyse the results for the APS-coated glass fibres. The failure strength distribution of 5 mm fibres appears to be controlled by only type *C* flaws, which account for high tensile strength in the range of 2.5–3.2 GPa. It is quite unlikely that type *A* and *B* flaws do not show up at all within a large number of 5 mm fibres tested but then emerge as a big portion in the Weibull distribution for 10 mm fibres. This may be due to the end effect, which affects the short fibres to a greater degree in a sense that the failure that occurs near the fibre ends is more likely to be treated as the end effect-related event. Moreover, weaker fibres at 5 mm gauge length were more likely to be broken when the section on both sides of the card is cut away, leaving the fibre free to loading because of less slack in 5 mm fibres. In addition, the test started off with 5 mm fibres and there could be the tendency to the selection of strong fibres because of operator's skills at the early stage. To partly deal with this problem, a card puncher will be designed and manufactured for the further work to more efficiently produce the card frame with small cut-out as well as reduce the width of the card section that will be cut away. It can also be observed from Figure A-1 that the distribution related to type *C* flaws gradually fades out the Weibull distribution as the fibre length increases. In contrast, the distribution associated with type *A* and *B* flaws form the majority of the Weibull plot as the gauge length increases. It is obvious that

the more severe flaws have greater separation and vice versa. The analysis of the Weibull plot can be effectively supported by fractography, which should also be recommended as further work.

So far we have not touched the most interesting feature in Figure A-1. The comparison of Weibull plots between uncoated and APS-coated glass fibres clearly shows that there is no doubt about strength improvement brought about by the APS coating on the glass fibres. In the same Weibull coordinate the Weibull plots of uncoated fibres tested at every gauge length are all located on the left of those obtained from APS-coated fibres. More interestingly, the distribution related to type *A* flaws in APS-coated fibres tends to overlap with unimodal Weibull distribution for uncoated fibres, indicating that the failure of uncoated glass fibres are dominated by type *A* flaws. At gauge length 40 and 80 mm the overlap even extends to the distribution related to type *B* flaws. This supports the early speculation on multiple flaw distribution for uncoated glass fibres at 40 and 80 mm, suggesting that the failure of glass fibre at 40 and 80 mm are dominated by both type *A* and *B* flaws. In general, the difference in Weibull plots between uncoated and APS-coated fibres becomes less dramatic as greater portions of both plots overlap between them with the increase of the fibre length. Therefore the effectiveness of strength improvement resulting from APS is dependent on the fibre length. Without knowing the specific mechanism for strength improvement, one of the possibilities for this length dependence could be related to the nonuniformity of APS distribution on fibre surface, which is known to be the case in most sizing applications. The coated fibres with long length, thus, may have a greater probability to encounter an area uncoated by the APS and in turn more likely fracture due to pre-existing severe flaws. As for

the mechanism for strengthening E-glass fibres by coating, it has been proposed that surface coating can have ability to heal the surface flaws when the aggregates chemical species in the coating are small enough to effectively fill the flaw space and increase the crack tip radius. Consequently the concept of critical dimension of flaws was introduced to account for the fact that little difference was found for the strength controlled by the small flaws (i.e. high strength) between uncoated and APS-coated E-glass fibres. Apparently the Weibull plots presented in this work have showed the opposite situation, in which the strength improvement is actually exhibited in high strength part of Weibull plots. In other words, the silane affects the relatively small flaws (e.g. type *B* and *C*) rather than large flaws (e.g. type *A)*. However, this does not necessarily lead to the conclusion that APS coating appears to heal small flaws and leave large flaws unaffected. There may be other possibilities under the healing effect reported in the literature: Compared to the coated fibres, the uncoated fibres suffer more adverse disruption to the fibre surface after fibre forming due to less protection from stress corrosion and more severe abrasion between fibres. The flaws therefore can be created and/or altered in series of processes before testing, including roving process, transportation, and any additional fibre handling in this case. Consequently tensile failure of the uncoated fibres may be controlled by the type A flaws within the gauge lengths studied in this work. However, such explanation only accounts for the fact that there is no overlapping in high strength data in Weibull plots between uncoated and APS-coated fibres and leaves occurrence of overlapping in low strength data unexplained. The latter may be partially attributed to nonuniform silane distribution on the fibre surface as mentioned earlier. More work needs to be carried out to further investigate this.

If the unimodal Weibull distribution is appropriate to explain the experimental data, theoretically the mean strength vs. length plot in log coordinates should yield a linear relation, which can then be fit by the least square method. According to the Equation 1.10, the slope of this plot is another way to obtain the Weibull modulus. Such plot is presented in Figure A-2.

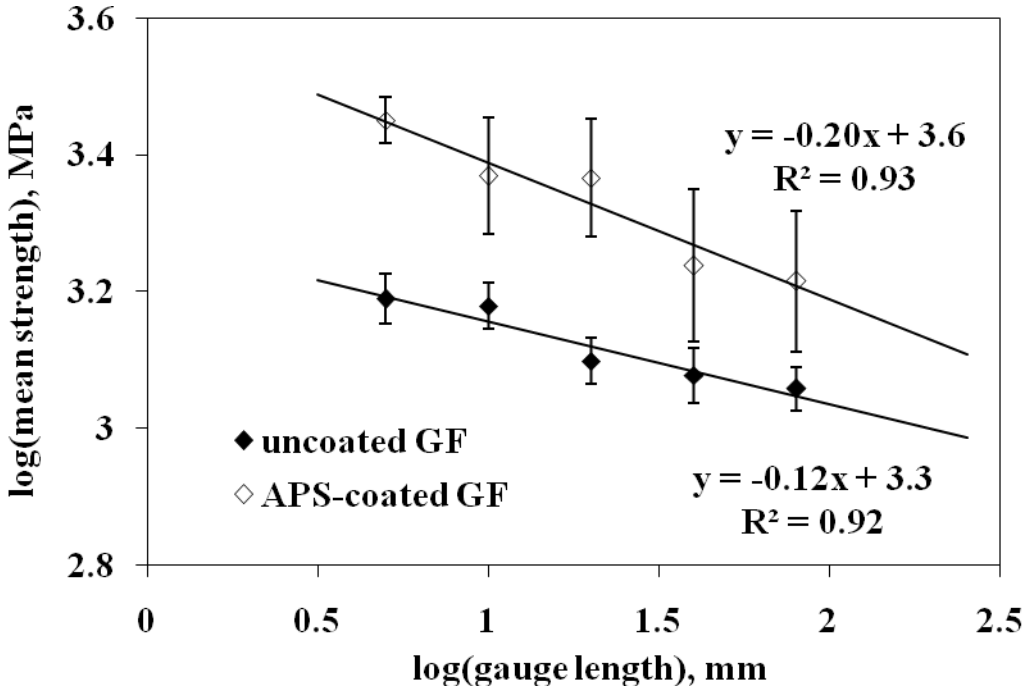

Fig. A-2 Dependence of the mean strength of uncoated glass fibres and average strength of APS-coated glass fibre on gauge length

The error bars correspond to the average strength standard deviation estimated as $S_\sigma / \sqrt{n}$, where S_σ and n are standard deviation of the fibre strength and the number of tests at the given gauge length respectively. Although the data for APS-coated fibre cannot be fit by unimodal Weibull distribution, its log (average strength) vs. log (length) plot is still included into Figure A-2. It turns out that not only the data for uncoated fibre form a straight line in agreement with Equation 1.10, but those for APS-coated fibre appear to show a linear relation as well. It implies that

using this method to analyse the results can sometimes be very misleading. The least squares method only provides a mean value between all the points as shown in Figure A-2. The Weibull modulus for uncoated fibre obtained from the slope of the linear fitting line is 8.3, much higher than any values obtained at individual gauge lengths. The similar situation has been reported in other work and treated as one of the inherent drawbacks in Weibull theory. Despite this discrepancy, the gauge length dependency of fibre strength allows the prediction of average fibre strength at untested gauge lengths. This can be very informative and useful for short fibre applications such as chopped fibre reinforced composites, in which the chopped fibres usually start with the initial length ~4mm and end up with the sub-millimetre length. In practice, extrapolation outside the range of data is always subject to greater uncertainty. Thus, multiple gauge lengths should be tested before using these techniques in an effort to obtain as much information as possible concerning the gauge length dependency of average fibre strength. Nevertheless, one can see from Figure A-2 that there could be no difference in average strength between uncoated and APS-coated E-glass fibres when the length is enough long.

Appendix (B)

Technical Drawings For The Microvise: (i) Vise top, (ii) Vise Bottom And (iii) Vise End

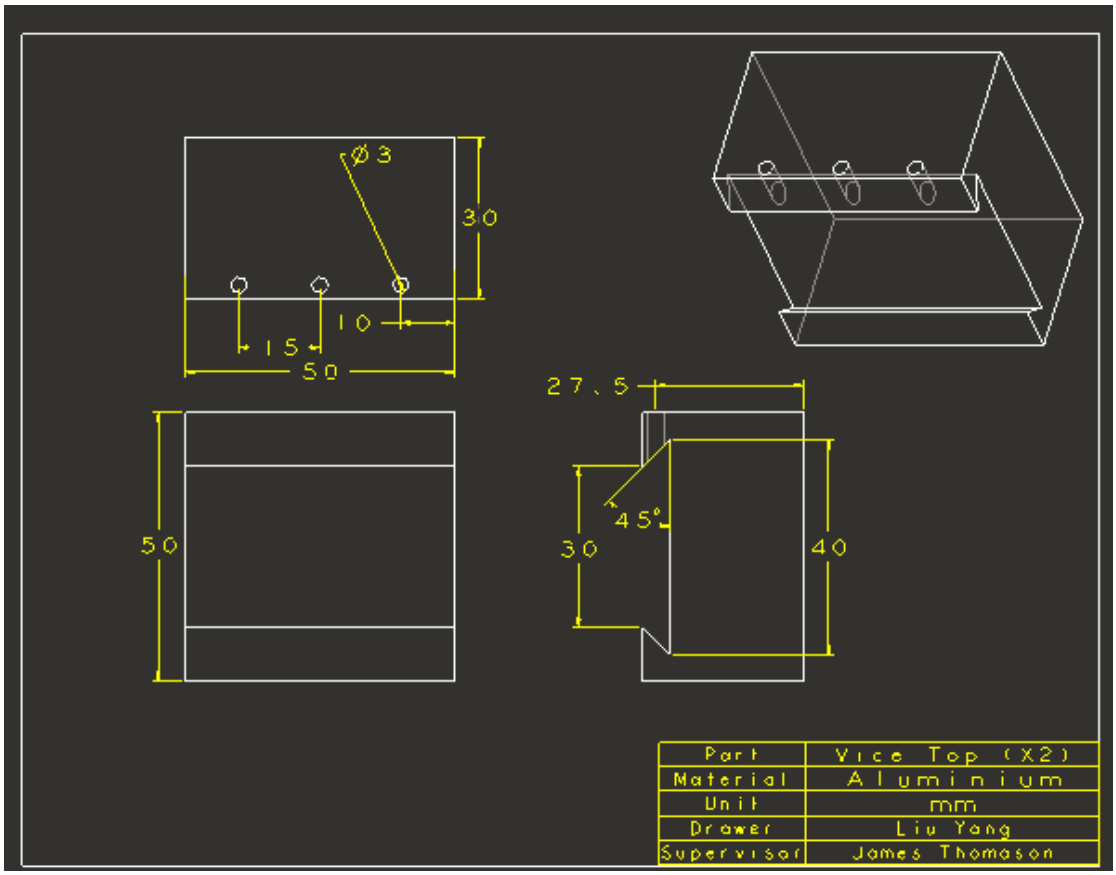

(i)

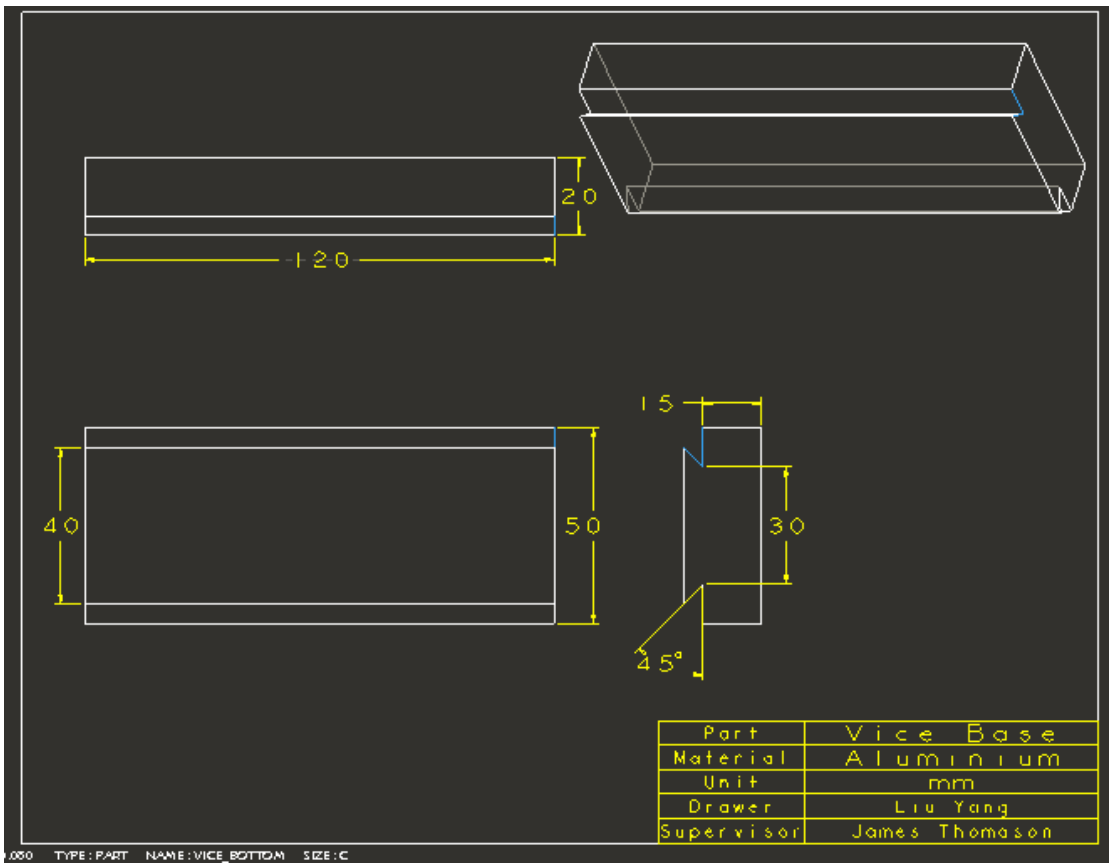
20
120
15
40
50
30
45°
Part
Vice Base
Material
Aluminium
Unit
mm
Drawer
Liu Yang
Supervisor
James Thomason
TYPE:PART
NAME:VICE_BOTTOM
SIZE:C

(ii)

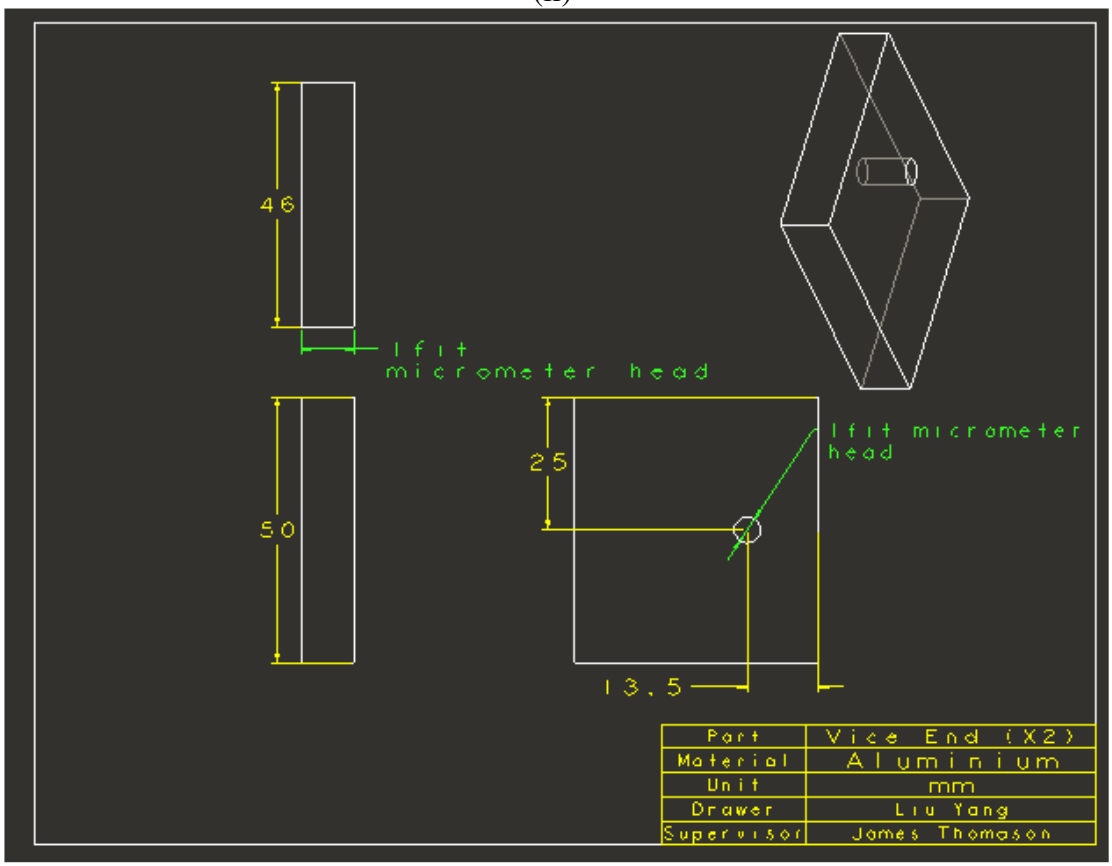
46
1 fit
micrometer head
50
25
1 fit micrometer
head
13.5
Part
Vice End (X2)
Material
Aluminium
Unit
mm
Drawer
Liu Yang
Supervisor
James Thomason

(iii)

Appendix (C)

Contact Angle Analysis for PP Droplet On A Single Glass Fibre

Direct measurement of contact angles, θ, by methods which work well with planar surfaces proved inaccurate when applied to monofilaments and indirect measurement by means of Wilhelmy technique or inverse gas chromatography also have some serious disadvantages. Therefore a number of numerical methods have been developed based on Young-Laplace equation:

$$\Delta P = \gamma_{LV}\left(\frac{1}{R_1}+\frac{1}{R_2}\right) \qquad [C1]$$

where ΔP is the pressure difference between liquid and vapour, γ_{LV} is the interfacial tension and R_1, R_2 are two principal radii of curvature at a point in the surface. The numerical method developed by Wagner was employed here to determine the contact angles for PP47 microdroplets on uncoated E-glass fibres. The programme was run by Mathematica 5.2 and the code can be found in Appendix (D). The results for θ as a function of time are shown in Figure C-1.

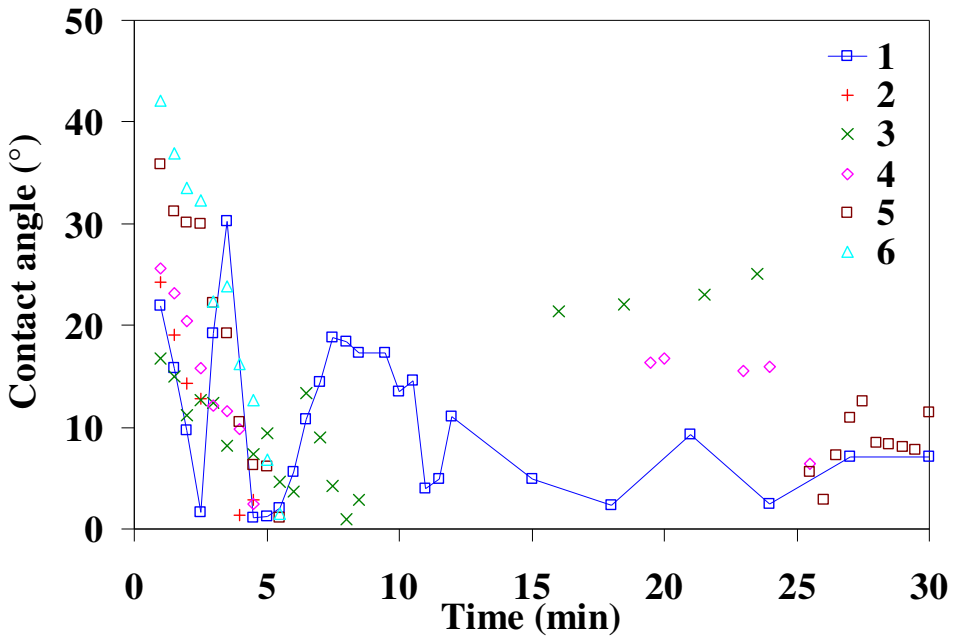

Fig. C-1 Variation in calculated contact angle of PP microdroplets on uncoated E-glass fibres during thermo-oxidative degradation

The contact angle for most samples can only be determined in the early time of heating except the smallest sample, whose calculated contact angle can almost cover the entire heating process. This is not surprising since the numerical method is based on the Young-Laplace equation, which accounts for the pressure difference in equilibrium state. In other words, the method applies to the static fluids, which are in stable equilibrium. However, the system in this study hardly achieves such equilibrium state as described above. Moreover, the numerical method proved quite sensitive to the inputs. Continuously determinable contact angle in the early period of heating may be related to the quasi-equilibrium and the results consistently show a decrease in θ with time. Unexpectedly, θ in the sample 1 can be determined almost in the entire time range of its heat treatment and these data points are connected with each other as shown in Figure C-1. Regardless of the absolute values, it can be clearly seen that θ initially decreases considerably until it reaches 2.5 minutes.

There is abrupt fluctuation in θ between 2.5 minutes and 4.5 minutes, after which the values increases with time and almost goes back to the initial magnitude at 7.5 minutes. After that θ again decreases with time and finally drops to a level, which appears to be less dependent on time. The variation of θ in the sample 1 with the processing time seems to agree well with the results in Figure 4.20 and the relevant discussion. The decrease of θ within the first 2.5 minutes implies the rapid decrease in the droplet diameter. The time range for the abrupt fluctuation in θ coincides with that for occurrence of the kink as shown in Figure 4.22(b). Afterwards the increase of θ corresponds to the rapid decrease of the embedded length as seen in Figure 4.22(b). Less dependence of θ on the processing time after 12 minutes correlate well with the little change in droplet dimensions during that time as shown in Figure 4.22.

Appendix (D)

Mathematica Programme Code For The Calculation Of Contact Angle

```
l = reduced droplet length;

t = reduced droplet thickness;

theta1 = 48.0*Pi/180;

theta2 = 55.0 * Pi / 180;

a = (t*Cos[theta1] - 1.0)/(t - Cos[theta1]);

k =1 - a^2/t^2;

phi = ArcSin[Sqrt[(1 - 1/t^2)/k^2]];

l1 = 2*(a*EllipticF[phi, k] + t*EllipticE[phi, k]);

a = (t*Cos[theta2] - 1.0)/(t - Cos[theta2]);

k = 1 - a^2/t^2;

phi = ArcSin[Sqrt[(1 - 1/t^2)/k^2]];

l2 = 2*(a*EllipticF[phi, k] + t*EllipticE[phi, k]);

theta3 = (theta1 - theta2)*l/(l1 - l2) + (l1*theta2 - l2*theta1)/(l1 - l2);

While[(Abs[theta3 - theta2] > 0.00001), {theta1 = theta2, l1 = l2,

   theta2 = theta3, a = (t*Cos[theta2] - 1.0)/(t - Cos[theta2]),

   k = 1 - a^2/t^2,

   phi = ArcSin[Sqrt[(1 - 1/t^2)/k^2]],

   l2 = 2*(a*EllipticF[phi, k] + t*EllipticE[phi, k]),
```

```
    theta3 = (theta1 - theta2)*
          l/(l1 - l2) + (l1*theta2 - l2*theta1)/(l1 - l2)}
  ]
theta3 = theta3*180/Pi
```

Appendix (E)

Theory Of Pressurized Thick-Walled Cylinder

One cylinder

If a single hollow cylinder with free ends is subjected to the constant axial strain and every cross-section perpendicular to the axis undergoes radial strains only as shown in Figure [1], the equations of equilibrium for an element of material are

$$\frac{d\sigma_r}{dr}+\frac{\sigma_r-\sigma_\theta}{r}=0 \quad \text{[E1]}$$

and

$$\frac{d\sigma_z}{dr}=0 \quad \text{[E2]}$$

The strain-displacement equations are

$$\varepsilon_r=\frac{du}{dr} \quad \text{[E3]}$$

$$\varepsilon_\theta=\frac{u}{r} \quad \text{[E4]}$$

$$\varepsilon_r=\frac{dw}{dz} \quad \text{[E5]}$$

The stress-strain relationships are

$$\varepsilon_r=\frac{\sigma_r}{E}-\frac{v}{E}(\sigma_\theta+\sigma_z)=\frac{du}{dr} \quad \text{[E6]}$$

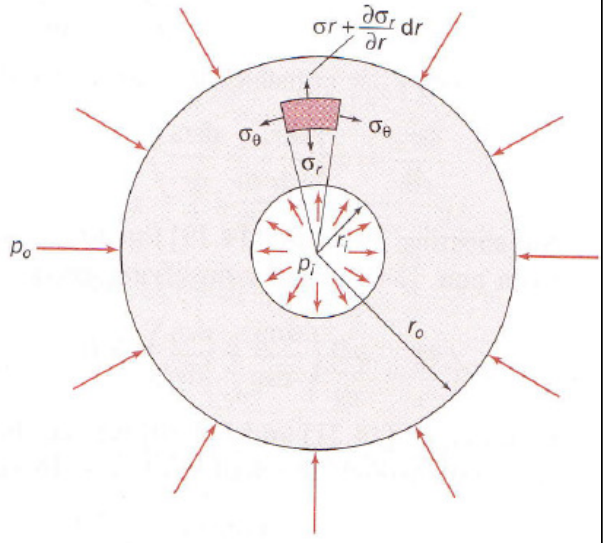

Fig. E-1 Arbitrary cross-sectional slice of a long hollow cylinder subjected to uniformly distributed internal, P_i, and external, P_o,

$$\varepsilon_\theta = \frac{\sigma_\theta}{E} - \frac{v}{E}(\sigma_r + \sigma_z) = \frac{u}{r} \qquad \text{[E7]}$$

$$\varepsilon_z = \frac{\sigma_z}{E} - \frac{v}{E}(\sigma_r + \sigma_\theta) = \frac{dw}{dz} \qquad \text{[E8]}$$

Differentiating eqn. [E7] with respect to *r* gives

$$\frac{E}{r}\left(\frac{du}{dr} - \frac{u}{r}\right) = \frac{d\sigma_\theta}{dr} - v\frac{d\sigma_z}{dr} - v\frac{d\sigma_r}{dr} \qquad \text{[E9]}$$

Substituting for du/dr and u/r from eqns. [E6] and [E7] and simplifying,

$$\frac{1+v}{r}(\sigma_r - \sigma_\theta) = \frac{d\sigma_\theta}{dr} - v\frac{d\sigma_z}{dr} - v\frac{d\sigma_r}{dr} \qquad \text{[E10]}$$

Since ε_z is constant, $d\varepsilon_z/dr = 0$ and differentiating eqn. [E8] gives

$$\frac{d\sigma_z}{dr} = v\left(\frac{d\sigma_r}{dr} + \frac{d\sigma_\theta}{dr}\right) \qquad \text{[E11]}$$

Substituting into eqn. [E10] for $d\sigma_z/dr$ from eqn. [E11] and $(\sigma_r - \sigma_\theta)/r$ from eqn. [E1] and simplifying gives

$$(1 - v^2)\left(\frac{d\sigma_r}{dr} + \frac{d\sigma_\theta}{dr}\right) = 0 \qquad \text{[E12]}$$

From eqns. [E12] and [E11] we see that $d\sigma_z/dr = 0$ and therefore σ_z is constant through the wall thickness. Integrating eqn. [E12] shows that

$$\sigma_r + \sigma_\theta = \text{constant} = 2A \qquad \text{[E13]}$$

Eliminating σ_θ between eqns. [E11] and [E1] gives

$$\frac{d\sigma_r}{dr} + \frac{2\sigma_r - 2A}{r} = 0 \qquad \text{[E14]}$$

from which, multiplying by r^2,

$$2rA - 2r\sigma_r - r^2 \frac{d\sigma_r}{dr} = 0 \qquad \text{[E15]}$$

and

$$2rA - \frac{d}{dr}\left(r^2\sigma_r\right) = 0 \qquad \text{[E16]}$$

By integration,

$$Ar^2 - r^2\sigma_r = B \qquad \text{[E17]}$$

Hence

$$\sigma_r = A - \frac{B}{r^2} \qquad \text{[E18]}$$

and from eqn. [E13],

$$\sigma_\theta = A + \frac{B}{r^2} \qquad \text{[E19]}$$

where A and B are constants which may be found using the boundary conditions. For a linear elastic, isotropic cylinder under internal pressure P_i and external pressure P_o,

the boundary conditions are: at $r = r_i$, $\sigma_r = -p_i$ (pressure being negative in sign); and at $r = r_0$, $\sigma_r = -p_o$,

$$-p_i = A - \frac{B}{r_i^2} \text{ and } -p_o = A - \frac{B}{r_o^2} \qquad \text{[E20]}$$

from which, we get

$$B = \frac{(p_i - p_o) r_i^2 r_o^2}{r_o^2 - r_i^2} \text{ and } A = \frac{p_i r_i^2 - p_o r_o^2}{r_o^2 - r_i^2} \qquad \text{[E21]}$$

Therefore the radial and hoop stresses become

$$\sigma_r = \frac{p_i r_i^2 - p_o r_o^2}{r_o^2 - r_i^2} - \frac{(p_i - p_o) r_i^2 r_o^2}{r^2 (r_o^2 - r_i^2)} \qquad \text{[E22]}$$

$$\sigma_\theta = \frac{p_i r_i^2 - p_o r_o^2}{r_o^2 - r_i^2} + \frac{(p_i - p_o) r_i^2 r_o^2}{r^2 (r_o^2 - r_i^2)} \qquad \text{[E23]}$$

Two cylinders

Let us now consider two concentric cylinders, where the internal cylinder (the fibre) is solid rather than hollow and external cylinder is regarded as the matrix. At the centre of the fibre $r_f = 0$ and this might imply that radial stress in the fibre σ_r^f is infinite, but this cannot be so and therefore *B* must be zero; hence, at all point in the fibre

$$\sigma_r^f = \sigma_\theta^f = A^f \qquad \text{[E24]}$$

and

$$\sigma_z^f = C^f \qquad \text{[E25]}$$

where A^f and C^f are constants. On the other hand, the matrix is subjected to internal pressure from the fibre. The external pressure is atmospheric only and can be neglected in relation to the internal pressure (i.e. $p_o = 0$). According to eqns. [E22] and [E23], we get

$$\sigma_r^m = A^m - \frac{B^m}{r^2} \qquad \text{[E26]}$$

$$\sigma_\theta^m = A^m + \frac{B^m}{r^2} \qquad \text{[E27]}$$

$$\sigma_z^m = C^m \qquad \text{[E28]}$$

where A^m , B^m and C^m are constants. Thus, the problem is reduced to the determination of those five constants. The radial stress boundary conditions are associated with continuity of tractions at interfaces:

$$\sigma_r^m = 0 \text{ at } r = r^m \qquad \text{[E29]}$$

$$\sigma_r^m = \sigma_r^f \text{ at } r = r^f \qquad \text{[E30]}$$

A force balance in the longitudinal direction yields

$$\sigma_z^f V^f + \sigma_z^m V^m = 0 \qquad \text{[E31]}$$

where $V^f = \left(r^f / r^m\right)^2$ and $V^m = 1 - V^f$. By using eqns [E24]–[E28], the conditions [E29]–[E31] yield

$$B^m = A^m \left(r^m\right)^2 \qquad \text{[E32]}$$

$$A^f = A^m \left[1 - \left(\frac{r^m}{r^f}\right)^2\right] = -A^m \frac{V^m}{V^f} \qquad \text{[E33]}$$

$$C^f = -C^m \frac{V^m}{V^f} \qquad \text{[E34]}$$

These expressions reduce the number of unknowns to only two, namely, A^m and C^m, which can be determined by applying the strain-stress relationships:

$$\begin{pmatrix} \varepsilon_r \\ \varepsilon_\theta \\ \varepsilon_z \end{pmatrix} = \begin{pmatrix} 1/E & -v/E & -v/E \\ -v/E & 1/E & -v/E \\ -v/E & -v/E & 1/E \end{pmatrix} \times \begin{pmatrix} \sigma_r \\ \sigma_\theta \\ \sigma_z \end{pmatrix} + \begin{pmatrix} \alpha \\ \alpha \\ \alpha \end{pmatrix} \left(T - T_{ref}\right) \qquad \text{[E35]}$$

where v stands for the Poisson's ratio, E is the Young's modulus, T is the use temperature and T_{ref} is the stress-free temperature. This equation applies to both the fibre and the matrix and superscripts *f* and *m* are used respectively. Assuming there is no interfacial slip between the fibre and the matrix, we have

$$\varepsilon_z^f = \varepsilon_z^m \text{ at } r = r^f \qquad \text{[E36]}$$

$$\varepsilon_\theta^f = \varepsilon_\theta^m \text{ at } r = r^f \qquad \text{[E37]}$$

The eqns [E36] and [E37], combined with the eqn. [E35], yield two simultaneous equations with two unknowns:

$$\begin{pmatrix} Q_1 & Q_2 \\ Q_3 & Q_4 \end{pmatrix} \times \begin{pmatrix} A^m \\ C^m \end{pmatrix} = \begin{pmatrix} K_1 \\ K_2 \end{pmatrix} \left(T - T_{ref}\right) \qquad \text{[E38]}$$

where:

$$Q_1 = 2\left(\frac{v^m}{E^m} + \frac{v^f}{E^f}\frac{V^m}{V^f}\right) \qquad \text{[E39]}$$

$$Q_2 = -\left(\frac{1}{E^m} + \frac{1}{E^f}\frac{V^m}{V^f}\right) \qquad \text{[E40]}$$

$$Q_3 = -\left[\left(\frac{1-v^f}{E^f} + \frac{1+v^m}{E^m}\right)\frac{V^m}{V^f} + \frac{2}{E^m}\right] \qquad \text{[E41]}$$

$$Q_4 = \frac{v^m}{E^m} + \frac{v^f}{E^f}\frac{V^m}{V^f} \qquad \text{[E42]}$$

$$K_1 = K_2 = \alpha^m - \alpha^f \qquad \text{[E43]}$$

Appendix (F)

Matlab Programme Code For The Calculation Of Residual Thermal Stress Based On Two Cylinders (the sign "%" is used to indicate the description only and will not be run in the programme)

```
function [fr,fz,mz]=fun1(Data)

% fr is the residual radial stress (MPa) on the fibre, fz is the residual longitudinal stress (MPa) in the fibre, and mz is the residual longitudinal stress (MPa) in the matrix

[R, L]=size(Data);

fr = zeros(R, 1);

fz = zeros(R, 1);

mz = zeros(R, 1);

for i=1:R

   Em=Data(i,2);

   em=Data(i,3);

   [sfr,sfz,smz]=f(Em,em);

   fr(i, 1)=sfr;

   fz(i, 1)=sfz;

   mz(i, 1)=smz;

end
```

```
end

function [sfr,sfz,smz]=f(Em,em)

um=0.35;

%  um is Poisson's ratio of the matrix

uf=0.22;

%  uf is Poisson's ratio of the fibre

Ef=78700;

%  Ef is Young's modulus (GPa) of the fibre

ef=5e-6;

%  ef is CLTE (°C^-1) of the fibre

rf=9;

%  rf is fibre radius (μm)

rm=160;

%  rm is droplet radius (μm)

vf=rf^2/rm^2;

vm=1-vf;

k1=2*(um/Em+uf/Ef*vm/vf);

k2=-(1/Em+1/Ef*vm/vf);

k3=-(((1-uf)/Ef+(1+um)/Em)*vm/vf+2/Em);

k4=k1/2;
```

```
k5=(ef-em);

K=[k1 k2;k3 k4];

b=[k5;k5];

x=K\b;

Am=x(1);

Cm=x(2);

Bm=Am*rm^2;

Af=-Am*vm/vf;

Cf=-Cm*vm/vf;

sfr=Af;

sfl=Af;

sfz=Cf;

smz=Cm;

end
```